Calhoun
Institutional Archive of the Naval Postgraduate School

Calhoun: The NPS Institutional Archive

DSpace Repository

Theses and Dissertations 1. Thesis and Dissertation Collection, all items

1972-09

A numerical investigation of the long-term transient behavior in a coupled atmosphere-ocean model.

Lambertson, Wayne Roger

Monterey, California. Naval Postgraduate School

http://hdl.handle.net/10945/16266

This publication is a work of the U.S. Government as defined in Title 17, United States Code, Section 101. Copyright protection is not available for this work in the United States.

Downloaded from NPS Archive: Calhoun

DUDLEY
KNOX
LIBRARY

Calhoun is the Naval Postgraduate School's public access digital repository for research materials and institutional publications created by the NPS community. Calhoun is named for Professor of Mathematics Guy K. Calhoun, NPS's first appointed -- and published -- scholarly author.

Dudley Knox Library / Naval Postgraduate School
411 Dyer Road / 1 University Circle
Monterey, California USA 93943

http://www.nps.edu/library

A NUMERICAL INVESTIGATION OF THE LONG-TERM TRANSIENT BEHAVIOR IN A COUPLED ATMOSPHERE-OCEAN MODEL

Wayne Roger Lambertson

NAVAL POSTGRADUATE SCHOOL
Monterey, California

THESIS

A Numerical Investigation of the Long-Term
Transient Behavior in
a Coupled Atmosphere-Ocean Model

by

Wayne Roger Lambertson

Thesis Advisor: R. T. Williams

September 1972

T149510

Approved for public release; distribution unlimited.

A Numerical Investigation of the Long-Term Transient Behavior in a Coupled Atmosphere-Ocean Model

by

Wayne Roger Lambertson
Lieutenant Commander, United States Navy
B.S., Naval Postgraduate School, 1965

Submitted in partial fulfillment of the
requirements for the degree of

DOCTOR OF PHILOSOPHY

from the

NAVAL POSTGRADUATE SCHOOL
September 1972

ABSTRACT

A two-level, quasi-geostrophic atmospheric model on a mid-latitude β-plane with a single wave in the x-direction was coupled with a three level primitive equation ocean model through the exchange of sensible heat and momentum to investigate the effect of the ocean circulation on transients in the atmospheric circulation and vice versa. A long-term (79 years) simulation of the atmosphere-ocean system was carried out. The experiment was conducted in three phases that consisted of integrating the combined, the ocean-only and the atmosphere-only model equations.

The combined model produced realistic patterns of both atmospheric and oceanic circulations. Energy studies of the atmosphere were completed with the results comparing favorably with the existing knowledge of the energy balance in the real atmosphere.

Data were retained at selected points on a daily basis and spectrally analyzed for a simulated six year period. Transients with periods on the order of one and two months appeared in the spectra of both atmospheric and oceanic variables from the combined model. These transients were not observed in the ocean-only or atmosphere-only phases of the experiment, and are attributed to the interaction occurring in the combined model.

TABLE OF CONTENTS

I. INTRODUCTION -- 7

II. THE ATMOSPHERIC MODEL ------------------------------ 20

A. DESCRIPTION --- 20

B. METHOD OF SOLUTION ---------------------------------- 30

1. Finite Differencing Scheme ------------------------- 30

2. Boundary Conditions -------------------------------- 31

3. Initial Conditions --------------------------------- 31

4. Time Integration Process --------------------------- 32

C. PRELIMINARY EXPERIMENTS ----------------------------- 33

1. Hadley Regime -------------------------------------- 33

2. Energy Examination --------------------------------- 38

III. THE OCEAN MODEL ------------------------------------ 46

A. DESCRIPTION AND EQUATION OF THE MODEL -------------- 46

B. COMPUTATIONAL PROCEDURES --------------------------- 50

C. HEATING AND FRICTION ------------------------------- 53

D. FINITE DIFFERENCE TECHNIQUES ----------------------- 58

E. INITIAL CONDITIONS --------------------------------- 62

IV. THE COMBINED MODEL -------------------------------- 64

A. TIME SYNCHRONIZATION ------------------------------- 65

B. MOMENTUM EXCHANGE --------------------------------- 66

C. HEAT EXCHANGE ------------------------------------- 68

1. Atmospheric Radiation, R', and Solar Radiation, S_N ---------------------------- 73

2. Latent Heat Terms, L•E' and L•P' ------- 76

3. The Sensible Heat Transfer, $H_1(T_{sea} - T_4)$ ---------------------------- 81

V. PROCEDURES -- 89
  A. PHASE I -------------------------------------- 89
    1. Variations of the Combined Model -------- 89
    2. The Coarse Grid (400 km) Model ---------- 91
    3. Data Retention -------------------------- 94
    4. The Fine Grid (200 km) Model ------------ 96
  B. PHASE II ------------------------------------- 98
  C. PHASE III ------------------------------------ 99
  D. REVIEW OF COMPUTING TIME REQUIREMENTS ------- 100
VI. DISCUSSION --------------------------------------- 102
  A. SYNOPTIC STUDIES ----------------------------- 103
    1. The 400 km Grid Combined Model Experiment ------------------------------ 103
    2. The 200 km Grid Combined Model Experiment ------------------------------ 108
    3. The Ocean-Only Experiment --------------- 135
    4. The Atmosphere-Only Experiment ---------- 144
    5. Energy Balance -------------------------- 152
  B. SPECTRUM ANALYSIS ---------------------------- 156
    1. Basic Definitions ----------------------- 156
    2. Spectral Techniques --------------------- 157
    3. Results of Spectral Investigation ------- 159
      a. Study of data at point C ------------ 160
      b. Study of data at point A ------------ 186
      c. Study of data at points B, D and E -- 187
VII. SUMMARY --- 189
APPENDIX A - DERIVATIONS OF EQUATIONS (2.22) to (2.27)- 196

APPENDIX B - DERIVATION OF ω AND v_1 EQUATIONS --------- 203

APPENDIX C - DERIVATIONS OF ENERGY AND ENERGY TRANSFORMATION EQUATIONS ----------------- 205

APPENDIX D - FINITE DIFFERENCE FORMS OF PREDICTION EQUATIONS ------------------------------------ 210

LIST OF REFERENCES ------------------------------------ 215

INITIAL DISTRIBUTION LIST ----------------------------- 219

FORM DD 1473 -- 228

ACKNOWLEDGEMENTS

I wish to express my appreciation to Dr. R. Terry Williams, whose guidance and advice were invaluable in the formulation and completion of this experiment. I also want to thank Dr. Robert L. Haney who generously allowed the modification of his ocean model and whose interest, reflected in untold numbers of discussions, was truly inspiring. The time and effort expended by the other members of my committee were also greatly appreciated.

The W. R. Church Computer Center provided the computer services required for this project in a truly outstanding manner. The assistance rendered by the operators and consultants was greatly appreciated. A thank you is offered to Lieutenant Commander Frank Taylor, United States Navy, who allowed the modification of his atmospheric model for use in this experiment.

Finally, I want to thank my wife, Joyce, whose patient encouragement and manifest selflessness made this effort possible.

I. INTRODUCTION

The use of numerical models to simulate physical concepts that would otherwise be restricted to limited observational studies has advanced the knowledge of both the atmosphere and ocean and their large scale interaction a great deal over the last several years. But that knowledge is far from complete and it is the intent of this work to reveal more information on the long term, large scale interactions and the frequencies of the response between the atmosphere and ocean. The primary goal of this study was to identify the effects of the ocean circulation on the transient (time-dependent) atmospheric circulation, and similarly the effect of the atmospheric circulation on the ocean.

The development of a large scale air-sea interaction model that would remain computationally stable throughout a long-term numerical integration of the dynamical equations of motion was required to achieve this goal. It was desired that the method by which the integrations proceeded be one which allowed the synchronization of the oceanic and atmospheric time steps so that a "one-to-one" relationship existed between the two media. Many complex numerical models of both the ocean and the atmosphere have been developed in the past. However, those models all require large amounts of computer time because of the very short

time steps required to satisfy the linear computational stability requirement. The model developed in this work had fewer degrees of freedom in the atmosphere and this resulted in faster integration of the atmospheric equations. It also utilized certain approximations and assumptions that permitted the use of longer time increments in the integrations. The necessity of employing a technique to simulate time synchronization was thereby avoided.

Many numerical general circulation models have been developed in the last two decades. Phillips (1956) made a long period forecast with a two-level, quasi-geostrophic model, starting with an atmosphere at rest. Diabatic effects were included in the equations as a linear function of latitude, and such quantities as the intensity of the heating, the value of the vertical stability and the type of frictional dissipation, were empirically specified. The flow patterns which developed were quite realistic. With the development of this model, Phillips demonstrated the feasibility of numerical simulation of the atmospheric general circulation with a simple model.

Mintz (1958) proposed numerical general circulation experiments that specified a heating function in which the diabatic heating of the air depended on the air-sea temperature difference. He showed that this heating function could be used to study the circulation of the atmosphere on a planet covered by either land or ocean or a combination thereof.

In both of the above works, the partial differential equations were formulated in finite differences. Lorenz (1960) discussed a method of expressing a dependent variable as a series of orthogonal functions. An example of such an analysis, in one dimension, is the Fourier series, in which the orthogonal functions are sines and cosines. The coefficients of these orthogonal functions become the new dependent variables and a finite number of variables are retained for prediction. Bryan (1959) reported on his work with Lorenz in which this technique was applied to the variables in a two-layer, quasi-geostrophic model. The variables were expanded into a few leading terms of a spherical harmonic series to conduct a simple general circulation experiment.

Smagorinsky (1963) reported on an extended period numerical integration of a two-level, baroclinic primitive equation model which had "land" as its underlying surface. This experiment was made for the simulation and study of the dynamics of the atmospheric general circulation. The solutions corresponding to external gravitational oscillations were filtered by requiring the vertically integrated divergence to vanish identically. This was a major departure from earlier work in that many hydrodynamic and kinematic constraints were removed.

Mintz (1964) conducted an experiment in climate simulation by numerically integrating the primitive equations of atmospheric motion, with friction and heating terms included, over a long period of time. His two-level model domain

encompassed the entire earth, with the underlying oceans and continents having different thermal properties. Leith (1965) described a six-level numerical model with which an attempt was made to compute the hydrodynamic and thermodynamic evolution of a moist atmosphere on the whole globe. The model took into account such external influences as solar heating, evaporation and surface friction.

Smagorinsky, Manabe and Holloway (1965) reported the results of a nine-level general circulation model of the atmosphere. The primitive equations were used in that study in which the atmosphere attained a state of quasi-equilibrium. The nine levels of the model were distributed to resolve surface boundary layer fluxes as well as radiative transfer by the prescribed distribution of ozone, carbon dioxide and water vapor. This model was an outgrowth of Phillips' two-level quasi-geostrophic model and Smagorinsky's two-level primitive equation model.

Arakawa (1966) derived a finite difference Jacobian expression for the advection term in the difference vorticity equation for two-dimensional incompressible flow that properly represented the interaction between grid points. He showed that the use of this differencing technique maintained the integral constraints on quadratic quantities of physical importance and that this was sufficient to prevent nonlinear computational instability. Before Arakawa's work, long-term integrations had been possible only with the use

of large friction and diffusion terms. Arakawa's scheme permitted long-term integrations without the requirement for such artificialities.

Kasahara and Washington (1967) described a model of the general circulation of the earth's atmosphere which was developed at the National Center for Atmospheric Research (NCAR). A distinguishing feature of this model was that the vertical coordinate was height rather than pressure, though hydrostatic equilibrium was maintained in the system. Experiments with a two-level version of this model were conducted. Long-term (over 100 days) integrations were conducted testing various physical parameters and examining their affect on the results.

Numerical models have also been developed for predicting the atmospheric conditions in enough detail to provide daily forecasts for given areas. Kesel and Winninghoff (1972) reported on the U. S. Navy operational five-level primitive equation model that has been used successfully for operational forecasts since 1970. This hemispheric model perhaps typifies the state of sophistication to which numerical weather prediction has progressed.

Early mathematical models of the ocean circulation were very simple as were the early atmospheric models. Munk (1950) utilized the oceanic mass transport to examine a wind-driven ocean which did not include specification of the vertical distribution of density or currents. He adhered to the linear theory in obtaining analytic solutions

to the equations for steady horizontal motions. Fofonoff (1954) studied frictionless, steady horizontal flow which could occur in a homogeneous ocean of constant depth. The effects of the thermohaline structure and compressibility were neglected everywhere. By considering this idealized case he avoided the analytical difficulties presented by the nonlinear terms in the hydrodynamical equations.

Veronis (1963a, 1963b, 1965, 1966) conducted numerous numerical experiments using both a grid point method of examination and a Fourier method of analysis and made comparisons of the two methods. He generated flow patterns in a rectangular, β-plane, barotropic ocean by assuming the basin could be divided into an interior region in which the dynamical balance was quasi-geostrophic and a boundary region where the dynamical balance was governed by inertial forces much the same as Munk. He developed both linear and nonlinear models and experimentally determined optimum values of parameters, such as the Rossby number and the bottom friction parameter, needed for the numerical work.

Bryan (1963) obtained solutions for a time dependent, nonlinear, barotropic model of a wind driven ocean by numerical integration. He varied parameters such as the wind stress, the Rossby number for the interior flow and an effective Reynolds number for the boundary current and examined the results. He examined boundary currents and the separation of the western boundary current from the coast for both linear and nonlinear cases. Bryan and Cox

(1967) investigated the ocean circulation using a baroclinic model to numerically integrate the primitive equations in almost complete form for different values of Reynolds numbers. The near linear solutions for low Reynolds number were most accessible to a numerical net with coarse resolution and gave valuable information for understanding the more complicated regimes at higher Reynolds number.

Gates (1968) integrated the primitive equations for a rectangular homogeneous ocean with a free surface on a β-plane starting from an initial state of rest. He investigated the transient Rossby waves and found a well-marked life cycle of amplification and decay as they propagated westward at about 1 m sec^{-1}.

Bryan (1969) continued his earlier work with Cox by adding new features to their five-level model. He treated salinity separately from temperature and allowed sea ice formation in the new model. This work is discussed in more detail later in the section on the combined model. Haney (1971) discussed the formulation of the net downward heat flux at the ocean surface, and used this formulation in experiments with a six-level baroclinic ocean model similar to Bryan's with emphasis on the equatorial regions. This model is representative of the present state of knowledge in ocean modeling.

In recent years research on the problem of atmosphere-ocean interaction has progressed to the point where very

complex atmospheric numerical models have been combined with similarly complex ocean models and integrated for extended periods of time. The major work in this area combined a multilevel, primitive equation atmospheric model including the earth's hydrology reported on by Manabe (1969) with a multilevel, primitive equation ocean model (Bryan 1969). The goal of their study, quite different from the present one, was to determine the effect of the ocean circulation on the time average climate of the atmosphere. Their experiments produced some notable results such as realistic heat transports and reasonable distribution of the poleward transport of energy. In one sense, however, this experiment was considered incomplete in that the goal of calculating a climate equilibrium with the combined system was not completely attained.

That research was carried out in three steps:

a. A study of the atmospheric model without the effect of ocean circulation. The effect of heat transfer by the ocean current was neglected. The ocean had zero heat capacity and simply acted as an infinite reservoir of moisture for the atmosphere.

b. A study of the oceanic model without any feedback from the atmosphere. The distribution of surface temperature, wind stress and precipitation over the ocean were given and held constant with respect to time.

c. A study of the joint ocean-atmosphere model in which the two systems were allowed to interact fully with each other.

A comparison of the results of the three experiments yielded some insight into the role of the ocean in maintaining the climate and of the atmosphere in maintaining the thermal and dynamical structure of the ocean.

In the Manabe-Bryan model more computing time was needed to obtain a one day integration with the atmospheric model than with the ocean model. Therefore, attempts were made to economize computer time by integrating the atmospheric equations for only one year while integrating the oceanic equations for 100 years. This resulted in a distorted response of the ocean circulation to fluctuations of atmospheric circulation, since an atmospheric disturbance that should have an effect for possibly one week influenced ocean conditions for up to two years. For example, it took one week for a cyclone wave to traverse the oceanic region. Because of the synchronization, the oceanic part of the model felt that cyclone for as long as two oceanic model years.

Wetherald and Manabe (1972) reported on the effect of seasonally varying the solar radiation in the combined model just discussed. Many of the results obtained in the new version of the model were different, the most significant of which was a warming trend which occurred when seasonal variations of the solar radiation were introduced.

It should be pointed out that an exact statistical equilibrium was not obtained in any part of the region of this integration.

After an extensive review of the literature which included all of the above works, it was decided that to reach a state of quasi-equilibrium with a coupled and time-synchronous atmosphere-ocean model the simplest atmosphere-ocean system which still contained the essential features of the dynamics of each media was required. The atmospheric model selected was a version of Phillips' (1956) two level, quasi-geostrophic model modified by implementing Lorenz's (1960) idea of replacing the dependent variable with Fourier coefficients. This decision was based primarily on the speed with which the equations of this model could be integrated. The equations governing the atmosphere could be integrated for one model year in about 30 minutes on the IBM 360/67. A model similar to the one desired had been used in an earlier atmosphere-only study at the Naval Postgraduate School by Taylor (1970) and was readily available for further modification. The details of the atmospheric model are described in Section II.

The ocean model selected was a modified form of Haney's (1971a) six level baroclinic model. The number of levels was reduced to three and the horizontal domain reduced to an area in the Northern Hemisphere. The depth was reduced and it was further simplified by using the β-plane approximation. While this primitive equation model was fairly

complex, it was readily available for modification. Details of the ocean model are described in Section III.

The ocean and atmosphere models were joined through the exchange of momentum and sensible heat. Unlike the model of Manabe (1969a), the atmosphere contained no moisture so there was no explicit exchange of moisture. Instead, the effects of evaporation and precipitation processes were simulated by other means. These simulations as well as the details of the coupling of the two models are described in Section IV.

In a manner somewhat similar to the experiment of Manabe and Bryan, the research was conducted in three phases. In phase I, equations of the combined model were integrated until a state of quasi-equilibrium was achieved. This required 79 years of simulation using more than 100 hours on the IBM 360/67 computer. The solution of a complex nonlinear system of equations by numerical integration over a long time period as was conducted in this simulation caused some concern over the accuracy of the numerical results. Error analysis studies by Fisher (1965) and others have shown that, even for short time integrations, errors in amplitude and phase arise in the numerical solution. This is not to say that such errors make the results meaningless because even if fairly large errors were present at the end of a long-term simulation of the atmospheric circulation, the gross features of the solution would not be changed significantly. However, the results should be examined more

from a qualitative than a quantitative point of view. The results in this long-term experiment surely contain numerical errors but these results are considered to be satisfactory for this study of the coupled atmosphere-ocean system.

One hundred day averages of the atmospheric surface stress and surface temperature were calculated and used as driving mechanisms for the ocean in phase II, an ocean-only experiment. The time of this experiment corresponded to the last six years of phase I. Similarly averaged sea surface temperatures were used as a forcing function during phase III, an atmosphere-only experiment. This also was initialized so that the time corresponded to the last six years of phase I. Details of the procedures used in all three phases are described in Section V.

The resulting data were examined in two ways. The first was a synoptic-type study in which maps of both ocean and atmospheric parameters were studied and their interactions noted. The combined model produced both atmospheric and oceanic features that compared favorably with observed features. Energy balance diagrams were constructed for the atmosphere and these compared well with existing knowledge of the real atmosphere. These synoptic results are shown in Section VI A.

The second method of examining results was a spectral method. Time series of data recorded over the last six years for selected locations in the ocean and atmosphere were spectrally analyzed to determine if any short or

intermediate term fluctuations such as those studied by Bjerknes (1962) and Namias (1969) appear due to the interactions. The results of this analysis are discussed in Section VI B of this work. By comparing the spectral characteristics of the coupled atmosphere with those of the atmosphere with fixed ocean surface temperatures, the role of the ocean circulation in producing certain transient atmospheric responses may be studied.

II. THE ATMOSPHERIC MODEL

A. DESCRIPTION

The atmospheric model was based on the selective application of the quasi-geostrophic theory to the equations of motion. Since the large-scale motions in extra-tropical latitudes are quasi-geostrophic in nature, the domain of this model was limited to the middle latitudes. The model was constructed on a β-plane with a central latitude of 45 degrees. Phillips (1963) discussed geostrophic motions that were characterized by approximate uniformity of potential vorticity. These motions have characteristic wavelengths of about 4000 km. He used an expansion in the Rossby number about latitude 45 degrees to show that the β-plane approximation is justified for geostrophic motions of this type.

Phillips (1956) developed a two-level quasi-geostrophic model that he considered was the simplest model in which heating and friction could be incorporated. The basic model described in this thesis followed Phillips' work in the manner in which the quasi-geostrophic equations were derived.

The quasi-geostrophic vorticity equation on a β-plane is

$$\frac{\partial}{\partial t} (\nabla^2 \psi) + \mathbf{k} \times \nabla \psi \cdot \nabla (\nabla^2 \psi) + \beta \frac{\partial \psi}{\partial x} - f_o \frac{\partial \omega}{\partial p}$$

$$= - g \frac{\partial}{\partial p} \left[\frac{\partial \tau_y}{\partial x} - \frac{\partial \tau_x}{\partial y} \right], \qquad (2.1)$$

where τ_x is the component of the stress in the $\mathbf{i}$ direction,

τ_y is the component of the stress in the $\mathbf{j}$ direction

and other symbols have their usual meteorological meaning.

The model is restricted to two levels with a vertical structure as shown in Figure 1. The stream function ψ_1 and ψ_3 are representative of the flow patterns in the upper and lower layers of the atmosphere respectively.

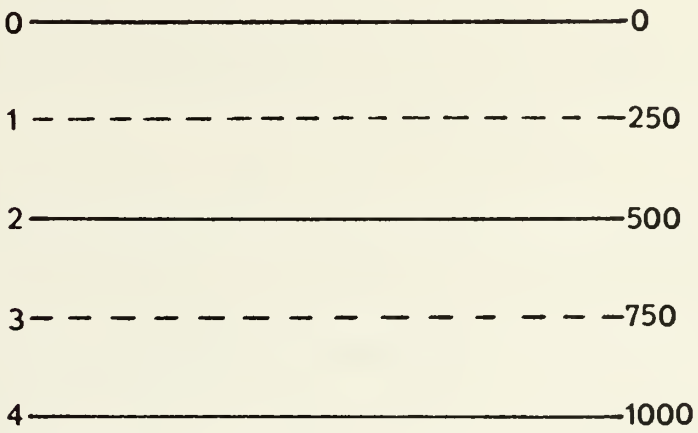

Figure 1. Vertical structure of atmospheric model.

Boundary conditions at the top and bottom are:

$$\omega = 0 \quad \text{at} \quad p = 0$$

and

$$\omega = 0 \quad \text{at} \quad p = p_4. \qquad (2.2)$$

The stress $\boldsymbol{\tau}_1$ vanishes at p = 0. The stress at anemometer level was computed from

$$\boldsymbol{\tau} = \rho (C_D)_4 \, |\mathbf{V}| \, \mathbf{V} \qquad (2.3)$$

where $(C_D)_4$ is a constant drag coefficient and $\mathbb{V}$ is the wind at anemometer level. The stress at level four was obtained by assuming that $\mathbb{V}$ was a fraction, ℓ, of the vectorially extrapolated wind, $\mathbb{V}_4$. Phillips (1956) suggested that for simplicity in stress calculations, the anemometer wind speed can be assumed to be 70 per cent of the geostrophic wind speed $\mathbb{V}_4$. The stress was therefore taken to be

$$\mathbb{\tau}_4 = \rho (C_D)_4 \ell^2 |\mathbb{V}_4| \mathbb{V}_4 \qquad (2.4)$$

where $\ell = 0.7$

A method for estimating C_D used by Manabe (1969a) is

$$C_D = [k_o / \ln (\frac{h}{z_o})]^2 , \qquad (2.5)$$

where k_o = Von Karman's constant,

h = height at which the stress is to be evaluated

and z_o = roughness parameter.

The quantity C_D was assumed to be a constant equal to 4.5 x 10^{-3}. This is larger than values normally used for this coefficient, but since C_D depends on where in the surface layer the stress is evaluated, the appropriateness of the value can best be examined from the resulting momentum exchange between the atmosphere and surface. Values of parameters at level four were obtained by linear extrapolation in p. The quantity $\mathbb{V}_4$ was thereby obtained from

$$\mathbb{V}_4 = \frac{3}{2} \mathbb{V}_3 - \frac{1}{2} \mathbb{V}_1 . \qquad (2.6)$$

Smagorinsky (1963) derived a formula for calculating the internal stress at level two, by assuming that the

stress was proportional to the vertical wind shear. A slightly modified form of this formula was used in this work and can be written

$$\tau_2 = (\rho k)_2 \left(\frac{g\rho}{p}\right)_2 (\mathbf{V}_3 - \mathbf{V}_1), \qquad (2.7)$$

where $(\rho k)_2$ is an exchange coefficient probably dependent on the local Richardson number. An estimate of this from Rossby and Montgomery (1935) and used by Smagorinsky was 50 gm $\text{cm}^{-1}\text{sec}^{-1}$. Other values of this coefficient are 225 gm $\text{cm}^{-1}\text{sec}^{-1}$ (Palmen, 1955) and 500 gm $\text{cm}^{-1}\text{sec}^{-1}$(Riehl, 1951). The choice of 50 gm $\text{cm}^{-1}\text{sec}^{-1}$ for this model was based on many preliminary numerical experiments with the model. The quantity $\left(\frac{g\rho}{p}\right)_2$ is the inverse thickness of the 750-250 mb layer and it is equal to 0.1266 km^{-1}. If typical atmospheric wind values are used, the ratio of τ_4 to τ_2 is on the order of ten to one.

The horizontal domain of the model is shown in Figure 2. The east-west extent is 4800 km and the north-south distance is 6000 km. The width was chosen as 4800 km to coincide with the wavelength of the x-wave that will be discussed shortly. The southern boundary is at 18N and the northern boundary is at 72N. The use of the β-plane over such a latitudinal extent may affect the results, but only in a quantitative manner.

If the hydrostatic approximation, the equation of state, and the geostrophic condition ($\psi = \frac{g}{f_o} z$) were applied to the first law of thermodynamics, a quasi-geostrophic

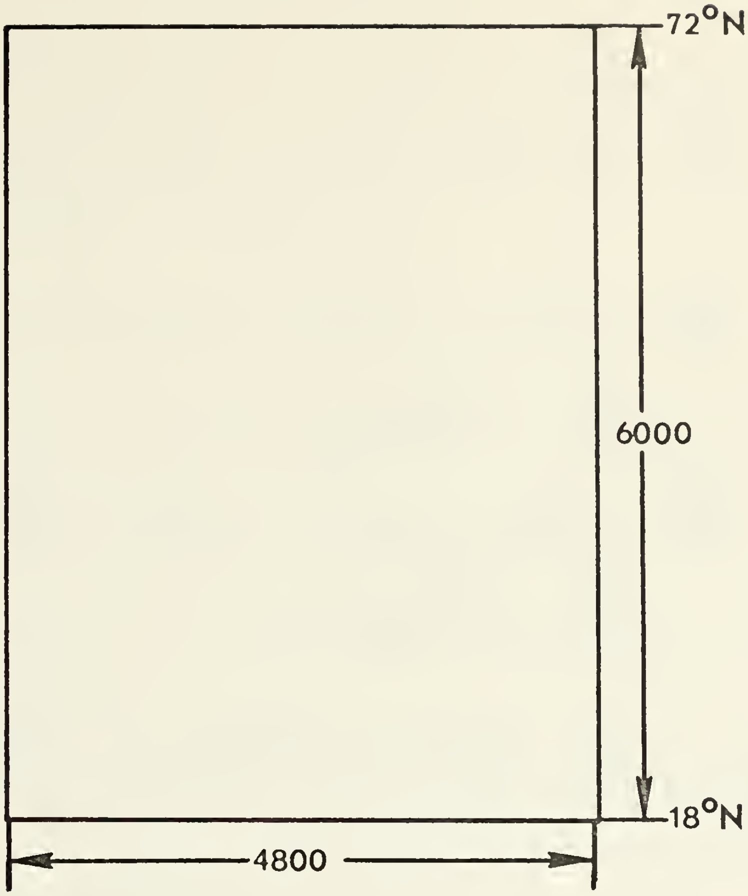

Figure 2. Horizontal domain of the model. Distance in kilometers.

version of that equation would be written

$$\frac{\partial}{\partial t}\left(\frac{\partial\psi}{\partial p}\right) + \mathbb{k} \times \nabla\psi \cdot \nabla\left(\frac{\partial\psi}{\partial p}\right) + \frac{\sigma}{f_o}\,\omega = -\frac{\kappa}{f_o p}\,\dot{Q}\ , \qquad (2.8)$$

where

$$\sigma = \frac{R^2 T_s}{p^2 g}\left[\frac{\partial T_s}{\partial Z} + \frac{g}{C_p}\right] = 2.3\ \mathrm{m}^2\mathrm{sec}^{-2}\mathrm{cb}^{-2},$$

$$\kappa = R/C_p\ , \qquad (2.9)$$

$\dot{Q}$ = heating rate per unit mass

and T_s = temperature from the standard atmosphere.

The above constant value of σ, the static stability, was used throughout the experiment.

Equation (2.1) was applied at levels one and three and Equation (2.8) was applied at level two. The following equations were obtained:

$$\frac{\partial}{\partial t}(\nabla^2\psi_1) + \mathbb{k} \times \nabla\psi_1 \cdot \nabla(\nabla^2\psi_1) + \beta_o \frac{\partial\psi_1}{\partial x} - \frac{f_o\omega_2}{\Delta p} = - g \frac{\partial}{\partial p}\left[\frac{\partial\tau_y}{\partial x} - \frac{\partial\tau_x}{\partial y}\right]_1 , \tag{2.10}$$

$$\frac{\partial}{\partial t}(\nabla^2\psi_3) + \mathbb{k} \times \nabla\psi_3 \cdot \nabla(\nabla^2\psi_3) + \beta_o \frac{\partial\psi_3}{\partial x} + \frac{f_o\omega_2}{\Delta p} = - g \frac{\partial}{\partial p}\left[\frac{\partial\tau_y}{\partial x} - \frac{\partial\tau_x}{\partial y}\right]_3 \tag{2.11}$$

and

$$\frac{\partial}{\partial t}\left(\frac{\psi_1 - \psi_3}{\Delta p}\right) + \mathbb{k} \times \nabla\left(\frac{\psi_1 + \psi_3}{2}\right) \cdot \nabla\left(\frac{\psi_1 - \psi_3}{\Delta p}\right) - \frac{\sigma\omega_2}{f_o} = - \frac{\kappa}{f_o P_2} \dot{Q}_2 \tag{2.12}$$

where $\Delta p = 500$ mb.

Following Lorenz (1960), ψ_M and ψ_T were defined as follows:

$$\psi_M = \frac{\psi_1 + \psi_3}{2}$$

and (2.13)

$$\psi_M = \frac{\psi_1 - \psi_3}{2}$$

Then Equations (2.10) and (2.11) were added and divided by two to yield:

$$\frac{\partial}{\partial t}(\nabla^2\psi_M) + \mathbb{k} \times \nabla\psi_M \cdot \nabla(\nabla^2\psi_M) + \mathbb{k} \times \nabla\psi_T \cdot \nabla(\nabla^2\psi_T) + \beta_o \frac{\partial\psi_M}{\partial x} = - \frac{g}{\Delta p}\left[\frac{\partial\tau_y}{\partial x} - \frac{\partial\tau_x}{\partial y}\right]_4 . \tag{2.14}$$

Equation (2.12) was solved for ω_2. Equation (2.11) was subtracted from Equation (2.10) and the result divided by two. The quantity ω_2 was replaced and the following was obtained:

$$\frac{\partial}{\partial t}(\nabla^2 - \mu^2)\psi_T + \mathbf{k} \times \nabla\psi_M \cdot \nabla(\nabla^2 - \mu^2)\psi_T + \mathbf{k} \times \nabla\psi_T \cdot \nabla(\nabla^2\psi_M)$$

$$+ \beta_o \frac{\partial\psi_M}{\partial x} = - \frac{\mu^2\kappa}{2f_o}\dot{Q}_2 - \frac{g}{\Delta p}\left\{ 2\left[\frac{\partial\tau_y}{\partial x} - \frac{\partial\tau_x}{\partial y}\right]_2 - \left[\frac{\partial\tau_y}{\partial x} - \frac{\partial\tau_x}{\partial y}\right]_4 \right\} \qquad (2.15)$$

where $\mu^2 = \frac{2f_o^2}{\Delta p\sigma} = 3.69 \times 10^{-16}\ \mathrm{cm}^{-2}$.

To reduce computing requirements, the model was further simplified by expressing the dependent variables, ψ_M and ψ_T as functions limited to one wave in the zonal direction. The wave chosen was of the predominate baroclinic scale. Its wavelength was 4800 km, the zonal width of the model atmosphere. Any atmospheric model that is developed with the intention of reasonably portraying air-sea interaction must include baroclinic disturbances containing wave numbers of about five to eight. The baroclinic processes that are responsible for the resupply of kinetic energy to the atmosphere are reasonably represented by the wave number chosen. Phillips (1956) and Smagorinsky (1963) have demonstrated in experiments with no forcing functions in the east-west direction that much of the disturbance energy is isolated in a single predominate wave number.

By transforming the system of equations to wave-number space in the zonal direction, grid points were eliminated in the x direction and the requirement for relaxation in order to solve for ψ was removed. This type of approach had further computational advantages in that no linear truncation errors arose in x-space. Also, the fact that there were no nonlinear truncation errors in x-space reduced the possibility of nonlinear instability. Therefore, errors caused by aliasing due to x-differencing were eliminated. The fields were defined as follows:

$$\psi_M = E(y,t) + A(y,t)\cos kx + B(y,t)\sin kx \quad (2.16)$$

and

$$\psi_T = F(y,t) + C(y,t)\cos kx + D(y,t)\sin kx \quad (2.17)$$

where A, B, C, and D are Fourier amplitudes of the disturbance, and E and F are the zonal means. The quantity k is the zonal wave number and a value of $(2\pi/4800)\text{km}^{-1}$ was chosen.

In the initial development of the atmospheric model the heating was simply proportional to the air-sea temperature difference. A sea surface temperature, T_{sea}, was specified from climatological data and held constant in time. Later in the work a more complete form of the heating was used and this will be discussed in a later section of this thesis.

The mean temperature of the layer one-three is proportional to ψ_T. By using the geostrophic approximation and the equation of state, the following equation was obtained:

$$T_2' = \frac{2f_o}{R} \psi_T \qquad (2.18)$$

where T_2' is a departure from the mean temperature at level two. To obtain physically reasonable values for the atmospheric temperature at level two a constant was added to T_2'. Then

$$T_2 = \frac{2f_o}{R} \psi_T + 250.3 \, . \qquad (2.19)$$

By using the standard lapse rate, T_2 was extrapolated downward to obtain the temperature at level four, T_4, and

$$T_4 = T_2 - \frac{\partial T_s}{\partial Z} (\Delta z) \qquad (2.20)$$

where Δz is the standard thickness of the 1000-500 mb layer and $\partial T_s / \partial z$ is the standard lapse rate. Therefore, T_4 only differs from T_2 by a constant.

Since the static stability was held constant, the heating at level two was proportional to the air-sea temperature difference and was expressed as

$$\dot{Q}_2 = \frac{g}{\Delta p} H_1 (T_{sea} - T_4) \qquad (2.21)$$

where H_1 is a factor derived by Haney (1971) and is a slowly varying function of latitude. In this work a value of 55 cal $cm^{-2} deg^{-1}$ was used and held constant in both latitude and time.

When Equations (2.16) and (2.17) were substituted into Equations (2.14) and (2.15) and terms of wave number 2k and higher were neglected, equations in the Fourier coefficients were obtained. The various terms were separated and

coefficients of the cosine terms, sine terms and terms independent of x were equated. This yielded six predictive equations for A, B, C, D, E, and F. The derivation of these equations is contained in Appendix A.

The equations are:

$$\frac{\partial}{\partial t}\left[\frac{\partial^2 A}{\partial y^2} - k^2 A\right] = k\left[\frac{\partial E}{\partial y}\frac{\partial^2 B}{\partial y^2} + \frac{\partial F}{\partial y}\frac{\partial^2 D}{\partial y^2} - \frac{\partial^3 E}{\partial y^3} B - \frac{\partial^3 F}{\partial y^3} D - k^2\left(\frac{\partial E}{\partial y} B + \frac{\partial F}{\partial y} D\right)\right] - \beta_o Bk + \frac{g}{\Delta p}\rho C_D \left\{ |\overline{W}_4| k^2 (A-2C) + \frac{\partial}{\partial y}\left[|\overline{W}_4|\left(2\frac{\partial C}{\partial y} - \frac{\partial A}{\partial y}\right)\right]\right\}, \tag{2.22}$$

$$\frac{\partial}{\partial t}\left[\frac{\partial^2 B}{\partial y^2} - k^2 B\right] = k\left[-\frac{\partial E}{\partial y}\frac{\partial^2 A}{\partial y^2} - \frac{\partial F}{\partial y}\frac{\partial^2 C}{\partial y^2} + \frac{\partial^3 E}{\partial y^3} A + \frac{\partial^3 F}{\partial y^3} C + k^2\left(\frac{\partial E}{\partial y} A + \frac{\partial F}{\partial y} C\right)\right] + \beta_o Ak + \frac{g\rho}{\Delta p} C_D \left\{|\overline{W}_4| k^2 (B-2D) + \frac{\partial}{\partial y}\left[|\overline{W}_4|\left(2\frac{\partial D}{\partial y} - \frac{\partial B}{\partial y}\right)\right]\right\}, \tag{2.23}$$

$$\frac{\partial}{\partial t}\left[\frac{\partial^2 C}{\partial y^2} - k^2 C - \mu^2 C\right] = k\left[\frac{\partial E}{\partial y}\frac{\partial^2 D}{\partial y^2} + \frac{\partial F}{\partial y}\frac{\partial^2 B}{\partial y^2} - \frac{\partial E}{\partial y} D(k^2 + \mu^2) - \frac{\partial F}{\partial y} B(k^2 - \mu^2) - \frac{\partial^3 F}{\partial y^3} D - \frac{\partial^3 F}{\partial y^3} B\right] - \beta_o Dk - \frac{\mu^2 \kappa g}{2f_o \Delta p} H_1\left(-\frac{2f_o}{R} C\right) + \frac{g}{\Delta p} 4(\rho k)_2 \left(\frac{g\rho}{p}\right)_2 \left(\frac{\partial^2 C}{\partial y^2} - k^2 C\right) + \frac{g}{\Delta p}\rho C_D \left\{|\overline{W}_4| k^2 (2D-B) - \frac{\partial}{\partial y}\left[|\overline{W}_4|\left(2\frac{\partial D}{\partial y} - \frac{\partial B}{\partial y}\right)\right]\right\}, \tag{2.24}$$

$$\frac{\partial}{\partial t}\left[\frac{\partial^2 D}{\partial y^2} - k^2 D - \mu^2 D\right] = k\left[\frac{\partial E}{\partial y} C (k^2 + \mu^2) + \frac{\partial F}{\partial y} A (k^2 - \mu^2) - \frac{\partial E}{\partial y}\frac{\partial^2 C}{\partial y^2} - \frac{\partial F}{\partial y}\frac{\partial^2 A}{\partial y^2} + \frac{\partial^3 F}{\partial y^3} A + \frac{\partial^3 F}{\partial y^3} C\right] + \beta_o Ck - \frac{\mu^2 \kappa g}{2f_o \Delta p} H_1\left(-\frac{2f_o}{R} D\right) + \frac{g}{\Delta p} 4(\rho k)_2 \left(\frac{\partial^2 D}{\partial y^2} - k^2 D\right)\left(\frac{g\rho}{p}\right)_2 + \frac{g}{\Delta p}\rho C_D \left\{|\overline{W}_4| k^2 (2D-B) - \frac{\partial}{\partial y}\left[|\overline{W}_4|\left(2\frac{\partial D}{\partial y} - \frac{\partial B}{\partial y}\right)\right]\right\}, \tag{2.25}$$

$$\frac{\partial}{\partial t}\left[\frac{\partial^2 E}{\partial y^2}\right] = \frac{k}{2}\frac{\partial}{\partial y}\left(A\frac{\partial^2 B}{\partial y^2} - B\frac{\partial^2 A}{\partial y^2} + C\frac{\partial^2 D}{\partial y^2} - D\frac{\partial^2 C}{\partial y^2}\right)$$

$$+ \frac{g}{\Delta p}\rho C_D \frac{\partial}{\partial y}\left[|\overline{W}_4|\left(2\frac{\partial F}{\partial y} - \frac{\partial E}{\partial y}\right)\right] , \qquad (2.26)$$

$$\frac{\partial}{\partial t}\left[\frac{\partial^2}{\partial y^2} - \mu^2\right]F = \frac{k}{2}\left\{\frac{\partial}{\partial y}\left[\frac{\partial^2 D}{\partial y^2}A - B\frac{\partial^2 C}{\partial y^2} + C\frac{\partial^2 B}{\partial y^2} - D\frac{\partial^2 A}{\partial y^2}\right]\right.$$

$$\left. + \mu^2\frac{\partial}{\partial y}[BC-AD]\right\} - \frac{\mu^2\kappa g}{2f_o\Delta p}H_1\left[T_{sea} - \left(\frac{2f_o}{R}F + C_1\right)\right]$$

$$+ \frac{g}{\Delta p}4(\rho k)_2\left(\frac{\rho g}{p}\right)_2\frac{\partial^2 F}{\partial y^2} + \frac{g}{\Delta p}\rho C_D$$

$$\frac{\partial}{\partial y}\left[|\overline{W}_4|\left(\frac{\partial E}{\partial y} - 2\frac{\partial F}{\partial y}\right)\right] \qquad (2.27)$$

where

$$C_1 = \left[250.3 - \frac{\partial T_s}{\partial Z}(\Delta Z)\right]\frac{R}{2f_o} .$$

B. METHOD OF SOLUTION

1. Finite Difference Scheme

Centered time differences were used for all terms except those involving friction and heating. Those terms were computed at time ($t-\Delta t$). A forward time step was utilized to start the marching process. A finite difference scheme developed by Matsuno (1966) was used every 24 time steps. This was a two-step iteration to simulate the backward difference method. This scheme was applied in this situation to eliminate the computational mode that would arise from using the centered time differencing exclusively and also helps eliminate nonlinear instability. A time step of 30 minutes was used.

Since a wave number representation was used in the x direction, finite differencing was not required in that direction. However, centered space differences were taken in the y direction. A uniform grid distance of 200 km was used for Δy.

2. Boundary Conditions

Free-slip walls existed at the north and south boundaries. The boundary conditions at these walls were

$$A,\ B,\ C,\ D = 0 \quad \text{at} \quad y = 0, \quad y = w \tag{2.28a}$$

and

$$\frac{\partial}{\partial t}\left(\frac{\partial E}{\partial y}\right) = 0, \quad \frac{\partial}{\partial t}\left(\frac{\partial F}{\partial y}\right) = 0 \text{ at } y = 0,\ y = w. \tag{2.28b}$$

Condition (2.28a) was imposed to force the meridional flow to equal zero and correspond to the statement that the normal geostrophic velocity vanished at the wall. From the zonally averaged equation of motion, $\frac{\partial u_g}{\partial t} = 0$ at the north and south walls. The boundary condition (2.28b) ensures that this was true and was also a requirement for proper energy conservation.

3. Initial Conditions

Initial conditions of a mean zonal current with a superimposed disturbance were specified. The vertical shear and hence the thermal wind were near the critical value for baroclinic instability. The initial disturbance had a wavelength, previously discussed, and a structure such that when superimposed on a baroclinic current with no horizontal shear it had the maximum growth rate.

The initial conditions were:

$$A = \frac{200}{f_o} \sin\left(\frac{\pi y}{w}\right) \text{ cm}^2 \text{ sec}^{-1} ,$$

$$B = C = D = 0 ,$$

$$E = 1200 \frac{w}{\pi} \cos\left(\frac{\pi y}{w}\right) \text{ cm}^2 \text{ sec}^{-1}$$

and

$$F = 600 \frac{w}{\pi} \cos\left(\frac{\pi y}{w}\right) \text{ cm}^2 \text{ sec}^{-1} . \qquad (2.29a)$$

It was further desired that the mean surface wind vanish initially, which can be achieved by requiring that

$$\bar{U}_4 = - \frac{\partial \bar{\psi}_4}{\partial y} = - \frac{\partial}{\partial y}[\bar{\psi}_M - 2\bar{\psi}_T] = - \frac{\partial}{\partial y}[E-2F] = 0 \qquad (2.29b)$$

or

$$E = 2F.$$

4. Time Integration Process

Different methods for solving the time tendencies of the Fourier coefficients were utilized. A Gauss-Jordan elimination method was used to solve equations (2.22), (2.23), (2.24), (2.25), and (2.27). Richtmyer (1957) discussed the use of such a procedure for solving a set of equations that had all the elements of its corresponding matrix vanish except those on the three main diagonals. These equations had that property. The method of solution for Equation (2.27) was discussed by Phillips (1956) and modified to ensure that the equation satisfied the boundary conditions. Equation (2.26) was solved by a direct marching process utilizing the proper boundary conditions.

C. PRELIMINARY EXPERIMENTS

1. Hadley Regime

To examine the effect of the disturbances on the model atmosphere, an experiment was conducted which should have produced a single Hadley type cell in the meridional circulation. A linear sea surface temperature was imposed, with warm temperatures in the south.

The amplitudes of the disturbance were set equal to zero (A, B, C, and D) and Equations (2.22) through (2.27) reduced to:

$$\frac{\partial^2}{\partial y^2}\left(\frac{\partial E}{\partial t}\right) = \frac{\partial}{\partial y}\left[\frac{g}{\Delta p}\,\rho C_D\,|\overline{V}_4|\left(2\frac{\partial F}{\partial y} - \frac{\partial E}{\partial y}\right)\right] \tag{2.30}$$

and

$$\left[\frac{\partial^2}{\partial y^2} - \mu^2\right]\frac{\partial F}{\partial t} = \frac{\partial}{\partial y}\left[\frac{g}{\Delta p}\,4(\rho k)_2\left(\frac{\rho g}{p}\right)_2\frac{\partial F}{\partial y} + \frac{g}{\Delta p}\,\rho C_D\,|\overline{V}_4|\left(\frac{\partial E}{\partial y} - 2\frac{\partial F}{\partial y}\right)\right] - \frac{\mu^2 \kappa g}{2 f_o \Delta p} H_1\left[T_{sea} - \left(\frac{2 f_o}{R}(F + C_1)\right)\right]. \tag{2.31}$$

For simplicity the following definitions were made:

$$S_1 \equiv \frac{g}{\Delta p}\,\rho C_D \quad ,$$

$$S_2 \equiv \frac{g}{\Delta p}\,4(\rho k)_2\left(\frac{\rho g}{p}\right)_2 ,$$

$$\text{and } S_3 \equiv \frac{\mu^2 \kappa g}{2 f_o \Delta p} . \tag{2.32}$$

An assumption that a steady state condition existed in the model was made, i.e. $\frac{\partial}{\partial t}(\ ) = 0$, yielding

$$0 = \frac{\partial}{\partial y}\left[S_1\,|\overline{V}_4|\left(2\frac{\partial F}{\partial y} - \frac{\partial E}{\partial y}\right)\right]. \tag{2.33}$$

Since S_1 was not equal to zero,

$$|\overline{V}_4| = 0 \quad \text{and} \quad \frac{\partial E}{\partial y} = 2\,\frac{\partial F}{\partial y} \tag{2.34}$$

and Equation (2.31) can be written

$$S_2\,\frac{\partial^2 F}{\partial y^2} - S_3 H_1 \left[T_{sea} - \frac{2f_o}{R}(F + C_1) \right] = 0 \tag{2.35}$$

or

$$S_2\,\frac{\partial^2 F}{\partial y^2} - S_3 H_1 \frac{2f_o}{R} F - S_3 H_1 T_{sea} + S_3 H_1 \frac{2f_o}{R} C_1 = 0 . \tag{2.36}$$

Since F represents the mean temperature throughout the layer, the zonal mean thermal wind can be defined as

$$\overline{U}_T \equi - \frac{\partial F}{\partial y} . \tag{2.37}$$

Equation (2.36) was solved analytically, using the boundary condition that $\overline{U}_T = 0$ at $y = 0, W$.

The solution is

$$F = \frac{U_c}{S_5} \left[(y - \tfrac{W}{2}) - \frac{1}{(S_4 S_5)^{1/2}} \; \frac{\sinh[(S_4 S_5)^{1/2} (y - \frac{W}{2})]}{\cosh[(S_4 S_5)^{1/2} \frac{W}{2}]} \right],$$

where

$$U_c = \frac{\partial T_{sea}}{\partial y} , \quad S_4 \equiv \frac{S_3}{S_2} H_1 ,$$

and

$$S_5 \equiv \frac{2f_o}{R} . \tag{2.38}$$

This solution, along with the condition that A thru D equal zero and E equals 2F, was used as an initial state to expedite reaching a steady state. The initial mean thermal wind obtained from (2.38) was

$$\overline{U}_T = \frac{U_c}{S_5} \left[\frac{\cosh[(S_4 S_5)^{1/2} (y - \frac{W}{2})]}{\cosh[(S_4 S_5)^{1/2} \frac{W}{2}]} \right] - \frac{U_c}{S_5} , \tag{2.39}$$

where $U_c = 0.00433$ degrees per kilometer and the change in the thermal wind with time was examined.

The complete equations were integrated in time starting from this initial state. After 40 days, values of $\overline{U}_T$ were within two percent of the initial value. The mean meridional circulation taken from the numerical solution is shown in Figure 3a. It consisted of a single cell with northward flow at the upper level and southward flow in the lower level. The vertical motion field consisted of upward motion in the southern part and downward motion in the north. The central portion displayed weak and variable vertical motion patterns and were interpreted as being meaningless. It follows from the equations, that the quantities A through D will remain zero. The method by which vertical motions and the mean meridional motions were calculated is described in Appendix B.

A similar experiment was made with the same linear sea surface temperature profile as before but with the initial conditions given by Equation (2.29a). This initial condition primarily differs from the previous one in that it contains a finite amplitude disturbance with wave number k in the barotropic part of the motion ($A \neq 0$). This integration required more computer time to reach a quasi-steady state. A three cell structure as shown in Figure 3b developed after 230 days. The northward and southward motions were stronger and the vertical motion patterns were more intense and well defined.

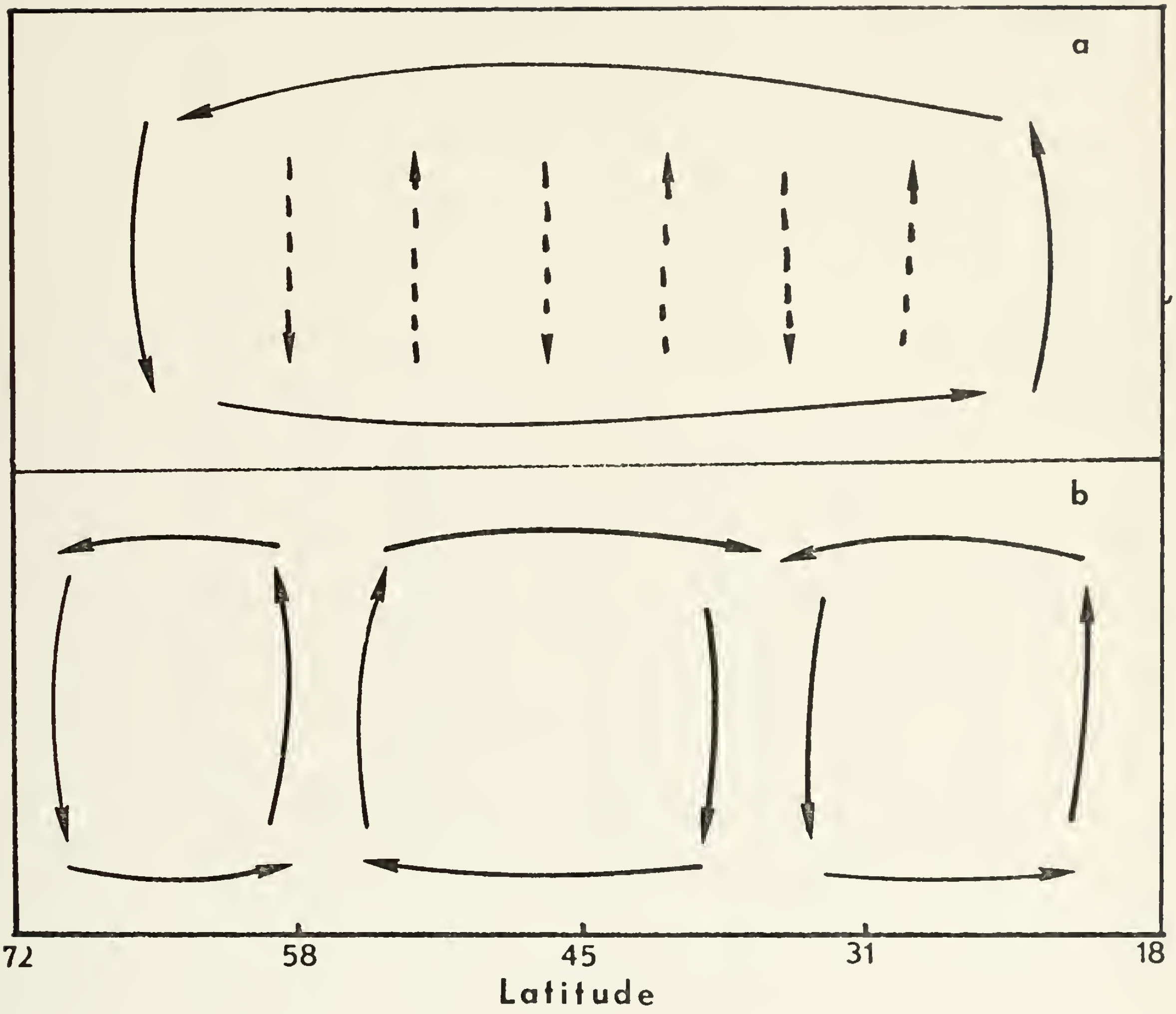

Figure 3. a. Meridional circulation arrived at in Hadley regime experiment. b. Meridional circulation of atmosphere with disturbances included.

A quantitative comparison was made of velocities obtained in the two experiments. Table 1 lists the values of the upper level meridional velocity in cm sec^{-1} and the mean zonal velocities in m sec^{-1} at levels one and three.

LATITUDE	MEAN MERIDIONAL VELOCITY UPPER LEVEL		ZONAL VELOCITY			
			LEVEL 1		LEVEL 3	
	HAD	DISTURB.	HAD	DIST.	HAD	DIST.
72.0	0.0	0.0	0.0	0.0	0.0	0.0
68.4	2.9	3.4	20.5	6.6	8.0	-0.1
64.8	3.5	12.2	18.9	6.0	6.8	-1.9
61.2	3.6	16.0	19.2	5.0	6.8	-1.1
57.6	3.5	6.0	19.4	16.3	6.7	5.1
54.0	3.6	-5.3	19.2	27.3	6.8	11.7
50.4	3.6	-13.7	19.3	34.9	6.7	15.6
46.8	3.6	-22.2	19.3	36.8	6.8	16.6
43.2	3.6	-28.8	19.3	33.3	6.7	14.6
39.6	3.6	-23.8	19.2	24.7	6.8	9.8
36.0	3.5	-8.6	19.4	14.3	6.7	3.7
32.4	3.6	6.4	19.2	7.2	6.8	-0.3
28.8	3.5	10.1	19.3	7.7	6.8	-0.8
25.2	3.5	3.1	18.9	13.0	6.8	0.7
21.6	2.9	1.4	20.6	11.3	8.0	1.8
18.0	0.0	0.0	0.0	0.0	0.0	0.0

Table I. Comparison values of meridional and zonal velocities from Hadley experiment and disturbed atmosphere experiment. Positive values are northward or eastward flow. Upper level is 500-0 mb layer. Units are m sec^{-1}.

2. Energy Examination

Equations for the components of potential and kinetic energy and energy transformations in terms of the Fourier coefficients are as follows: (The derivation of these equations is shown in Appendix C.)

$$\int P_z \, dy = \frac{\mu^2}{2} \int F^2 \, dy \, , \tag{2.40}$$

$$\int P_e \, dy = \frac{\mu^2}{2} \int (C^2 + D^2) \, dy \, , \tag{2.41}$$

$$\int K_z \, dy = \frac{1}{2} \int [(\frac{\partial E}{\partial y})^2 + (\frac{\partial F}{\partial y})^2] \, dy \, , \tag{2.42}$$

$$\int K_e \, dy = \frac{1}{2} \int [(\frac{\partial A}{\partial y})^2 + (\frac{\partial B}{\partial y})^2 + (\frac{\partial C}{\partial y})^2 + (\frac{\partial D}{\partial y})^2 + k^2 (A^2 + B^2 + C^2 + D^2)] \, dy \, , \tag{2.43}$$

$$G_z = \int \left\{ \frac{\mu^2 \kappa g}{2 \Delta p f_o} H_1 [T_{sea} - \frac{2 f_o}{R} (F + C_1)] F \right\} dy \, , \tag{2.44}$$

$$C_p = - \int [\frac{k}{2} \mu^2 (BC - AD) \frac{\partial F}{\partial y}] \, dy \, , \qquad (2.45$$

$$C_k = - \int \left\{ \frac{k}{2} [\frac{\partial E}{\partial y} (A \frac{\partial^2 B}{\partial y^2} - B \frac{\partial^2 A}{\partial y^2} + C \frac{\partial^2 D}{\partial y^2} - D \frac{\partial^2 C}{\partial y^2}) + \frac{\partial F}{\partial y} (A \frac{\partial^2 D}{\partial y^2} - D \frac{\partial^2 A}{\partial y^2} + C \frac{\partial^2 B}{\partial y^2} - B \frac{\partial^2 C}{\partial y^2})] \right\} dy, \tag{2.46}$$

$$D_{ei} = - \int \left\{ \frac{g}{\Delta p} 4 (\rho k)_2 (\frac{\rho g}{p})_2 [C (\frac{\partial^2 C}{\partial y^2} - C k^2) + D (\frac{\partial^2 D}{\partial y^2} - D k^2)] \right\} dy \, , \tag{2.47}$$

$$D_{es} = - \int \left\{ \frac{g}{\Delta p} \rho C_D \left[(A-C) \left(|\overline{\mathbb{V}}_4| k^2 (A-2C) + \frac{\partial}{\partial y} [|\overline{\mathbb{V}}_4| (2 \frac{\partial C}{\partial y} - \frac{\partial A}{\partial y})] \right) + (B-C) \left(|\overline{\mathbb{V}}_4| k^2 (B-2D) + \frac{\partial}{\partial y} [|\overline{\mathbb{V}}_4| (2 \frac{\partial D}{\partial y} - \frac{\partial B}{\partial y})] \right) \right] \right\} dy, \tag{2.48}$$

$$D_{zi} = - \int \left\{ \frac{g}{\Delta p} 4(\rho k)_2 (\frac{\rho g}{p})_2 [F \frac{\partial^2 F}{\partial y^2}] \right\} dy, \tag{2.49}$$

$$D_{zs} = - \int \left\{ \frac{g}{\Delta p} \rho C_D \left[(E-F) \frac{\partial}{\partial y} [|\overline{V}_4| (2 \frac{\partial F}{\partial y} - \frac{\partial E}{\partial y})] \right] \right\} dy, \tag{2.50}$$

$$C_z = - \int [\frac{2 f_o}{\Delta p} \overline{\omega} F] dy \tag{2.51}$$

and

$$C_e = - \int [\frac{2 f_o}{\Delta p} (\omega_C C + \omega_D D)] dy . \tag{2.52}$$

The relationship of these quantities can be expressed by the following equations:

$$\frac{\partial}{\partial t} \int P_z dy = G_z - C_p + C_z \quad , \tag{2.53}$$

$$\frac{\partial}{\partial t} \int P_e dy = C_p - C_e \quad , \tag{2.54}$$

$$\frac{\partial}{\partial t} \int K_e dy = C_e - C_k - D_{ei} - D_{es} \tag{2.55}$$

and

$$\frac{\partial}{\partial t} \int K_z dy = - C_z + C_k - D_{zi} - D_{zs} . \tag{2.56}$$

If Equations (2.53) to (2.56) are summed, the following equation is obtained:

$$\frac{\partial}{\partial t} \int (P+K) dy = G_z - D_{ei} - D_{es} - D_{zi} - D_{zs} \tag{2.57}$$

and shows that the time rate of change of total energy in the system is equal to that generated minus that dissipated.

The quantity C_p represents the conversion of mean potential energy to eddy potential energy that is accomplished by the horizontal transport of sensible heat by the eddies. The temperature in the layer one-three is proportional to ψ_T and $k(BC - AD) \frac{\partial F}{\partial y}$ is proportional to $v'T'$

$\frac{\partial T}{\partial y}$. The quantity $k(BC - AD)$ represents $\overline{v'T'}$ which is the transfer of heat across a latitude circle, and since $\frac{\partial T}{\partial y}$ tends to be negative, $k(BC - AD)$ must be positive to convert P_z to P_e.

The Term C_e represents the conversion of eddy potential energy to eddy kinetic energy by the vertical circulation in the zonal plane. The conversion depends on the correlation between ω' and α' (α' is a departure from a mean specific volume of air). Since $\omega'\alpha'$ is proportional to $\omega'\psi_T'$, ω_C and C, and ω_D and D must be negatively correlated to convert P_e to K_e.

The quantity C_k represents the conversion of eddy kinetic energy to zonal kinetic energy and is dependent on the correlation between the mean zonal wind and the meridional convergence of the eddy momentum transport. The quantity $\overline{u}\,\frac{\partial}{\partial y}(u'v')$ is proportional to

$$k\frac{\partial E}{\partial y}\left(A\frac{\partial^2 B}{\partial y^2} - B\frac{\partial^2 A}{\partial y^2} + C\frac{\partial^2 D}{\partial y^2} - D\frac{\partial^2 C}{\partial y^2}\right)$$
$$+ k\frac{\partial F}{\partial y}\left(A\frac{\partial^2 D}{\partial y^2} - D\frac{\partial^2 A}{\partial y^2} - B\frac{\partial^2 C}{\partial y^2} + C\frac{\partial^2 B}{\partial y^2}\right).$$

Since $\frac{\partial E}{\partial y}$ and $\frac{\partial F}{\partial y}$ tend to be negative, $\frac{\partial}{\partial y}(u'v')$ must be positive in order to have conversion of K_e to K_z.

The term C_z represents conversion of zonal potential energy to zonal kinetic energy by the mean meridional circulation. It depends on the correlation between $\overline{\omega}$ and $\overline{\alpha}$, which is proportional to $\overline{\omega}\ \overline{\psi}_T$. This conversion is small in nature (Oort, 1964) and requires a positive correlation to convert K_z to P_z.

The quantity G_z is the generation of zonal potential energy through diabatic process. In this model the heating is a function of the air-sea temperature difference. The correlation of $\overline{T}$ and $\dot{Q}$, or F and $\dot{Q}$, must be positive to generate zonal potential energy. This means that heating of relatively warm air and cooling of relatively cool air occurred in the model.

The dissipation terms D_{ei}, D_{es}, D_{zi} and D_{zs} provide an energy loss mechanism for eddy and zonal kinetic energies. The second subscript, s or i, refers to dissipation by surface or internal friction respectively.

An interesting way to examine the system energy is by considering an energy flow diagram. Figure 4 depicts such a diagram. The boxes contain time rate of change of energy, and the arrows show the direction of the flow of energy if the transformation is positive.

The model equations were integrated until a statistically steady state was reached. Energy calculations were made and instantaneous values for the quantities just discussed are shown in Figure 5.

The diabatic heating from the sea surface creates zonal potential energy that amounts to 1.27 watt m^{-2}. The conversion from zonal potential energy into its eddy counterpart occurs at the rate of 1.32 watt m^{-2}. The eddy potential energy is converted to eddy kinetic energy through the eddy circulation at a rate of 1.34 watt m^{-2}. The

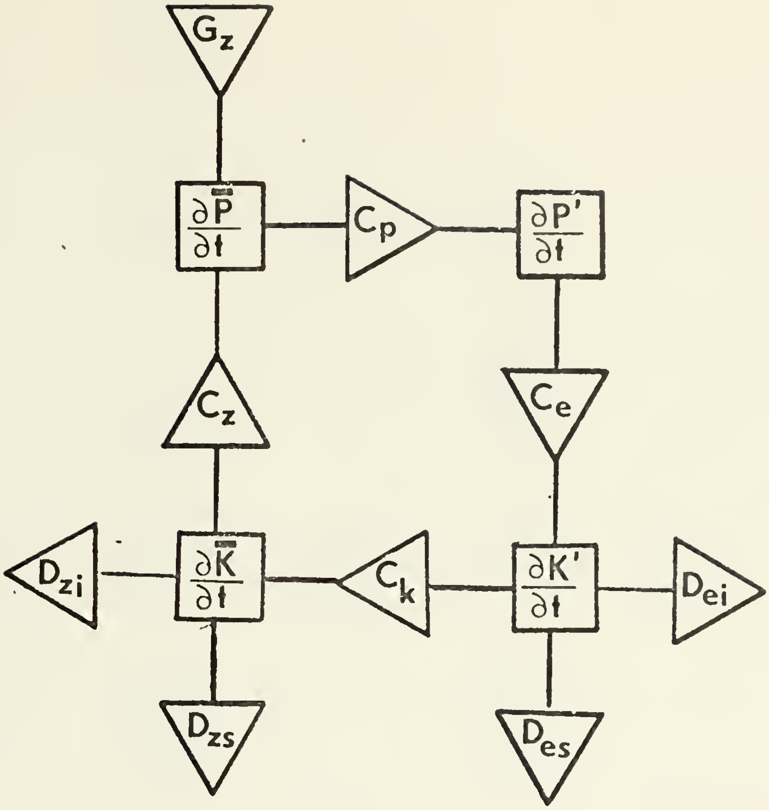
G_z
$\frac{\partial \bar{\bar{P}}}{\partial t}$
C_p
$\frac{\partial P'}{\partial t}$
C_z
C_e
D_{zi}
$\frac{\partial \bar{\bar{K}}}{\partial t}$
C_k
$\frac{\partial K'}{\partial t}$
D_{ei}
D_{zs}
D_{es}

Figure 4. Energy flow diagram. Flow is in the direction of the arrows if the transformation is positive.

conversion of eddy kinetic to zonal kinetic energy, which maintains the zonal currents against frictional dissipation is 0.63 watt m^{-2}. The dissipation of eddy kinetic energy by surface friction is 0.79 watt m^{-2}. This is substantially larger than dissipation by internal friction and the dissipation of zonal kinetic energy by surface friction.

It should be noted that the change of potential energy, both zonal and eddy, was very small while the change in kinetic energy was substantial. The atmospheric model

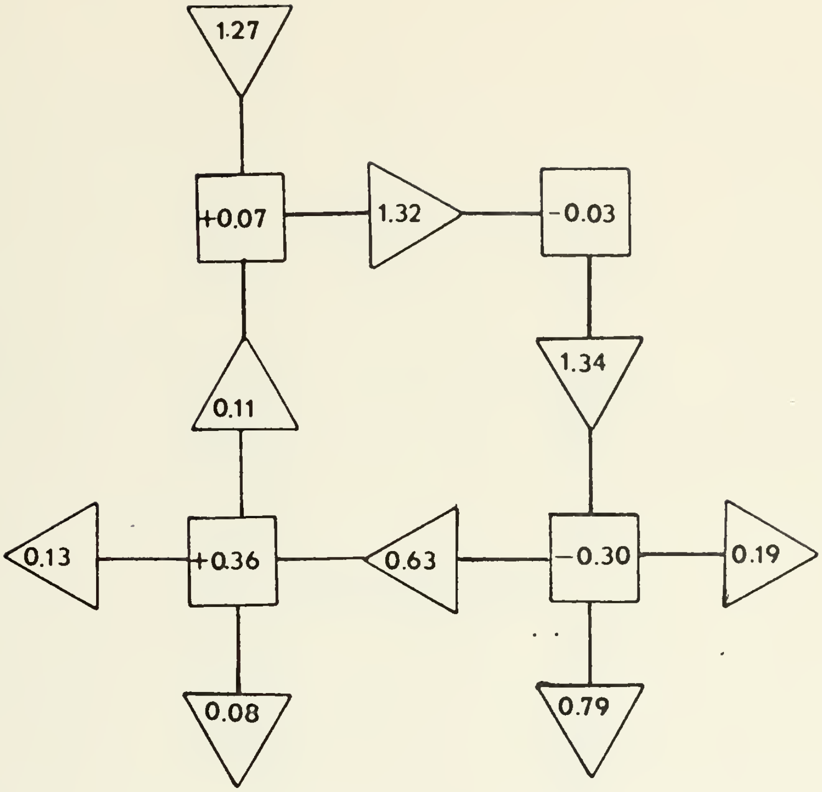

Figure 5. Flow diagram of the model atmosphere energy. Energy and energy transformation units are in watt m^{-2} (10^3 erg cm^{-1} sec^{-1}).

had reached a statistically steady state at the time the energy computations were made, but the energy continued to fluctuate about a mean value. This undoubtedly influenced these calculations.

An exact balance was not achieved throughout the entire system. It is believed that these very small discrepancies were due to truncation or roundoff errors and should not be considered a serious defect in the calculations. Figure 6 is included to show that these values are

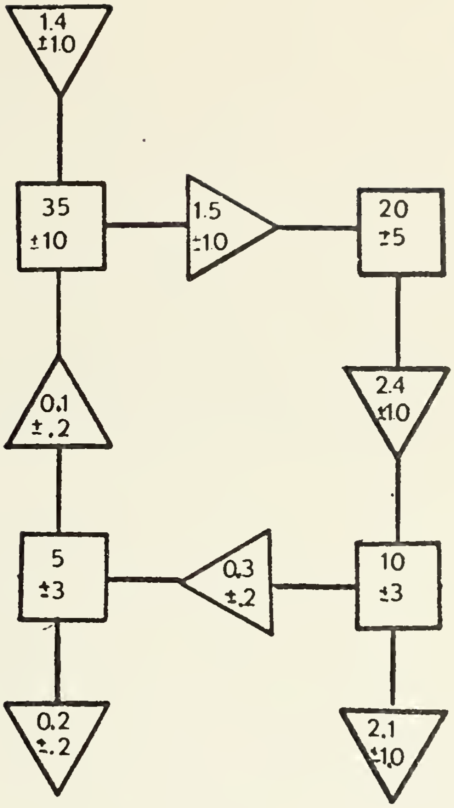

Figure 6. Flow diagram of atmospheric energy as constructed by Oort(1964). Energy units are in 10^5 joule m^{-2}; energy transformation units are in watt m^{-2}.

not only qualitatively correct but also quantitatively acceptable. Figure 6 shows the atmospheric energy flow diagram as constructed by Oort (1964). The values enclosed in the boxes are no longer time rates of change of energy but the amount of energy present.

It is satisfying to note that the transformations in the model atmosphere compare favorably with those of Oort. The conversion C_p and C_z agree very well while C_e and C_z lie just outside the extreme values as proposed by

Oort. The dissipation of eddy kinetic energy is much smaller than Oort's. Since his value itself is considered too small, this points out a weakness in the dissipative mechanism of the model. This may be due to the lack of horizontal diffusion terms in the model equations. It was decided that diffusion was unnecessary in the model and this decision may be reflected in the energy dissipation. Also, energy loss through nonlinear interaction between waves has been eliminated in this model by the single wave formulation.

III. THE OCEAN MODEL

A. DESCRIPTION AND EQUATIONS OF THE MODEL

The ocean model is similar to that studied by Bryan (1969) and Haney (1971a). It is a baroclinic model based on the primitive equations in which steady state solutions are sought by direct numerical integrations of an initial value problem. The circulation produced in the ocean-only model is primarily driven by surface forces that simulate wind stresses, and horizontal pressure gradient forces due to internal stratification. The horizontal stress exerted on the ocean surface by large scale wind systems causes the surface water to move as an Ekman layer and drift to the right of the stress in the Northern Hemisphere. This causes the curl of the wind stress to become important as it causes convergence or divergence of the Ekman layer transport and corresponding vertical velocities below the Ekman layer.

Heating in low latitudes and cooling in high latitudes causes a thermal circulation to develop. A thermal current is set up where there are easterlies in the south and westerlies in the north. These currents converging into the continental boundaries contribute to the resulting circulation.

The rectangular ocean basin is everywhere 1700 meters deep and is 4800 km wide and 6000 km in length. To coincide with the atmospheric domain the basin extends from 18 degrees to 72 degrees north (Figure 2). As in the model

atmosphere, the β-plane approximation is used. Veronis (1963a,b) has shown that the β-plane approximation is satisfactory for the intermediate scale motions in middle latitudes. This formulation is also used to maintain consistency with the atmosphere and prepare for future joining of the two models. The β-plane approximation in both models eliminates the need for mapping and reduces the possibility of confusion that might arise if an ocean model in spherical coordinates were joined with an atmospheric model using cartesian geometry.

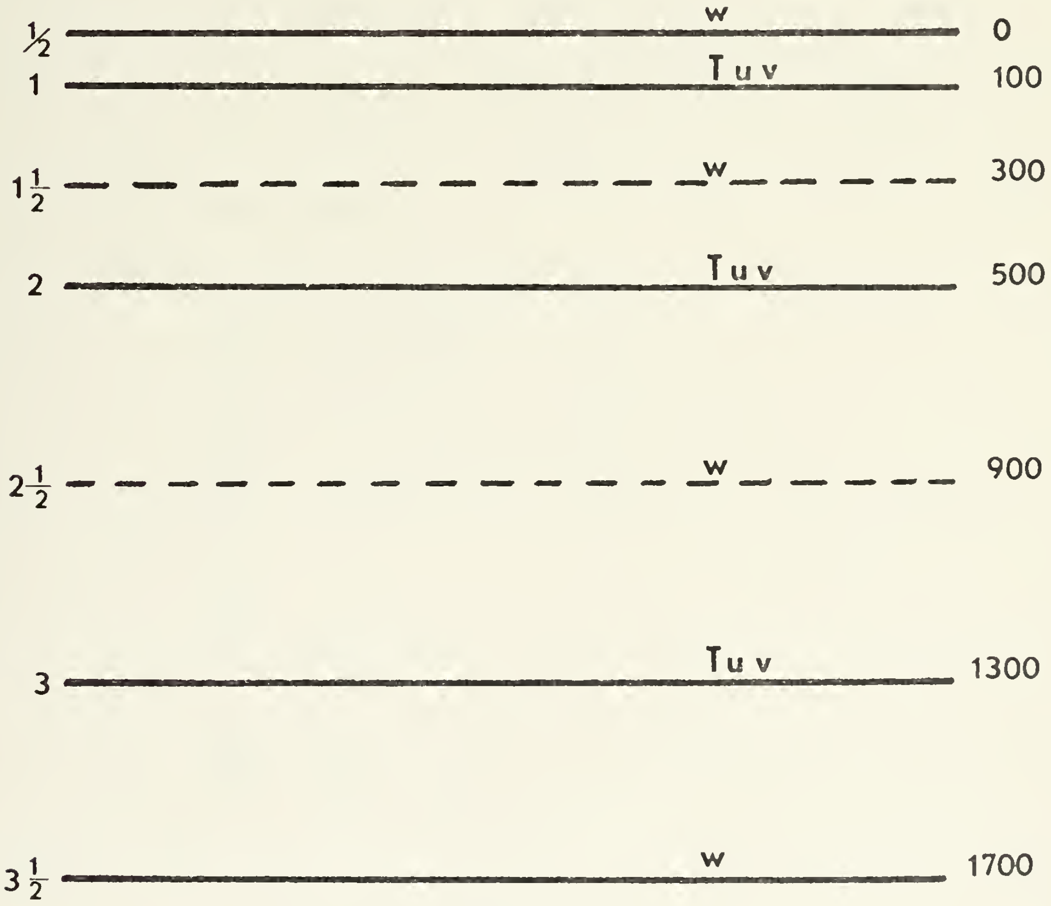

Figure 7. Vertical structure of the ocean model.

The vertical structure of the three-level model, shown in Figure 7, is changed considerably from that described by Haney. The three levels are placed at 100, 500, and 1300 meters below an undisturbed surface. Temperature and horizontal velocities are predicted at these levels while the vertical velocity is diagnostically computed at the intermediate levels. The vertical layering is defined in such a way that there is a finer resolution near the surface than near the bottom.

The Boussinesq approximation (variations of density are neglected except in terms involving gravitational acceleration) and the hydrostatic approximation are applied. In the equation of state, the dependence of density on salinity is neglected. Density is assumed to be a linear function of temperature only.

The governing equations are

$$\frac{du}{dt} = -\frac{1}{\rho_o}\frac{\partial p}{\partial x} + vf + \frac{1}{\rho_o}F_x \quad , \qquad (3.1)$$

$$\frac{dv}{dt} = -\frac{1}{\rho_o}\frac{\partial p}{\partial y} - uf + \frac{1}{\rho_o}F_y \quad , \qquad (3.2)$$

$$\frac{\partial p}{\partial z} = -\rho g \quad , \qquad (3.3)$$

$$\nabla \cdot \mathbb{V} + \frac{\partial w}{\partial z} = 0 \quad , \qquad (3.4)$$

$$\frac{dT}{dt} = \frac{\dot{Q}}{\rho_o C} \quad , \qquad (3.5)$$

and

$$\rho = \rho_o[1 - \alpha(T - T_o)]. \qquad (3.6)$$

where F_x = eastward frictional force per unit volume,

F_y = northward frictional force per unit volume,

and $\dot{Q}$ = heating rate per unit volume.

The quantities F_x, F_y and $\dot{Q}$ represent the assumed contributions of sub-grid scale motions to the exchange of momentum and heat in the ocean. The internal redistribution is accomplished by utilizing a linear lateral diffusion of heat and momentum. Similarly, the vertical mixing of these two quantities by sub-grid scale eddies is specified by a linear vertical diffusion coefficient. The vertical mixing of temperature is enhanced by the use of an instantaneous adjustment mechanism to eliminate unstable lapse rates.

For the initial experiments with the ocean model a constant wind stress was imposed. Figure 8 shows the mean zonal stress that was used in this phase. The data was taken from Hellerman (1967).

Following Haney (1971a) the downward heat flux at the ocean surface is expressed as

$$K\frac{\partial T}{\partial z})_{z=\frac{1}{2}} = [H_o + H_1(T_a - T_{sea})]/\rho_o C \ . \tag{3.7}$$

The quantity H_o contains the net downward flux of solar radiation across the ocean surface, minus the upward flux of longwave radiation and latent heat from an ocean surface at a temperature equal to T_a, the prescribed atmospheric equilibrium temperature. The second term contains the upward longwave radiation and sensible and latent heat. The

coefficient H_1 was found by Haney to vary with latitude by about 20 percent. It was set equal to a constant in this work.

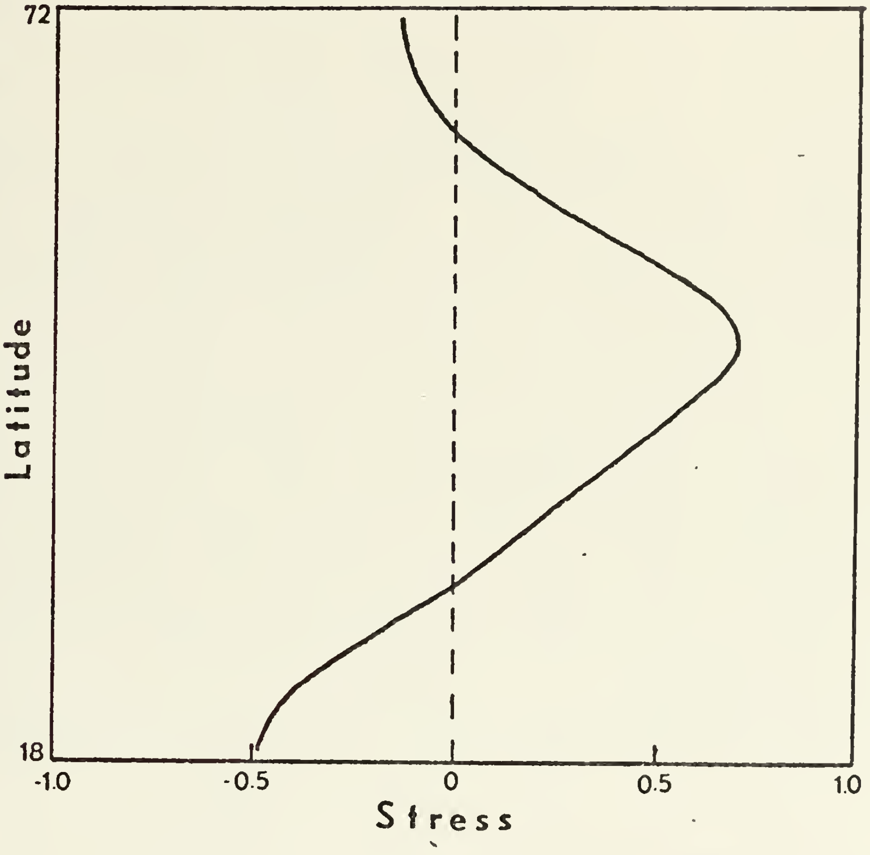

Figure 8. Mean zonal stress used in the ocean model experiments. The data is from Hellerman (1967); units in dynes cm^{-2}.

B. COMPUTATIONAL PROCEDURES

Since the ocean bottom is flat, w = 0 is the boundary condition on the vertical velocity there. Following the method used by Bryan and Cox (1967), Haney (1971a) and others, the ocean surface was considered a balanced surface

at which $w = 0$. The height of the surface was not obtained from the continuity equation so external gravity waves were eliminated, which permitted a much larger time step to be used. However, the technique also removed the vertical mean divergence from all scales of motion, including Rossby waves, and introduced an artificial constraint on the phase speed of these waves (Gates 1968). The necessity for the longer time step to accomplish long-term integrations made this technique mandatory. This filtering technique does not affect the thermally driven part of the motion.

A new set of equations was formed by subtracting the vertically integrated form of Equations (3.1) and (3.2) from Equations (3.1) and (3.2) respectively. After eliminating the pressure deviation in favor of the temperature by the hydrostatic equation and the equation of state, equations for the time rate of change of the vertical shear current (u'v') were obtained. These equations have the form

$$\frac{\partial}{\partial t}(u') = F_1(u,v,T) \tag{3.8}$$

and

$$\frac{\partial}{\partial t}(v') = F_2(u,v,T), \tag{3.9}$$

where

$$u'(x,y,z,t) = u(x,y,z,t) - \bar{u}(x,y,T) \tag{3.10}$$

and

$$v'(x,y,z,t) = v(x,y,z,t) - \bar{v}(x,y,T), \tag{3.11}$$

and $\bar{u}$ and $\bar{v}$ are the vertical mean motions discussed shortly. Equations (3.8) and (3.9) were numerically solved to obtain new values of the vertical shear current.

A vorticity equation, from which the vertical mean current was predicted, was formed by eliminating the pressure between Equations (3.1) and (3.2). The result was vertically averaged and had the form

$$\frac{\partial}{\partial t} \frac{1}{H} \int_{-H}^{0} \zeta dz = F_3(u,v) \qquad (3.12)$$

where ζ is the relative vorticity and H is the depth of the basin. Vertical integration of the continuity equation (3.4) allowed the introduction of a stream function for the vertically integrated velocity since the vertical mean divergence was zero. The vertically averaged vorticity therefore had the form

$$\frac{1}{H} \int_{-H}^{0} \zeta dz = \nabla^2 \psi \qquad (3.13)$$

and Equation (3.12) can be written

$$\frac{\partial}{\partial t} \nabla^2 \psi = F_3(u,v) \, . \qquad (3.14)$$

A relaxation technique was used to solve Equation (3.14) for the time rate of change of ψ. The quantity ψ was then set to zero on the boundaries. A time integration was then performed to obtain the new value of the stream function and then the vertically averaged velocity components from

$$\frac{1}{H} \int_{-H}^{0} u dz = - \frac{\partial \psi}{\partial y} \equiv \bar{u}$$

and

$$\frac{1}{H} \int_{-H}^{0} v dz = \frac{\partial \psi}{\partial x} \equiv \bar{v} \, . \qquad (3.15)$$

The total current was then obtained by adding the vertical shear components predicted by Equations (3.8) and (3.9) to the vertically averaged components predicted by (3.14).

To obtain new values of the temperature, Equation (3.5) was written as

$$\frac{\partial T}{\partial t} = F_4 \ (u,v,T) \tag{3.16}$$

and integrated in time to obtain T. The quantities ρ and w were then diagnostically calculated from (3.6) and (3.4) respectively.

The boundary conditions on momentum and heat at the walls were those of zero slip and perfect insulation. The ocean bottom was also considered to be perfectly insulated. As a simplification of the model, bottom friction was neglected and free slip was allowed.

C. HEATING AND FRICTION

It was assumed that all solar radiation penetrating the ocean's surface was absorbed in the top layer which was 300 meters thick. Since the side walls and bottom of the basin were insulated, the only source of heat was at the surface and was calculated from the thermal boundary condition (Equation 3.7). A parameterization scheme by which the internal redistribution of heat by sub-grid scale phenomena was represented by a simple linear eddy diffusion of heat and an instantaneous convective adjustment mechanism was used in the model. The right hand side of Equation (3.5) can be written

$$\frac{\dot{Q}}{\rho_o C} = A_H \nabla^2 T + \frac{\partial}{\partial z}\left(K\frac{\partial T}{\partial z}\right) + \frac{(\delta T)_c}{\Delta t} . \qquad (3.17)$$

Bryan and Cox (1967) have shown that the lateral mixing coefficient, A_H, for the apparent temperature should be less than that for momentum given by A_M. This is due to the larger scales of turbulent motion in the ocean having a tendency to take place along isentropic surfaces rather than strictly horizontal surfaces. The lateral mixing of momentum and temperature in the model is somewhat dictated by the resolution of the numerical grid. The coefficient should be sufficiently small so as not to obscure the lateral transfer of the quantities. A minimum value of both A_M and A_H is needed to satisfy the zero slip boundary conditions, and to simulate the horizontal eddy transport of heat and momentum by scales of motion too small to be resolved by the numerical grid. In this phase of the work, coefficients were held constant with

$$A_H = .25 \times 10^8 \text{ cm}^2 \text{ sec}^{-1}$$

and

$$A_M = 1.0 \times 10^8 \text{ cm}^2 \text{ sec}^{-1} .$$

The vertical diffusion coefficient, K, differs in that the exact physical processes by which vertical exchange takes place within the thermocline is unknown. Following Bryan (1969) a value of 1.5 $\text{cm}^2 \text{ sec}^{-1}$ was used throughout this study.

The convective adjustment mechanism $(\delta T)_c$ is difficult to state mathematically. This device is a means by which the temperature structure in the model was forced to remain stable. After the convective and diffusive heating terms were added, the vertical temperature profile was examined for unstable lapse rates. If the temperature field resulted in an unstable lapse rate, the temperatures were instantaneously adjusted to the vertical mean temperature of those unstable layers. When this first adjustment was completed, the temperature field was again examined to determine if any other layers had been made unstable. The adjustment process was repeated until all layers were gravitationally stable.

The quantity $K\frac{\partial T}{\partial z}$ was evaluated as follows:

$$K\frac{\partial T}{\partial z})_{k=\frac{1}{2}} = [H_o + H_1(T_a - T_{sea})]/\rho_o C \quad ,$$

$$K\frac{\partial T}{\partial z})_{k=1\frac{1}{2}} = K(\frac{T_1 - T_2}{z_1 - z_2}) \quad ,$$

$$K\frac{\partial T}{\partial z})_{k=2\frac{1}{2}} = K(\frac{T_2 - T_3}{z_2 - z_3})$$

and

$$K\frac{\partial T}{\partial z})_{k=3\frac{1}{2}} = 0 \ . \qquad (3.18)$$

The last equality imposed the condition that the ocean floor was insulated since the vertical temperature gradient vanishes.

The vertical eddy diffusion of heat at level one, for example, was then defined to be

$$\frac{\partial}{\partial z}\left(K\frac{\partial T}{\partial z}\right)_1 = \frac{[H_o + H_1(T_a - T_{sea})]/\rho_o C - \dfrac{K(T_1 - T_2)}{(z_1 - z_2)}}{(z_{1/2} - z_{1\frac{1}{2}})} . \qquad (3.19)$$

The heating term due to lateral eddy diffusion of heat in (3.16) may be written as

$$A_H \nabla^2 T = A_H\left[\frac{\partial}{\partial x}\left(\frac{\partial T}{\partial x}\right) + \frac{\partial}{\partial y}\left(\frac{\partial T}{\partial y}\right)\right] . \qquad (3.20)$$

The terms $\frac{\partial T}{\partial x}$ and $\frac{\partial T}{\partial y}$ were defined at points one-half grid distance to the east and north, respectively, of points at which T was stored (see Figure 9). The boundary conditions were

$$\left.\frac{\partial T}{\partial x}\right)_{i=\frac{1}{2}} = - \left.\frac{\partial T}{\partial x}\right)_{i=\frac{3}{2}}$$

and

$$\left.\frac{\partial T}{\partial x}\right)_{i=i_{max}+\frac{1}{2}} = - \left.\frac{\partial T}{\partial x}\right)_{i=i_{max}-\frac{1}{2}} \qquad (3.21)$$

where $i = \frac{1}{2}$ is a point one-half grid distance west of the western boundary of the grid(located at i=1) and $i_{max} + \frac{1}{2}$ is a point one-half grid distance east of the eastern boundary (located at $i=i_{max}$). These conditions force $\frac{\partial T}{\partial x}$ to pass through zero at the eastern and western boundaries thereby producing thermal insulation. Similar boundary condition on $\frac{\partial T}{\partial y}$ at the northern and southern boundaries ensure that the normal temperature gradient vanished at the walls, making them perfect insulators.

The frictional terms $\frac{F_x}{\rho}$ and $\frac{F_y}{\rho}$ in Equations (3.1) and (3.2) are composed of two parts. These are the sub-grid

scale vertical eddy stress and the sub-grid scale lateral diffusion of momentum. These can be expressed as

$$\frac{F_x}{\rho_o} = \frac{1}{\rho_o} \frac{\partial \tau_x}{\partial z} + A_M \nabla^2 u$$

and

$$\frac{F_y}{\rho_o} = \frac{1}{\rho_o} \frac{\partial \tau_y}{\partial z} + A_M \nabla^2 v . \tag{3.22}$$

As with the term $K\frac{\partial T}{\partial z}$, the quantities τ_x and τ_y were defined at the half integer vertical levels. The vertical eddy stress was prescribed at the surface and defined to be zero at the bottom. The zonal stress was defined at each level as

$$\left.\frac{\tau_x}{\rho_o}\right)_{k=\frac{1}{2}} = \text{prescribed surface stress},$$

$$\left.\frac{\tau_x}{\rho_o}\right)_{k=1\frac{1}{2}} = K \frac{(u_1 - u_2)}{(z_1 - z_2)} ,$$

$$\left.\frac{\tau_x}{\rho_o}\right)_{k=2\frac{1}{2}} = K \frac{(u_2 - u_3)}{(z_2 - z_3)} ,$$

$$\left.\frac{\tau_x}{\rho_o}\right)_{k=3\frac{1}{2}} = 0 , \tag{3.23}$$

and the meridional stress was defined as

$$\left.\frac{\tau_y}{\rho_o}\right)_{k=\frac{1}{2}} = 0 ,$$

$$\left.\frac{\tau_y}{\rho_o}\right)_{k=1\frac{1}{2}} = K \frac{(v_1 - v_2)}{(z_1 - z_2)} ,$$

$$\left.\frac{\tau_y}{\rho_o}\right)_{k=2\frac{1}{2}} = K \frac{(v_2 - v_3)}{(z_2 - z_3)} ,$$

$$\left.\frac{\tau_y}{\rho_o}\right)_{k=3\frac{1}{2}} = 0 . \qquad (3.24)$$

Thus the prescribed stress was purely zonal.

The x component of the term involving the lateral eddy diffusion of momentum can be expressed as

$$A_M \nabla^2 u = A_M \left[\frac{\partial}{\partial x}\left(\frac{\partial u}{\partial x}\right) + \frac{\partial}{\partial y}\left(\frac{\partial u}{\partial y}\right)\right] . \qquad (3.25)$$

The quantities $\frac{\partial u}{\partial x}$ and $\frac{\partial u}{\partial y}$ were defined one-half grid distance to the west and south respectively of the velocity storage points. The boundary conditions were

$$\left.\frac{\partial u}{\partial x}\right)_{i=1} = \frac{\left.2u\right)_{i=1\frac{1}{2}}}{\Delta x} ,$$

$$\left.\frac{\partial u}{\partial x}\right)_{i=i_{max}} = -\left.\frac{2u}{\Delta x}\right)_{i=i_{max}-\frac{1}{2}} ,$$

$$\left.\frac{\partial u}{\partial y}\right)_{j=1} = -\left.\frac{2u}{\Delta y}\right)_{j=1\frac{1}{2}} ,$$

and

$$\left.\frac{\partial u}{\partial y}\right)_{j=j_{max}} = -\left.\frac{2u}{\Delta y}\right)_{j=j_{max}-\frac{1}{2}} . \qquad (3.26)$$

These conditions impose the zero slip boundary condition on the velocity at the north and south walls and the no flux condition at the east and west walls. Similar definitions for the meridional components impose the zero slip condition on the east and west walls and the no flux condition on the north and south walls.

D. FINITE DIFFERENCE TECHNIQUES

A space differencing scheme that utilized a centered differencing with a staggered grid was used in the integration of the primitive equations. When a centered space

scheme is used with an unstaggered grid, a computational mode in space arises that is analogous to the computational time mode that occurs with a centered time differencing (leap frog) scheme. The use of the staggered grid not only prevents the appearance of the computational mode in space but is responsible for considerable savings in computing time because variables are retained at alternate grid points. Arakawa (1966) has shown that maintaining integral constraints on certain quadratic quantities of physical importance is sufficient to guarantee nonlinear computational stability. The space differencing used in this model is a simplified, energy conserving version of the scheme used in the UCLA general circulation model, as documented by Gates *et al* (1971).

Total energy is conserved in this model. The boundary conditions of zero normal flow through the side walls, and zero vertical velocity at the bottom, guaranteed that the following integral constraints were satisfied by the differential equations.

Kinetic Energy

$$\frac{d}{dt}\int_{v} \frac{1}{2}\rho_o(u^2 + v^2)\,dv = \int_{v} [-\rho g w + \rho_o(uF_x + vF_y)]\,dv . \qquad (3.27)$$

Potential Energy

$$\frac{d}{dt}\int_{v} \rho g(z+H)\,dV = \int_{v} [\rho g w - g(z+H)\,\frac{\alpha Q}{C}]\,dv . \qquad (3.28)$$

The potential energy was taken to be zero at the bottom.

If (3.27) is added to (3.28), a conservation equation for the total energy in the basin is derived and is given by

$$\frac{d}{dt} \int_v [\frac{1}{2} \rho_o (u^2 + v^2) + \rho g(z+H) dv =$$
$$\int_v [\rho_o (uF_x + vF_y) - g(z+H)\frac{\alpha Q}{C}] dv. \qquad (3.29)$$

Finite difference forms of the prediction Equations (3.8), (3.9), (3.12) and (3.16) are shown in Appendix D. Haney (1971a) has shown that these difference equations conserve total energy.

Figure 9 shows the staggered grid network. The velocity components, u and v, are located one-half grid increment east and one-half grid increment north of the points where corresponding scalar variables T, p and ψ are retained. The grid distance is 200 km in both the x and y directions.

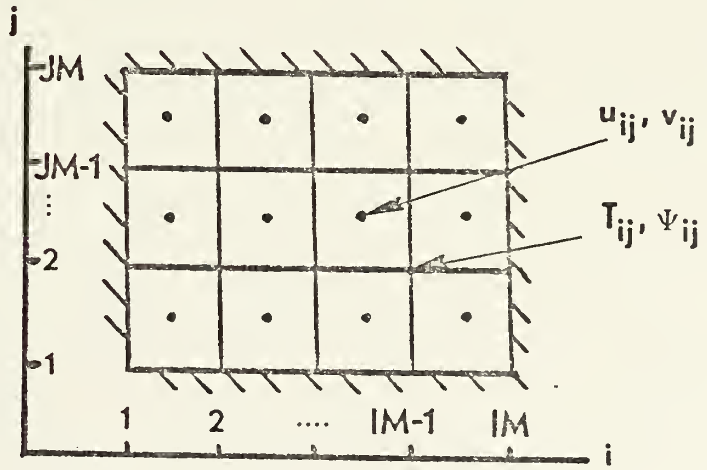

Figure 9. Location of variables in the horizontal staggered grid.

In the time differencing scheme, various terms in the equations of motion were treated differently. The pressure gradient term was evaluated using a centered difference. The Coriolis term was evaluated by a trapezoidal implicit scheme, and the friction term was evaluated using a forward time step to ensure linear computational stability.

The trapezoidal implicit scheme for the Coriolis acceleration reduces to a form

$$u^{n+1} - u^{n-1} = 2\Delta t[\alpha if\, u^{n+1} + (1-\alpha)if\, u^{n-1}]. \qquad (3.30)$$

It is easy to show that this scheme is linearly computationally stable for all Δt if $\frac{1}{2} \leqslant \alpha \lesssim 1$. In this model, $\alpha = 0.55$.

To supress computational modes in time that can arise when a leap-frog scheme is used exclusively in an oscillating system, a Matsuno (Euler-Backward) step was used periodically. This two-step scheme damps the computational mode and permits the long term integration.

The leap-frog scheme is conditionally stable and the maximum time step was determined by the highest frequency governed by this scheme. External gravity waves have been removed from the model which leaves internal gravity waves as the highest frequency waves present. The phase speed of these waves is $\sqrt{g'H'}$ where g' is a modified gravity equal to $g\frac{\Delta\rho}{\rho_o}$. In this model $g' \simeq 3.60$ cm sec^{-2}, $H' = 1200$ meters and $\Delta y = 200$ km, and the linear computational stability criterion is

$$\Delta t \lesssim \frac{\Delta y}{\sqrt{g'H'}} \sim .375 \text{ days.}$$

This was the time step used in this phase of the model.

E. INITIAL CONDITIONS

A state of rest was imposed on the ocean for the start of the first integrations. A stratified temperature structure was selected so that a minimum amount of computing time would be required to bring the ocean model to thermal equilibrium. Figure 10 shows the vertical temperature structure.

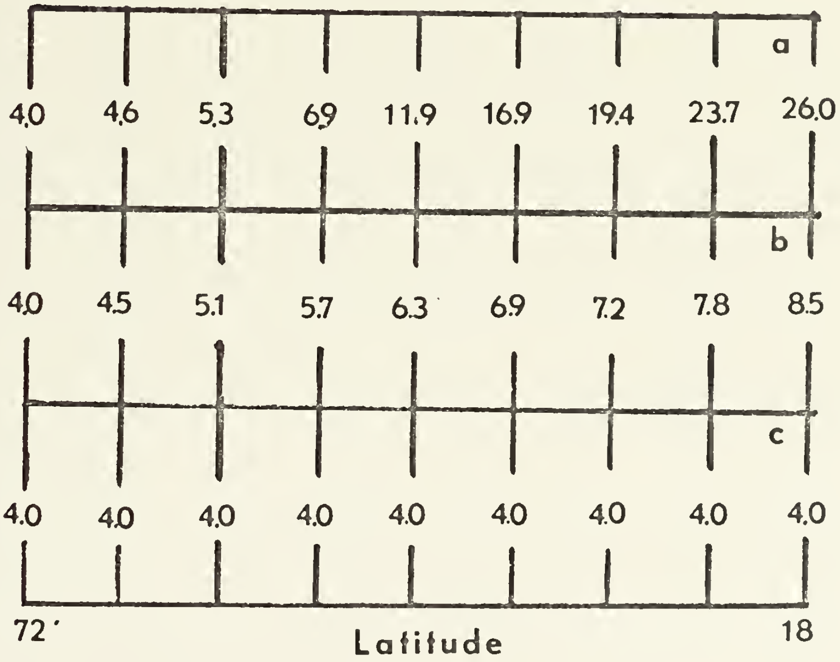
a
4.0
4.6
5.3
6.9
11.9
16.9
19.4
23.7
26.0
b
4.0
4.5
5.1
5.7
6.3
6.9
7.2
7.8
8.5
c
4.0
4.0
4.0
4.0
4.0
4.0
4.0
4.0
4.0
72
Latitude
18

Figure 10. a) Initial temperature field at level one; b) Same at level two; c) Same at level three.

The northernmost temperature at each level is 4 degrees Centigrade and the vertical structure is isothermal in that column. The temperature at level one increased from 4C at the northern boundary to 26C at the southern wall. At level two the temperature increases from 4C to 8.5C and at level three it is a constant 4C throughout. The stability varies from isothermal in the northernmost column to very stable in the southernmost column. No zonal variations were initially imposed.

IV. THE COMBINED AIR-SEA MODEL

A combined model was developed by joining the atmosphere and ocean models. The exchange of momentum and heat across the air-sea interface is the mechanism upon which the coupling of the two models was based. An exchange of moisture was not possible since the atmospheric model was "dry", but a crude attempt at parameterizing latent heat transport in the atmosphere was incorporated and will be discussed in the section on heat exchange.

The physical aspects of the combined models remained the same as they were in the individual models. The spatial grid in the ocean, and time increments for each model, remained the same. The time marching process allowed the time integration to remain synchronized and avoided a distorted response of the ocean circulation to atmospheric fluctuations. The atmospheric solution was evaluated at grid points in the x-direction in the atmospheric model. This was done to construct a complete stress field from the atmospheric Fourier coefficients in order to calculate the air-sea momentum exchange. The ocean surface temperature was transformed to wave number space to calculate the air-sea heat exchange. The overall techniques of integration used in each separate model remained unchanged in the combined model.

A. TIME SYNCHRONIZATION

One of the problems that arose in early air-sea models, such as that developed by Manabe (1969a,b) and Bryan (1969) was the impracticality of using a marching process that would keep the ocean and atmosphere synchronized. Primitive equation atmospheric models require time steps on the order of minutes and cannot be realistically integrated in sequence with ocean models that have time steps on the order of hours, because the computing time requirements are prohibitive. Techniques have been developed to simulate time synchronization but little success has been achieved in long-term one-to-one integrations.

Since the present atmospheric model is quasi-geostrophic, a time step of one-half hour was utilized. The ocean time step was nine hours as discussed previously. The resulting ratio of atmospheric time steps to ocean time steps was eighteen to one. The marching process consisted of 18 thirty-minute time steps in the atmosphere followed by one nine hour time step in the ocean.

Conservation of momentum and heat in the exchange process during the integration was crucial to the development of a realistic interaction model. Therefore, the quantities such as the total surface stress and heating calculated during the 18 atmospheric time steps had to equal the quantity as it was applied during the one ocean time step. The method by which this was accomplished will be discussed in the next two sections.

B. MOMENTUM EXCHANGE

The surface stress discussed earlier and computed from Equation (2.3) was used as an upper boundary condition for the ocean. The calculation of this stress was based on the assumption that there was no motion in the ocean. That assumption is also used in the stress formulation in the combined model. Since the velocity of ocean currents is much smaller than the velocity of air flow, the effect of ocean currents on momentum exchange can be neglected. Manabe (1969b) used the same argument in justifying his use of a similar formulation of the stress. Simplicity and computing requirements also entered into the decision to use this formulation here.

Starting from a prescribed initial state, the atmospheric equations were integrated over 18 time steps. The surface stress was calculated each time and an average was computed to be used for the ocean integration. A general numerical procedure for carrying out the computation of the time mean surface stress is given by

$$STXX_{ij} = \frac{1}{NM}\left[\sum_{n=1}^{NM} (\tau_x)ijn\right] \qquad (4.1)$$

and

$$STXY_{ij} = \frac{1}{NM}\left[\sum_{n=1}^{NM} (\tau_y)ijn\right], \qquad (4.2)$$

where $NM = (\Delta t)_{ocean}/(\Delta t)_{atmosphere}$

and i and j are horizontal grid indices having their usual directions.

Since the surface stress components in the atmospheric model, τ_x and τ_y, were not calculated directly, terms had to be collected and values for the stresses recovered at each grid point. The stresses were computed in three equations, (2.22), (2.23) and (2.26).

The following definitions were made:

$\tau_x)_A$, $\tau_Y)_A$ $\equiv$ Contributions of the A disturbance to the zonal and meridional components of stress computed in the A equation.

$\tau_x)_B$, $\tau_Y)_B$ $\equiv$ Contributions of the B disturbance to the zonal and meridional components of stress computed in the B equation.

$\tau_x)_E$, $\tau_Y)_E$ $\equiv$ Contributions of the mean field to the zonal and meridional components of stress computed in the E equation.

To reconstruct zonal and meridional stress fields from these quantities, the terms must be multiplied by trigonometric functions as follows:

$$(\tau_x)_{ij} = \tau_x)_E + \tau_x)_A \cos kx_i + \tau_x)_B \sin kx_i \qquad (4.3)$$

and

$$(\tau_y)_{ij} = \tau_y)_E + \tau_y)_A \cos kx_i + \tau_y)_B \sin kx_i \,. \qquad (4.4)$$

The locations at which the atmospheric surface stresses were calculated coincide with the points in the ocean at which the temperature and stream function were calculated. Since u and v were calculated at the staggered or half-grid points in the ocean system (see Figure 11), it was necessary

to average the stresses calculated in (4.3) and (4.4) before applying the stress to the ocean. The result is

$$(\tau_x)^u_{ij} = \frac{1}{4}[(\tau_x)_{ij} + (\tau_x)_{i+1,j} + (\tau_x)_{i,j+1} + (\tau_x)_{i+1,j+1}] \tag{4.5}$$

and

$$(\tau_y)^u_{ij} = \frac{1}{4}[(\tau_y)_{ij} + (\tau_y)_{i+1,j} + (\tau_y)_{i,j+1} + (\tau_y)_{i+1,j+1}]. \tag{4.6}$$

STXX and STXY were then calculated from $(\tau_x)^u_{ij}$ and $(\tau_y)^u_{ij}$ for application to the ocean. This procedure of averaging over the number of atmospheric integrations, and applying the stress at the proper position was continued throughout the duration of the long term integrations.

C. HEAT EXCHANGE

To satisfactorily conserve heat in the air-sea exchange process, a time averaging procedure similar to that used in the momentum exchange was utilized. The equations for the heat flux in both atmosphere and ocean must guarantee that the total heat lost by the ocean equals that gained by the atmosphere.

The atmospheric heating was previously discussed and given by Equation (2.21). In the coupled model, that formulation was expanded to include the net radiative heating of the atmosphere and a crude specification of the heat released through precipitation processes. The heat flux into the atmosphere was given by

$$Q_A = R + L \cdot P + H_1(T_{sea} - T_4) \tag{4.7}$$

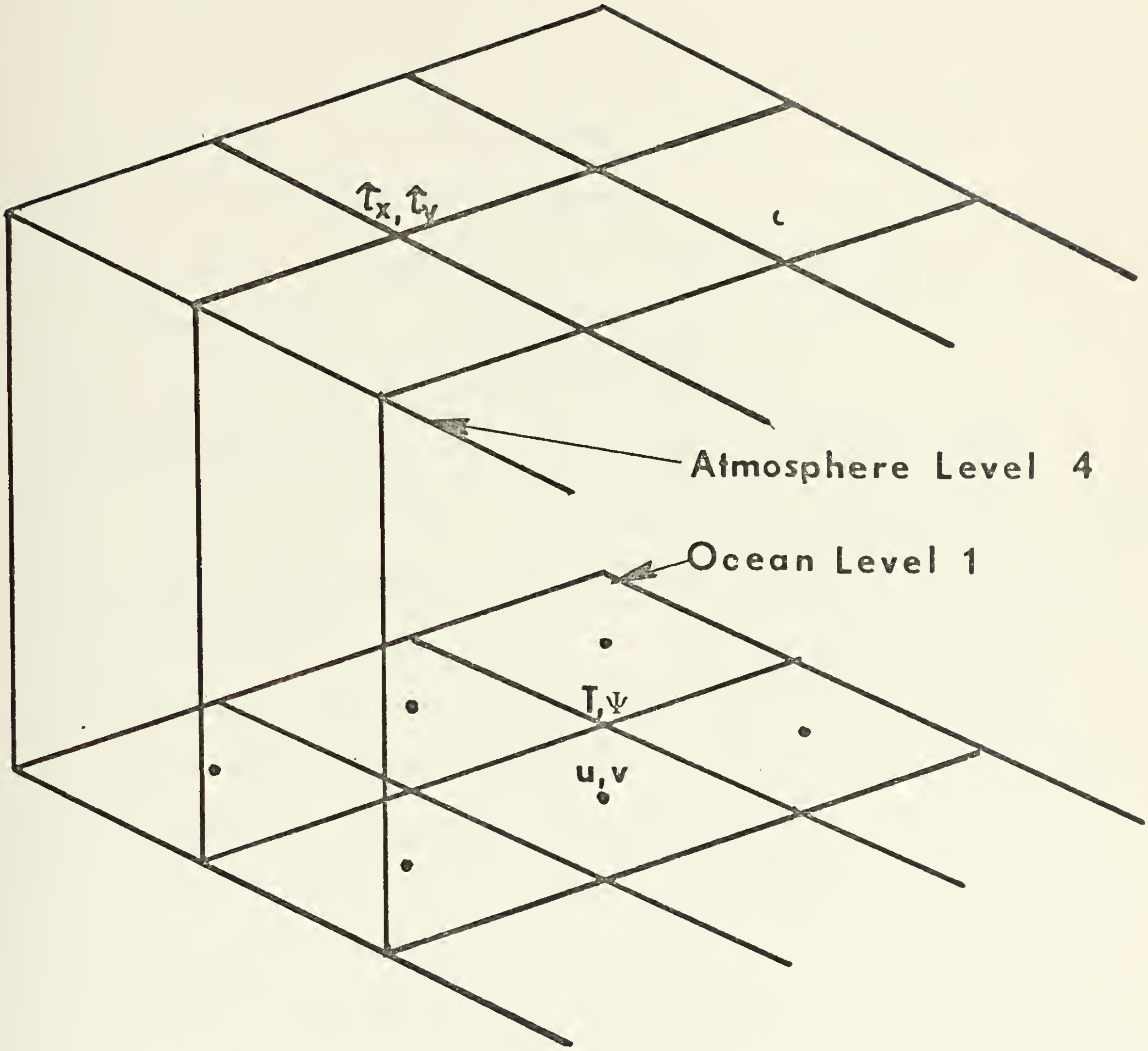

τ_x, τ_y
Atmosphere Level 4
Ocean Level 1
T, Ψ
u, v

Figure 11. Grid alignment of atmosphere and ocean to show non-coincidence of stress points in atmosphere and velocity storage points in the ocean.

where R ≡ net flux of radiation into the atmosphere. and L • P ≡ net flux of heat into the atmosphere due to precipitation. The specification of R and L • P are described below.

The ocean heat flux was also modified from the form used in the ocean only model. The necessity for modification arose from the fact that in the ocean-only model (like the atmosphere-only model) there was no requirement for an exact accounting of heat exchange. The ocean could give up any amount of heat into the non-existent atmosphere with no adverse effects. Similarly, when heat was required, there was an endless supply available from the same non-existent atmosphere. In the combined model, the loss of heat from the ocean by evaporation was a specified function of y only. The quantity H_o in Equation (3.7) was divided into a term representing the net downward flux of short and long wave radiation, S_N, minus the upward flux of latent heat, L•E. The equation for downward oceanic heat flux, Q_o, was therefore written as

$$Q_o = S_N - L \cdot E - H_1(T_{sea} - T_4) \qquad (4.8)$$

where S_N ≡ net downward radiative heat flux

and L•E ≡ net downward latent heat flux.

Figure 12 gives a schematic representation of the heat flux into the combined model and the calculated exchange $H_1(T_{sea}-T_4)$. The arrows originating or terminating outside the model atmosphere or ocean indicate externally specified heat fluxes.

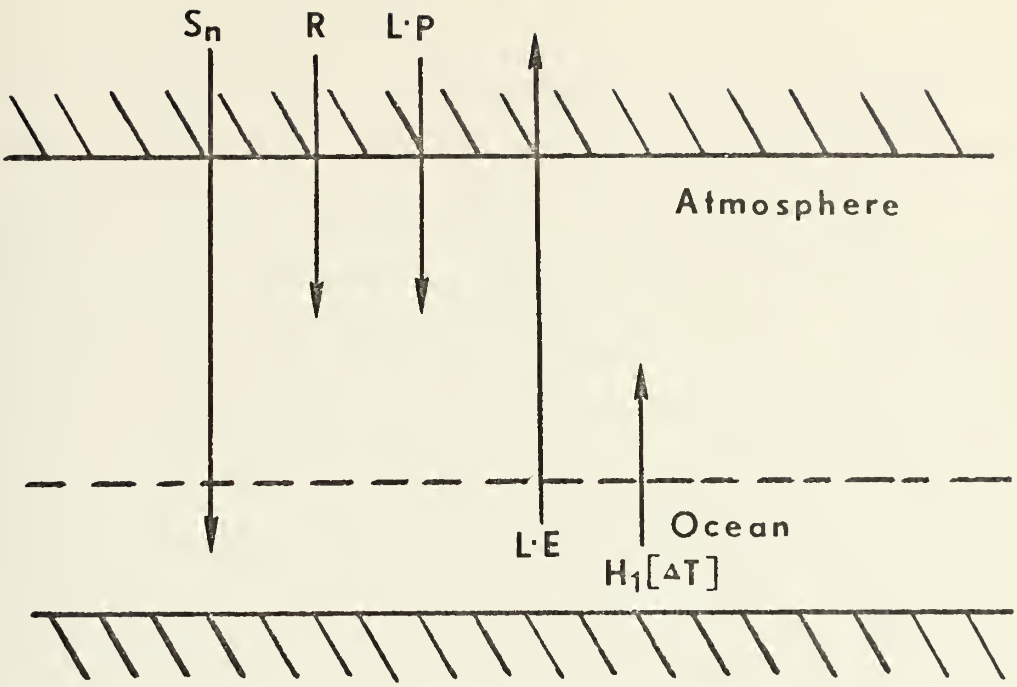

Figure 12. Schematic representation of simplified heat flux into combined model. See text for definition of symbols.

Annual mean values were used in the radiation terms in both Equations (4.7) and (4.8). Wetherald and Manabe (1972) recently reported on the effects of seasonal variation of the solar radiation on the joint ocean-atmosphere model developed by Manabe and Bryan. Their model atmosphere showed a marked warming in high latitude. Although a similar result might be expected in this model, varying the solar radiation should be the subject of a separate investigation and will not be included in this work.

From Equations (4.7) and (4.8), the total heat flux into the ocean-atmosphere system, $Q_a + Q_o$, is given by

$$Q_a + Q_o = S_N + R - L \cdot E + L \cdot P. \qquad (4.9)$$

When Equation (4.9) was integrated over the horizontal domain of the model, the total prescribed heat flux into the combined system was obtained. Time integration of the model cannot approach a steady state unless this total prescribed heat flux into the system is zero. Also, the atmospheric circulation is insensitive to the value of the total heat flux because only an input of available potential energy impulses the circulation. Since each of the heating components on the right hand side of (4.9) represent essentially different physical effects, each term was prescribed to give a zero net heat flux when integrated over the horizontal domain. The meridional mean was removed from R and S_N and the quantities $L \cdot P$ and $L \cdot E$ were made sinusoidal about zero in the y direction. Observed data shows that the ocean receives radiation and the atmosphere loses it at all latitudes. Removing the mean and using the new quantities R' and S_n' simulates the role that the media play as both a source and sink of radiative heating. Removing the mean from both $L \cdot P$ and $L \cdot E$ was necessary to insure that the net prescribed heating in both the atmosphere (given by (4.7)) and ocean (given by (4.8)) was zero. Thus, there is no net prescribed heat exchange between the two media - all of the heat exchange is calculated internally from the last term in (4.7) and (4.8) and

depends on the air-sea temperature difference. Denoting new quantities that have a zero meridional average by primes, Equations (4.7) and (4.8) become

$$Q_A = R' + L \cdot P' + H_1 (T_{sea} - T_4) \qquad (4.10)$$

and

$$Q_o = S_n' - L \cdot E' - H_1 (T_{sea} - T_4). \qquad (4.11)$$

These terms will be discussed in the next sections.

1. Atmospheric Radiation, R', and Solar Radiation, S_N

The observed annual mean net atmospheric radiative cooling plotted as a function of latitude is shown by the dashed line in Figure 13. The data is from London (1957). It shows a meridional average loss of heat due to radiative effects of 184 langleys day^{-1}. The dot-and-dashed line in this figure portrays the deviations from the mean radiation. As can be readily seen, the deviations from the mean are very small and are in all cases less than 10 langleys day^{-1}. These deviations were considered too small to be significant and were neglected. Therefore, $R' \equiv 0$ for future calculations.

Figure 13 also shows the observed annual mean solar radiation minus the mean upward longwave radiation at the earth's surface, S_N. This quantity with its mean removed, S_N', is shown by the dashed line in Figure 14. The values of this quantity used in the model are shown by the solid line in this figure. A profile that was both linear and symmetric was chosen and held constant in time.

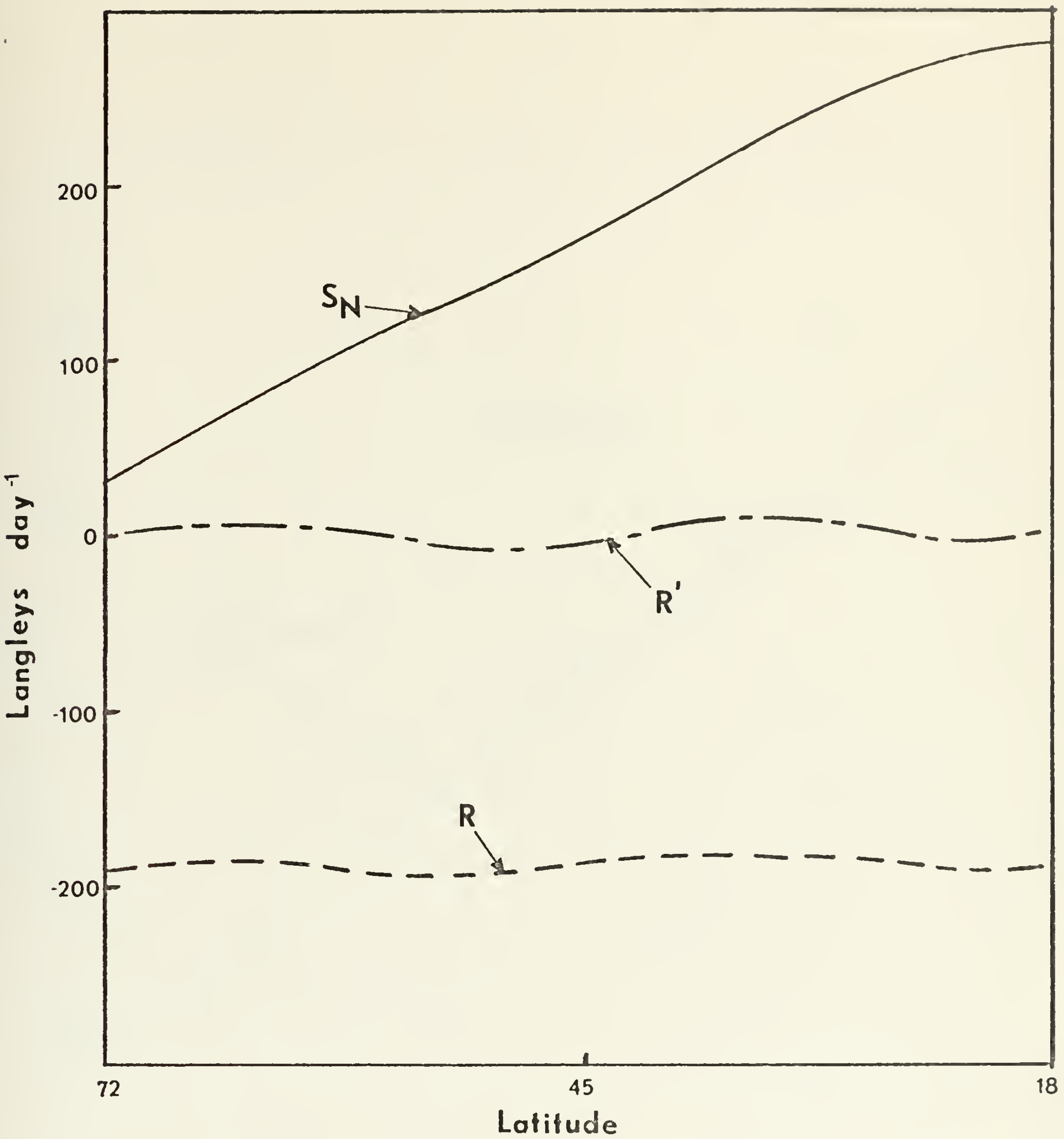

Figure 13. Net mean atmospheric radiation, R, (dashed line); deviation from mean atmospheric radiation, R', (dot-and-dashed line); annual mean net radiation arriving at surface, S_N, (solid line). Data from London (1957).

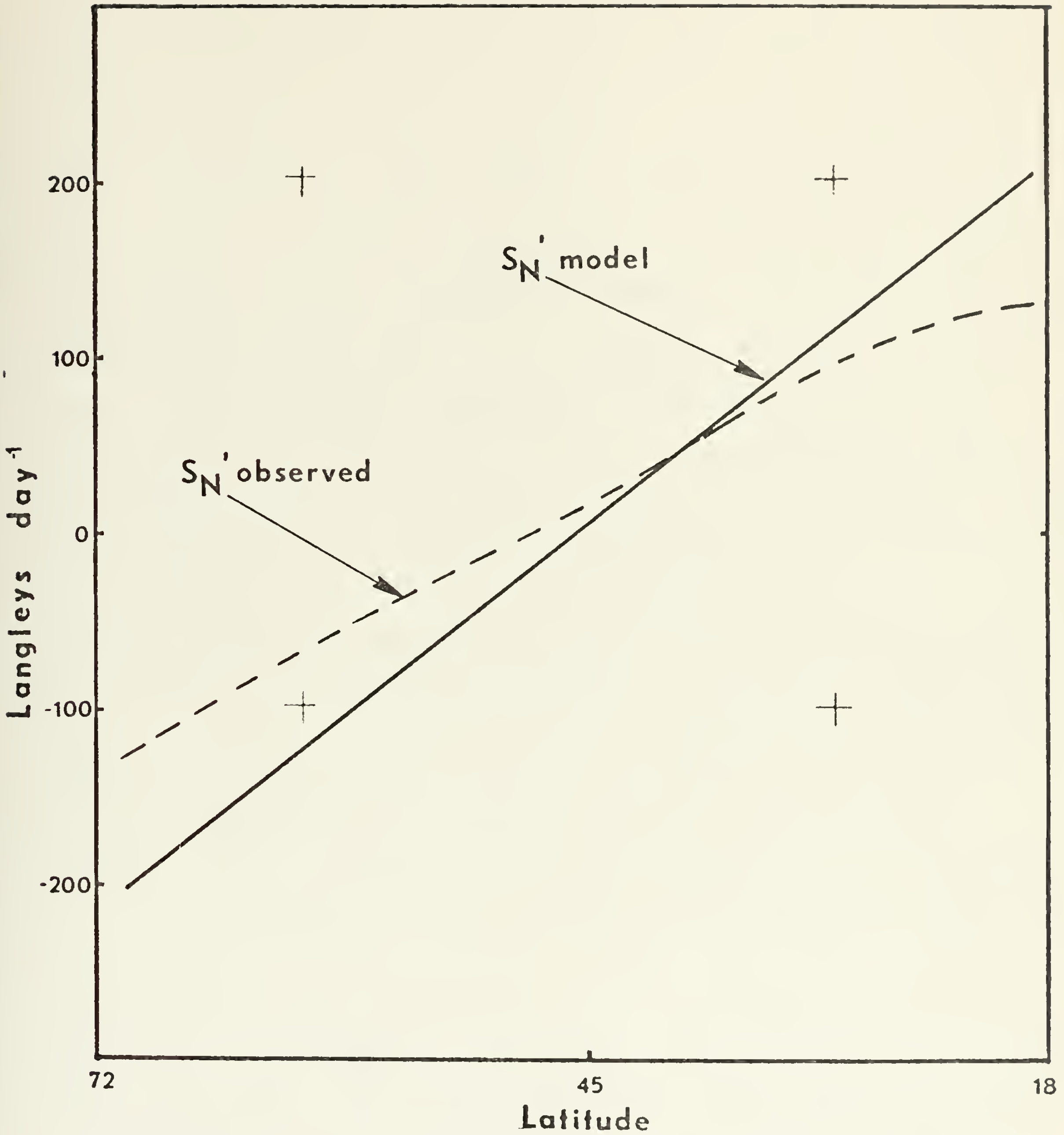

Figure 14. Deviation from mean net radiation, S_N', (dashed line) as observed by London (1957); model annual mean net radiation, S_N', (solid line).

2. Latent Heat Terms, $L \cdot E'$ and $L \cdot P'$

The parameterization of the latent heat processes could be accomplished in one of three ways. Since the atmospheric model contained no moisture, a direct exchange of this quantity and the associated releases of heat could not be considered. One possible formulation was based on the assumption that the air directly above the sea surface was saturated so no evaporation existed ($L \cdot E' = 0$). This formulation coupled with the assumption that no precipitation existed thereby eliminated the terms $L \cdot E'$ and $L \cdot P'$ from Equations (4.10) and (4.11). An experimental short term integration of the model equations was completed using this formulation. Results were unsatisfactory in that it became evident in this short test that an active air-sea model could not be developed with this scheme. The meridional gradient of the sea surface temperature became weak and the atmosphere consequently became baroclinically stable. After a short time this formulation was discarded.

A formulation of $L \cdot E'$ and $L \cdot P'$ that was similar to the observed profiles (Figure 15) was used in a second short term experiment. The result was similar to the case just described, only the meridional temperature gradient was weakened at a more rapid rate. The solar radiation absorbed at the ocean surface, S_N' was insufficient to maintain an adequate meridional sea surface temperature gradient and the addition of latent heating in the north and

cooling in the south further reduced the atmosphere's meridional temperature gradient. The results of this test were also unsatisfactory. One suggestion for the reason that the ocean did not maintain a strong temperature gradient even though the applied solar radiation was close to that observed in the real atmosphere is that the model cannot simulate the sharp separation of the western boundary current from the coast and the resultant tight gradient of temperature in the mid-latitude regions. This was probably due to the degree of linearity of the solution in this area (see Section VI A 1) and resulted in an oceanic and atmospheric meridional temperature gradient that was too weak for baroclinic instability. The system as a whole needs the latent heat released in the tropics of the real atmosphere.

The results of the above two experiments indicated that the ocean-atmosphere model required a somewhat different partitioning of the heating than is typically observed in the real ocean-atmosphere system. The heating formulation adopted for the model was equivalent to assuming that evaporation occurred in the ocean part of the model and that the moisture immediately precipitated out at the same latitude in the atmosphere ($L \cdot E' = L \cdot P'$). This formulation is somewhat unrealistic since, over the latitudinal domain of this model, the observed evaporation exceeds precipitation in lower latitudes while the reverse is true in the middle latitudes. Figure 15 shows curves of the latent

heat flux due to evaporation (solid line), and precipitation (dashed line), from Budyko (1962). The meridional average values have been removed from these values. The sinusoidal form of both L•E' and L•P' that was used to specify these fluxes in the model is shown by the dot-and-dashed line in Figure 15. While this formulation is quantitatively in agreement with the evaporation curve, it is a poor approximation to the precipitation related heat release. However, the greatest precipitation is in the equatorial region lying south of the wall at 18N. If the hemispheric precipitation were mapped into the domain of the model, the prescribed latent heat flux due to precipitation would be more in agreement with observed values. This is considered to be a weakness in the heating formulation and is an area that could be improved on in future work with this model. Nevertheless, it was believed that once the heating gradient in the atmosphere was sufficient to maintain it in a baroclinically unstable state, the resulting air-sea interactions would be realistic. That is, the interactions depend on the characteristic atmospheric motions, independent of the external forcing that maintain those motions.

Figure 16 shows the net prescribed atmospheric heat flux, R' + L•P' (dashed line) and the net prescribed ocean heat flux, S_N' - L•E (solid line). Prior to its final acceptance this form was tested in a short term experiment and found to satisfactorily contribute to the conditions desired for an active air-sea model. This fact coupled

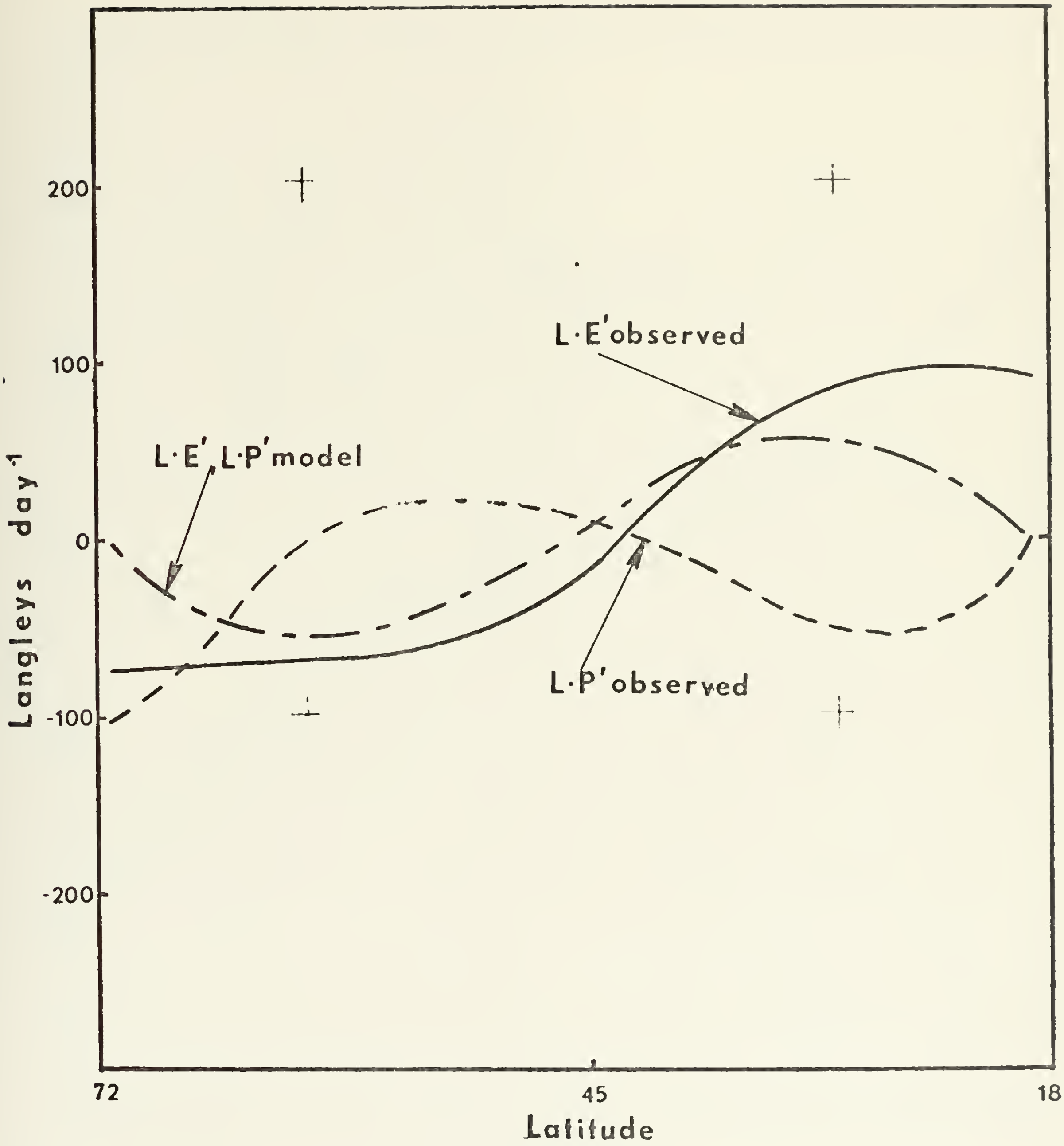

Figure 15. Latent heat flux due to evaporation (solid line); latent heat flux due to precipitation (dashed line) as observed by Budyko (1962). Model values of these quantities (dot-and-dashed line). All have the meridional averages removed.

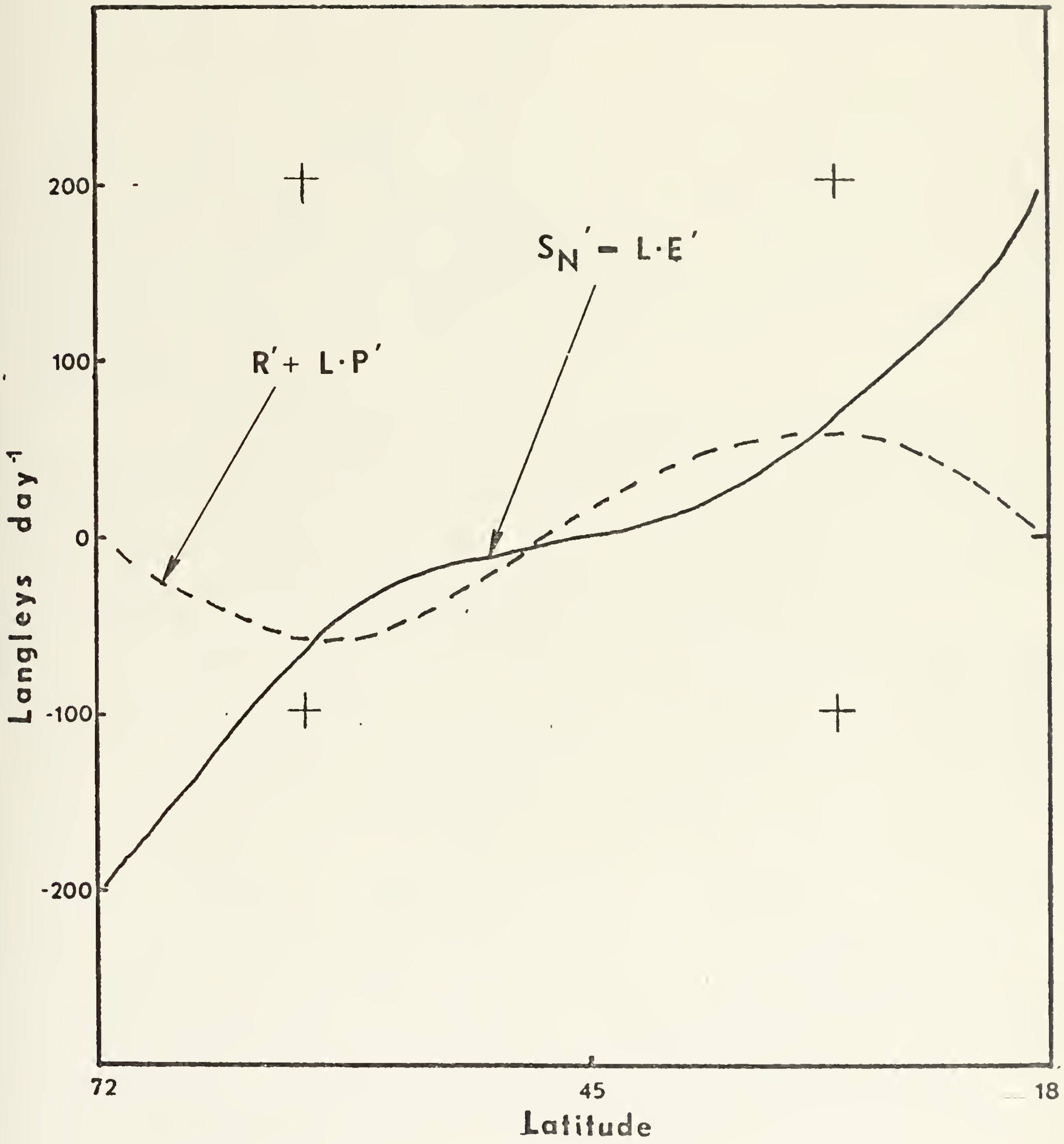

Figure 16. Net prescribed atmosphere (dashed line) and ocean (solid line) heat fluxes.

with the requirement for simplicity led to its use in the remainder of this work.

3. The Sensible Heat Transfer, H_1 $(T_{sea} - T_4)$

The quantity $H_1(T_{sea} - T_4)$ will be referred to as the sensible heat. In the derivation of H_1 by Haney (1971), it was shown that this quantity actually contained the net upward flux of longwave radiation and sensible and latent heat which occurs due to the air-sea temperature difference. Since the parameter H_1 varied little, a constant value was assumed. As in the ocean-only case a value of 55 langleys day^{-1} was chosen.

As shown above, all of the heat exchange between the atmosphere and the ocean must be accomplished through the sensible heat term. It is in this term that a strict accounting of heat exchange had to be done.

The sensible heat flux applied during an ocean time step was the average of the heat flux calculated during the 18 previous atmospheric time steps. The equation utilized was

$$\text{HEAT}_{ij} = \frac{1}{\text{NM}} [\sum_{n=1}^{\text{NM}} H_1 \ (T_{sea} - T_4)_{ijn}] \ , \qquad (4.12)$$

where NM = (Δt) ocean/(Δt) atmos = 18. Because of the x-wave formulation used in the atmospheric model the quantity $(T_{sea} - T_4)$ had to be calculated in several steps. By using Equations (2.17), (2.19) and (2.20) an equation for T_4 could be written:

$$(T_4)_{ij} = (T_4F)_j + (T_4C)_j \cos kx_i + (T_4D)_j \sin kx_i \quad , \qquad (4.13)$$

where

$$(T_4F)_j \equiv \frac{2f_o}{R} F_j + 250.3 - \frac{\partial T_S}{\partial z} (\Delta z) ,$$

$$(T_4C)_j \equiv \frac{2f_o}{R} C_j$$

and

$$(T_4D)_j \equiv \frac{2f_o}{R} D_j . \tag{4.14}$$

To be consistent with the wave number representation in the atmosphere and to facilitate coupling the models through a single wave number, a Fourier analysis was performed on the sea surface temperature. At each latitude, the sea surface temperature was analyzed in x-space to yield a mean zonal sea surface temperature and the Fourier coefficients of its first mode. This can be symbolized as

$$(T_{sea})_{ij} = (\overline{T}_{sea})_j + (T_{sea}C)_j \cos kx_i + (T_{sea}D)_j \sin kx_i . \tag{4.15}$$

The various modes of the sensible heat flux in the atmosphere were calculated from

$$\begin{aligned} H_1(T_{sea} - T_4) = H_1[(\overline{T}_{sea} - T_4F)_j \\ + (T_{sea}C - T_4C)_j \cos kx_i \\ + (T_{sea}D - T_4D)_j \sin kx_i] \end{aligned} \tag{4.16}$$

and were applied in Equations (2.24), (2.25) and (2.27) during each time step. The right hand side of Equation (4.16) was averaged over the 18 atmospheric time steps for incorporation in Equation (4.12). This in turn was applied in the oceanic heating formulation.

The model equations were integrated for a short time period (300 days) and zonally averaged values of the

sensible heat were calculated. The results are shown in Figure 17 by the solid line. The dashed line shows the observed zonal mean sensible heat flux as presented by Budyko (1962). These were added to the imposed values of L·P' to obtain the zonally averaged net atmospheric heating. Values of the observed sensible heat flux estimated by Budyko were added to the observed values of the radiative and latent heat contributions, and after their meridional averages were removed, these new quantities were plotted in Figure 18. The solid line shows the observed atmospheric heating over the ocean and the dashed line shows observed atmospheric heating over ocean and land combined. The dot-and-dashed line depicts corresponding values of $L \cdot P' + H_1(T_{sea} - T_4)$ generated in the model. In the northernmost segment of the domain, the model closely resembles the observed values over the ocean. From a region near 45N to the southern boundary, the model is in closer agreement with the data from a land and ocean environment.

There are several possible explanations of the "dip" in the model atmosphere heat flux near 50N. The formulation of the net solar radiation as shown in Figure 13 favors a sea surface temperature structure that would be colder than the atmosphere in the higher latitudes and warmer than the atmosphere in lower latitudes. This would lead to negative contributions from the sensible heat term in higher latitudes. The curve dips sharply in the area

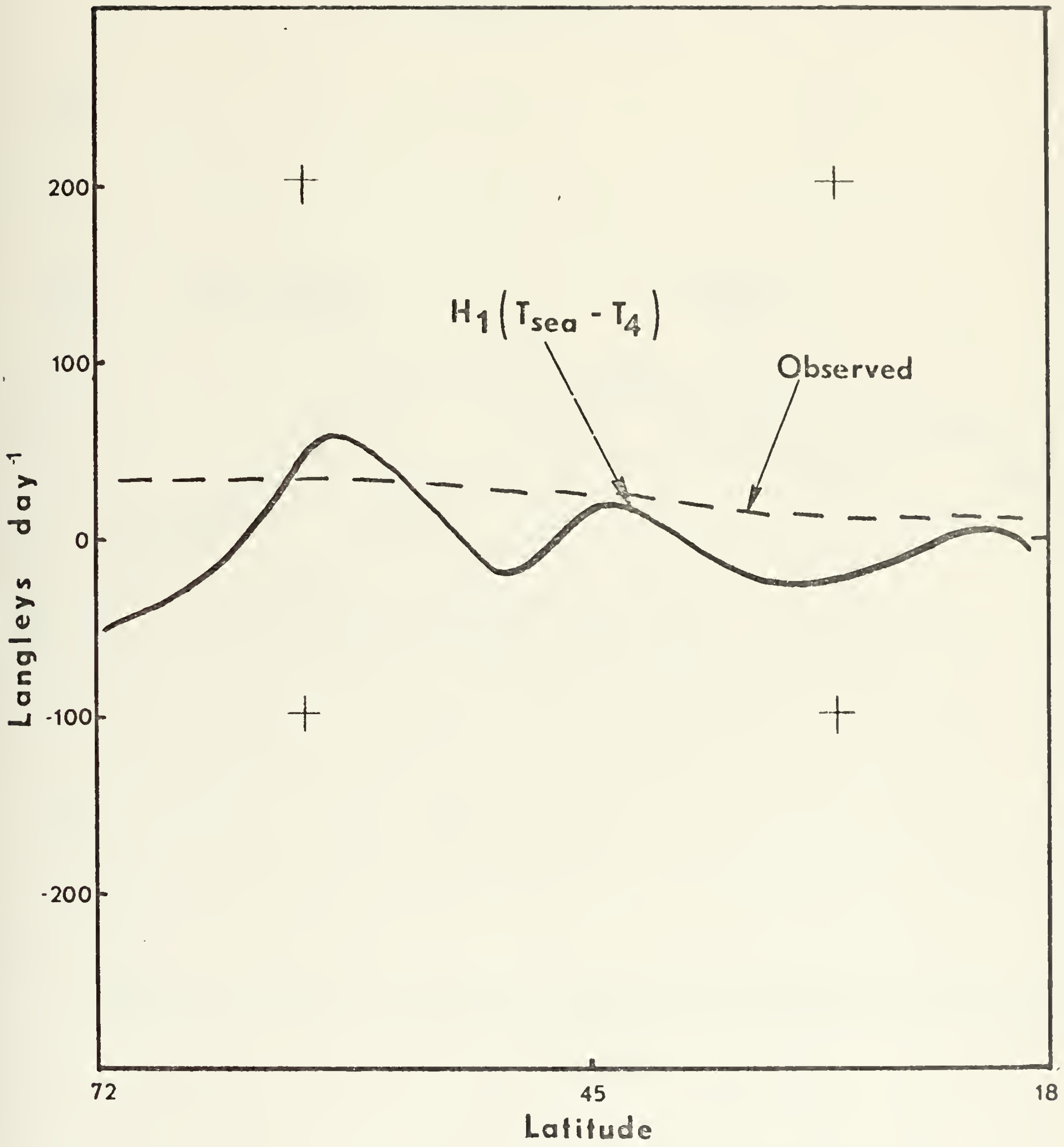

Figure 17. Heat flux due to sensible heat exchange. Positive is flux from the ocean; Model (solid line); Observed by Budyko (dashed line).

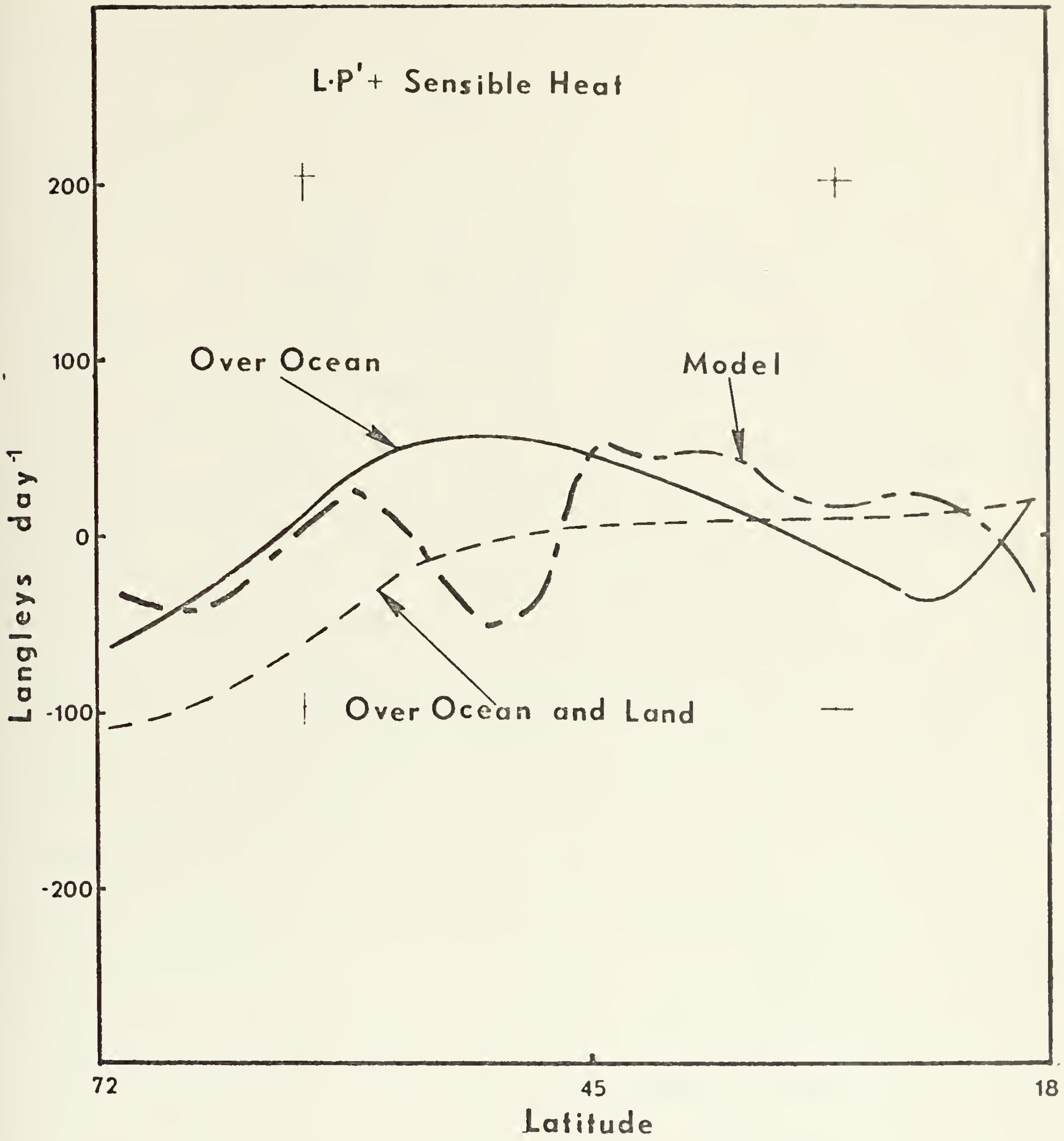

Figure 18. Observed zonally averaged atmospheric heat flux over ocean (solid line); observed zonally averaged atmospheric heat flux over land and ocean, combined (dashed line); model zonally averaged atmospheric heat flux (dot-and-dashed line); (observed data from Budyko, 1962).

where the solar radiation and sensible heat passes from positive to negative values.

The formulation of the latent heat released by precipitation in the atmospheric model contributes to heating in the south and cooling in the north. The sharp dip in the total atmospheric heating occurs at the latitude where the prescribed atmospheric heating becomes negative.

The sensible heat term may contribute to this abrupt decrease in another way. Large positive values of this quantity are seen in some regions and large negative values in others. The large negative values are physically unreal because the real atmosphere does not give large amounts of heat to the ocean through this term over large areas. These values are considered departures from a mean and can be interpreted as small heating where the values are negative and larger heating where they are positive. The prescribed heating of the combined model has already been shown to meridionally integrate to zero. There can be no net heat flux by the sensible heat term if a steady state condition is to be reached. If a different formulation for the prescribed quantities was chosen so that the net specified heat flux into the system was not zero, then the net heat flux by $H_1 (T_{sea} - T_4)$ would have to be adjusted. In the present formulation, however, there is no need to change the mean temperature of the atmosphere and the interpretation just discussed is justified.

Figure 19 shows the result of subtracting the sensible heat term from prescribed radiation and latent heat contributions in the ocean model. The curve has the general appearance of the S_N' curve in Figure 14. But a "hump" appears in the same area as the "dip" in the atmosphere curve and should be expected for the same reasons.

The oceanic heating formulation that was arrived at empirically and through experimentation was utilized in the remainder of the numerical study.

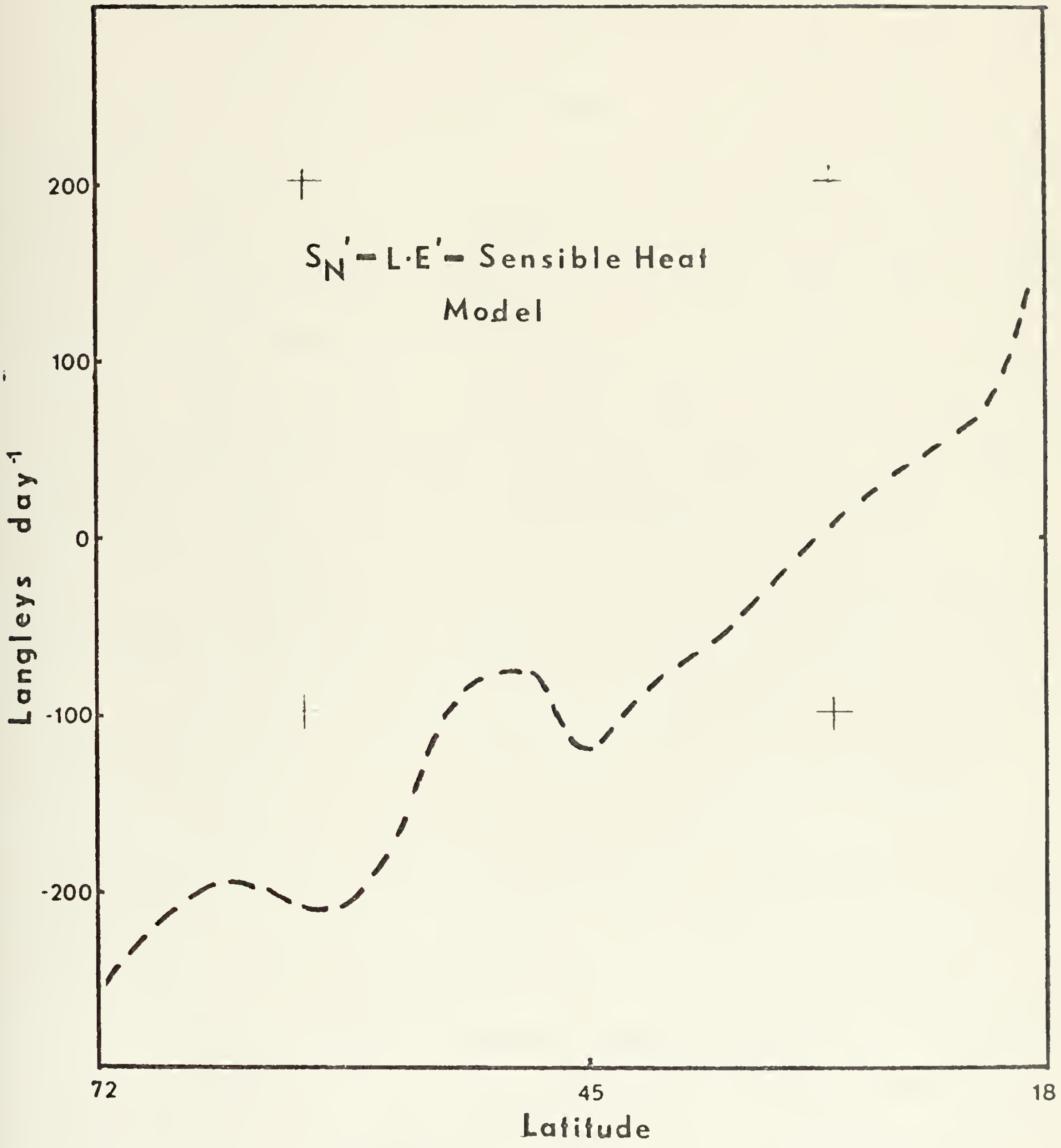

Figure 19. Average of heating in the ocean model.

V. PROCEDURES

A. PHASE I

1. Variations of the Combined Model

It became evident during the short term experiments discussed in the last section that the computing time required to achieve a state of quasi-equilibrium was excessive. Bryan (1969) has shown through scale analysis that the vertical advective time scale is on the order of decades while the vertical diffusive time scale is on the order of centuries. Both of these time scales must be relevant in the integration of the coupled ocean and atmosphere over long periods of time. The relatively shallow ocean depth and stratified temperature structure specified as the initial conditions enhanced the approach to an equilibrium state.

The combined model with a 200 km grid distance and time increments as previously described required approximately one hour of computing time for every 100 days of simulation on the IBM 360/67 computer. This would require 365 hours of operating time for 100 years of simulation in this phase of the experiment, and this was prohibitive.

Several ways to reduce computing time requirements were considered. These considerations involved the ocean model since the atmospheric model was formulated simply and could be integrated rapidly. In a combined model such as this, almost any change in either time increment or grid

distance in one part of the model would require an adjustment of that quantity in the other portion of the model.

A time reduction could be realized by linearizing the horizontal equations of motion, as was done by Haney in the first phase of his ocean experiments. This change was incorporated into the model, along with the assumption that the vertical mean motion was steady so there was no requirement to relax for ψ_t, the time rate of change of the stream function. It was this feature that produced the time reduction. This simplified form of the combined model was tested in a several hundred day simulation and the model advanced 140 days after one hour of computing time. While this was a fair improvement in computing requirements it was not enough to warrant changing the model in this way.

Changing the distance between grid points was considered. The model previously described had a 200 km grid distance in both x and y requiring horizontal fields of 775 points (25 by 31). If the grid distance was changed to 400 km in the y direction and remained 200 km in the x direction, the computing time would be reduced. The reduction was due to the fewer number of calculations to be made (now 400 grid points) and the doubling of the time increment in the atmospheric portion of the model. For prediction purposes the atmosphere had grid points only in the y direction and if this increment was doubled, the time step could also be doubled and the solution still remain stable in a linear sense. The time step in the ocean, however,

must remain the same since the grid distance in x was not changed. This version of the model was tested and produced a 320 day forecast in one hour. This was a substantial time savings but it was believed that an even more accelerated pace could be obtained.

The final modification to the original combined model was made by changing the grid distance in both the x and y directions to 400 km. When the time steps were doubled to one hour in the atmosphere and 18 hours in the ocean, computing time was reduced by a factor of about seven. A test showed that this version of the model produced a 666 day simulation in one hour of computing time. This was a satisfactory improvement and this form of the model was utilized in the early stages of the experiment.

2. The Coarse Grid (400 km) Model

Munk (1950) has shown that the development of a western (frictional) boundary current of several hundred kilometers is to be expected. It was assumed that the western boundary current was the width of the new grid distance, 400 km. It has been shown by Munk that the width of the boundary current (L_W) is proportional to the cube root of the ratio of the lateral momentum diffusion coefficient to the gradient of Coriolis parameter. This can be expressed as

$$L_W \propto \left(\frac{A_M}{\beta}\right)^{1/3} \quad . \qquad (5.1)$$

The ratio of the western boundary width to the grid size, $L_w/\Delta x$, is proportional to $[A_M/\beta(\Delta x)^3]^{1/3}$. In order to keep this ratio the same in both the 400 km and 200 km grid models, and thereby have similar horizontal resolution in both models, the following must hold,

$$A_{M(400)} = 8\ A_{M(200)} \quad . \tag{5.2}$$

Since a value of 1×10^8 cm^2 sec^{-1} was used for A_M with the 200 km grid, $A_M = 8 \times 10^8$ was used as an initial value in this model. Similarly A_H was increased so that a value of $A_H = 1 \times 10^8$ cm^2 sec^{-1} was used in the coarse grid model.

The initial conditions discussed previously were modified to conform to the new 13 by 16 point grid and the long term integration was started. Because of the large horizontal eddy diffusion of heat, the meridional sea surface temperature gradient dropped from its initial value of 22 degrees over the 6000 km length to 18 degrees in the first 400 days. To have an active air-sea interaction model the meridional temperature gradient in the ocean must be large enough to force strong meridional temperature gradients in the atmosphere so that a thermal wind larger than that required for baroclinic instability can exist. Such a large temperature gradient could be maintained in the ocean only by reducing the diffusion coefficient. However, that coefficient cannot be arbitrarily reduced because in the reduction, the western boundary width as given by (5.1) may become smaller than the grid size.

A stepwise reduction in the lateral diffusion coefficient was made. The solution was examined for computational stability after each step. At the end of the first 400 days, the lateral diffusion coefficients were halved, the decrease in meridional temperature gradient ceased and the solution remained stable. At the end of 1200 days the coefficients were again reduced and at the end of 7200 days they were reduced a final time to values of $A_M = 1 \times 10^8$ and $A_H = .25 \times 10^8$ with no effect on the computational stability. It was evident, however, that with the 400 km grid, the western boundary current was only marginally resolved.

The model equations were integrated over the coarse grid for a period of 20,200 days (~55 years). The volume average of temperature in the ocean basin was one parameter used to measure the approach to equilibrium. This water temperature had slowly cooled from an initial value of 6.3076 degrees to 5.2017 degrees at day 20,200. In the early stage of adjustment the cooling was at a very rapid rate, 5.2 degrees per century, but by the end of this part of the experiment, the net cooling rate had reached zero.

Another parameter monitored was the meridional gradient of sea surface temperature. This quantity had stabilized at 21.6 degrees per 6000 km after day 15,000 and remained so until the end of this time period. During this time the atmosphere remained very active. A thermal

wind, $(\overline{U}_1 - \overline{U}_3/2)$, with maximum values greater than 11 m $\sec^{-1}$, which is well above the critical value for baroclinic instability, was present in the mid-portion of the domain. A strong upper level jet and weaker lower level jet were present at the same latitude. The state of the atmosphere and ocean was very encouraging and the data for day 20,200 was used to initialize the fine grid (200 km) model to continue the experiment. More discussion of the state of the atmosphere-ocean system at that time is included in the section on discussion of results.

3. Data Retention

Prior to continuing with the description of the procedure used with the fine grid model, a brief discussion of data retention must be included. In a project requiring large amounts of computing time, it is mandatory that a great deal of consideration be given to which data should be saved. One must decide not only what parameters to retain, but how often and in what form. It is virtually impossible to repeat an experiment to extract parameters that were not saved.

The data obviously must be stored for analysis at the end of the experiment. Data must also be retained for use in restarting the model. It should not be expected that a long-term integration of this nature could be completed in one computing time period. The equations must be integrated and data stored periodically so that after a reasonable operating time, such as one hour, the model can

be stopped and restarted at a later time using the last data in storage as initial values.

Throughout the experiment with the coarse grid model, data were stored at 100 day intervals. The ocean variables saved were the stream function from which the vertical mean current was obtained, the zonal vertical shear current, u', the meridional vertical shear current, v', and the temperature, T, at all three levels. The atmospheric variables saved were the Fourier coefficients, A through F. The retention of such a large quantity of data posed a problem, but it was remedied through the judicious use of magnetic tapes. As one section of the experiment was completed, the data that would not be needed until the final analysis was moved from disk pack temporary storage to a set of magnetic tapes where it was permanently stored. The necessity for this became even more evident in the fine grid model integrations when the fields were increased from 208 data points per level to 775 points per level. Saving this much data would have been impossible without a large storage capability.

The last problem concerning data storage arose during the final part of the long term integration. After a state of quasi-equilibrium was approached, five points were chosen for retention of daily data for the last six years of the experiment and were carefully examined by spectral techniques. Data from an ocean-only and an atmosphere-only experiment were also saved over the last six years.

4. Fine Grid (200 km) Model

The data for day 20,200 from the coarse grid model was linearly interpolated in both x and y to obtain initial fields for the fine grid model. The lateral diffusion coefficients for both momentum and heat were held at the final values as used in the coarse grid model. While these coefficients might have been reduced over a time period as they were in the coarse grid, this was not done in order to avoid the readjustment that would be required. A further change in the diffusion coefficient would increase the adjustment period. It has been shown by Manabe (1969a), Gates (1968) and others that the values chosen previously are appropriate for the grid size used.

The equations were integrated over the fine grid model for another 6500 days with data retained every 100 days. At that time, 73 years, the ocean-atmosphere model was approaching an equilibrium state. The volume average of the temperature initially started to slowly decrease but after a few hundred days it commenced an increasing trend that it maintained throughout the remainder of the experiment. The warming trend began at the rate of 0.8 degrees per century but this decreased to about 0.5 degrees per century at 73 years. Compared to the warming rate of 2 degrees per century arrived at by the ocean in Manabe and Bryan's combined model, this was considered an acceptable time to start the last six years of the combined model experiment.

Beginning at the 73rd year, a final 2200 day (6 years) simulation was produced with the fine grid model. It was during this time that not only were all the data recorded every 100 days but for five selected points, the data were recorded every 1.125 days (every three oceanic time steps). These points were selected as being representative of features that existed in various parts of the ocean. Figure 20 shows the location of the five points,

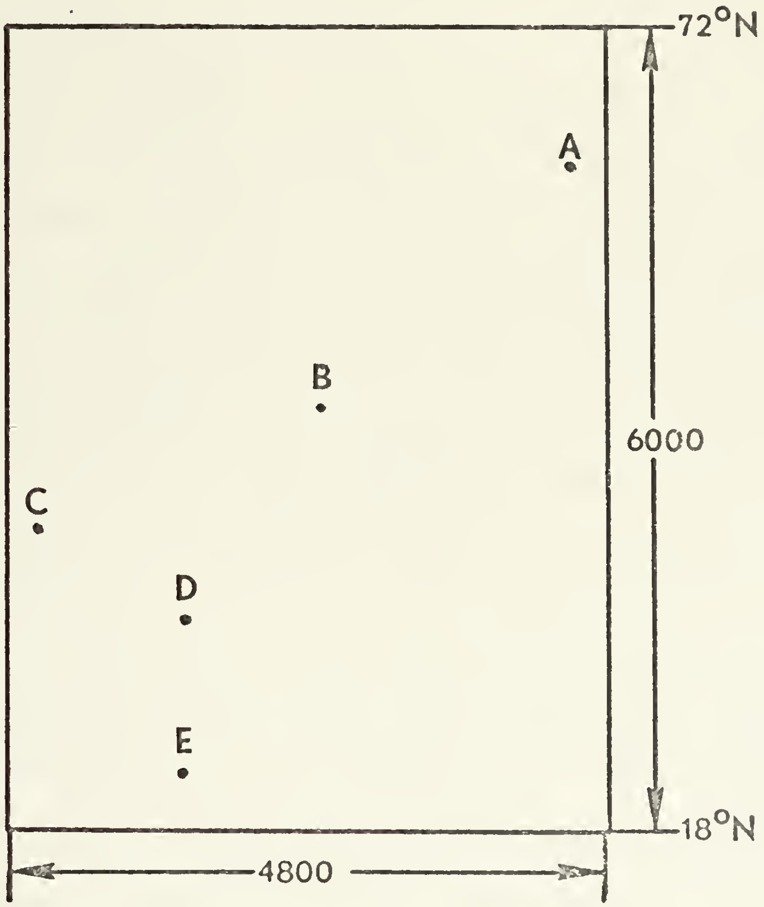

Figure 20. Location of points where selected data were recorded every 1.125 days.

lettered A through E. Point A is the northernmost point in the eastern sector where sea surface temperatures were warmer than the initial values and where strong sinking motion had occurred. Point B is in the center of the domain where the cyclonic scale atmospheric disturbances had their greatest effect. Point C is in the western boundary current and, if the model domain is likened to the North Atlantic Ocean, this point is close enough to an observation site used by Woods Hole Oceanographic Institution so that some comparisons can be made. Point D is an area in the south central portion of the domain and would be equivalent to an area near Bermuda. Point E is in the warm core of the ocean close to the southwestern corner of the domain. The data at these points were examined spectrally and the discussion of this technique is included in a later section.

At the conclusion of this part of the experiment, the combined model had been used for a 79 year integration of the equations. This completed phase I of this project.

B. PHASE II

This phase of the experiment consisted of integrating the equations of the ocean-only model for a six-year period using the fine grid. To simulate the coincidence of this time period with the final six years of the combined model, data from the combined model were used for initialization. Initial fields of temperature and velocities were taken from day 26,700.

A fixed surface stress and an atmospheric temperature had to be imposed. Rather than use climatology, the input stress and temperature were obtained from the combined model. In preparation for this phase of the experiment, the surface stress, and atmospheric surface air temperature were averaged over a 100 day period centered at day 26,700. These average values were then held fixed during the entire time integration of the ocean-only model.

Data were retained in exactly the same manner as in the combined model. Full fields of the ocean variables were stored every 100 days and data for the five special points were stored every 1.125 days. The variables were examined and comparisons were made with the results of Phase I. These results are discussed in a later part of this work.

C. PHASE III

The equations for the atmosphere-only model were integrated over the same six year time span with the fine grid. Initial values of A through F were taken from day 26,700 of the combined model data and the 100 day average sea surface temperatures were imposed as a lower boundary condition. Data were saved at the same times as in the first two phases.

Calculations of energy and energy transformations were made and are described later. The data from the five points were analyzed spectrally and this too is presented in a later section. With the completion of this phase of the experiment, the long-term integrations were concluded.

D. REVIEW OF COMPUTING TIME REQUIREMENTS

Since the integrations were conducted with a variety of numerical models, it is germain at this point to review the computing time requirements for each model. This review is presented in tabular form in Table 2.

MODEL	DESCRIPTION	LENGTH OF SIMULATION FOR 1 HR COMPUTING TIME
Combined (Fine Grid)	$\Delta x = \Delta y = 200$km $\Delta t_{atm} = 30$ min $\Delta t_{ocn} = 9$ hours	101 days
Combined (Coarse Grid)	$\Delta x = \Delta y = 400$km $\Delta t_{atm} = 1$ hour $\Delta t_{ocn} = 18$ hours	666 days
Ocean Only (Fine Grid)	$\Delta x = \Delta y = 200$km $\Delta t = 9$ hours	308 days
Atmosphere Only (Fine Grid)	$\Delta y = 200$km $\Delta t = 30$ min	697 days
Combined (Linear) (Not used)	$\Delta x = \Delta y = 200$km $\Delta t_{atm} = 30$ min $\Delta t_{ocn} = 9$ hours linear momentum equations	140 days
Combined (Mixed Grid) (Not used)	$\Delta x = 200$km $\Delta y = 400$km $\Delta t_{atm} = 1$ hour $\Delta t_{ocn} = 9$ hours	320 days

TABLE 2. Review of computing time requirements for variations of the numerical models used in this experiment.

It can be readily deduced from these time figures that the coupling processes required lengthy calculations. The method by which the sea surface temperatures are transferred into wave number space required many time consuming operations for every oceanic time step. The other summations and averaging procedures all contributed to a joining process that caused the combined model to run significantly slower than either of its individual components.

VI. DISCUSSION

The data that was collected during the long term integration can be placed in two categories. The full fields of data and the data collected at the five designated points differ widely in frequency of observations and area of coverage. Because of this, the methods by which the data were to be examined differ considerably. The full fields of data that were retained at 100 day intervals were examined in a synoptic-type study, while the five-point data, recorded at daily intervals, were examined using spectral techniques.

In the synoptic study the analyzed data were compared not only to observed climatological data, but also to the results obtained from the various phases of this numerical experiment. The atmospheric energy balance was examined and comparisons were made between phase I and phase III and with the work discussed in Chapter II. In the spectral study,power spectrum estimates that were obtained from data at one particular point were compared with estimates obtained from data at other points during the same phase of the experiment. Similarly, spectral estimates of one variable were compared with estimates of the same variable at the same point in a different phase of the work. Some comparisons were made with spectral estimates calculated from observed data collected by the Woods Hole Oceanographic Institution.

A. SYNOPTIC STUDIES

Throughout the experiment full fields of the stream function, vertical shear current components, and temperatures were retained as oceanic data and the Fourier coefficients were saved as the atmospheric data. These variables, along with fields of oceanic vertical motion and atmospheric zonal velocity, vertical motion, mean meridional velocity and disturbance amplitude and phase information were printed every 50 or 100 days. Many of these variables were examined in detail and discussion of the results is contained in the subsequent sections.

1. The 400 km Grid Combined Model Experiment

The 400 km grid combined model was merely a tool that was used to expeditiously integrate the model equations to reach a state of quasi-equilibrium. The ocean-atmosphere interaction at the end of this part of phase I was not of primary interest. The state of the system at the end of day 20,200 (55 years) was to be used only to initialize the fine grid model from which more realistic and more meaningful results may be obtained. However, a brief discussion of the conditions to which this form of the combined model evolved is necessary to explain why the 200 km grid was needed to complete this phase.

The initial conditions for this part of the experiment have previously been described. The initial adjustment of sea surface temperatures was due to the large horizontal

eddy diffusion coefficient then in use. The reduction of this coefficient and the necessity for maintenance of a large meridional sea-surface temperature gradient was already discussed. The coefficient of lateral diffusion could not be made small enough with the 400 km grid so that nonlinear terms would be important. Bryan and Cox (1967) have defined an "effective" Reynolds number, Re, as the Reynolds number associated with the lateral turbulent mixing. The nonlinearity of the solution is dependent on the size of the Reynolds number defined as follows:

$$Re \equiv \frac{U^*L}{A_M} , \qquad (6.1)$$

where U^* is the velocity component depending on the density gradient,

L is a scale length, and

A_M is the coefficient of lateral momentum diffusion.

Bryan and Cox conducted a series of experiments with values of Re = 0.8, which gave a highly diffusive, linear solution and Re = 8.0, which yielded a moderately diffuse, slightly nonlinear solution. The maximum value of Re used in this experiment was 6.5 and it is believed that a value greater than 10 was necessary to achieve a truly nonlinear solution. It is easily shown that with the 400 km grid, continued reduction of A_M produces a situation where the linear western boundary current becomes unresolvable [see Equation (4.1)] prior to the occurrence of nonlinear effects. Therefore, the solution with the 400 km

grid is similar to the viscous linear solution described by Munk (1950). Figure 21 shows the ocean stream function obtained at day 20,200 (about 55 years). According to Munk, the streamlines should represent an exponentially decaying series of vorticies centered on the latitudinal axis. The vorticies are present across the width of the domain but do not appear to decay as expected. Truncation error is a probable cause for insufficient decay in this area. In the gyre north of 45N, the maximum value of the vertically averaged meridional current was on the order of 10 cm sec^{-1}. In the southern gyre the maximum value of the same quantity was about 15 cm sec^{-1}. The magnitude of the total (vertical shear plus vertical mean parts) meridional currents in the northern and southern gyres were 10 and 35 cm sec^{-1} respectively. The higher latitudes in the model were more barotropic and the vertical mean current dominated, while the vertical shear current dominated in the highly baroclinic areas of the central portion. In the north the vertical shear current was about zero, while in the south the vertical shear current was about 20 cm sec^{-1} directed northward.

Figure 22 shows the sea surface temperature field at day 20,200. The mean meridional temperature gradient over the latitudinal domain was 21.4 degrees per 6000 km. The temperatures at both the north and south boundaries had decreased from their initial values. Upwelling along the central portion of the northern boundary was responsible

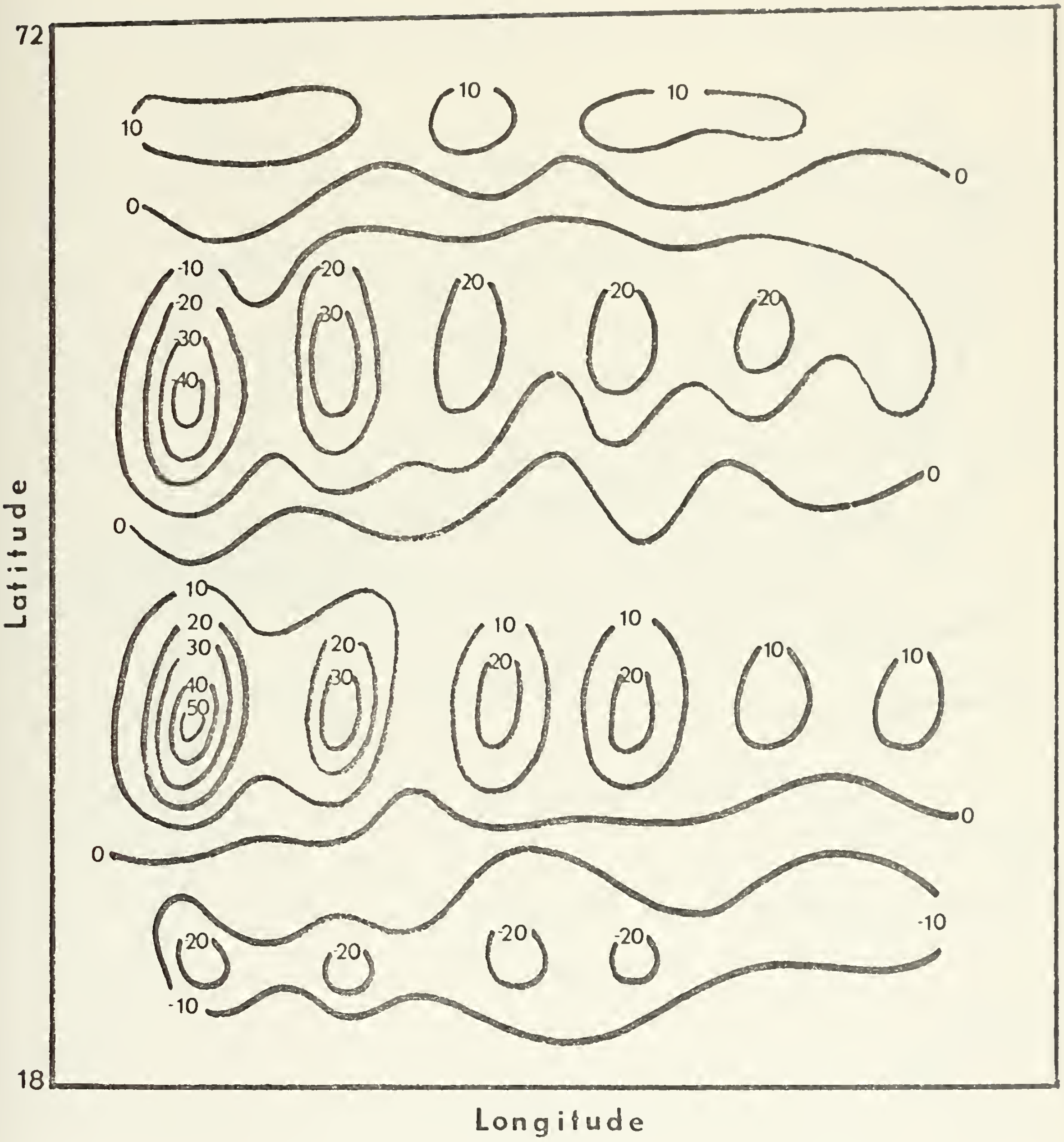

Figure 21. Ocean stream function obtained at day 20,200 from 400 km grid combined model.

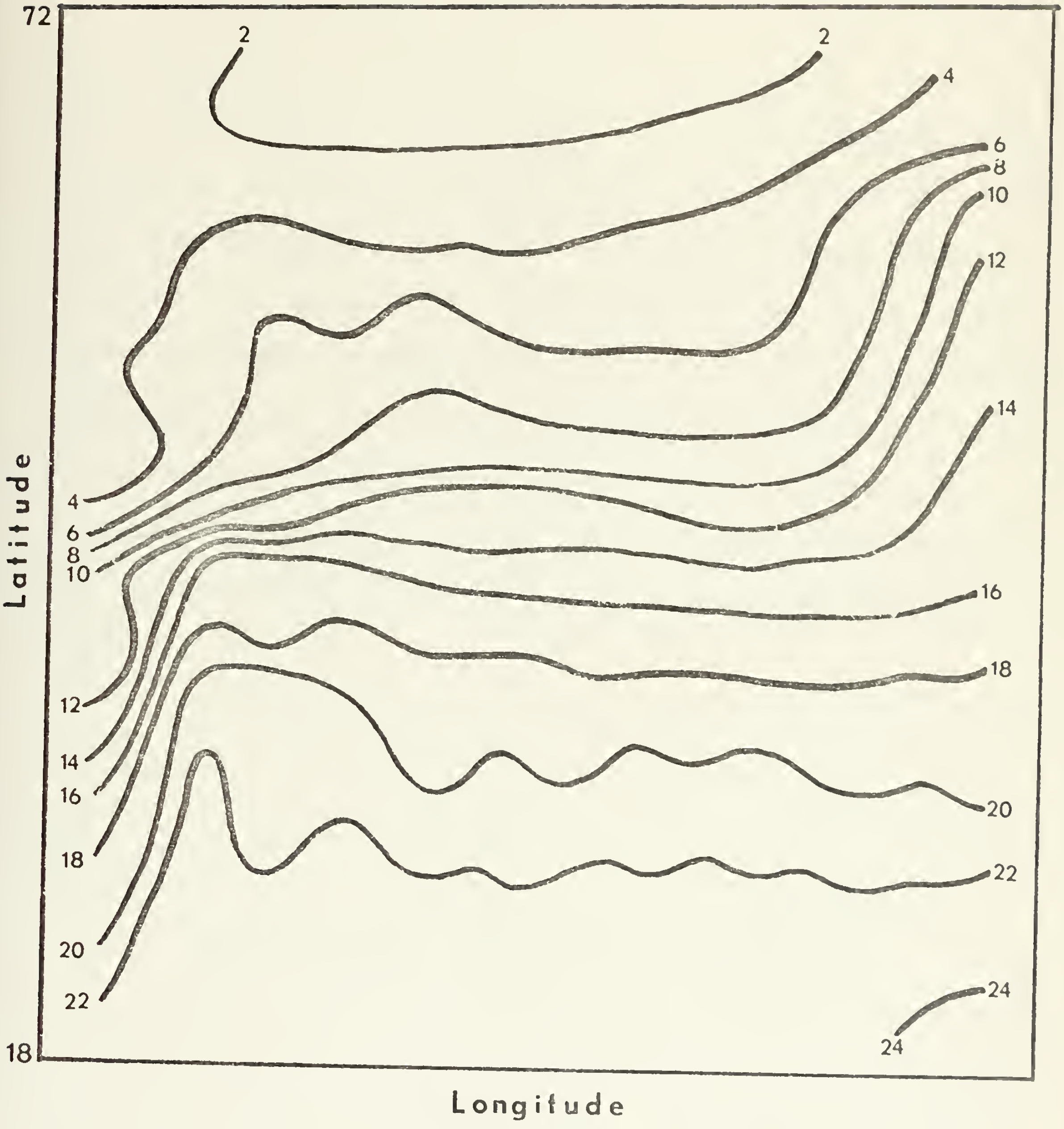

Figure 22. Sea surface temperature at day 20,200, (C).

for this cooling at the surface. The small scale spatial fluctuation in the temperature field in low latitudes appears to be a result of the linear viscous solution in which there is alternating northerly and southerly flow and therefore northerly and southerly advection of heat.

Figure 23 shows the zonal winds at three levels in the atmosphere. The curve labeled (a) depicts the zonal mean surface wind. The easterly, westerly, easterly pattern from north to south is qualitatively like the patterns in the real atmosphere. However, the latitudes at which the direction of flow change occur are slightly north of the actual latitude of change. Curve (b) is the zonal wind at 750mb and curve (c) is that quantity at the 250 mb level. The increase of westerlies with height in the central latitudes is in thermal wind balance with a temperature structure of warm air in the south and cold air in the north.

While the structure of the atmosphere-ocean system that evolved from integrating the model equations over the 400 km grid was not extremely accurate, it did suffice for initializing the integration of the fine grid model.

2. The 200 km Grid Combined Model Experiment

The fine grid or 200 km grid part of phase I was initialized with data from day 20,200 of the 400 km grid model after spatial interpolation. The model equations were then integrated in time for 8700 days (approximately 24 years). The adjustment to the fine grid was evident in

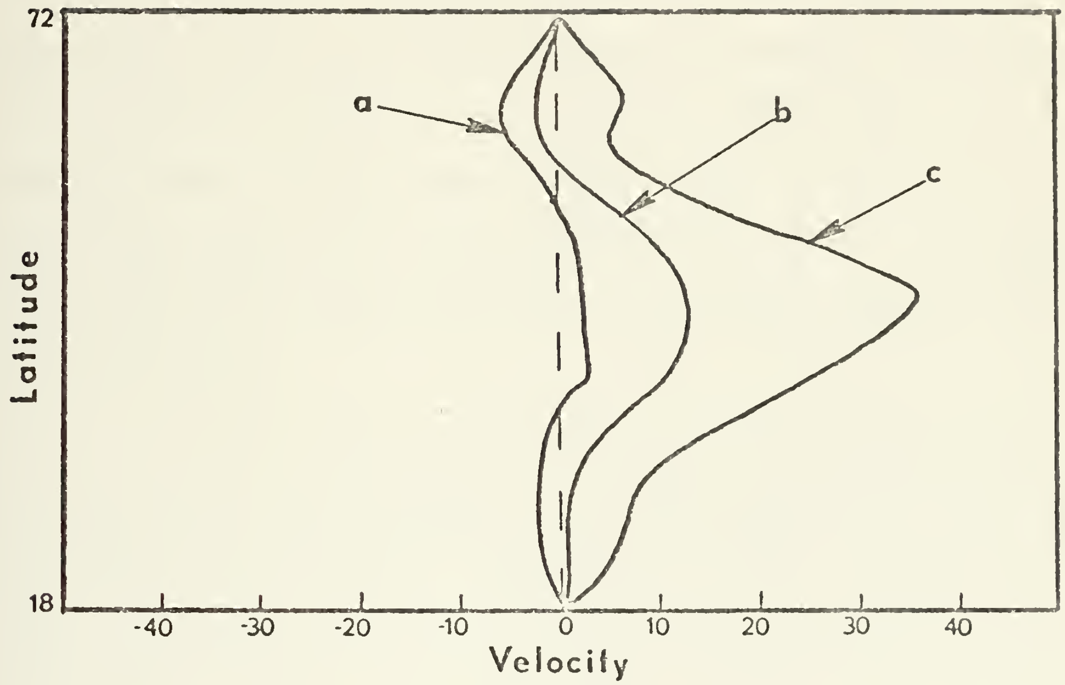

Figure 23. Zonal atmospheric winds in m sec^{-1} from 400 km grid model at a) surface; b) 750 mb; c) 250 mb.

a slight initial decrease of the oceans volume averaged temperature. After a few hundred days, this temperature started increasing and at day 21,000 the sea was warming at a rate of 0.8 degrees per century. This warming rate was maintained for over 1000 days and then the rate decreased gradually to 0.5 degrees per century at day 28,900, the last day of the experiment. This warming rate was caused by a downward heat flux across the air-ocean interface of about 2.3 cal $cm^{-2} day^{-1}$. While the experiment could have been continued until no heat flux was observed, it was believed that the large amount of computing time required to accomplish this would not have been worth the slight change in the final results.

At the end of the 400 km grid model experiment, the total disturbance energy in the atmosphere was statistically steady, oscillating about 50 $m^2\ sec^{-2}$. During the first few hundred days of the fine grid integrations the average disturbance energy jumped to about 70 $m^2\ sec^{-2}$, but then quickly returned to the statistically steady state which had previously been observed. The initial cooling of the ocean imparted an added amount of heat to the atmosphere in the southern half of the region generating more zonal potential energy which the baroclinic processes converted into disturbance energy. After the cooling ended, the warming of the ocean apparently occurred rather uniformly in space resulting in the generation of about the same amount of available potential energy as had been generated

prior to reducing the grid size. More discussion of the energy balance in the fine grid model is in a later section.

The mean state of the atmosphere over the last 100 days of this phase of the experiment is shown in Figures 24 to 26. These maps along with Figures 28 to 30 that will be discussed shortly are deviation values of the height fields at various levels obtained from the geostrophic condition. The zero contour and plus and minus deviation contours are drawn. These maps are displayed in this way because the deviation of the stream function is predicted by the quasi-geostrophic atmospheric equations. The quantity ψ appears as $\nabla\psi$ in all terms, and can be represented as $\nabla(\psi'(x,y,t) + \overline{\psi}(t))$, a deviation and mean part of the stream function. Therefore, any mean ψ could be added to (or subtracted from) the deviation quantity.

Figure 24 shows the extrapolated distribution of the 1000 mb height deviation analyzed at 12-meter intervals. There is a semi-permanent mid-latitude cyclone over the eastern ocean and a high at the same longitude south of the low. A high is present in the northernmost section of the region. This is worthy of note since there is no cold land mass modeled into the system to simulate a "Greenland" type effect. Figure 25 shows the distribution of the 250 mb height deviation analyzed at 60-meter intervals. The flow is zonal throughout the central portion of the domain with a cyclonic polar vortex present in the north and a weak ridge present at the same longitude in the south.

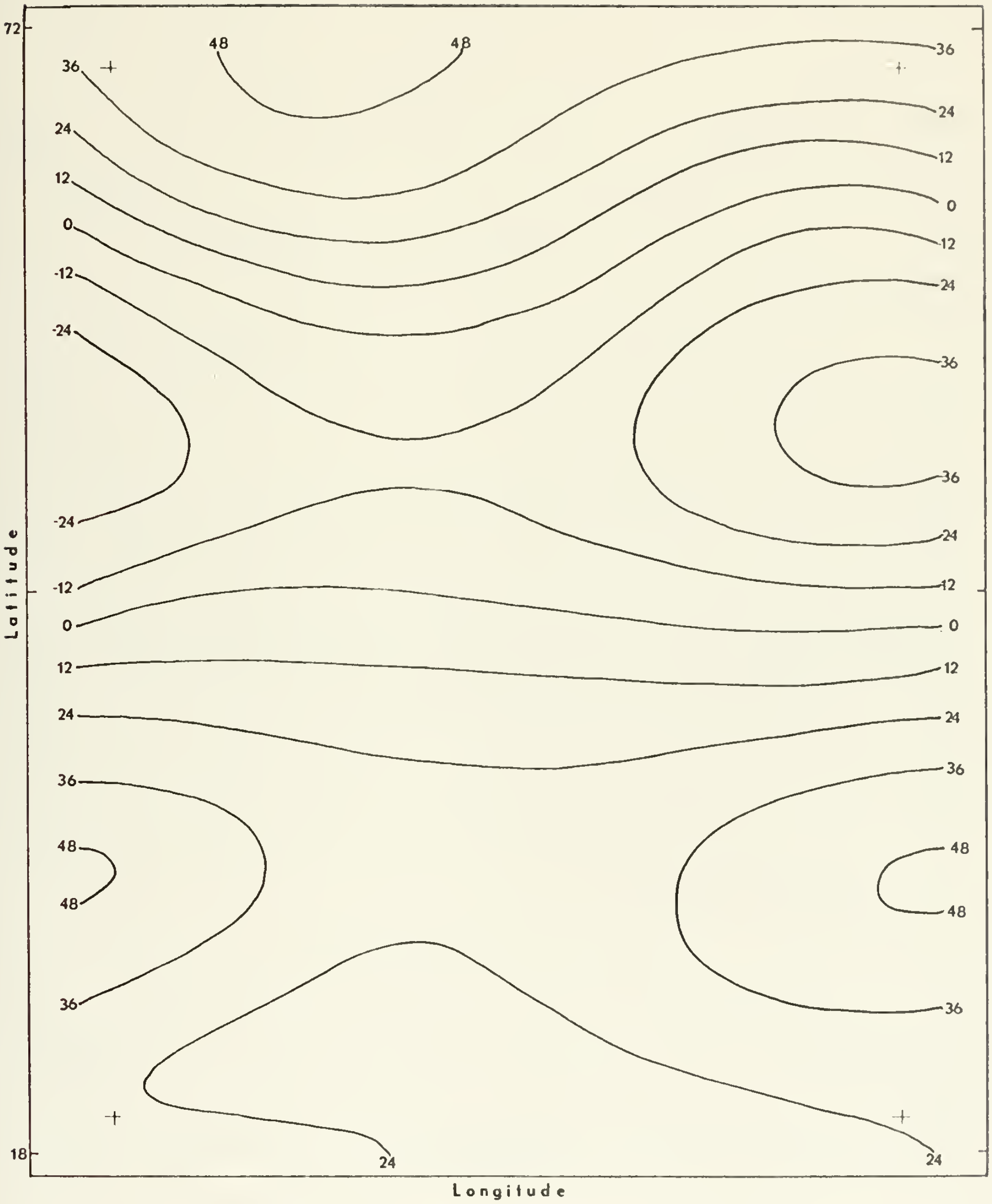

Figure 24. Distribution of 100 day mean 1000-mb height deviation in phase I.

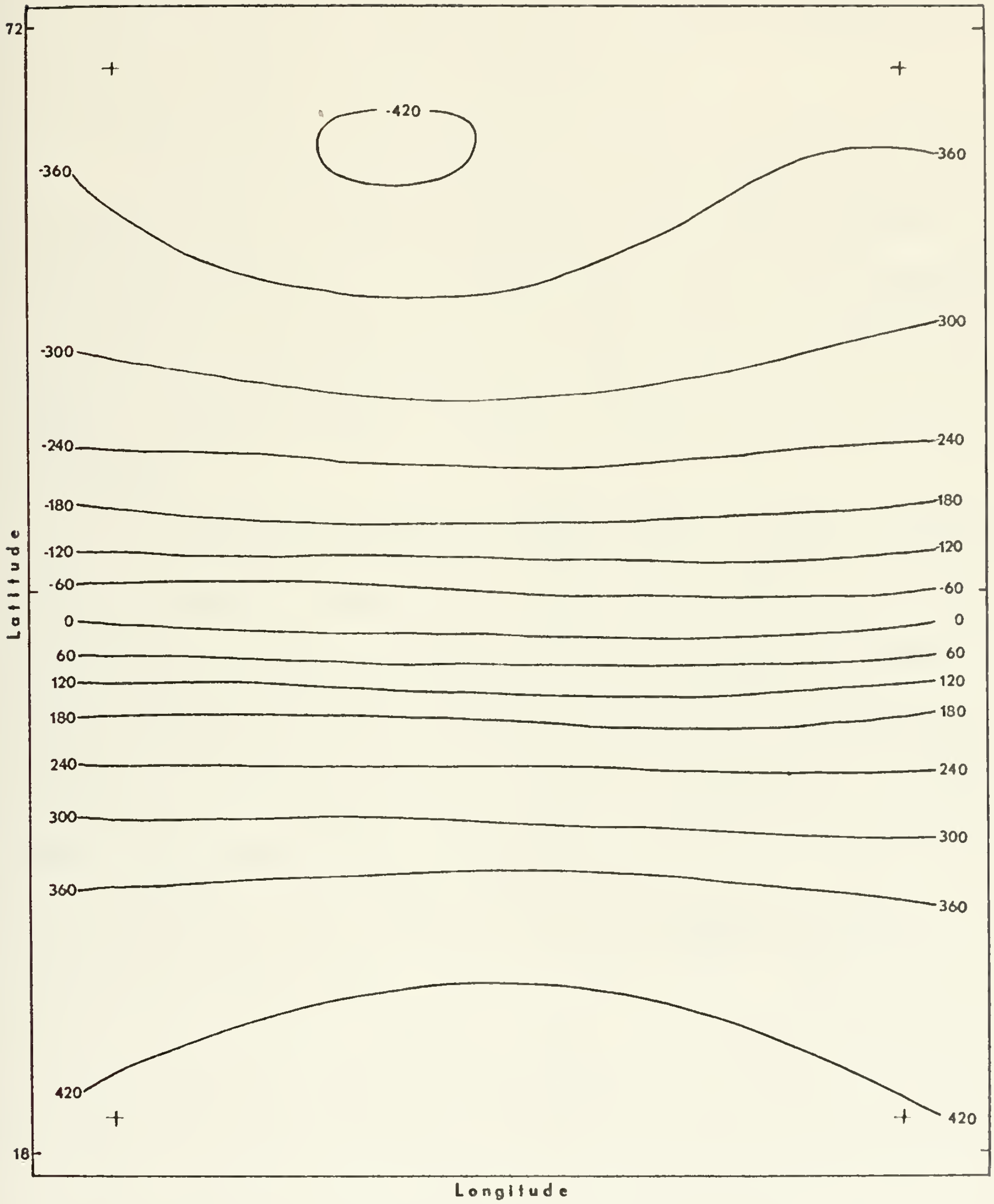

Figure 25. Distribution of 100 day mean 250 mb height deviation in phase I.

Figure 26 shows the distribution of the 750 mb height deviation analyzed at 30-meter intervals. The flow is again zonal throughout the central portion of the region. However, the lowest height is now in the northeastern corner of the area and the low latitude high is present in only the southernmost part of the domain.

The vertical structure of the standing disturbance is such that the 1000 mb high in the polar regions lies below the 250 mb low the same as in the real atmosphere. The warm low pressure area at the southern boundary at the 1000 mb level becomes an area of high pressure at the 250 mb level.

The zonal wind averaged over the same 100 day period is shown in Figure 27. The line labeled (c) shows a westerly flow at all latitudes at the 250 mb level with the jet located at 45N, coinciding with the strong height gradient in that region as seen in Figure 24. Curve (b) shows the weak polar easterlies at 750 mb level to the north of the low at 60N. The remainder of the flow is westerly with a weak jet at about 45N. Line (a) shows the zonal flow at the 1000 mb level. The polar easterlies extend from the northern boundary to a latitude just north of the cyclonic activity. Westerlies extend from that point to the latitude of the 1000 mb highs and easterlies exist to the southern boundary. A comparison of Figure 27 with Figure 23 shows that the mean zonal winds did not change significantly after reducing the grid size. This

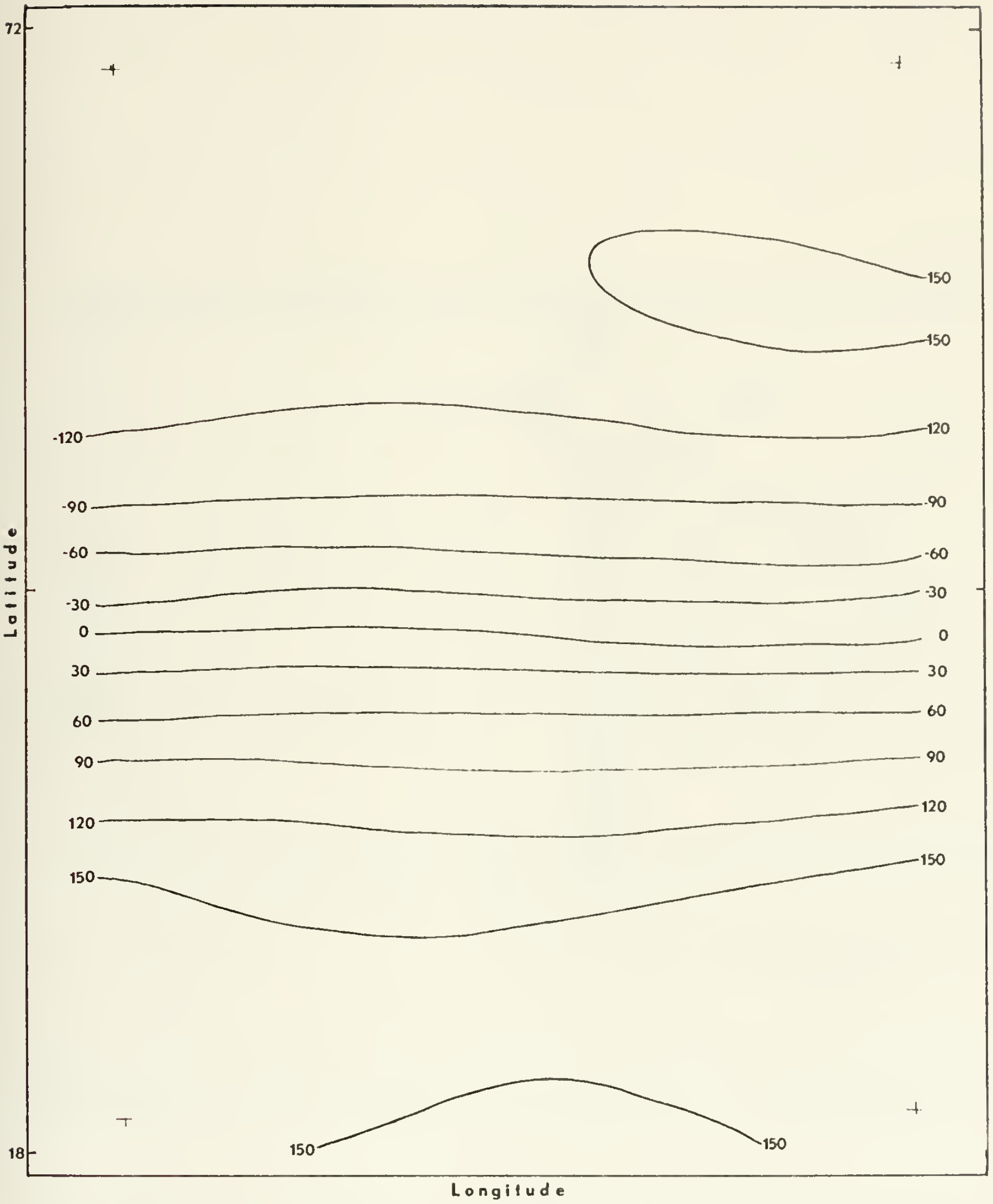

Figure 26. Distribution of 100 day mean 750 mb height deviation in phase I.

indicates that for the atmospheric model, a 400 km grid would have sufficed with little loss of resolution.

Figure 28 shows the distribution of the 1000 mb height contours at 25 meter intervals at day 28,900. A low dominates the western half of the region at this time and a high covers the eastern half. This figure was compared to the series of 1000 mb figures presented by Phillips (1956) and the gross features are almost identical to the early stages of his model atmospheric development. The main surface troughs and ridges are orientated so as to lean back

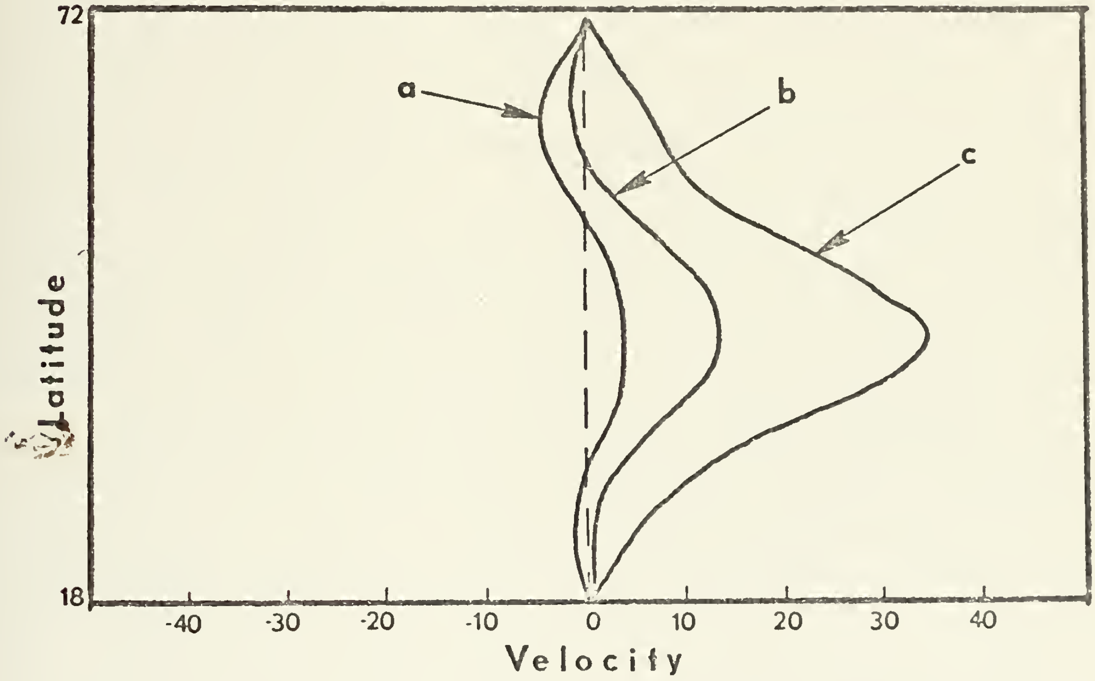

Figure 27. Zonal atmospheric winds in m sec^{-1} from 200 km grid model at a) 1000 mb; b) 750 mb; c) 250 mb.

toward the northwest in the northern half and slightly toward the southwest in the southern half of the region. The convergence of momentum in the central portion increases the westerlies and accounts for the mid-latitude jet observed in this area (Figure 29).

Figure 29 shows the distribution of the 250 mb height contours at 60 meter intervals for day 28,900 (79 years). A wave of moderate amplitude is superimposed on the zonal flow with a trough present over the western half of the region and a ridge dominating the eastern half. The polar vortex observed in Figure 25 exists at this time also. The single wave structure of the atmospheric model forces a pattern similar to this to be found at any given instant. The disturbance moves and its amplitude varies with time from a zonal pattern to a highly amplified wave pattern. At this time the disturbance kinetic energy had a value of 54 m^2 sec^{-2}. This is quite large compared to the disturbance kinetic energy of the more zonal flow in Figure 25. However, at other times in the experiment higher values of this quantity were observed. It is believed that the atmospheric state shown in Figure 28 is representative of a flow in which a wave disturbance of average amplitude is imbedded. At times the amplitude of the wave will be greater than it is at day 28,900 and at other times less. Also, the wave will propagate across the domain and yield a time mean upper level flow as shown in Figure 25.

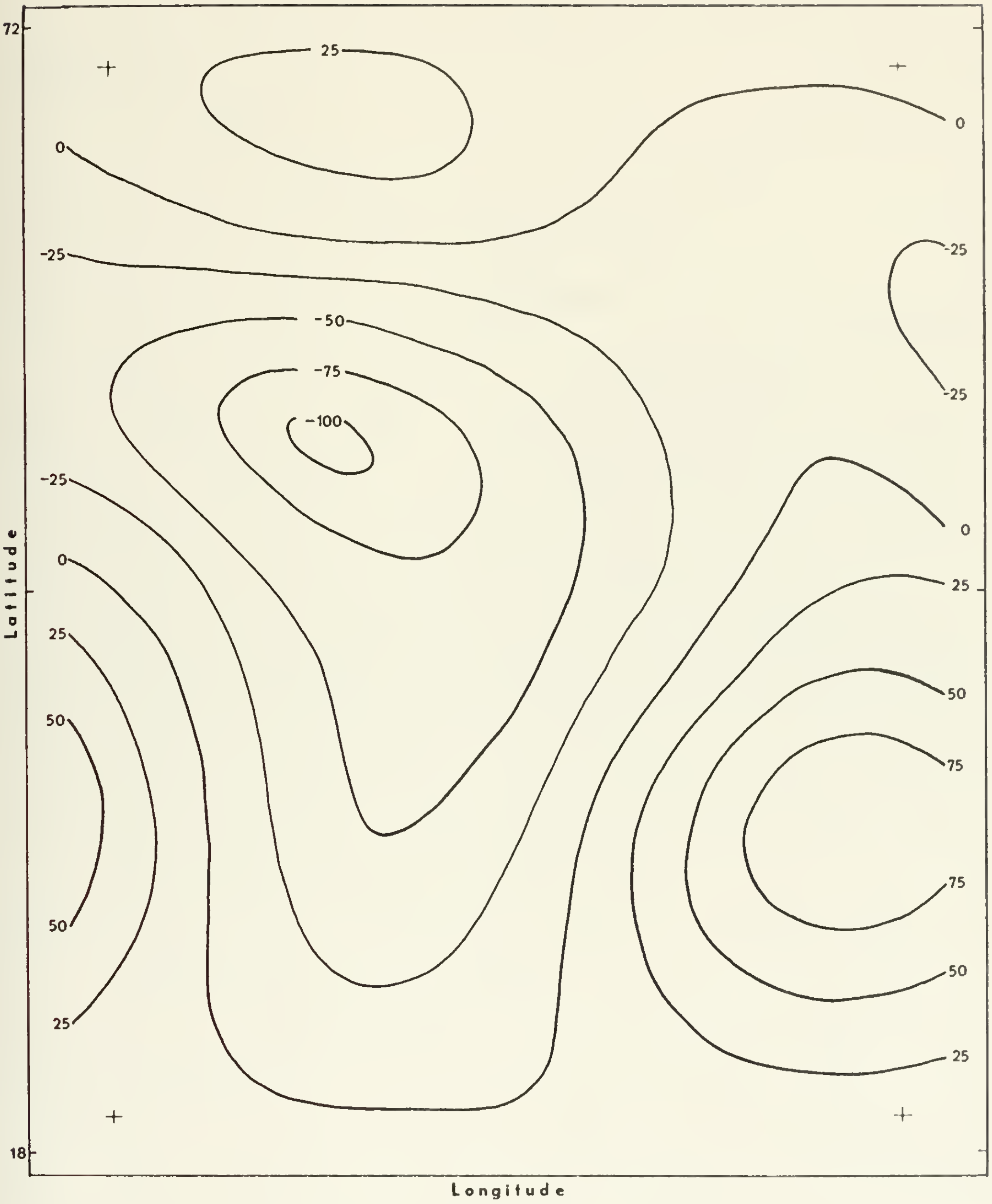
72
18
Latitude
Longitude
25
0
0
-25
-25
-25
-50
-75
-100
-25
0
0
25
25
50
50
75
75
50
50
25
25

Figure 28. Distribution of 1000 mb height deviation at day 28,900 in phase I.

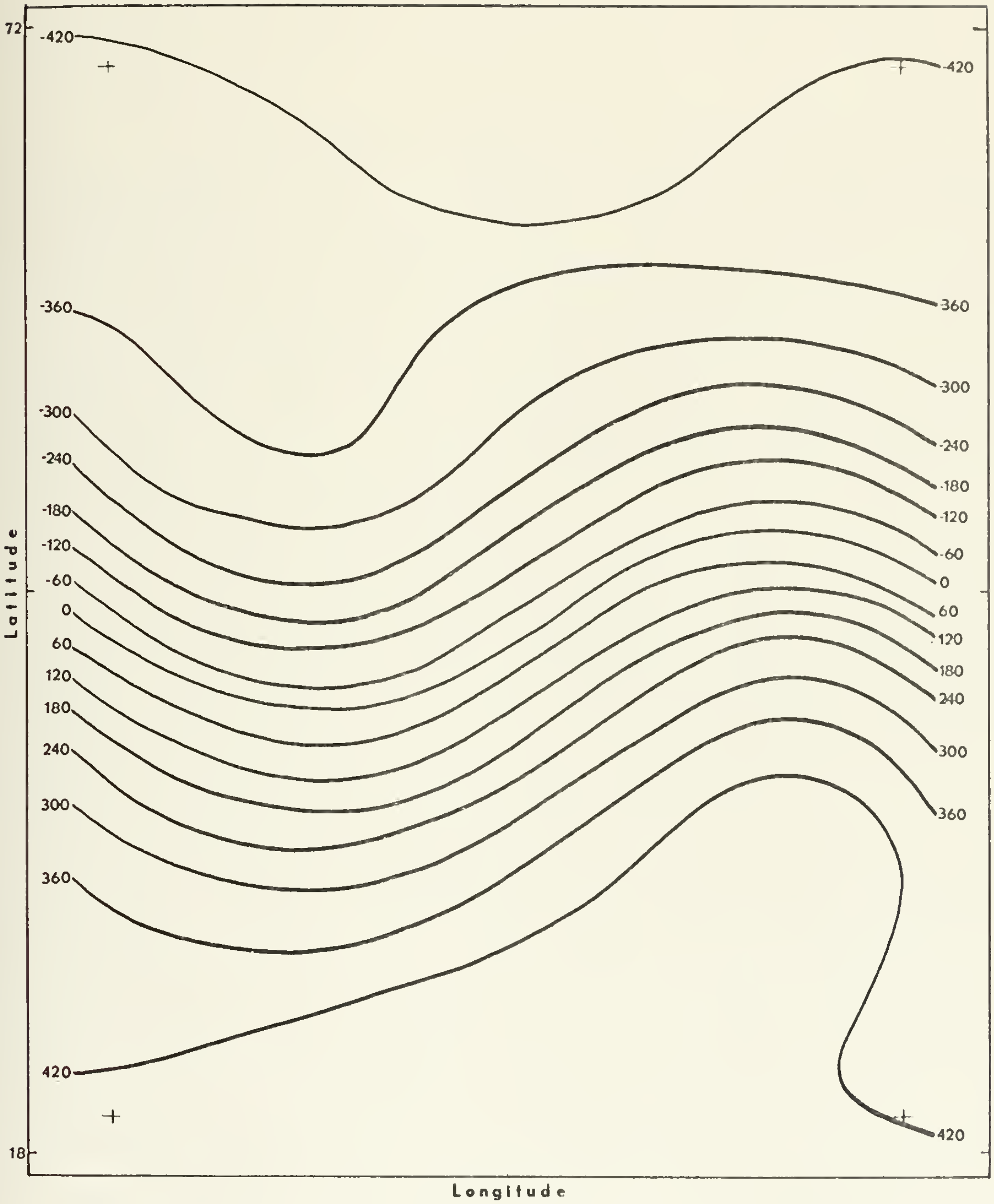

Figure 29. Distribution of 250 mb height deviation at day 28,900 in phase I.

Figure 30, the distribution of the 750 mb height contour at 30-meter intervals at day 28,900, shows a closed cyclonic circulation directly beneath the trough at 250 mb. The amplitude of the wave motion is about the same as at 250 mb and a closed high is present beneath the upper level ridge.

The suggestion that the single wave in the x-direction would produce a series of cyclonic scale disturbances moving over the domain of the atmosphere-ocean model was born out by these figures plus examination of preceding maps. The wave moves eastward with a speed of about 600 km per day. This is considerably slower than the wave motion in Phillips' experiments.

The vertical heat flux was discussed earlier as being proportional to the atmosphere-ocean temperature difference. However, due to the method by which the sensible heat exchange is calculated, the vertical heat flux is actually proportional to the difference between the atmospheric surface temperature and the Fourier analyzed sea surface temperature. This temperature difference, averaged over the last 100 days of the experiment, is shown in Figure 31. In general, there is cooling of the atmosphere in the western sector and warming of the atmosphere in the east. While this heating may be representative of what occurs in the northernmost latitudes of the real atmosphere, it does not accurately portray what occurs throughout the

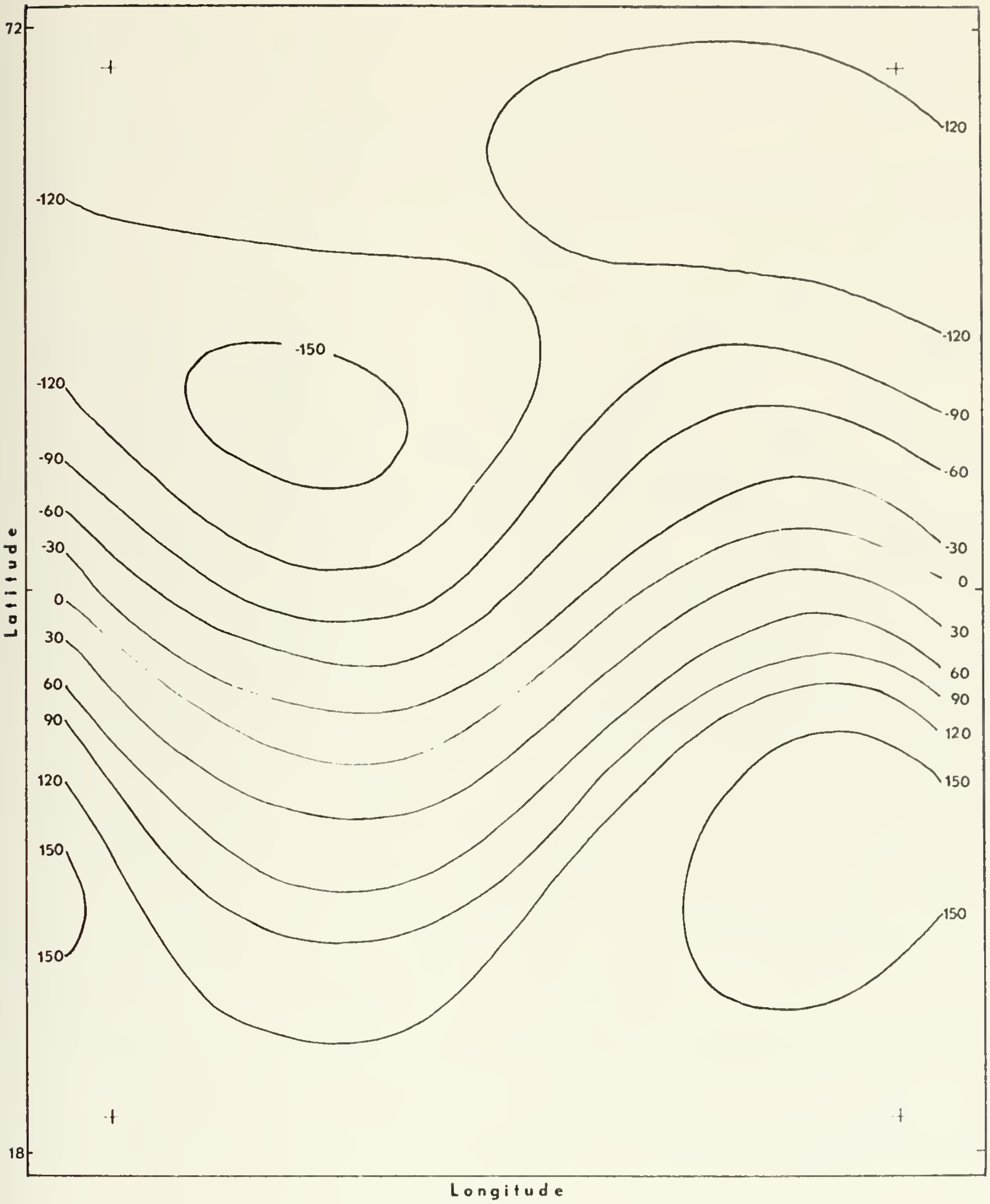
72
18
Latitude
Longitude
120
-120
-120
-150
-120
-90
-60
-30
0
30
60
90
120
150
150
-90
-60
-30
0
30
60
90
120
150
150

Figure 30. Distribution of 750 mb height deviation at day 28,900 in phase I.

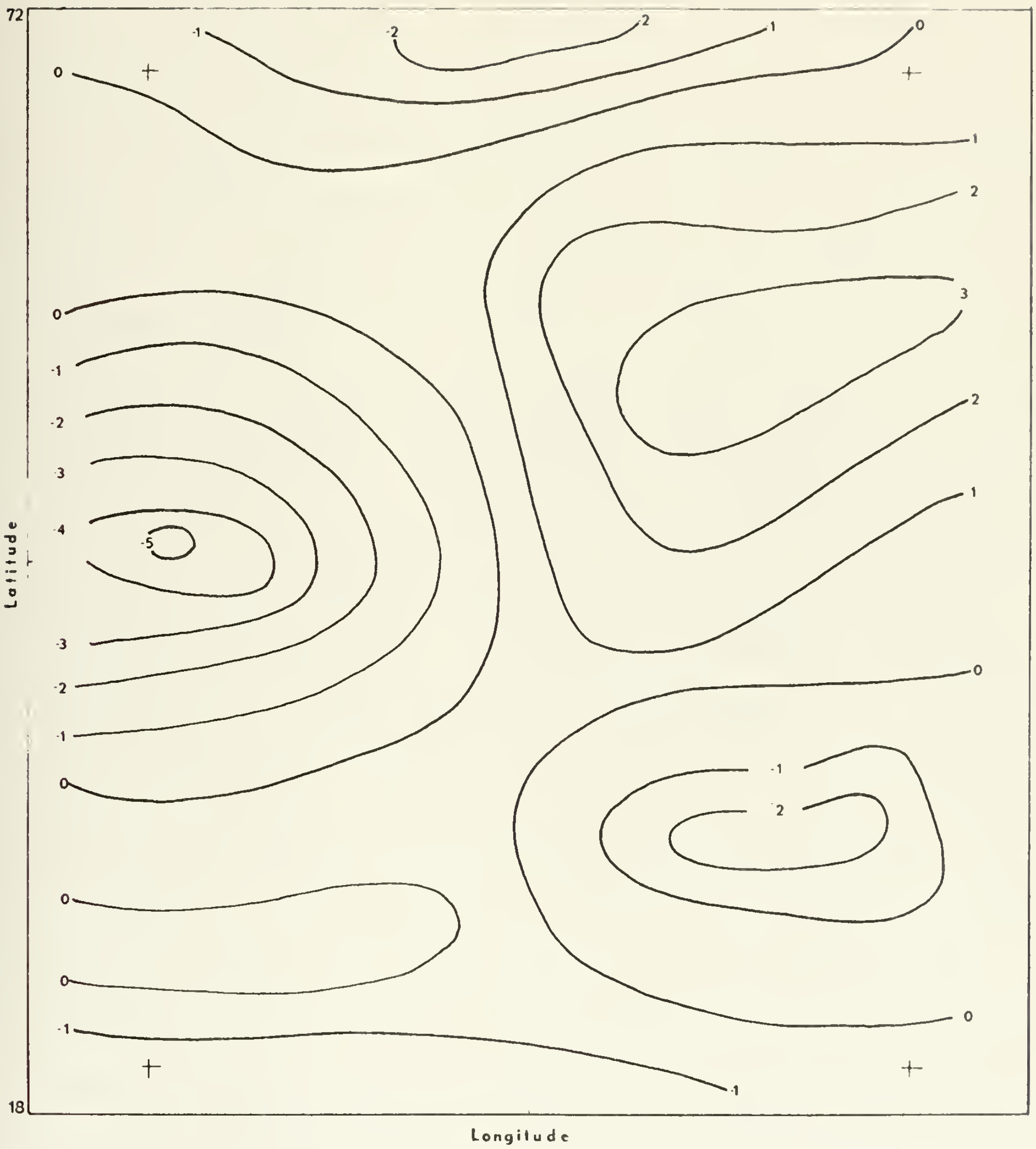

Figure 31. 100 day average difference between the Fourier transformed sea surface temperature and the atmosphere surface temperature computed in phase I. Heating of the atmosphere occurs where values are positive.

majority of the oceanic regions where cold atmospheric air masses move from over a cold continent to a position over warmer water and are heated from below. The lack of colder continents in the model and the use of cyclic boundary conditions makes it impossible to simulate this phenomena in this simple model. The use of the Fourier analyzed sea surface temperature also contributes to the unrealistic vertical heat flux pattern of the model. The strong temperature gradient observed in the real ocean along the east coast of continents and observed in the model along the western boundary of the ocean in Figure 34, had little effect on the heat flux pattern that evolved. The Fourier analysis smoothed this gradient and although the gradient did influence the new sea surface temperature somewhat, it did not have the same influence observed in the real atmosphere-ocean system. The Fourier analyzed sea surface temperature was used in the heat exchange to be consistent with the simple one-wave formulation of the atmosphere. The cyclic boundary condition forces the air to pass from a region of warm water on the eastern boundary immediately to the region of cooler water in the western area. The overall effect that the resulting heat flux pattern had on the results of this experiment are hard to determine. The strong heating observed in nature on the western side of the ocean in the mid-latitudes does not occur. The overall effect may be to smooth out the effect of the heating on the atmospheric temperature disturbance (only disturbance

quantities are of interest since domain mean temperatures of the atmosphere do not change) and cause a more zonal pattern. Figure 32 shows the time mean atmospheric surface temperature averaged over the last 100 days of the combined model experiment. The temperature in this figure has a more zonal appearance than was expected after examining the mean 1000 mb height deviations (Figure 24).

Figure 33 is the 100 day time mean of the stream function governing the vertical mean currents. The subarctic gyre, visible at about 55N in this figure, produces southward flow along the western boundary at that latitude and northward return flow 4-600 km east of the boundary. The subtropical circulation at about 35N has northward flow at the western boundary and southward flow 4-600 km to the east. The convergent flow in the boundary causes a sharp meridional temperature gradient at about 43N and contributes to the low temperature near 48N in the western boundary.

Figures 34, 35, and 36 show the 100 day time means of the ocean temperature at the surface, 500 meters and 1300 meters, respectively. These maps are vertically consistent and the low temperatures just described near 48N can be seen at all three levels. The thermal ridge observed in the northwestern sector of Figure 34, and also in Figure 35, is caused by the northwestward flow on the east side of the subarctic gyre and somewhat by the upwelling along

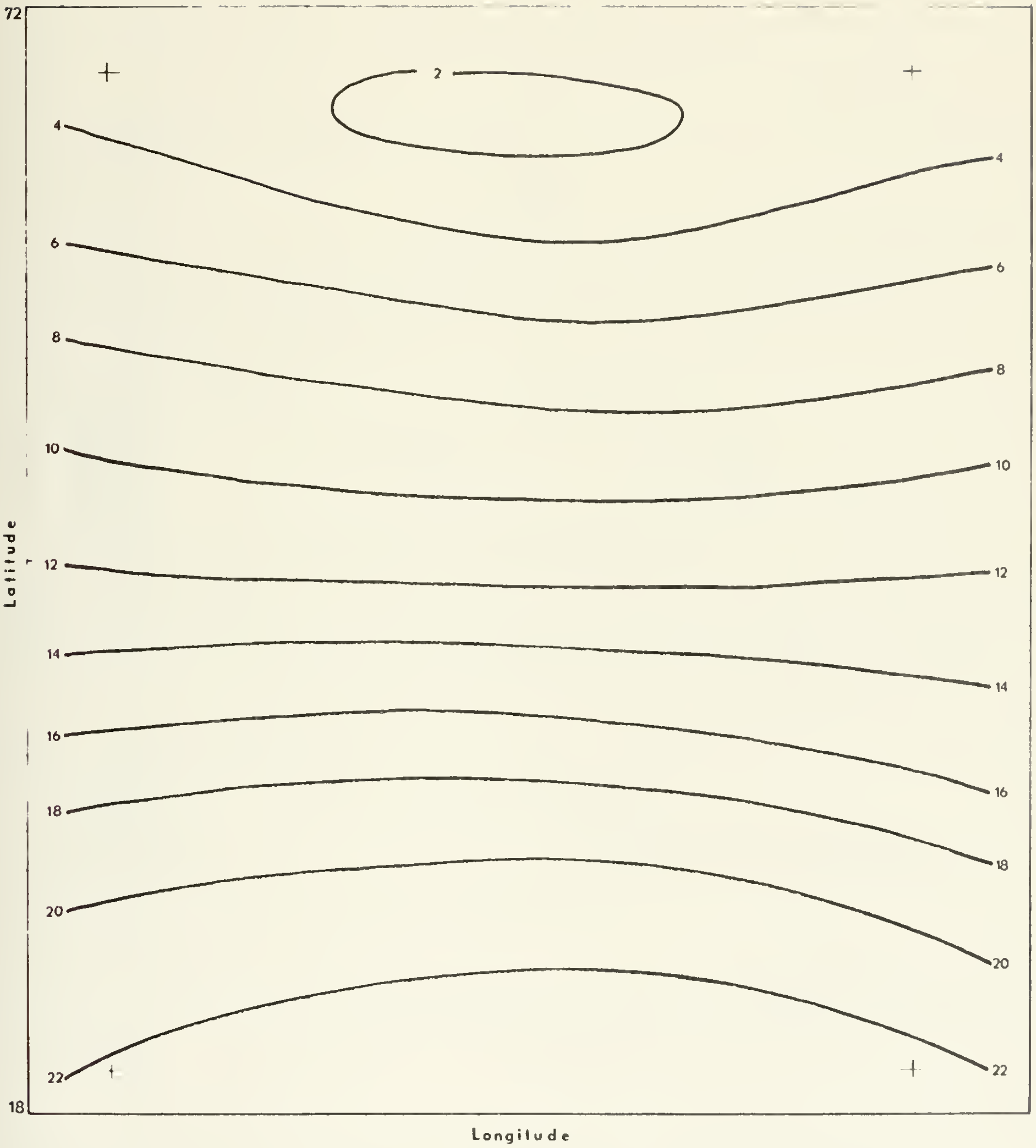

Figure 32. 100 day mean atmosphere surface temperature in phase I (C).

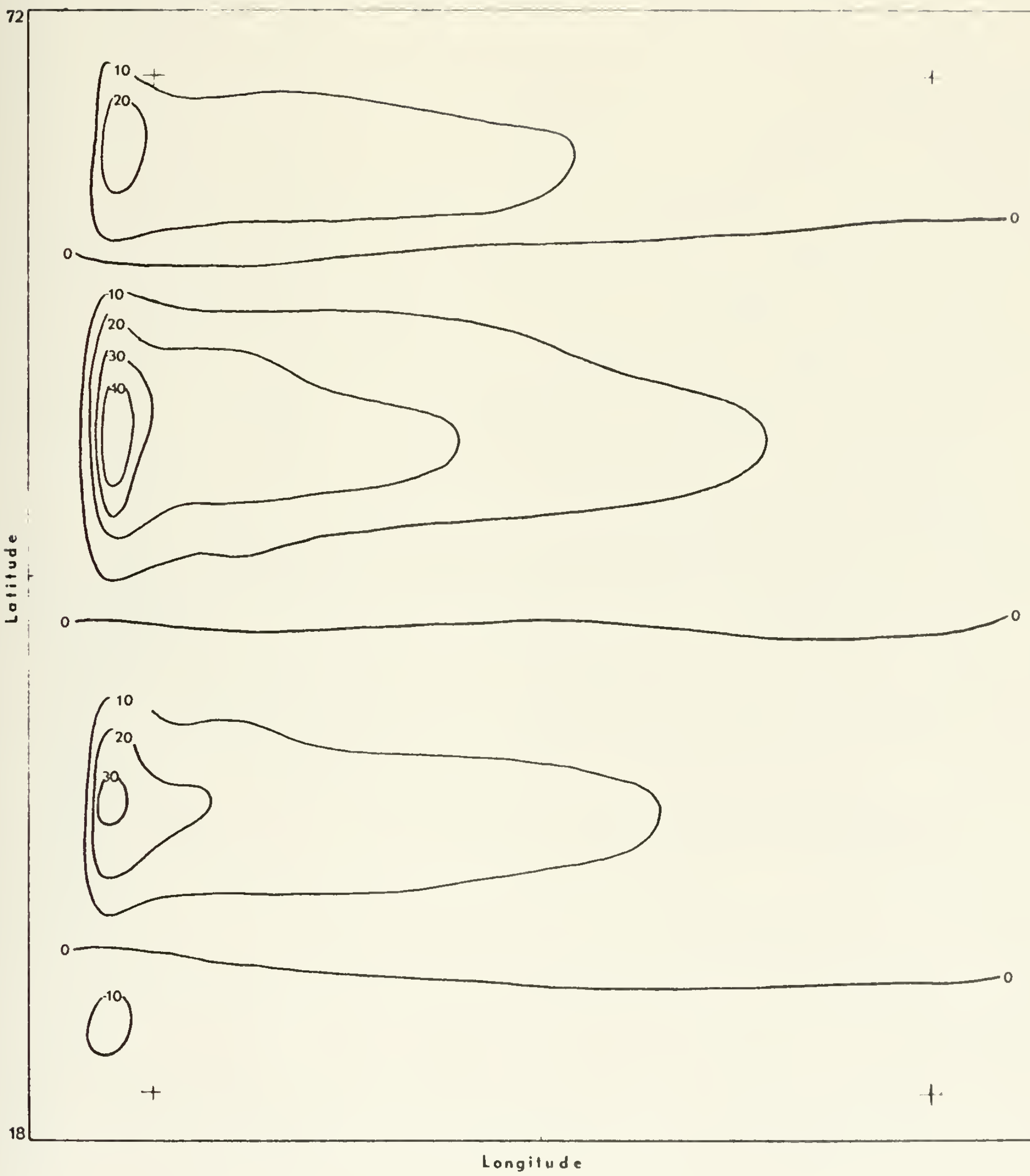

Figure 33. 100 day mean stream function pattern from phase I in units of 10^7 cm^2 sec^{-1}.

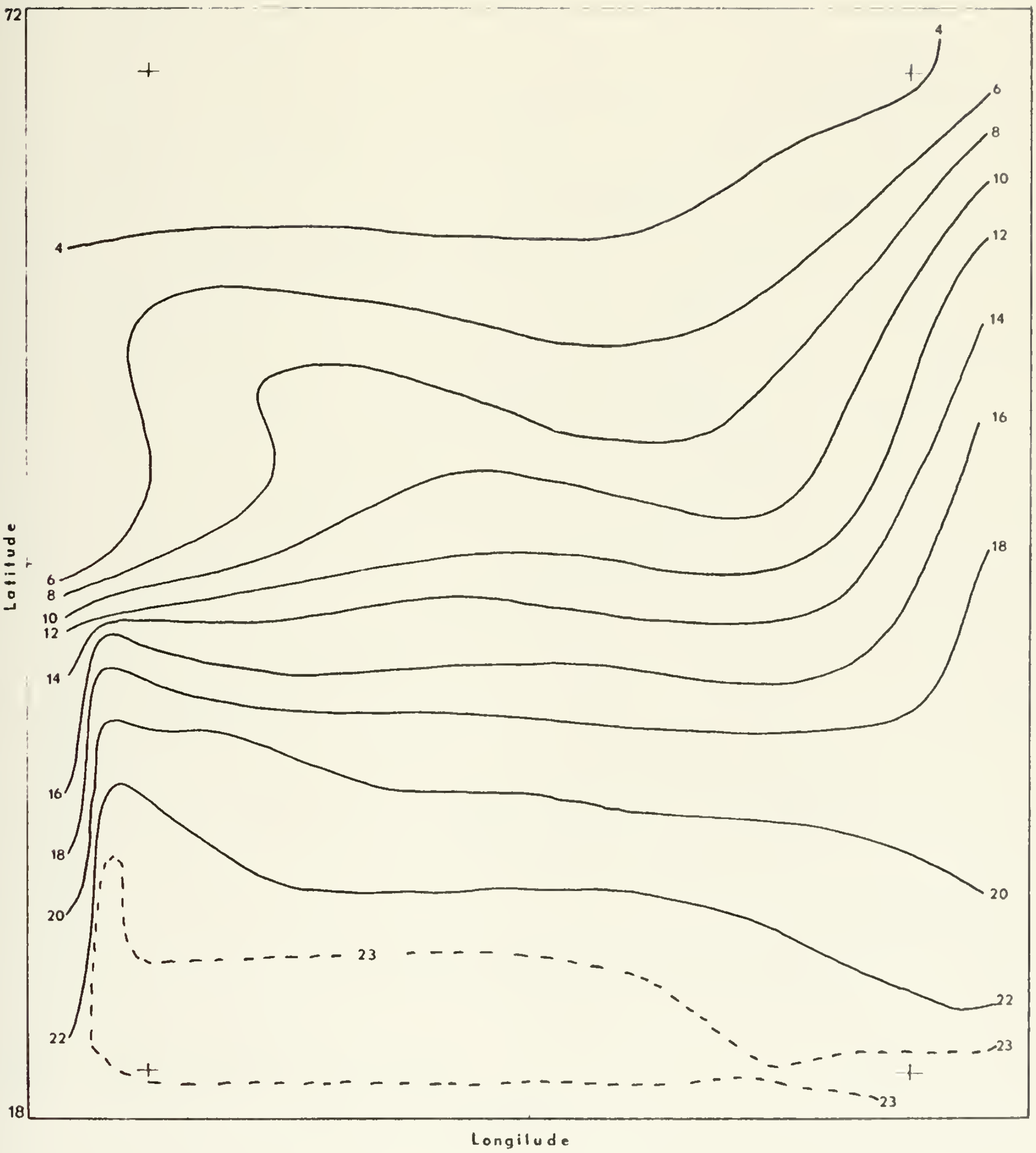
72
18
Latitude
Longitude
4
6
8
10
12
14
16
18
20
22
23

Figure 34. 100 day mean sea surface temperature (C) pattern in phase I.

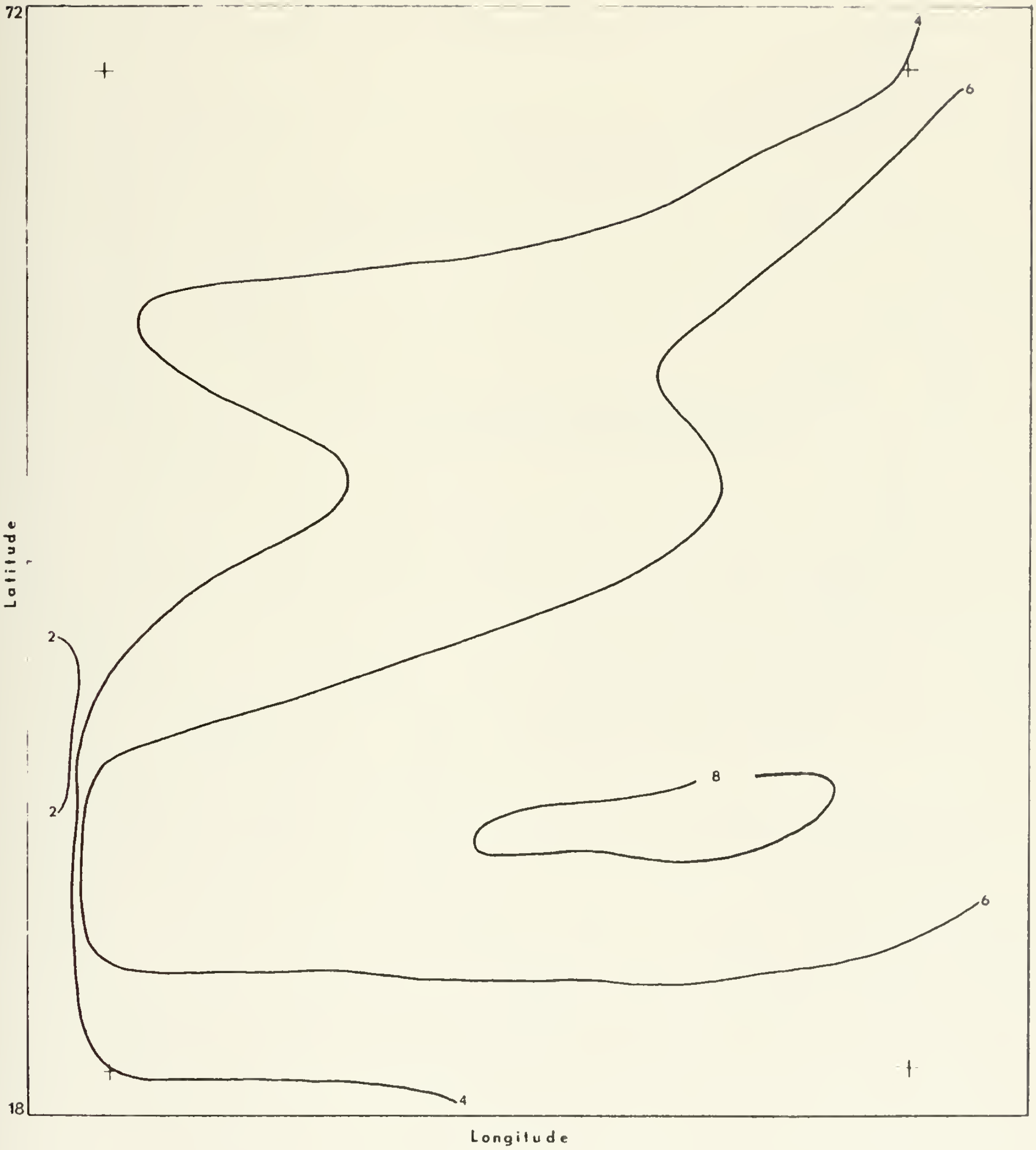
72
18
Latitude
Longitude
2
2
4
4
6
6
8

Figure 35. Temperature pattern at a depth of 500 meters in ocean in phase I (C).

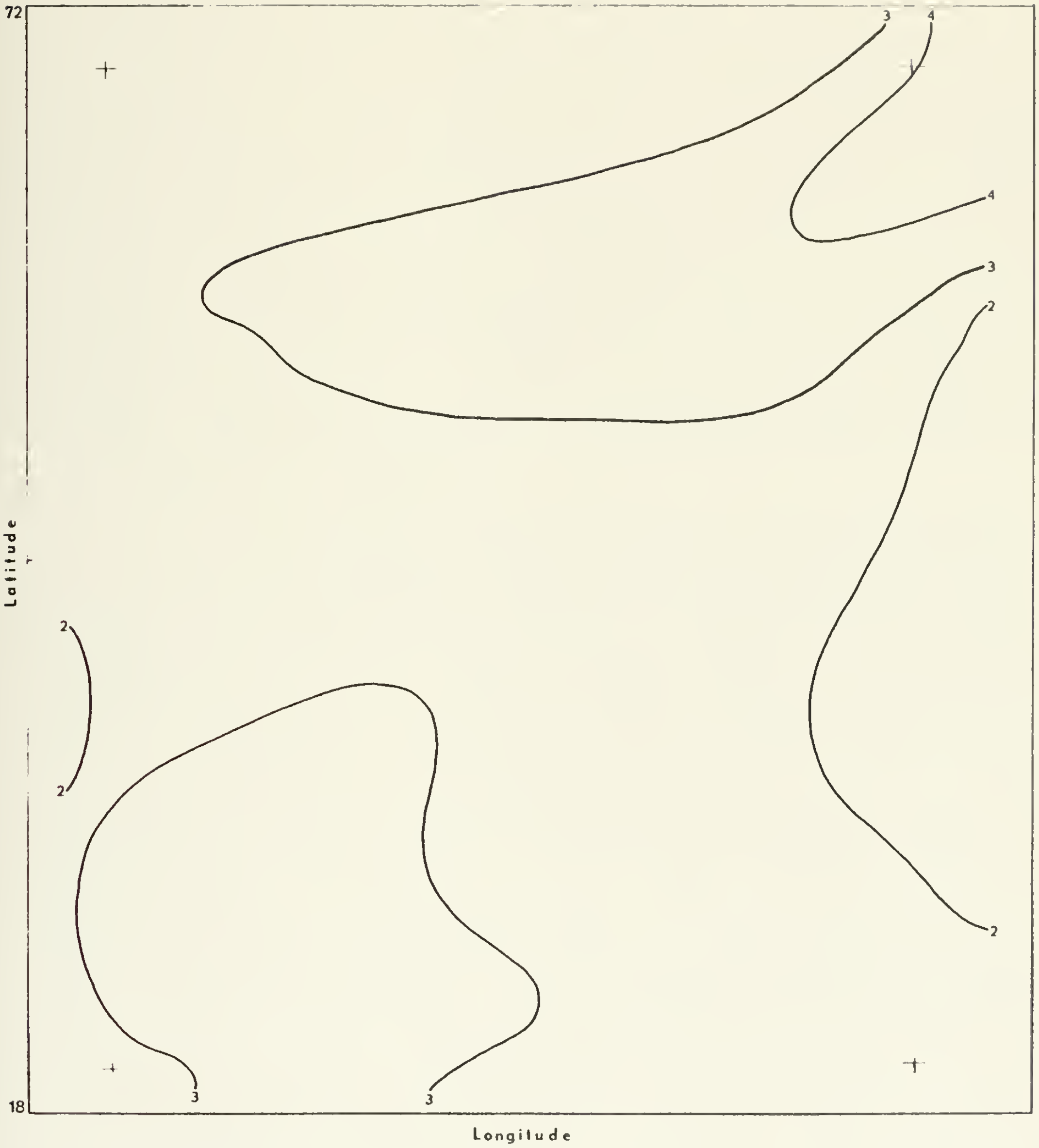

Figure 36. Temperature pattern at depth of 1300 meters in ocean in phase I(C).

the western boundary seen in Figure 37, which contains the time averaged vertical motion field at the depth of 300 meters. In the fine grid, as well as in the coarse grid discussed earlier, the flow in the western boundary regions in high latitudes is composed almost entirely of the vertical mean current. Here the flow is of this character and moves across the isotherms, advecting warmer water toward the northwest. The large area with horizontally isothermal water of about 5C located west of the ridging in the northwest quadrant of the ocean domain can be compared qualitatively to a similar feature found east of Newfoundland in the North Atlantic. Sverdrup et al (1942) presented sea surface temperature maps that contained this feature in both winter and summer.

In the northeastern quadrant the flow is weak and closely parallels the isotherms. Here, in the absence of appreciable vertical mean current, the vertical shear current is dominant and when the flow reaches the northeastern boundaries large sinking motions occur (see Figure 37) producing warm temperature at all depths there. Figures 34, 35 and 36 all show warmer water in the northeast corner due to this phenomenon. The isotherm pattern produced by the model in this area can be likened to the real sea surface temperature pattern off the west coast of the United States. The area of warmest surface water in Figure 34 is observed in the southwestern corner of the domain. This area is analogous to the Sargasso Sea with its warm temperatures and weak currents.

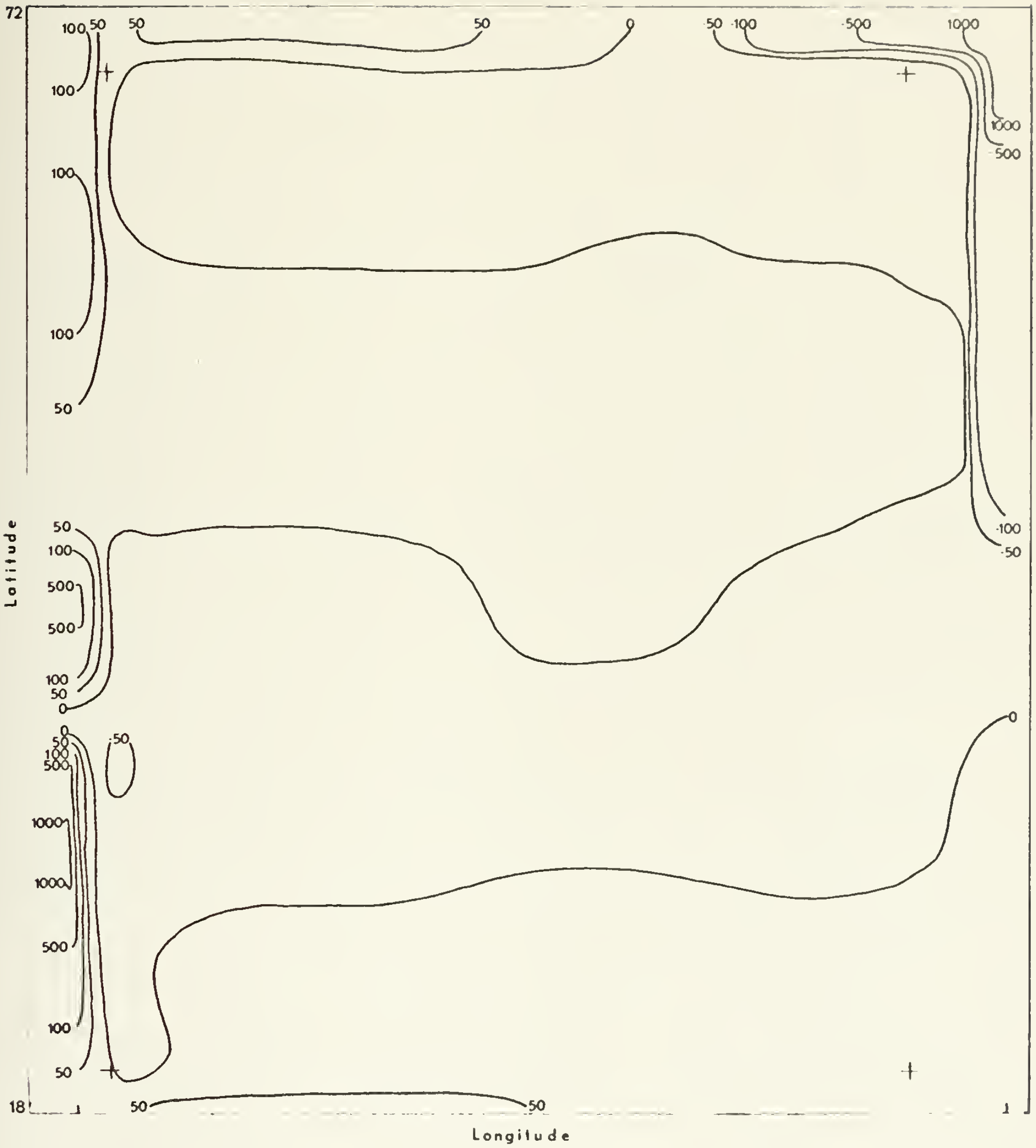

Figure 37. 100 day mean vertical motions in cm day^{-1} at 300 meters in phase I.

The temperatures along the western boundary are further affected by the upwelling that takes place due to the thermal circulation. The central latitude is a region of weak eastward flow in the surface layer and westward flow at the lower layers. The moderate upwelling brings colder water to the surface, lowering the surface temperature along the boundary. An area of weak sinking motion in the south central portion of the domain in Figure 37 brings about the warm 8C water at the 500 meter level (Figure 35).

From the stream function field in Figure 33, the vertical mean current can be computed. The subarctic gyre has a vertical mean current on the order of 20 cm sec^{-1}. The subtropical gyre has a vertical mean current on the order of 15 cm sec^{-1}. Table 3 shows the total meridional velocity, an estimate of the vertical mean meridional current as calculated from the stream function and the vertical shear meridional current calculated as a residual, in the western boundary current. The vertical mean current is almost entirely responsible for the meridional current in the boundary layer associated with the subarctic gyre, while the vertical shear current is dominant in the subtropical gyre. The maximum value of 51 cm sec^{-1} in the boundary current, representing a Gulf Stream type flow, is less than that found in the real world oceans where 100 cm sec^{-1} have been observed for this type of a boundary current.

Latitude	Total Merid. Current	Vertical Mean	Vertical Shear
71.1	2.6	2.8	-0.2
67.5	12.8	5.6	7.2
63.9	9.9	10.0	-0.1
60.3	-0.4	-1.7	1.3
56.7	-12.0	-14.0	2.0
53.1	-20.5	-19.0	-1.5
49.5	-18.7	-14.0	-4.7
45.9	-5.6	-6.5	0.9
42.3	11.1	0.8	10.3
40.5	17.7	3.8	13.9
36.9	37.5	12.5	25.0
33.3	51.1	15.5	35.6
29.7	41.0	8.0	33.0
26.1	20.5	2.5	18.0
22.5	6.7	-5.1	11.8
18.9	1.9	-0.7	2.6

TABLE 3. Total meridional current (cm $\sec^{-1}$) as produced by the combined model; vertical mean current as computed from the model stream function; vertical shear current calculated as a residual.

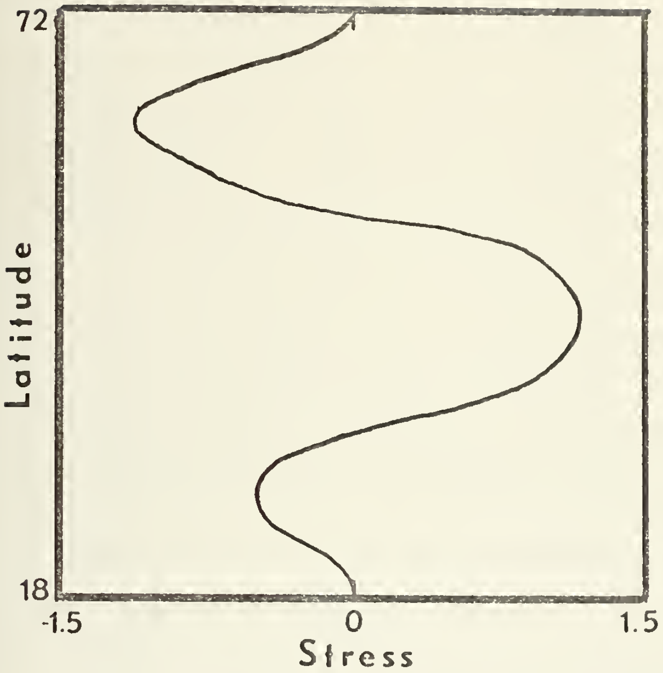

Figure 38. 100 day mean stress pattern produced by combined model.

The stress acting as a driving force on the ocean was continuously varying as the time integrations progressed. A 100 day time mean zonal stress was calculated at a time six years prior to the end of the integrations and is shown in Figure 38. This stress was used as a constant force acting on the ocean during the ocean-only phase of the experiment. Now it can be interpreted as the mean stress responsible for the stream function field observed in

Figure 33. The curl of the stress has maxima at about 34N and 50N which are the approximate positions of the centers of the subtropical and subarctic gyres, respectively. The positions of the maxima are about 5 degrees further north than actually observed in nature. This is responsible for the northward shift of the gyres and their associated boundary currents. The stress varies from 1.20 to -1.15 dynes cm^{-2}. These are reasonable values lending justification to the stress formulation discussed earlier.

The state to which the combined model progressed was acceptable in its resemblance to the real atmosphere-ocean system. While it was not the intention of this work to develop an operational model for forecasting either atmospheric or oceanic parameters, it is comforting to see a reasonable distribution of the various parameters.

3. The Ocean-Only Experiment (Phase II)

The zonal mean stress (Figure 38) that had been averaged over the 100 day period from day 26,650 to 26,750 was used as a constant forcing function for the subsequent six year period over which the ocean-only model equations were integrated. The atmospheric surface temperature, T_4, was also averaged over this same 100 day period. Figure 39 shows a plot of the zonal mean temperature as a function of latitude. The temperature varied from 2.7 degrees centigrade in the north to 23.3 degrees in the south. This temperature was used as an equivalent atmospheric temperature to which the sea surface temperature was compared to

determine the vertical heat flux. Except for the fixed atmospheric surface temperature which was independent of x, the same formulation was used for the heating as was used in the combined model. Now, however, one degree of freedom was removed and the ocean in a very short time became steady, except for a slow secular change.

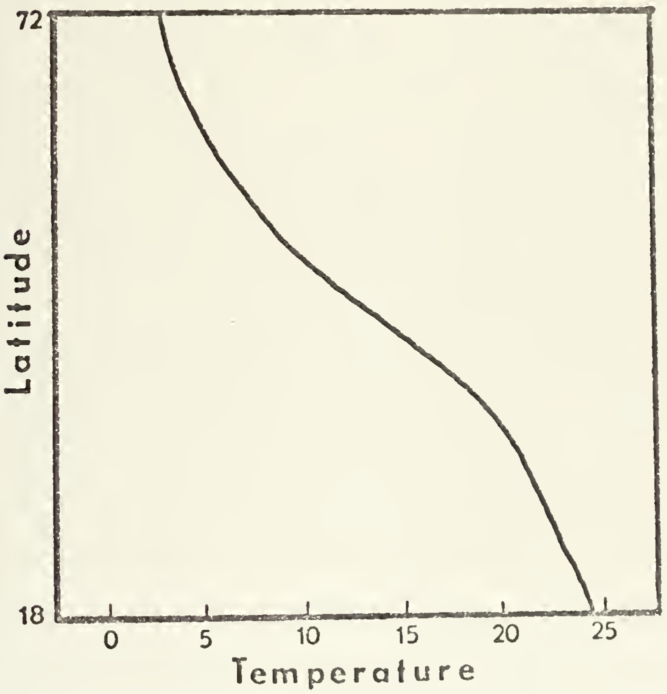

Figure 39. 100 day time mean atmospheric temperature (C) as a function of latitude.

The instantaneous fields of the ocean dependent variables from day 26,700 were used as initial conditions

for the ocean-only phase of the experiment. During the six-year ocean-only experiment, data fields for all oceanic variables were saved every 100 days and selected daily parameters were saved at the same five points as previously discussed.

The 2200 day (six year) integration of the ocean-only equations proceeded at a rapid pace. No problems were encountered with adjustment to the new constant forcing functions and a quasi-steady state was achieved. At the start of the 2200 day phase of the experiment the volume average temperature of the ocean was increasing at about 0.5 degrees per century as previously discussed. Throughout the six year period the warming rate remained about the same, with a 0.5 degree per century warming still present at the end. This makes this author believe that perhaps this is as close to an equilibrium state as could be reached with the model as formulated, without the expenditure of an excessive amount of computing time. An examination of the sea surface temperature, Figure 40, and the area average of the temperature at that level shows that the sea surface temperature is not changing at all. The rate of change of average temperature at the upper level is exactly zero. However, the average temperature at the lowest level is changing at a rate of 0.6 degrees per century, showing that the diffusive mechanism by which the deeper water must be changed is very slow.

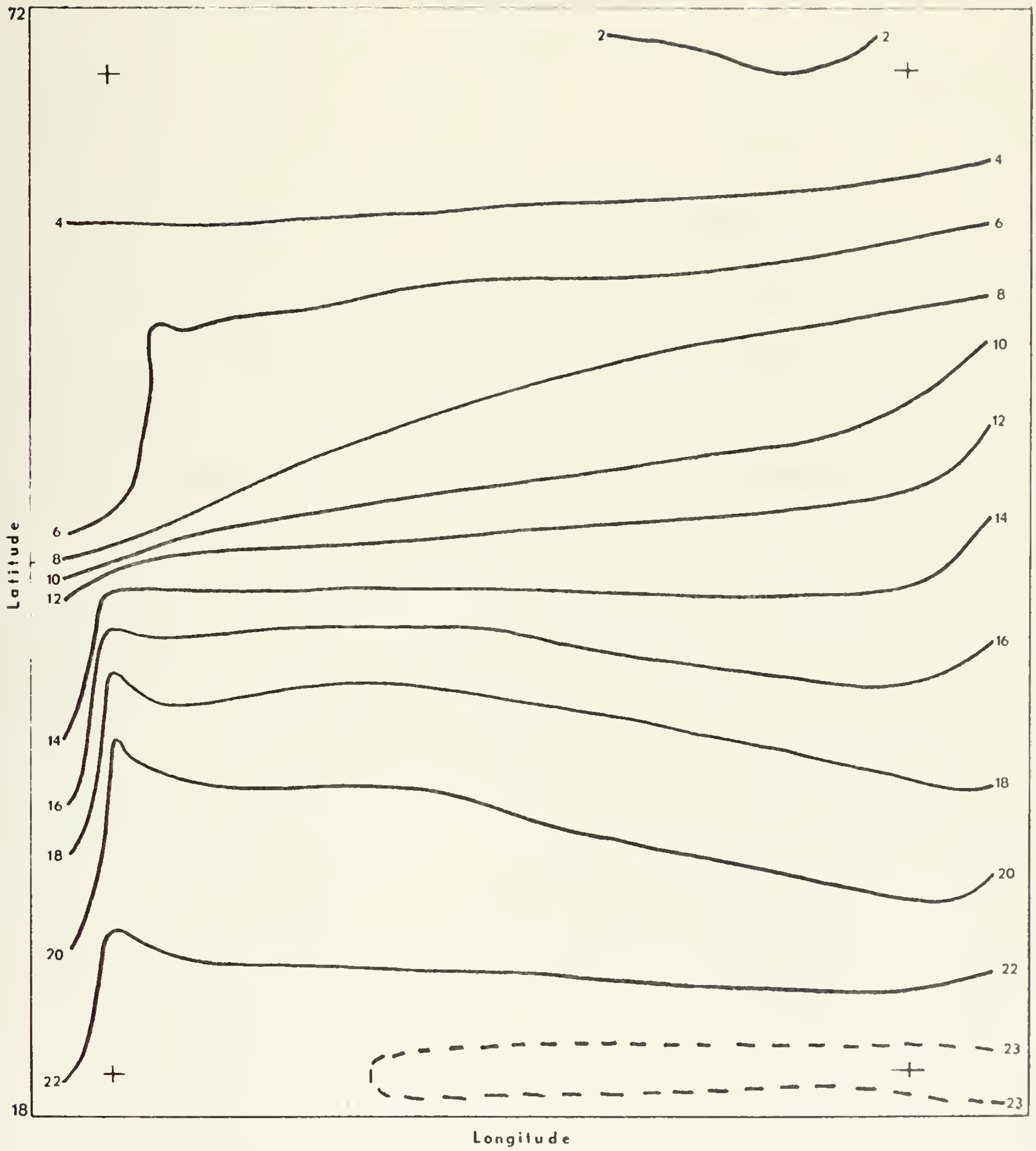

Figure 40. Sea surface temperature from ocean-only model at day 28,900.

Figure 40 shows the sea surface isotherms at day 28,900. An examination of this temperature field at day 28,800 was made and the two maps were identical. Therefore, it was considered unnecessary to derive time mean maps of this quantity. The pattern is similar to the sea surface temperature field at the end of phase I (Figure 34) in that a strong temperature gradient is present in the western boundary layer at about 35N. The isotherms throughout the central portion of the domain are slightly more zonal than in phase I where there is an x dependence in the forcing, but the meridional gradient in this area remained about the same. The warm core tropical water (above 23C) does not extend into the boundary layer but is visible as a narrow band of warm water just north of the southern boundary.

The major difference in the temperature fields between the two phases is in the northern half of the domain. The thermal ridge present in the northwest quadrant in phase I is observed only as a small perturbation in the 6C isotherm in this phase. The thermal trough to the west of this feature is similar to that present in the combined model with a region of water with temperature between 4 and 6 degrees extending over a thousand kilometers. The remainder of the isotherms in the north have a more zonal appearance. There is a small pocket of water below 2C in the northernmost region in phase II that is not present in phase I. The isotherms in the northeast sector vary significantly between the two phases. In phase I the thermal

current flows into the northeast corner when the strongest sinking motion occurs. In phase II the vertical shear current flows into the eastern wall on a more eastward heading. The maximum sinking motion is located about 800 to 1000 km south of its position in phase I. This can be verified by comparing Figure 41, the vertical velocity at a depth of 300 meters in the ocean-only case, with Figure 37, the same quantity in the combined model. The northward curvature of the isotherms in the central portions of the eastern boundary is present in both phases, but is less pronounced in the ocean-only case. An examination of the meridional current in this area showed that there was weak northward motion in the northeastern boundary region in both phases which when coupled with the downwelling in that area, was responsible for the warm water there. The temperature patterns for the levels at 500 and 1300 meters resemble their counterparts from phase I (Figure 35 and 36) with the same basic variations as were seen in the upper level. The maximum in the temperature in the northeast corner has moved south about 800km as the region of sinking motion moved. The isotherms show no unexpected results and will not be depicted here.

The vertical motion patterns play an important part in the adjustment of temperature patterns in the boundary regions. Strong vertical motions occur there due to the thermal circulation. A region of sinking water near 40N

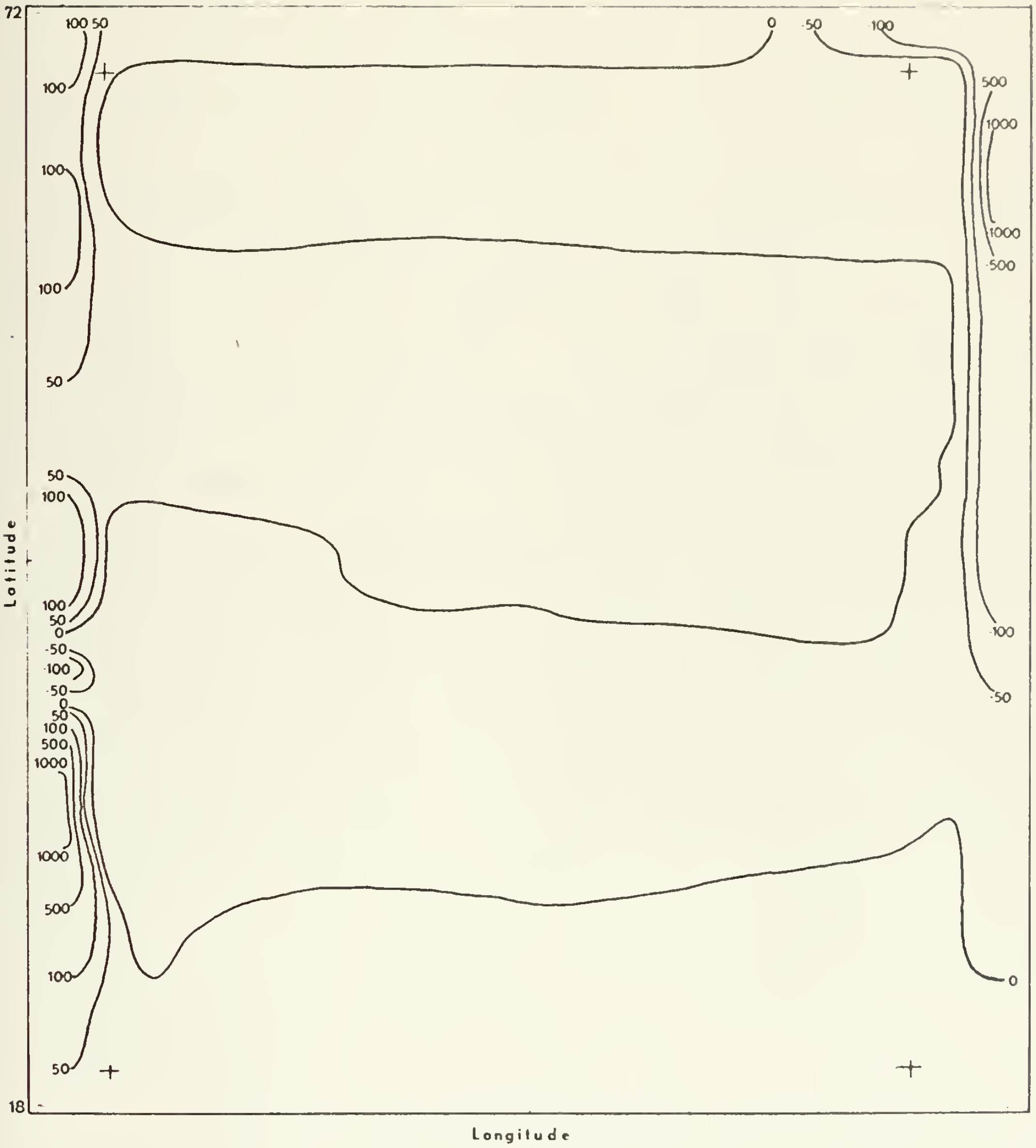

Figure 41. Vertical motion in cm day^{-1} at 300 meters at day 28,900 of phase II. Positive indicates upward motion.

in the western boundary region causes the weak gradient between the 12C and 14C isotherms. The isotherms along the western boundary are shifted southward. That is, the 14C isotherm in the ocean-only model is at the latitude at which the intermediate 15C line (not drawn) was in the combined model.

Figure 42 shows the stream function field for the ocean-only model at day 28,900. It was also found unnecessary to compute a time mean of this quantity. The subarctic gyre and the subtropical gyre both appear to be slightly further north in the ocean-only model than they are in the combined model (Figure 33). Those gyres have about the same intensity in the western boundary region as the corresponding gyres in phase I. This was expected since a mean stress from the combined model was their driving mechanism. The northwestward flow on the east side of the subarctic gyre is still present and causes some warm water to be advected, but at this time the large amplitude ridge that was observed in phase I was not present. The ocean-only sea surface temperature appears to be strongly tied to the imposed zonal atmospheric temperature, except in the western boundary region and to a lesser degree in the eastern boundary region.

The maximum value of the meridional current is reduced somewhat in the ocean-only model. In the western boundary region, the maximum meridional velocity is 47 cm sec^{-1} in the ocean-only model compared to 51 cm sec^{-1} in

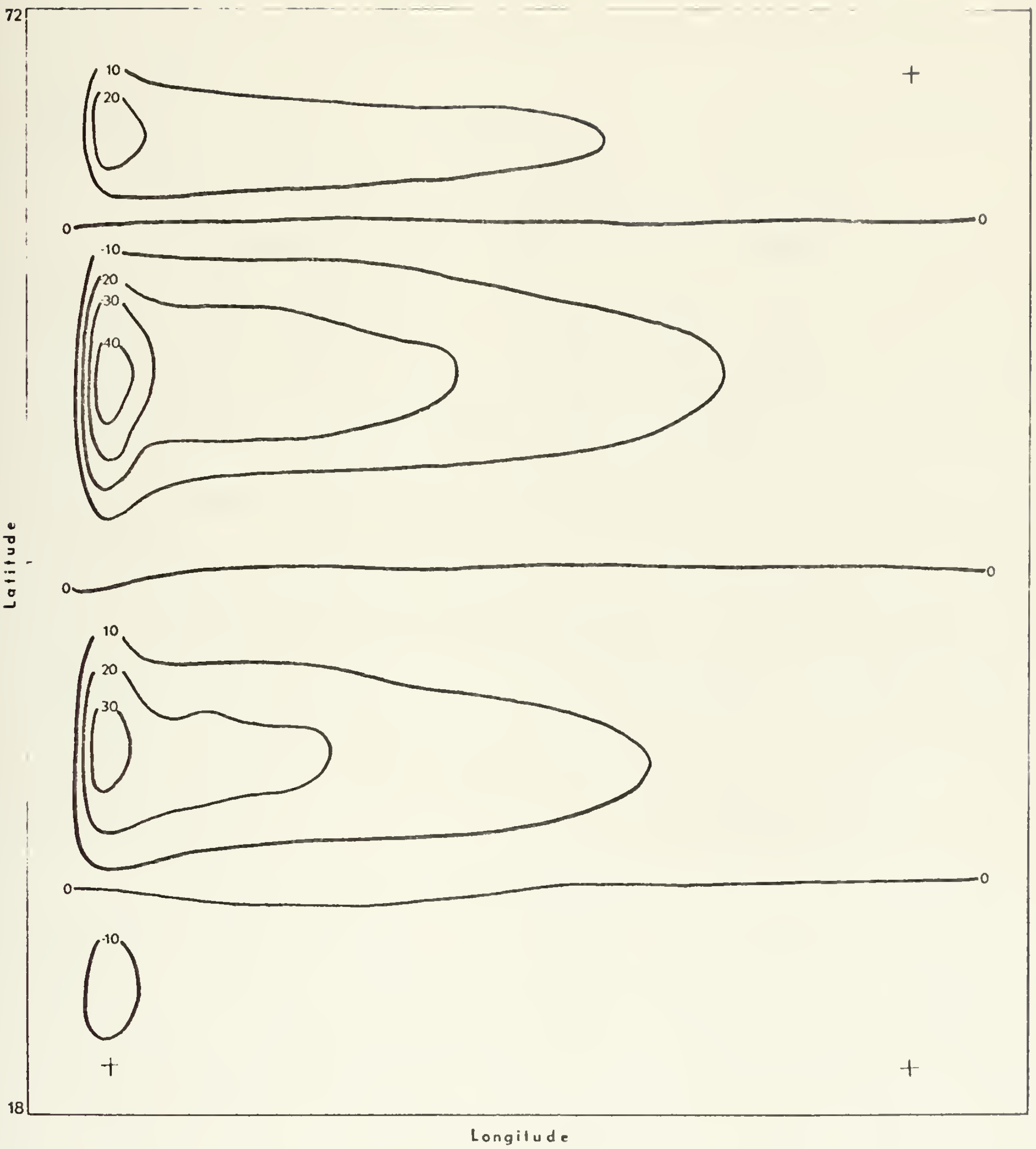

Figure 42. Stream function pattern at day 28,900 in phase II.

the combined model. Since the vertical mean current appears about the same in both models, the difference is in the vertical shear current. The difference in the predicted ocean variables between the ocean-only and combined model phases is small. Radical changes did not occur. The differences that are present are due to the removal of the time varying atmospheric forcing mechanism in both the exchange of momentum and heat in the ocean-only model.

4. The Atmosphere-Only Model (Phase III)

The zonal part, $\overline{T_{sea}}^{x}$, of the combined model sea-surface temperature was averaged over the same 100 day period as were the zonal stress and atmospheric surface temperature. This quantity was used as the underlying temperature with which the atmospheric temperature was compared for the calculation of the vertical flux of sensible heat. Figure 43 shows the profile of the time and longitudinal mean of sea surface temperature, $\overline{\overline{T_{sea}}^{x}}^{t}$, which closely resembles the mean atmospheric temperature shown in Figure 39.

The initial conditions for phase III were the Fourier coefficients, A through F, from day 26,700 of phase I. There was essentially no adjustment required and the 2200 day integration was conducted, with data retained as before, in a minimum of computing time. At the end of this phase the mean state of the atmosphere over the last 100 days was examined along with the state of the atmosphere from day 28,900. These maps were compared with the atmosphere at the end of phase I.

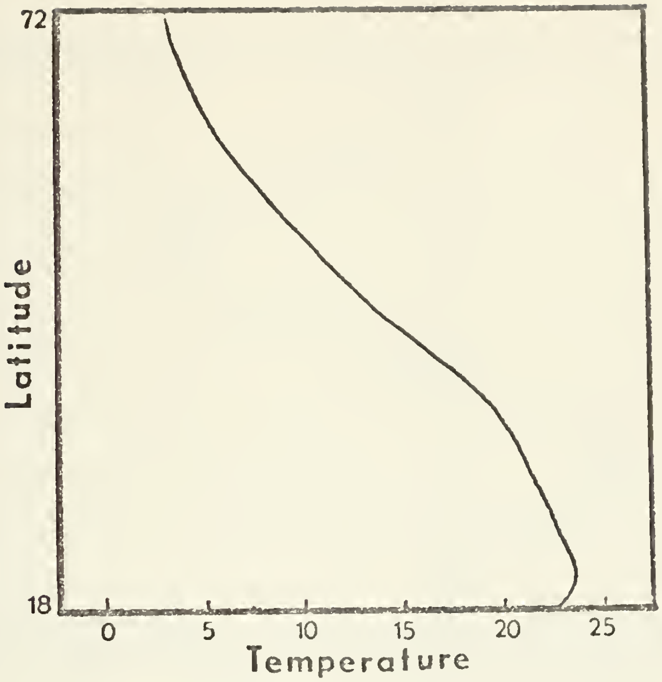

Figure 43. 100 day mean zonal component of sea surface temperature (C).

Figure 44 shows the 100 day mean distribution of the 1000 mb height deviation as a function of latitude. Since the thermal forcing is now a function of y only, the mean fields are purely zonal (with the exception of small errors due to averaging and truncation). The deviation in height extends from 18 meters at 35N to -28 meters at 54N and the deviation pattern is such that a geostrophic wind regime of easterlies, westerlies, easterlies would exist (as it does). Figure 45 shows the 100 day mean distribution of

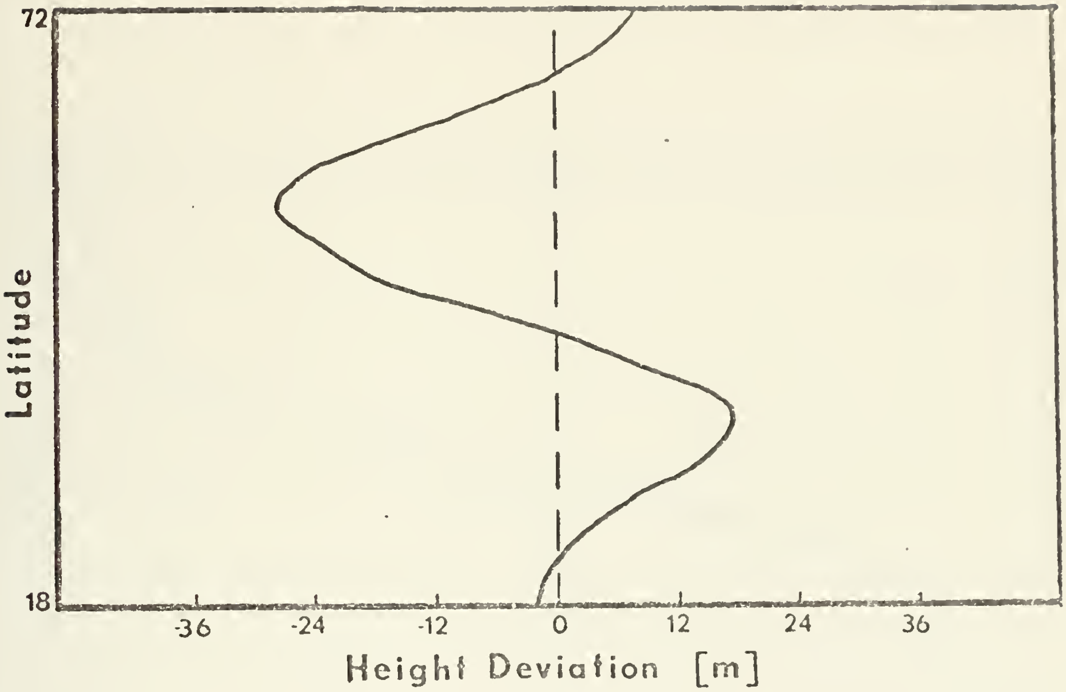

Figure 44. Distribution of 100 day mean 1000 mb height deviation as a function of latitude.

the 750 mb height deviation as a function of latitude. The deviation goes from 118 meters at the southern boundary to -120 meters at the northern boundary. The tight negative height gradient through the central latitudes agrees with the existence of a regime of westerlies in that area. Figure 46 depicts the distribution of the 100 day mean distribution of the 250 mb height deviation as a function of latitude. The gradient that exists from 410 meters in

the south to-407 meters in the north also agrees with the westerly regime at that level.

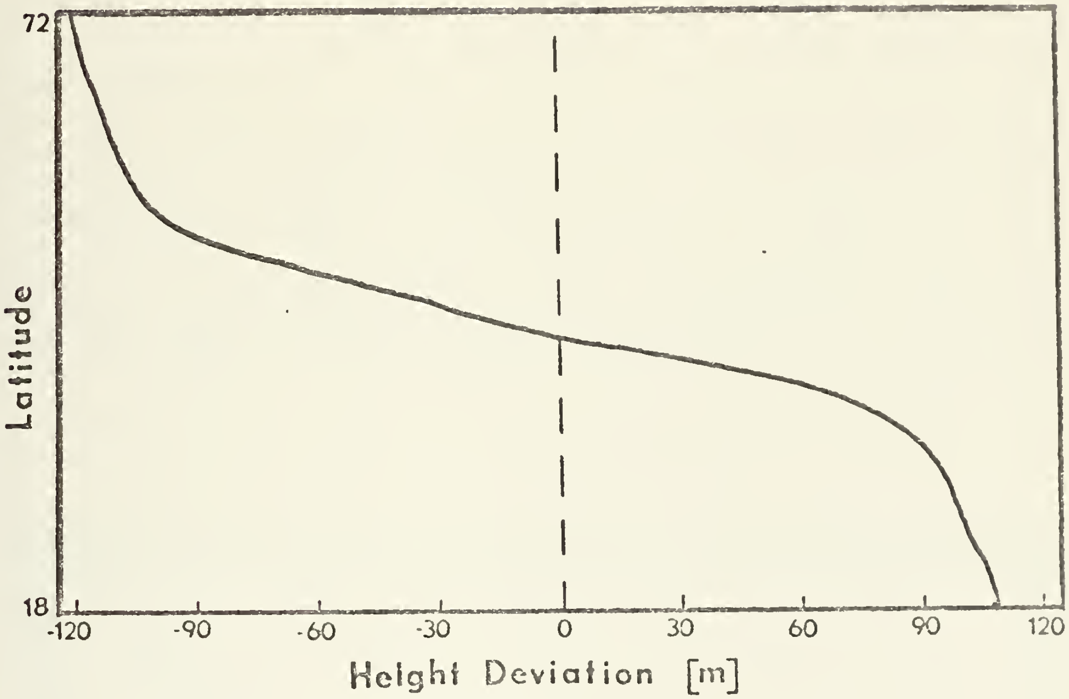

Figure 45. Distribution of 100 day mean 750 mb height deviation as a function of latitude.

Instantaneous maps at day 28,900 of the distribution of the height deviation show a highly disturbed atmosphere. Figure 47, the 1000 mb height deviation field at day 28,900 analyzed at 25-meter intervals, shows a pattern that has a disturbance amplitude which is about the same as its counterpart in the combined model (Figure 28). Figure 48 shows the distribution of the 250 mb height deviation

analyzed at 60 meter intervals. This flow is quite similar to that at the same level at the same time from the combined model (Figure 29). Figure 49 depicts the distribution of the 750 mb height deviation analyzed at 30 meter intervals. The wave-like structure here has a greater amplitude and the deviation is larger than the same fields in the combined model (Figure 30). The occurrence of the difference in the amplitude of the patterns is not surprising since the model atmosphere is continuously changing. It would be a coincidence if the structure of both the atmosphere-only and combined model atmosphere were identical at any given time.

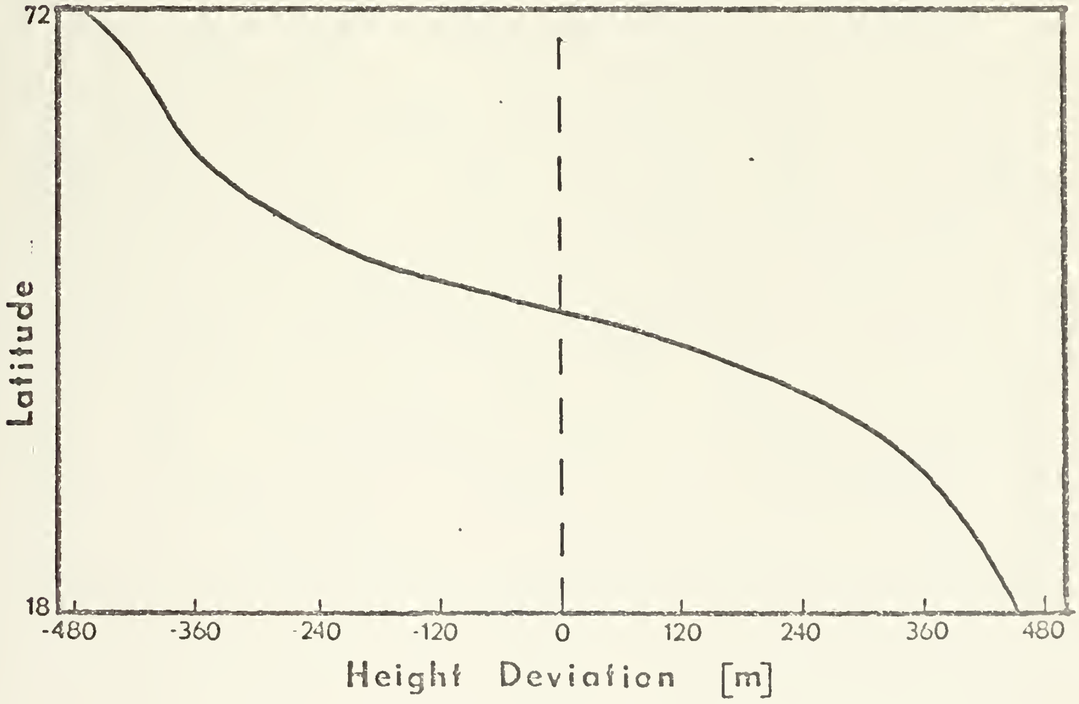

Figure 46. Distribution of 100 day mean 250 mb height deviation as a function of latitude.

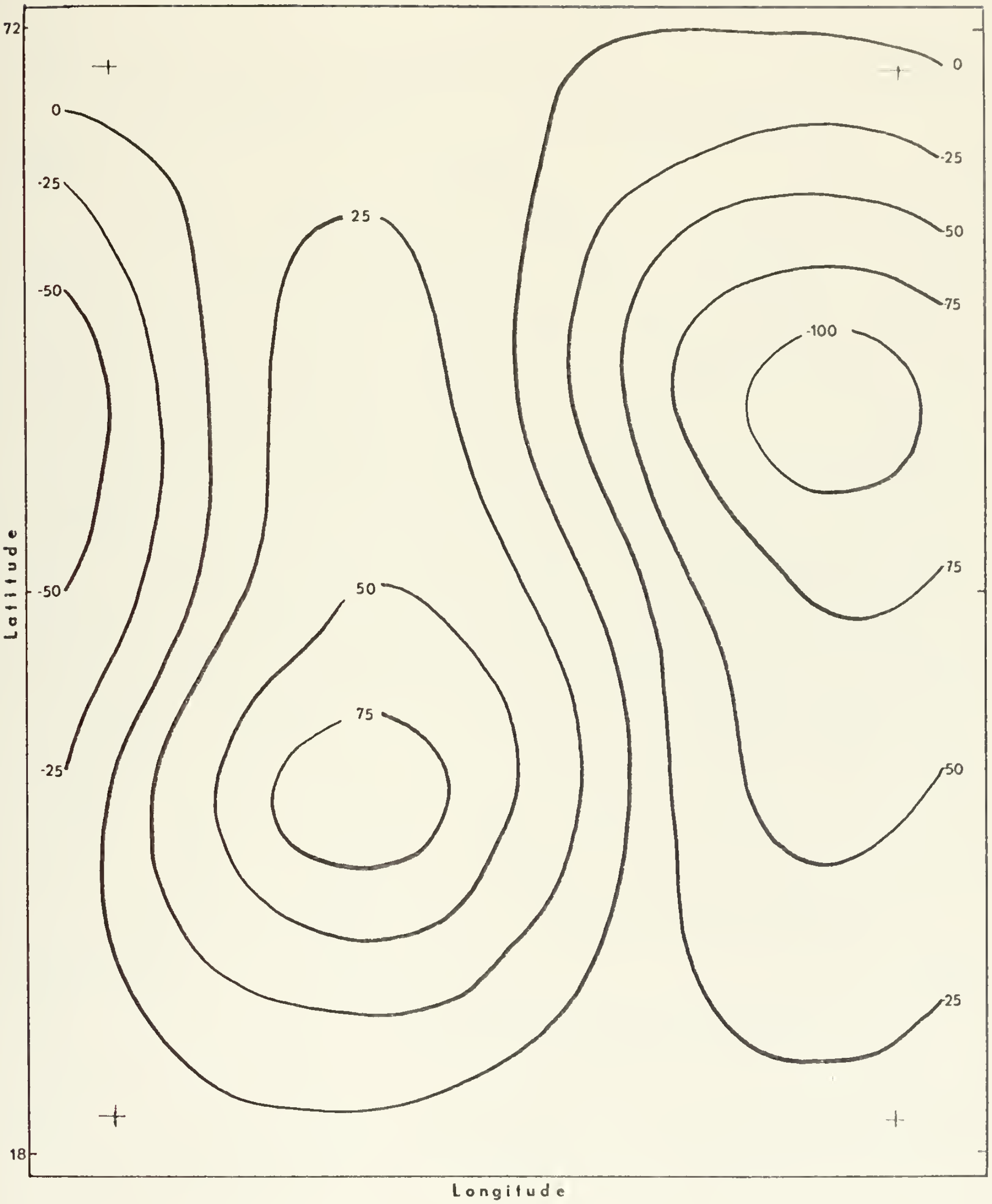
72
18
Latitude
Longitude
0
-25
-50
-50
-25
25
50
75
0
-25
-50
-75
-100
-75
-50
-25

Figure 47. Distribution of 1000 mb height deviation at day 28,900 in phase III.

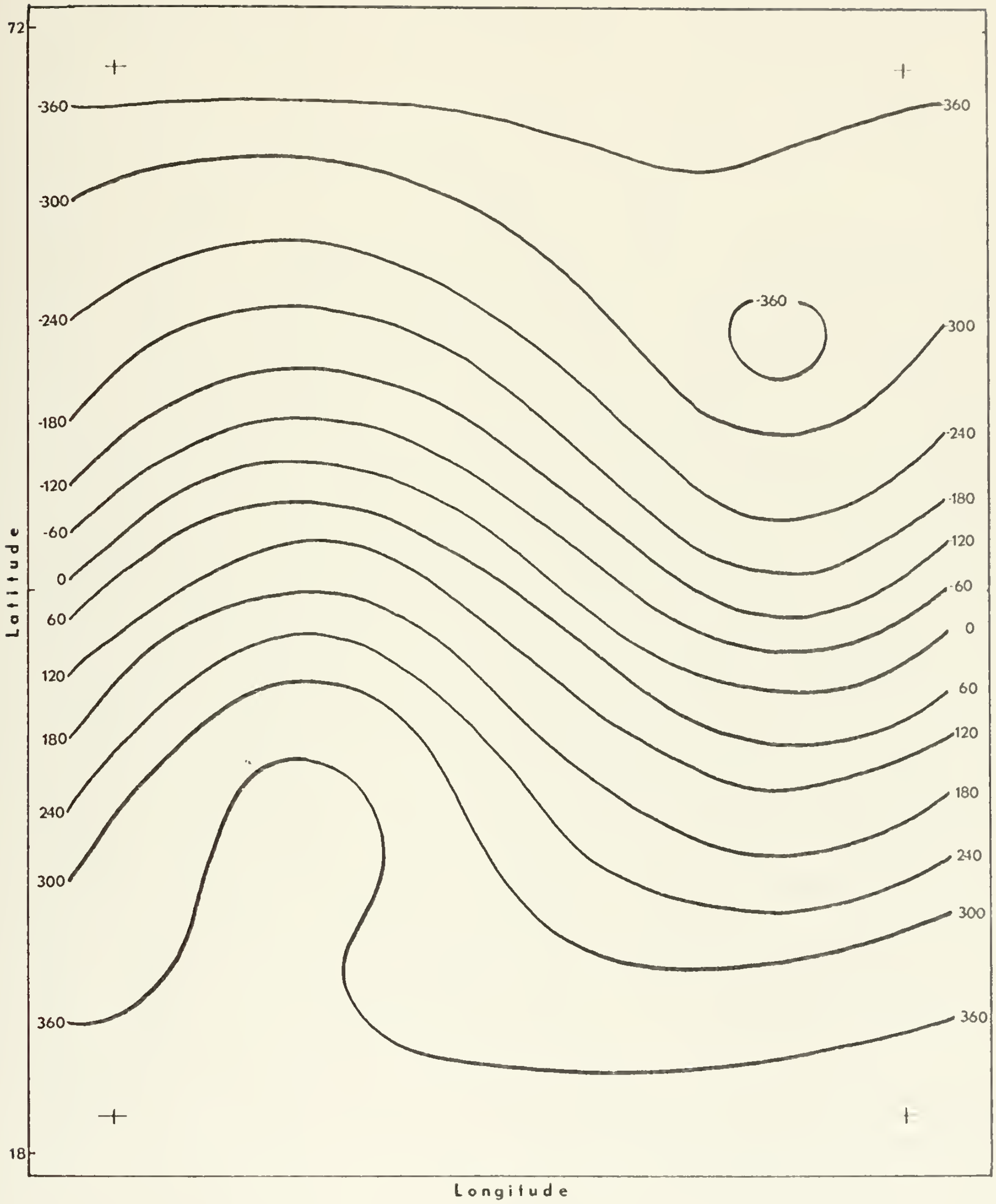

Figure 48. Distribution of 250 mb height deviation at day 28,900 in phase III.

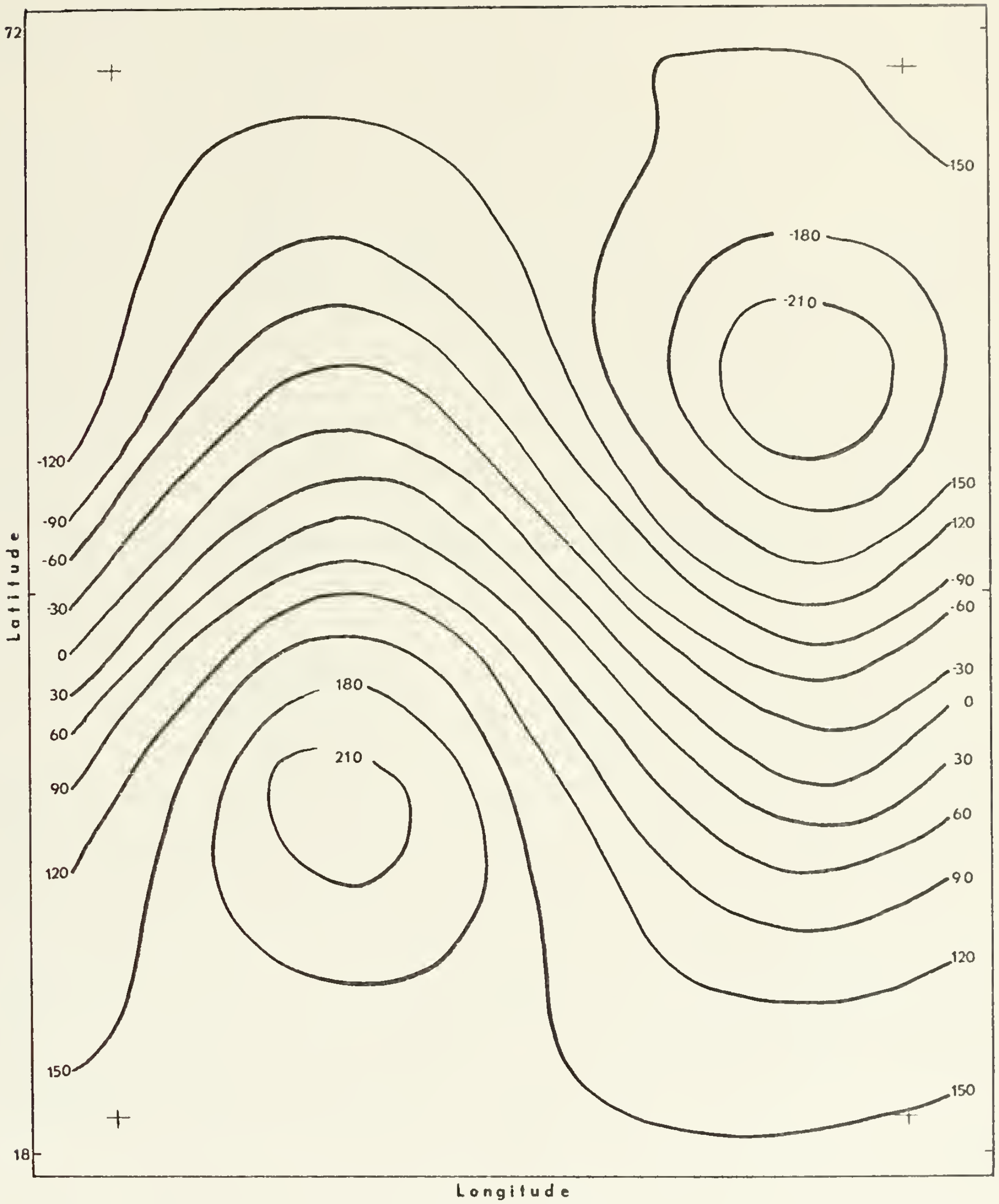
72
18
Latitude
Longitude
-120
-90
-60
-30
0
30
60
90
120
150
180
210
-180
-210
150
120
-90
-60
-30
0
30
60
90
120
150

Figure 49. Distribution of 750 mb height deviation at day 28,900 in phase III.

The 100 day average zonal wind profile in the atmosphere-only model is very similar to that in the combined model shown in Figure 27. A very slight reduction in the jet maximum at 250 mb is the only difference so the atmosphere-only wind profile will not be presented graphically.

The time averaged results of the atmosphere-only phase of the experiment were very similar to the time averaged atmospheric state arrived at by the combined model. Since the sea surface temperature is a slowly varying parameter compared to the atmospheric time scale, holding it constant approximates long term actual conditions fairly well. It would be surprising if a radical change occurred in the time averaged fields in the atmosphere-only formulation.

5. Energy balance

An examination of the energy in the atmosphere was made at the completion of phase I and phase III. Rather than study instantaneous values of the energies and energy transformation as was done in the earlier discussion of the energy balance, values averaged over the last 100 days of the experiment were examined. The energy flow convention as established in Figure 4 was used.

The mean energy exchanges for the combined model and the atmosphere-only model are shown in Figures 50 and 51, respectively. It is interesting to note the similarity in the flow diagrams in the two phases. The diabatic heating generates about the same amount of zonal potential

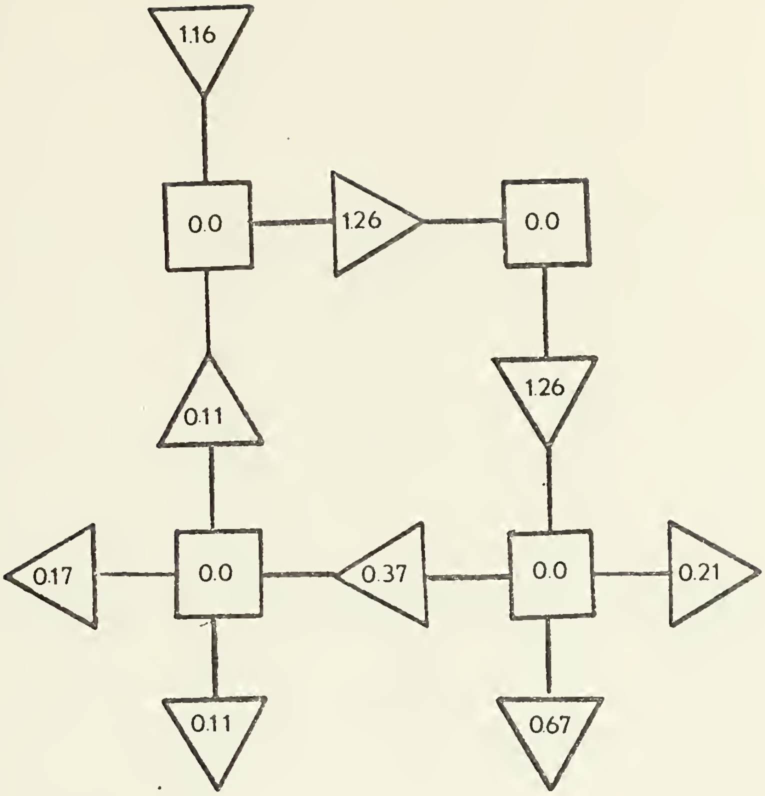

Figure 50. Flow diagram of mean atmospheric energy from the combined model. Energy and energy transformation units are in watt m^{-2} (= 10^{3} erg cm^{-2} sec^{-1}).

energy in both cases, 1.16 watt m^{-2} in phase I and 1.19 watt m^{-2} in phase III. The conversion of zonal potential to eddy potential and then into eddy kinetic energy is identical in both phases at a value of 1.26 watt m^{-2}. The conversion of eddy kinetic to zonal kinetic energy is also

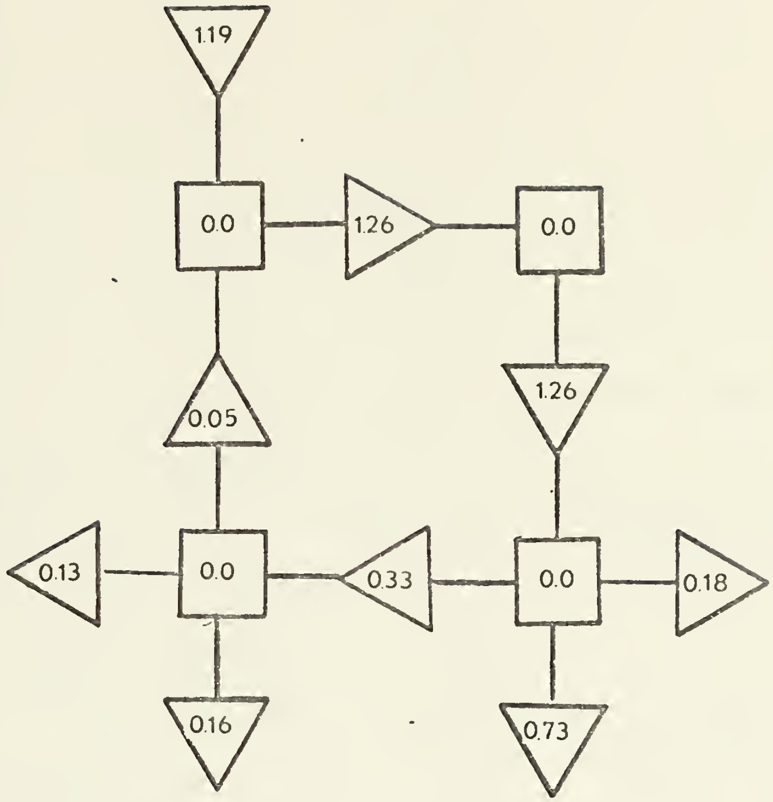

Figure 51. Flow diagram of mean atmospheric energy from the atmospheric-only model. Same units as in Figure 50.

very similar in the two phases with values of 0.37 and 0.33 watt m^{-2}. The dissipation of the kinetic energy (both zonal and eddy) by both internal and surface friction are also very similar. The only conversion that differs by a significant percentage is the conversion of zonal kinetic to zonal potential energy. However, this has been pointed

out earlier as being a very small quantity and no comment on the difference between the two phases is offered here.

It is not surprising that these flow diagrams resemble each other. The only difference in the two models lies in the method by which heat is exchanged between the atmosphere and ocean or underlying wet surface as the case may be. In the calculation of the sensible heat flux necessary for the generation of zonal potential energy in the combined model only the zonal part of the sea surface temperature was used. Therefore, when the disturbance part of the sea surface temperature was neglected in the atmosphere-only model, it did not affect the generation of energy very much. In the other energy exchanges the differences in the disturbance quantities were not sufficient to make much difference.

These diagrams compare favorably with Oort's diagram (Figure 6) as did the earlier energy diagram (Figure 5). The dissipation of eddy kinetic energy is still too low and no new explanation is offered for this. It is somewhat surprising that the instantaneous values of the energy exchange shown in Figure 5 compare so favorably with Figures 50 and 51 in so many ways. The fact that the time rate of change of kinetic and potential energy (both zonal and eddy) were other than zero in that case shows that either there were small errors in calculations, or an exact steady state in the energies did not exist, as was stated in the

earlier discussion. This is in accord with present knowledge of the real atmosphere which is never in exact steady state.

B. SPECTRUM ANALYSIS

This section will briefly discuss the spectrum analysis techniques used in this study. A computer program in the BIOMEDICAL series (BIMED 02T) developed at the UCLA Medical Center (Dixon 1970) was modified and utilized for all spectral analyses conducted on the data generated in this study.

1. Basic Definitions

Prior to discussing the procedures used or the results obtained, a brief review of the definition of some of the basic statistical parameters is given.

a. Variance - the mean square deviation from the mean of a variate.

b. Standard deviation - the positive square root of the variance, used to measure the degree of variability of a variate.

c. Auto-correlation coefficients - linear correlation coefficients between a time series and the same time series an interval of time later.

d. Auto-covariance - an auto-correlation function that has not been normalized by the variance.

e. Cross-correlation - correlation between two time series, one of which is at an interval of time later.

f. Cross-covariance - a cross-correlation function that has not been normalized by the variance.

g. Power spectrum of time series - a function of frequency which gives the contribution of oscillations at each frequency to the variance of a time series.

h. Cospectrum - a function of frequency which gives the contribution of oscillations at that frequency to the total cross-covariance of two time series.

i. Quadrature spectrum - a function of frequency which gives the contribution of oscillations at that frequency to the total covariance of two time series X(t) and Y(t) obtained when all the harmonics of time series X were delayed by a quarter period but the Y series remained unchanged.

j. Phase - the relative phase of the harmonics X(t) and Y(t) is measured by the ratio of the quadrature spectrum to the cospectrum.

2. Spectral Techniques

Many investigators (for example, Yanai et al, 1968; and Wallace 1971) have utilized spectral techniques to study tropospheric phenomena primarily in areas of sparse data where a single station's time varying record is extremely important. The same type of spectral techniques can be used to study the atmospheric and oceanic data obtained from the numerical integrations conducted in this study. At five selected points (Figure 20) six years of

data were recorded at 1.125 day intervals. At each point 1960 observations were obtained. These data were analyzed and a power spectrum was obtained for most variables at all five points. Cross-spectrum analyses were conducted on several variables yielding cospectra, quadrature spectra and phase relationships.

More attention was focused on point C because of its position in the western boundary region. It was located in an area where meridional velocities were strong, temperature gradients were tight and upwelling was important. However, the other points in Figure 20 were not neglected and comparisons of the resulting spectral statistics between points were made.

The data were recorded at an interval, $(\Delta t)_d$, of 1.125 days (three oceanic time steps) during the three six-year experiments. That is, the data were available for analysis from the combined, ocean-only and atmosphere-only phases of the experiment. The decision to record data at 1.125 days was a critical one. It would require an excessive amount of storage space to keep a longer record of data at shorter recording intervals and problems could be encountered if the interval was too long. It is important to ensure that the series which is being examined does not contain substantial amounts of variance from frequencies outside the range that can be resolved with the spectra. Spectral information for frequencies less than one cycle/ $2(\Delta t)_d$, the Nyquist folding frequency, can be obtained from

the data. Frequencies higher than this are "folded" or "aliased" into the lower frequency region. Wallace (1971) points out that the high frequency limit does not appear to pose any serious problem from aliasing because there is little variance associated with frequencies higher than 0.5 cycles per day in the intermediate to large scale disturbances. From experimental work Wallace concluded that there were only minor differences in spectra computed with daily or twice-daily data. Since the data examined in this study is of the daily variety, his conclusions, along with the fact that higher frequencies due to advection of short waves cannot exist in the model atmosphere leads the author to believe that the time interval chosen for this data record was a sound one.

In the BIMED 02T program, the power spectrum is obtained by performing a harmonic analysis on the auto-covariance function of the quantity to be studied. After each spectral estimate was multiplied by the interval of frequency (Δf) of the band width, the spectral estimates for that frequency band can be summed to obtain the contribution of the fluctuations within that specific frequency band width to the variance of the time series which is under examination.

3. Results of Spectral Investigation

The primary point of interest in the spectral investigation was point C (Figure 20) in the western boundary region. A thorough investigation of atmospheric and

oceanic variables was conducted at this point with the following results.

a. Study of data at point C.

The data obtained from phase I (combined model) of the experiment were examined first. The Fourier coefficients from the atmospheric part of the combined model were analyzed and Figure 52 shows the power spectrum of A and B (solid line) and C and D (dashed line), obtained from Equations (2.22) to (2.25), plotted on a linear scale against frequency (cycles per day). The power spectra of A and B are identical as are the spectra of C and D. The amplitude of the power spectra of C and D is slightly less than 10% of that of A and B. There is a pronounced peak at about 7.5 days in the power spectra for these quantities. This was expected since the phase speed of the imposed baroclinic disturbance in the combined model was estimated at 600 km per day, a phase speed that would yield a period of 8 days. In all likelihood, the estimate of the phase speed of the disturbance was slightly low. The 7.5 day period indicates that 640 km/day was the speed with which the disturbance moved across the 4800 km wide domain.

Figure 53 shows the power spectrum of atmospheric disturbance kinetic energy. There are some small peaks in the spectra in the frequency band from .08 to .24 cycles per day (12.5 to 4.2 days) but the major peaks are clearly at the lower frequencies. There are peaks at periods of about 32 and 62 days indicating cycles in the

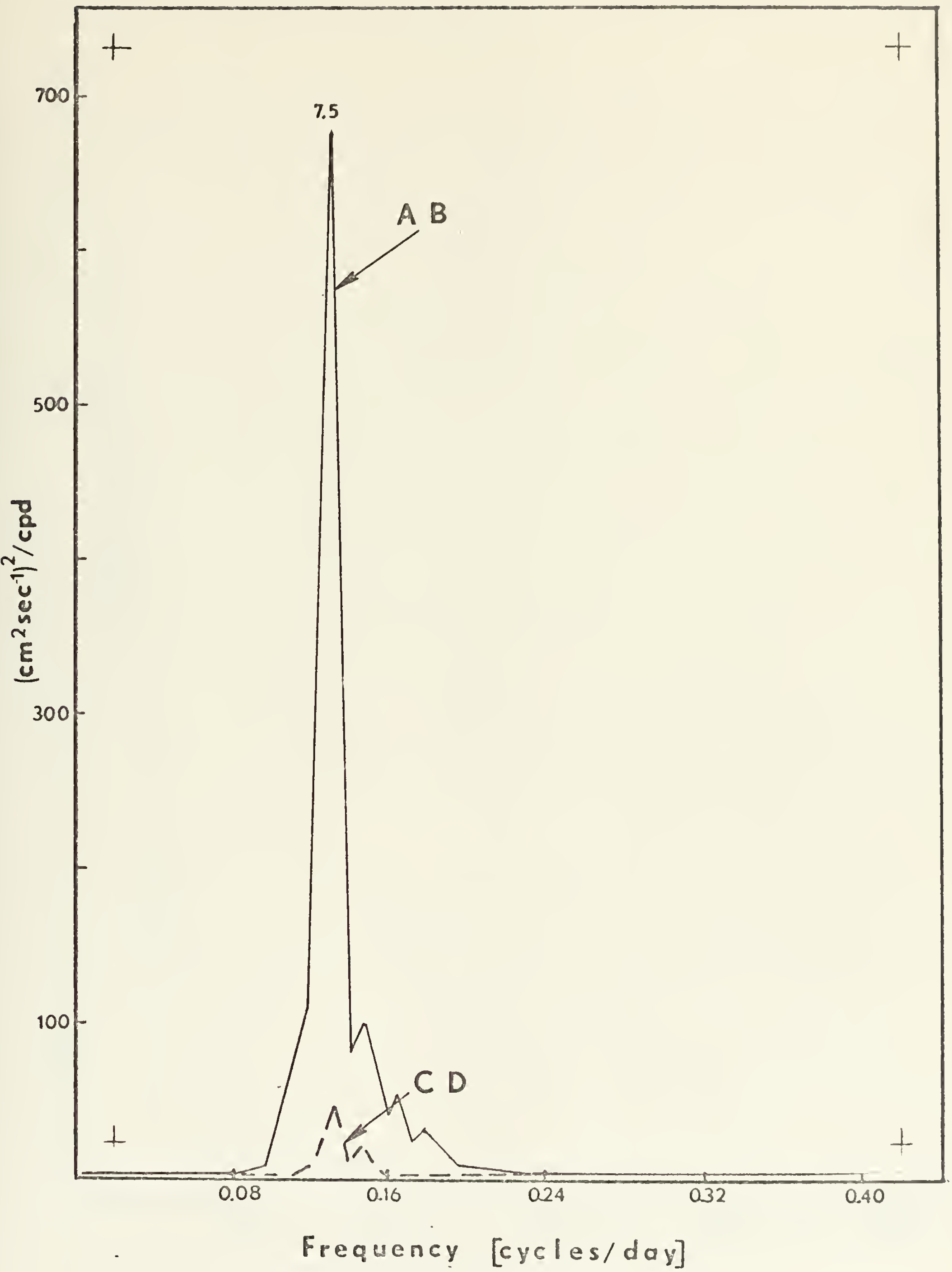

Figure 52. Power spectra of A,B,C and D at point C in phase I. Period of spectral peak indicated in days.

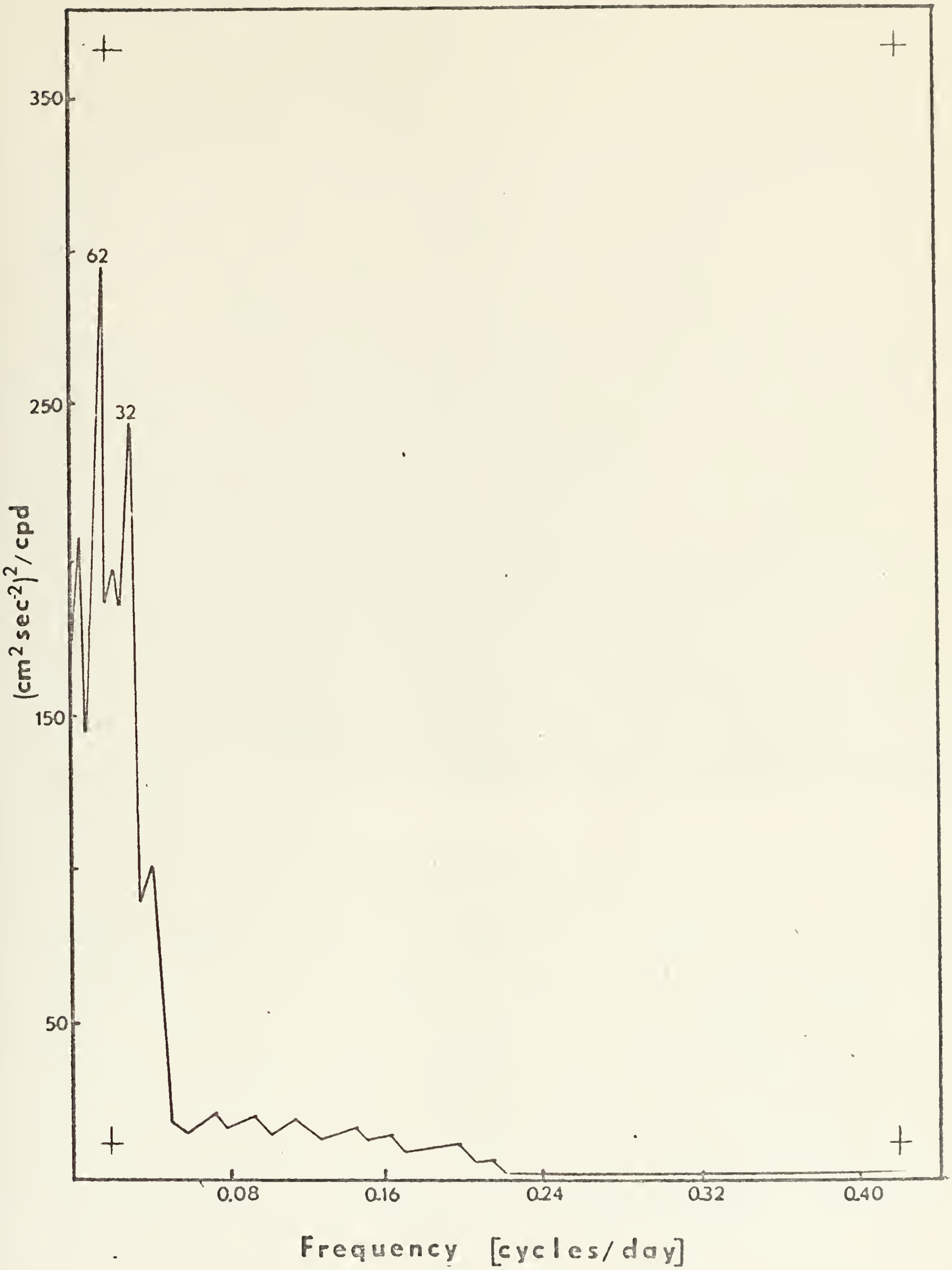

Figure 53. Power spectrum of atmospheric disturbance kinetic energy in phase I. Period of spectral peaks indicated in days.

atmospheric energy on the order of one and two months. If seasonal variations had been included in the specification of the solar radiation and latent heat release, different frequencies of oscillation would probably be observed. The annual fluctuation in the above mentioned parameters would probably be reflected in the energy spectrum.

Figure 54 shows the power pectrum of E, the zonal mean part of ψ_M that is proportional to the mean height and related to the mean geostrophic wind in the atmosphere. The quantity has a large spectral peak at a period of 32 days and smaller peaks at 25 and 62 days. An examination of the cospectrum and phase between E and the disturbance energy shows that the disturbance energy rise at the 32 day period lags the increase in the spectrum of E at that period. This suggests that the mean flow increased first and because of barotropic amplification transferred energy to the disturbance.

Figure 55 depicts the power spectrum of the oceanic stream function. Peaks in the spectra are seen at periods of 7.5 days (small), and 32 and 62 days (large). This is the first quantitative indication of an air-sea interaction phenomenon in the model. The 7.5 day peak in the power spectrum of the stream function is caused by the contribution of the A and B coefficients to the disturbance component of the atmospheric wind stress (Figure 52). Since the disturbance components of the stress are small the fluctuations they cause are small and therefore the peak in

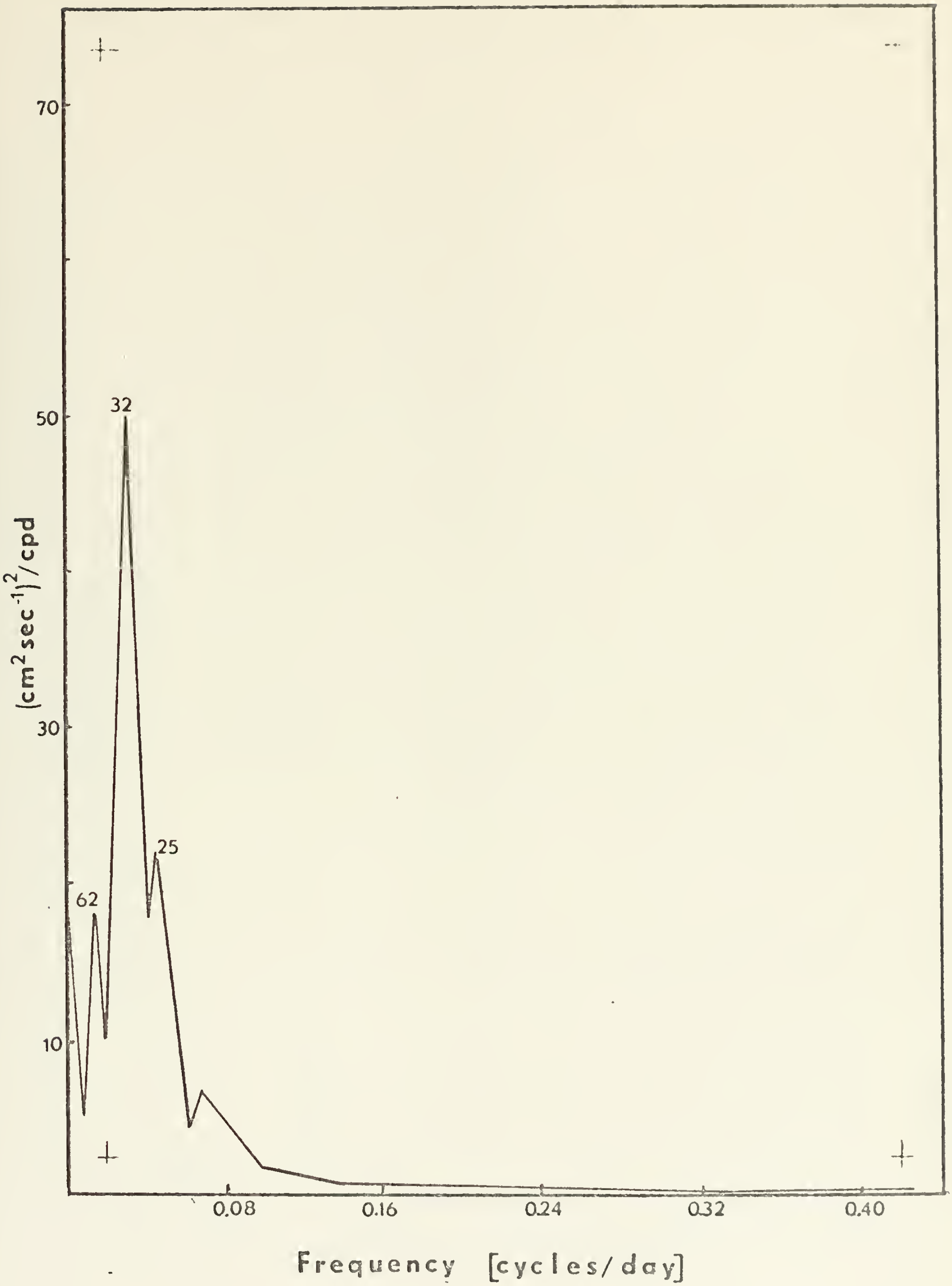

Figure 54. Power spectrum of E at point C in phase I. Period of spectral peaks indicated in days.

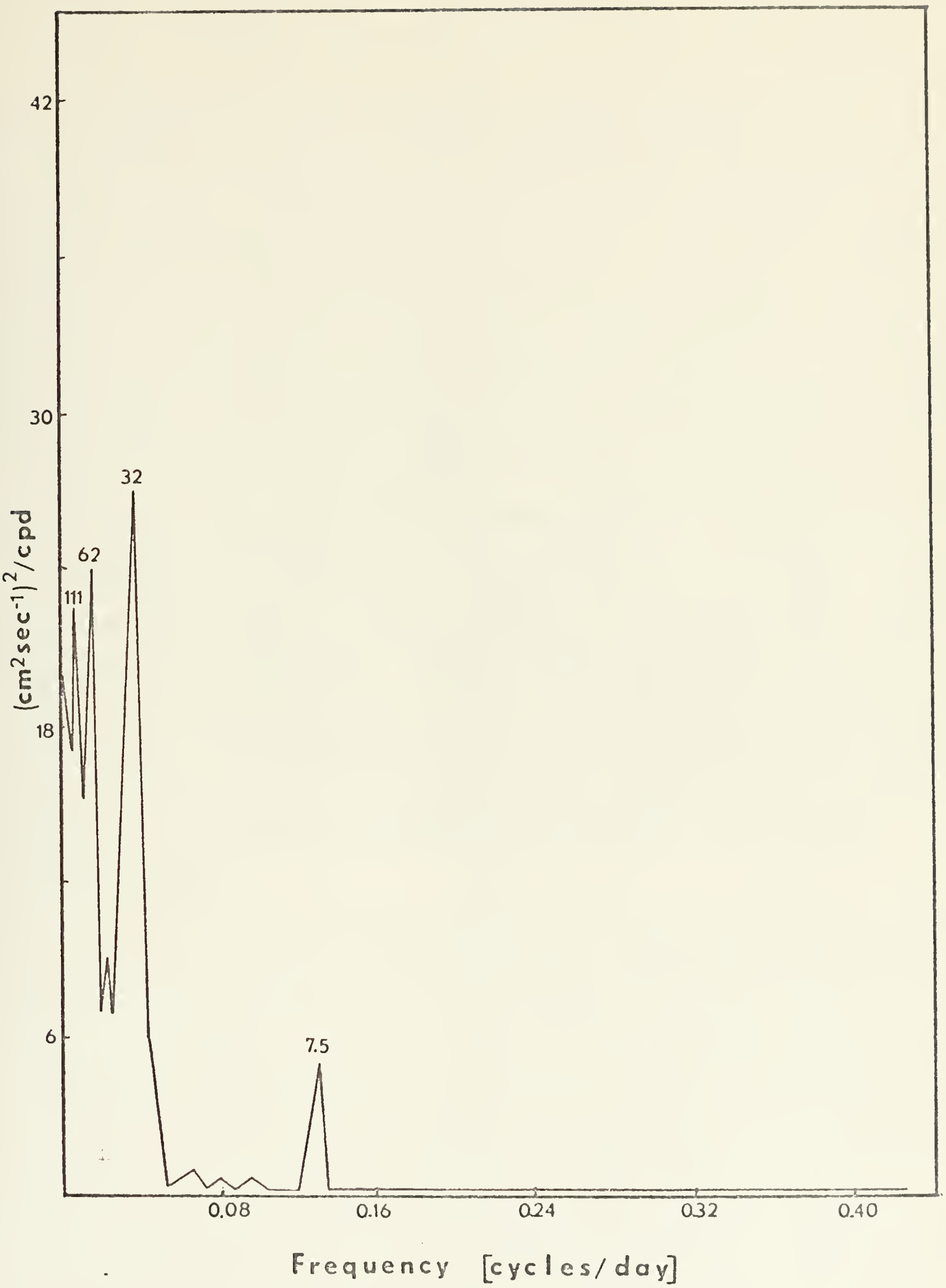

Figure 55. Power spectrum of ocean stream function at point C in phase I. Period of spectral peaks indicated in days.

the spectrum is smaller at this frequency. The larger peaks at about 32 and 62 days are caused by the oscillations in the zonal component of the wind stress which is proportional to E. An examination of the cospectrum and phase between E and the ocean stream function shows that the increase in the mean atmospheric flow occurs 3.5 days prior to the fluctuation in the stream function at the 32 day period. Since E had spectral peaks at these frequencies it is not surprising that peaks in the same region of the spectrum appear in the ocean stream function. Figure 56 shows a 100 day time series of E and the oceanic stream function obtained by averaging the recorded data over seven day intervals. The averaging was done to remove the 7.5 day oscillation from the data to examine the longer period fluctuations in more detail. It is easy to see that the long period oscillations are present in both E and the stream function and that the maxima in E leads the maxima in the stream function by several days.

Figure 57 shows the power spectrum of the zonal mean of the atmospheric surface temperature, $\overline{T}_4$. Since $\overline{T}_4$ is proportional to F, the peaks in the spectrum are also representative of peaks in the spectrum of F. This was verified by spectrally analyzing F separately, the plot of which is not presented. There are peaks in $\overline{T}_4$ of almost equal amplitude at 7.5 and 32 days, and smaller peaks at periods of 25, 62 and 111 days. Figure 58 shows the power spectrum of T_{sea}, the sea surface temperature. Small peaks

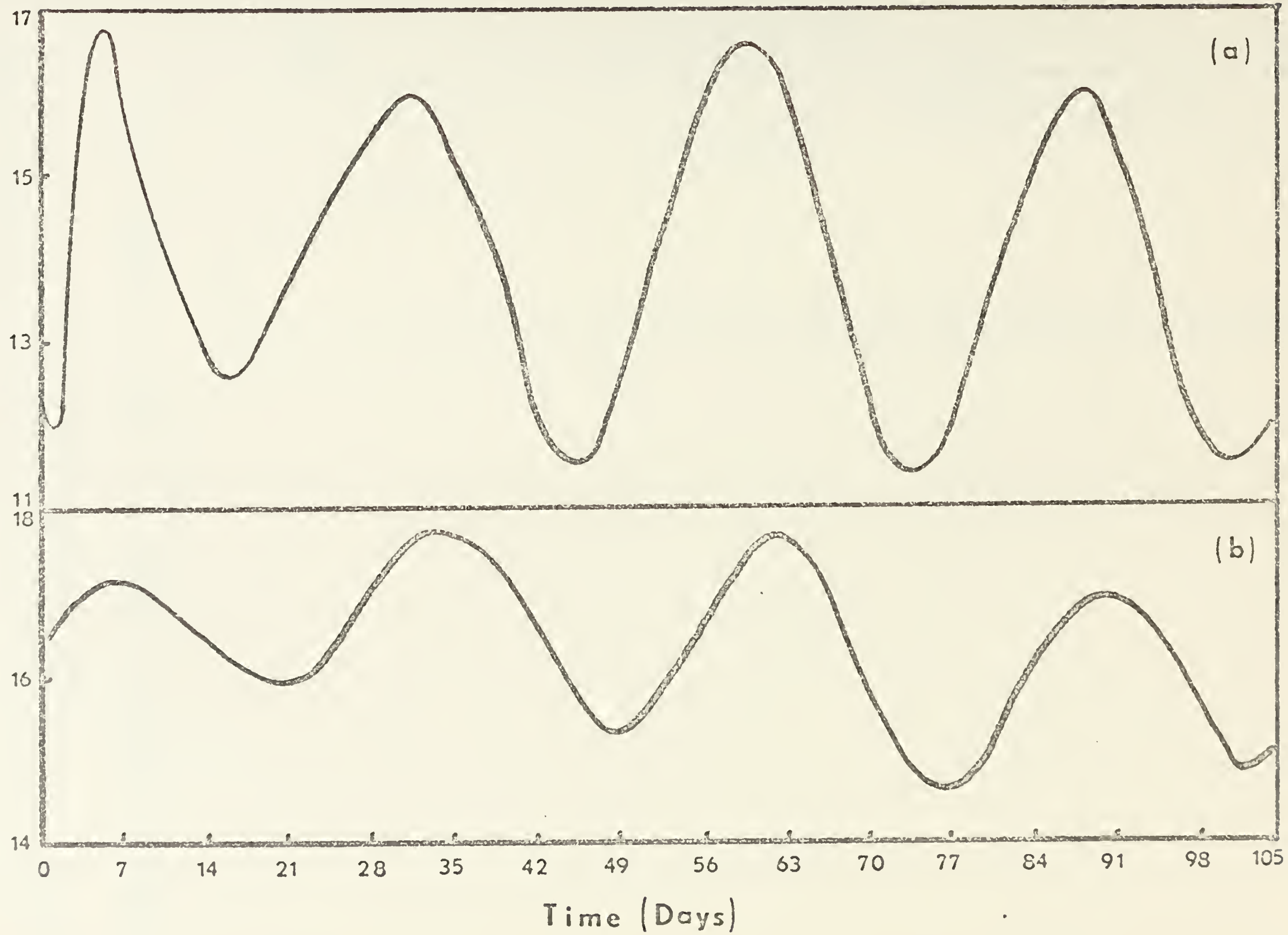

Figure 56. Time series of (a) E, mean part of ψ_M(10^{-10}cm^2 sec^{-1}); (b) oceanic stream function (10^{-7} cm^2 sec^{-1}). Data from point C in combined model.

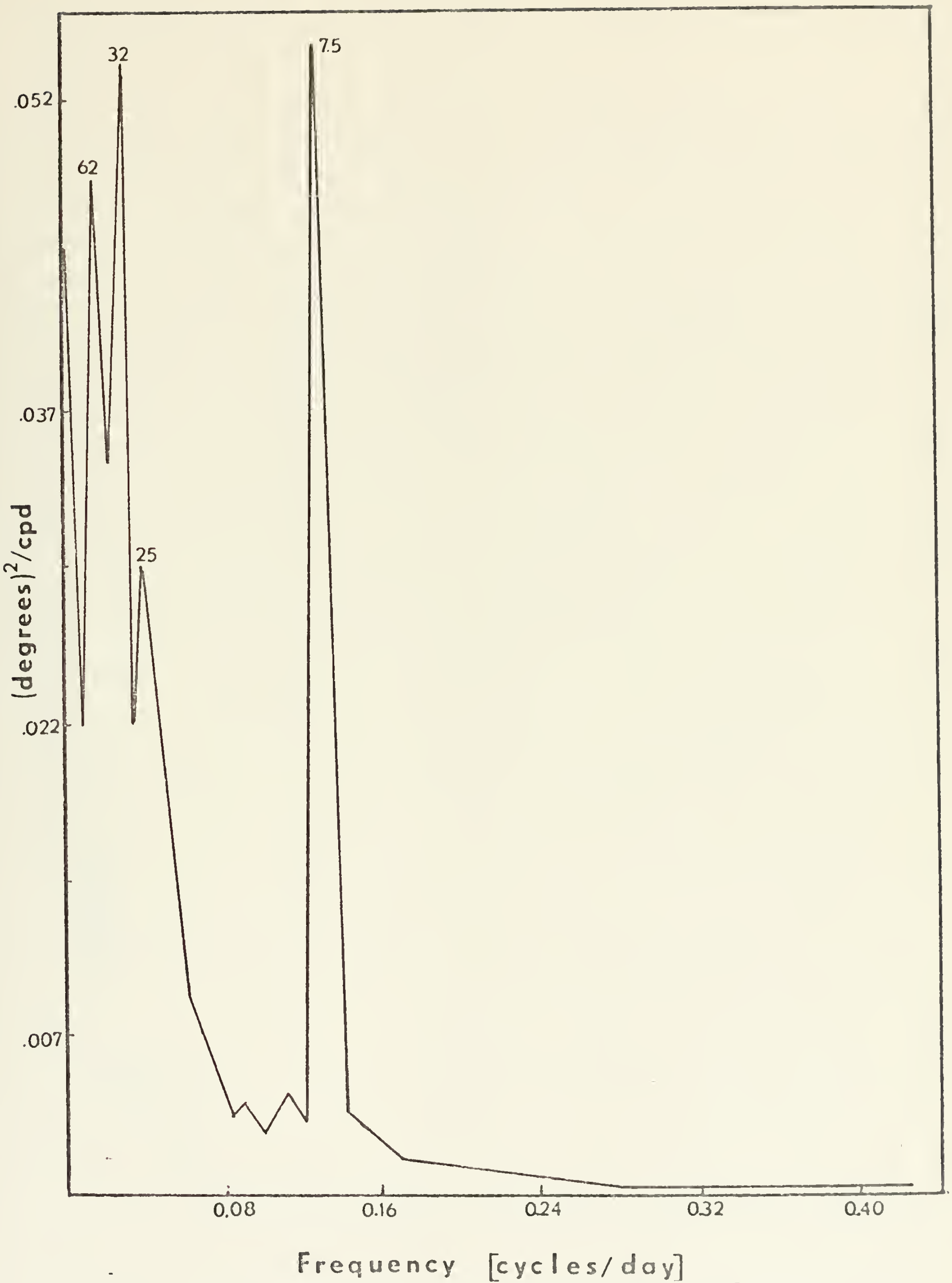

Figure 57. Power spectrum of atmospheric surface temperature at point C in phase I. Period of spectral peaks indicated in days.

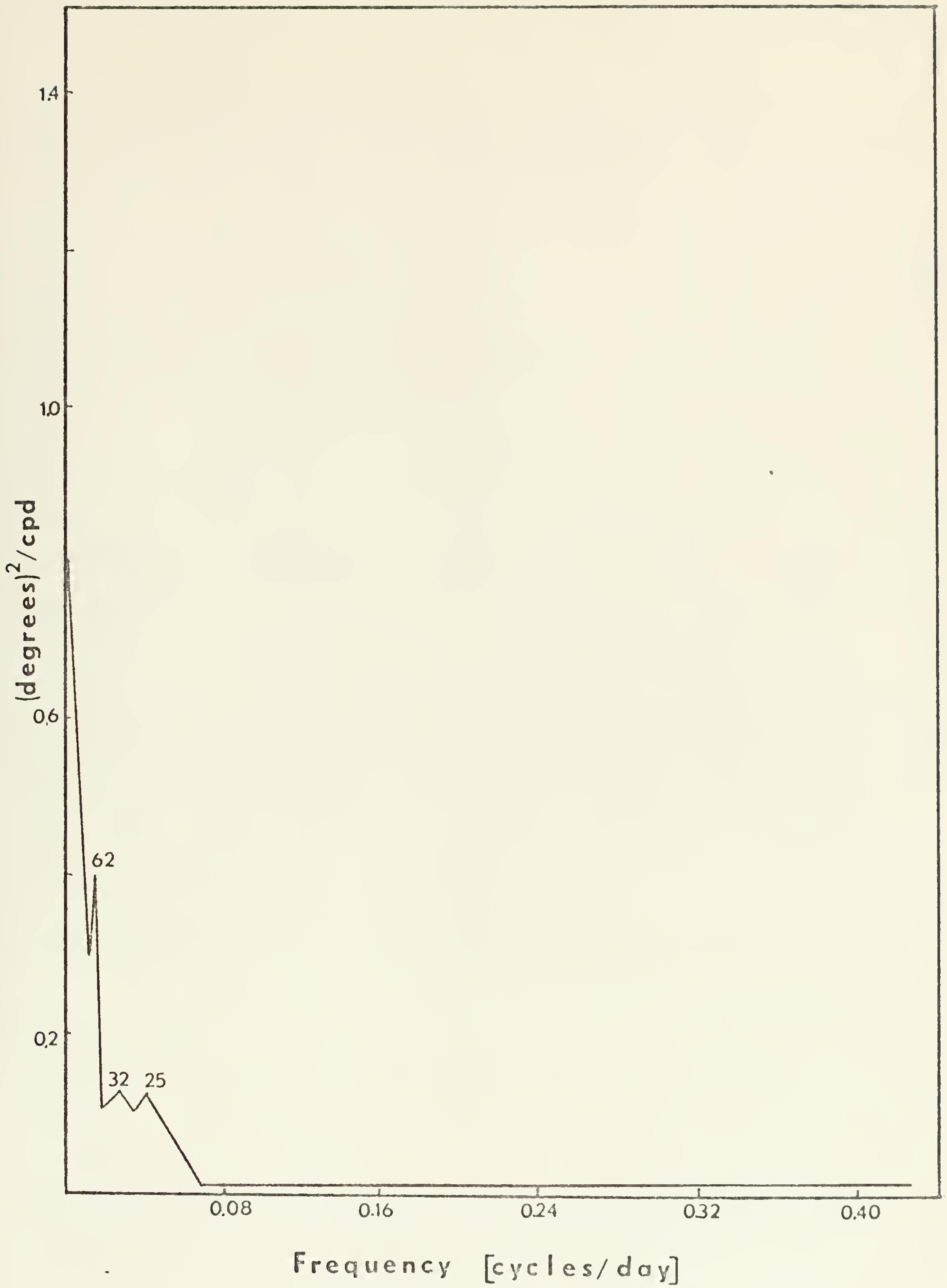

Figure 58. Power spectrum of sea surface temperature at point C in phase I. Period of spectral peaks indicated in days.

can be seen at periods of about 25 and 32 days and a larger peak at a period of about 62 days. These peaks coincide with some of the peaks in the spectrum of $\overline{T}_4$. Figure 59 shows the power spectrum of the vertical heat flux between the atmosphere and the ocean. Peaks in the spectrum occur at 7.5, 32 and 62 days. The longer period peaks are at the same period as the peaks in the atmosphere and ocean surface temperatures, indicating an exchange of heat due to a temperature difference between the two media. A comparison of the time series of the atmospheric surface temperature, the vertical heat flux and the sea surface temperature obtained by averaging over seven day periods is shown in Figure 60. It is readily observed that oscillations on the order of 30 days are present in all three series and not so obvious fluctuations on the order of 60 days are present in the sea surface temperature and the vertical heat flux. It can be seen that peaks in the sea surface temperature led peaks in the vertical heat flux which in turn led peaks in the atmospheric surface temperature.

An examination of the cospectrum and phase between E and T_{sea} shows that the increase in E at about 32 days precedes the fluctuation in sea surface temperature by 11 days. This was perhaps a result of an increase in the mean zonal wind stress causing an increase in the wind driven part of the ocean circulation and an increase in the advection of heat from the south at point C. An examination of the cospectrum of T_{sea} and the ocean stream function

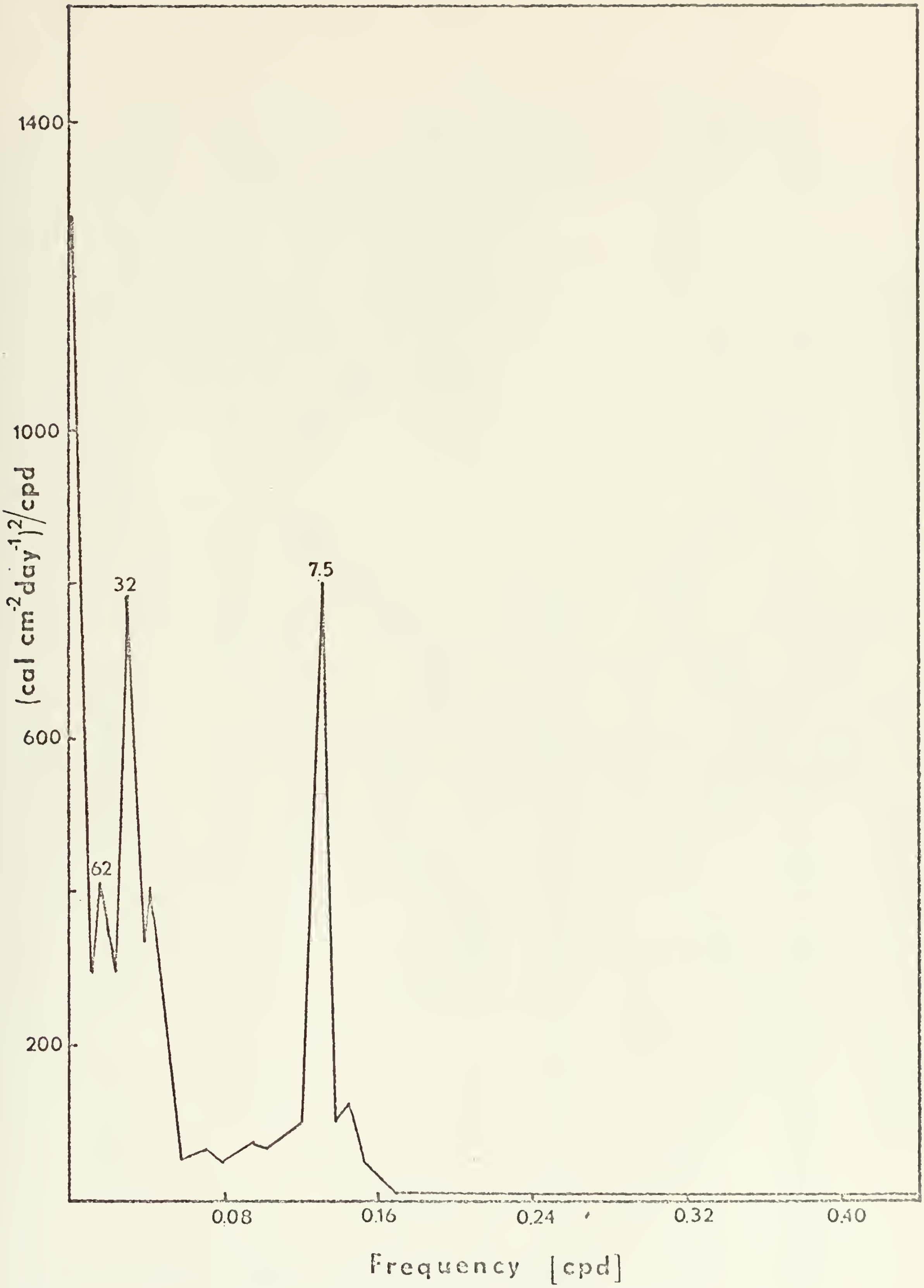

Figure 59. Power spectrum of vertical heat flux at point C in phase I. Period of spectral peak indicated in days.

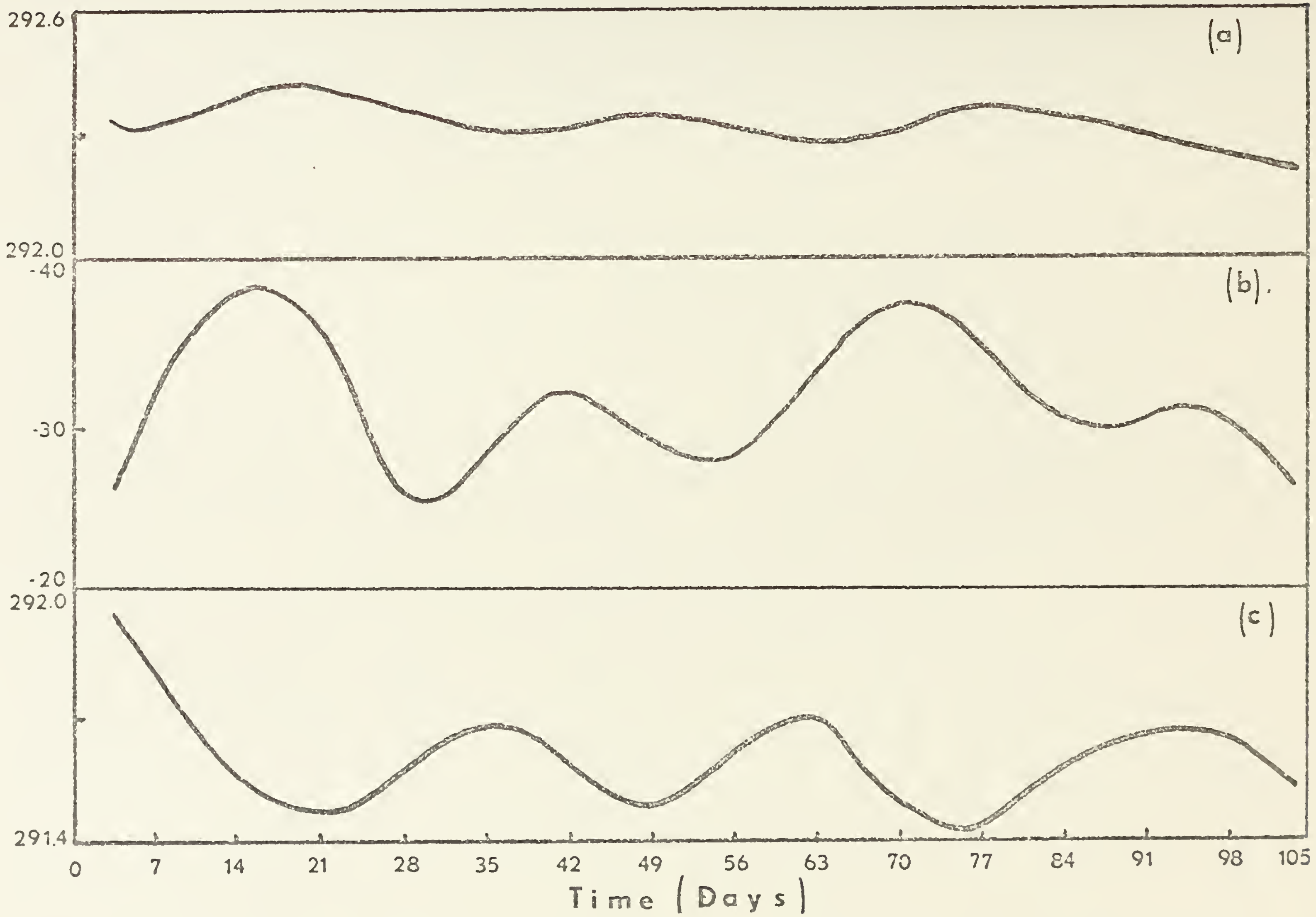

Figure 60. Time series of (a) atmospheric surface temperature(C); (b) vertical heat flux (cal $cm^{-2}day^{-1}$); (c) sea surface temperature(C). Data from point C in combined model.

shows that the fluctuations in the stream function at 32 days occurs 7.6 days prior to the oscillation in T_{sea}. These phase relationships coupled with the previously stated facts leads to the following conclusions. The oscillations which were reflected as peaks in the power spectra of the variables were caused by an air-sea interaction phenomenon and were not merely spurious reflections of energy due to sampling or calculating problems. An explanation of the probable series of events causing these interactions is as follows. The increase in the mean atmospheric flow, reflected in E, caused an increase in the wind driven part of the ocean circulation 3.5 days later. This increased circulation brought about an increase in the advection of heat from the south at point C and an oscillation in the sea surface temperature, at a period of 32 days, occurred 7.6 days later. The total time from the increase in E to the increase in T_{sea} was about 11 days. The increase in T_{sea} caused an increase in the vertical heat flux and an increase in the atmospheric surface temperature. An examination of the cospectrum and phase of T_{sea} and $\overline{T}_4$ shows that the oscillation in T_{sea} at 32 days leads the rise in the spectrum of T_4 by 6.2 days. An exchange of energy between T_4(F) and E is then required to maintain the cycle. An examination of the cospectrum and phase of E and F shows that the peak in F occurs prior to the peak in E at 32 days. When these interactions are taking place in the combined

model and oscillations at various frequencies are present, almost every dependent variable in the model will be affected in some way. It has been shown that the long period oscillations which are present in the coupled model include the ocean as an important part in the oscillation cycle. It should not be surprising to find that these long period oscillations do not exist when either the atmosphere or ocean is held constant in time.

The data from phase II of the experiment were examined next. With the time varying forcing functions removed, the ocean became steady in a short time with no significant peaks in any of the spectra. Figure 61 shows the power spectrum for T_{sea}. This is typical of all the ocean variables in this phase in that the power in the spectrum is in the lowest frequencies. A comparison of Figure 61 and 58 provides a convincing argument that the time varying atmospheric circulation is responsible for the transient responses of the ocean surface temperature at periods of about one and two months.

An interesting, and initially perplexing, peak appeared in the ocean stream function at 7.5 days in the ocean-only data (not shown). The ocean-only model required a period of time to adjust to the new forcing and during that time the stream function oscillated and then became constant. Although the energy in the spectrum was diluted by the long period of constancy, the initial oscillation made itself evident at the frequency at which it fluctuated.

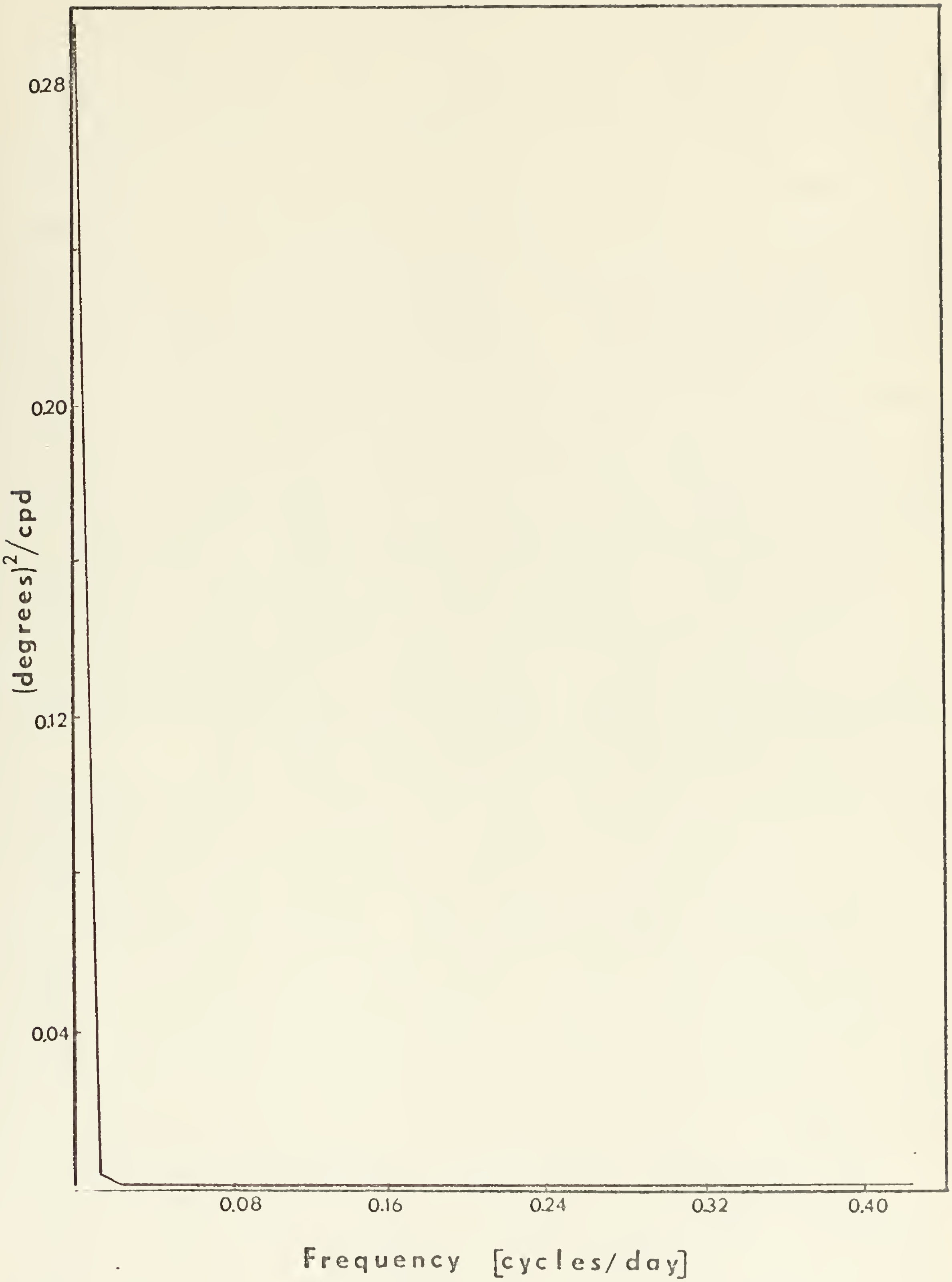

Figure 61. Power spectrum of sea surface temperature at point C in phase II.

The data from phase III (atmosphere-only) were analyzed and Figure 62 shows the power spectra of A and B (solid line) and C and D (dashed line). The four quantities all have a peak at a period of 8.4 days. This is different than the period at which there is a peak in the spectra of the same quantities in the combined model. For the 4800 km wavelength used in this study, a period of 8.4 days yields a phase velocity of 570 km day^{-1}. This is about 12% slower than the phase speed for the atmospheric wave in the combined model. By eliminating the zonal variation in the sea surface temperature, the sensible heat exchange was changed. A comparison of the combined model and atmosphere-only model shows that the thermal wind was reduced in the latter. This reduction in the thermal wind, shown in Table 4, was influential in retarding the phase speed of the disturbance.

The power spectrum of the disturbance kinetic energy is shown in Figure 63. A large peak at the 6.7 period is observed along with a smaller, wider peak in the 45 to 50 day period range. The peak at the 6.7 day period, which is near the 8.4 day period in the disturbance quantities, is perplexing in light of the fact that there is no sharp peak around the 7.5 day peak in the disturbance kinetic energy (Figure 53) in the combined model. A possible explanation is that the 6.7 day peak is very sharp and while it has a considerable amplitude, the total contribution to the variance of the disturbance is not much greater

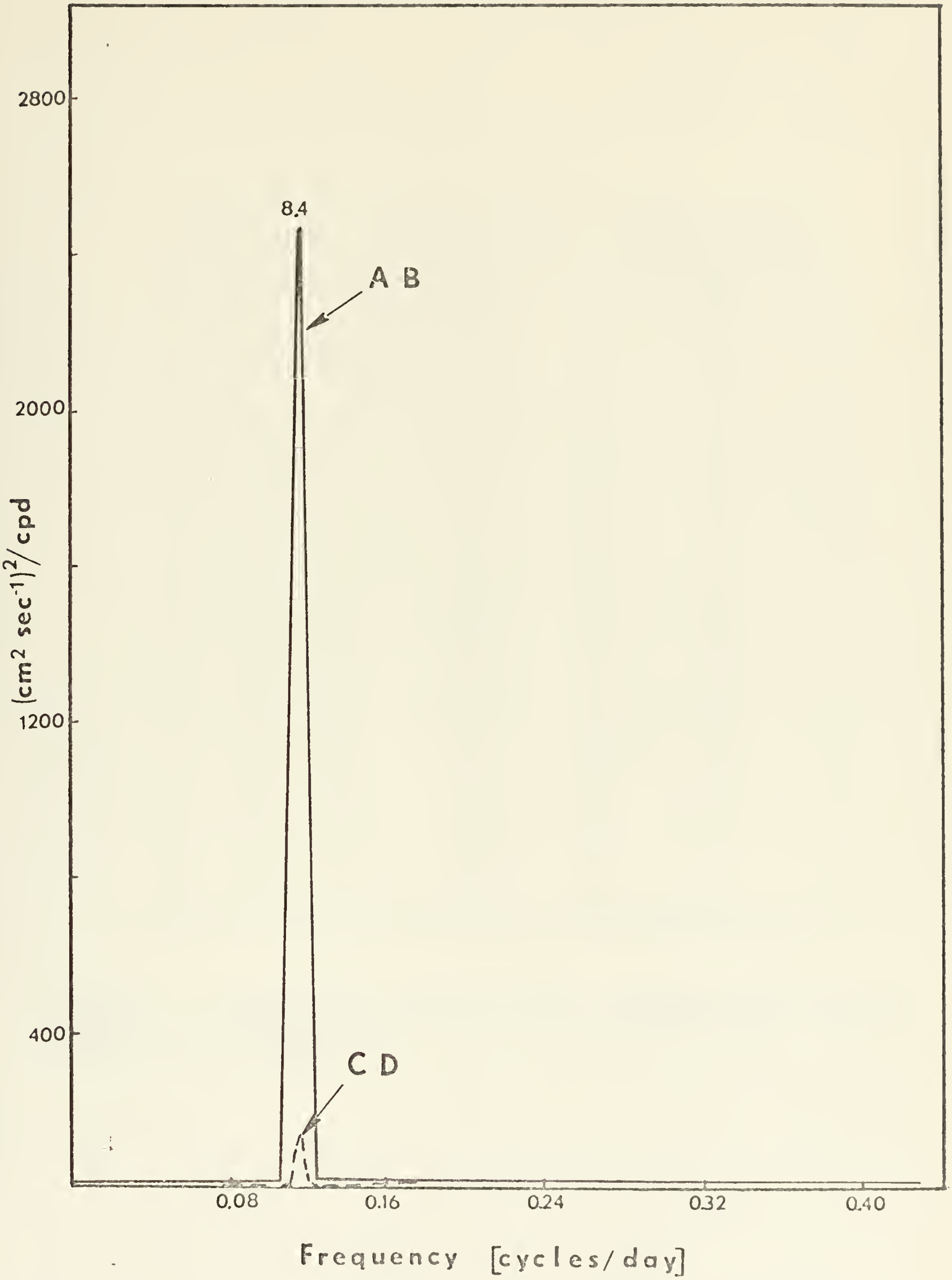

Figure 62. Power spectrum of A,B,C and D at point C in phase III. Period of spectral peaks indicated in days.

LATITUDE	THERMAL WIND (I)	THERMAL WIND (III)
72.0	0.0	0.0
68.4	1.2	3.0
64.8	4.2	3.7
61.2	3.9	3.5
57.6	4.6	4.3
54.0	5.7	5.6
50.4	6.6	7.5
46.8	8.5	9.4
43.2	10.2	9.2
39.2	9.1	7.5
36.0	6.8	5.6
32.4	4.4	3.9
28.8	3.0	3.1
25.2	2.3	2.8
21.6	1.3	2.5
18.0	0.0	0.0

TABLE 4. Comparison values of mean atmospheric thermal wind from combined model (I) and atmosphere-only model (III). (in m sec^{-1}).

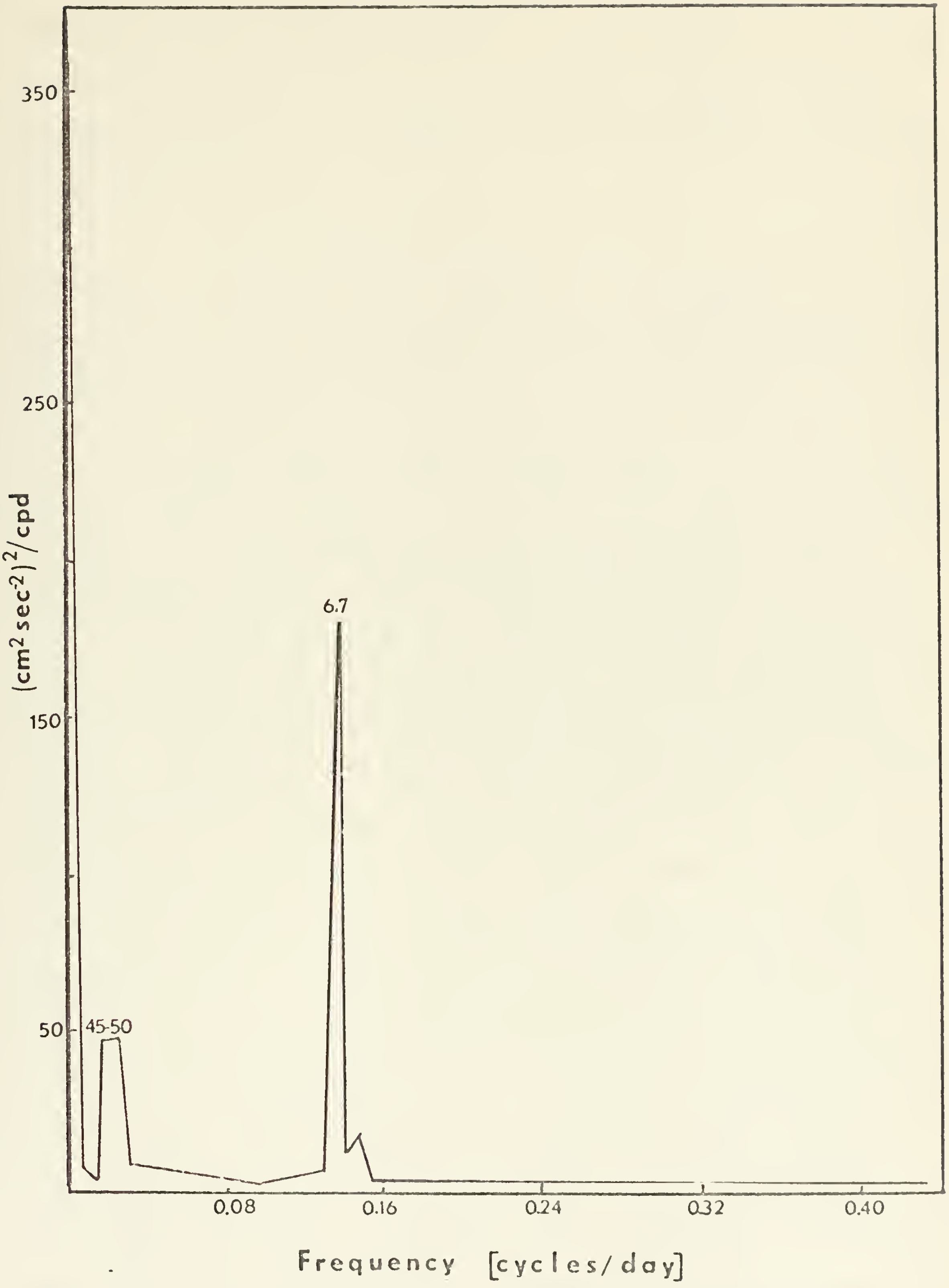

Figure 63. Power spectrum of atmospheric disturbance energy in phase III.

than the small diffuse indication of a peak around the 7.5 day period in the combined case. In the spectra for the quantities E and F, peaks at these same periods are observed, showing the exchange occurring between the disturbance and mean flow.

An examination of data in phases I, II and III at point C indicates that the peaks in the spectra noted at about one and two months in the combined model depend on atmosphere-ocean interactions for their existence and are not simply spurious or caused by aliasing. The fact that these interactions are on the order of one and two months is not the most significant point, because the period would undoubtedly change with some other period of atmospheric forcing. What is significant is that these longer period fluctuations can be attributed to air-sea interactions. The absence of such peaks in the spectra in either the atmosphere-only or ocean-only phases shows that the fluctuations causing the peaks are phenomena occurring only when the freedom found in the coupled model is allowed. Although there is a peak in both atmospheric and oceanic variables in the coupled model at 7.5 days, this is not considered as significant as the peaks at the longer periods because this frequency of oscillation was forced into the model with the selection of the 4800 km wavelength for the single wave in x. Changing this wavelength would cause the peak in the spectrum at 7.5 days to shift and undoubtedly would have many other effects on the model. It would

be interesting to see if the peaks in the spectra at the lower frequencies would be shifted.

Spectral analyses of the kinetic energy in the ocean of the combined model at the three ocean levels were made at point C. An approximation to the total kinetic energy at point C was used for this study. The total kinetic energy should include the vertical mean kinetic energy and the vertical shear kinetic energy. A mathematical formulation for this is

$$K \cdot E_{ocean} = \frac{1}{2}[(u' - \frac{\partial\psi}{\partial y})^2 + (v' + \frac{\partial\psi}{\partial x})^2] \qquad (6.2)$$

In recording the data at point C no provisions were made for the calculation of $\frac{\partial\psi}{\partial y}$ and so the zonal component of the vertical mean current at this point was neglected. The zonal component of the vertical mean current was small and therefore this was not a bad assumption. The kinetic energy computed at each oceanic level was

$$K \cdot E_{ocean} = \frac{1}{2}[(u')^2 + (v' + \frac{\partial\psi}{\partial x})^2]. \qquad (6.3)$$

Figure 64 shows the power spectrum of kinetic energy at 100 meters in the ocean of the combined model versus frequency in cycles per day, both plotted on log scales. Figure 65 is the same plot for 500 meters and Figure 66 shows the 1300 meter depth analysis. Peaks in the spectra at periods of 62, 25-32, and 7.5 days are observed at all three levels. This is consistent with earlier findings. The amplitude of the 25-32 day period

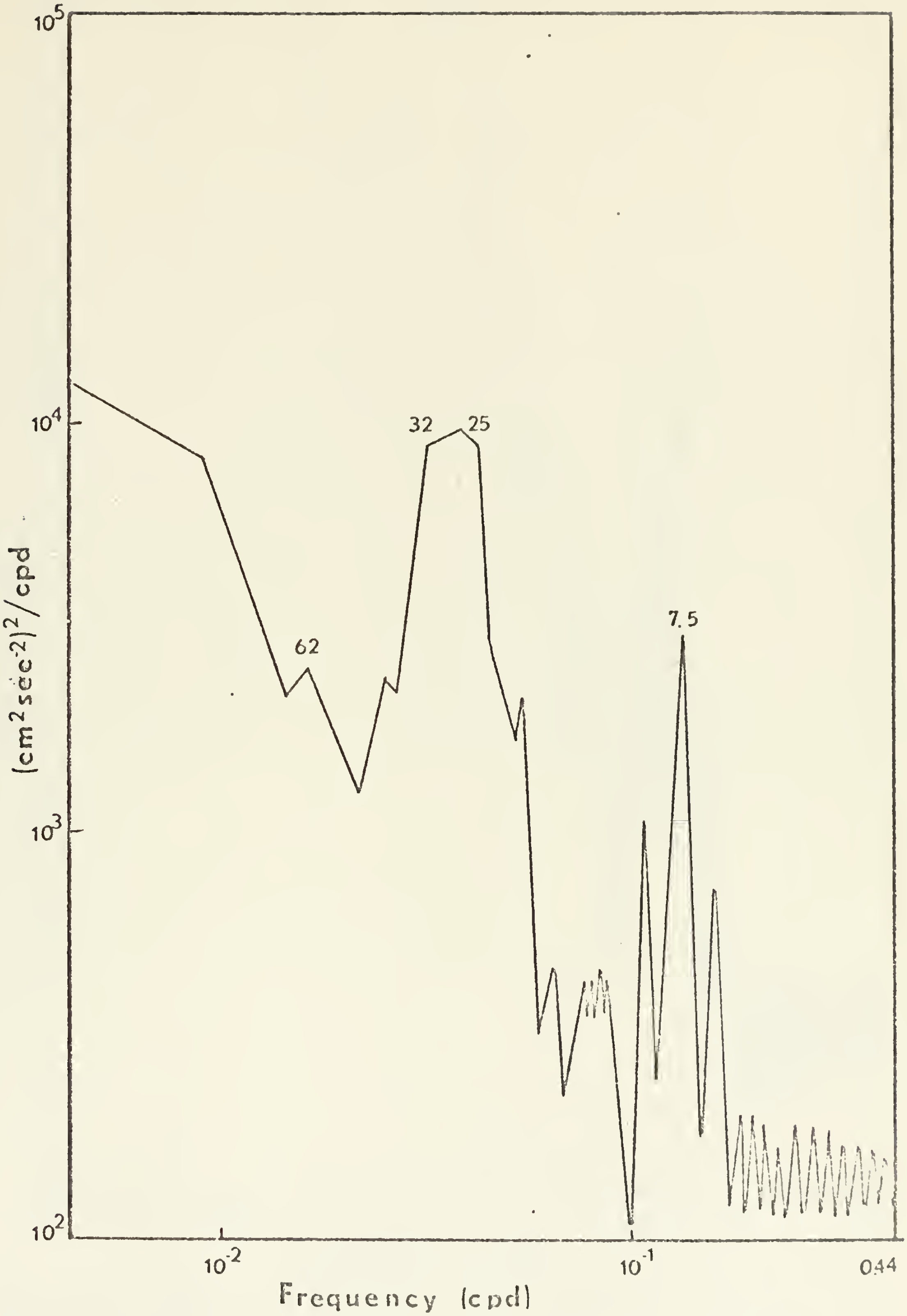

Figure 64. Power spectrum of oceanic kinetic energy at 100 meters at point C in phase I. Periods of spectral peaks indicated in days.

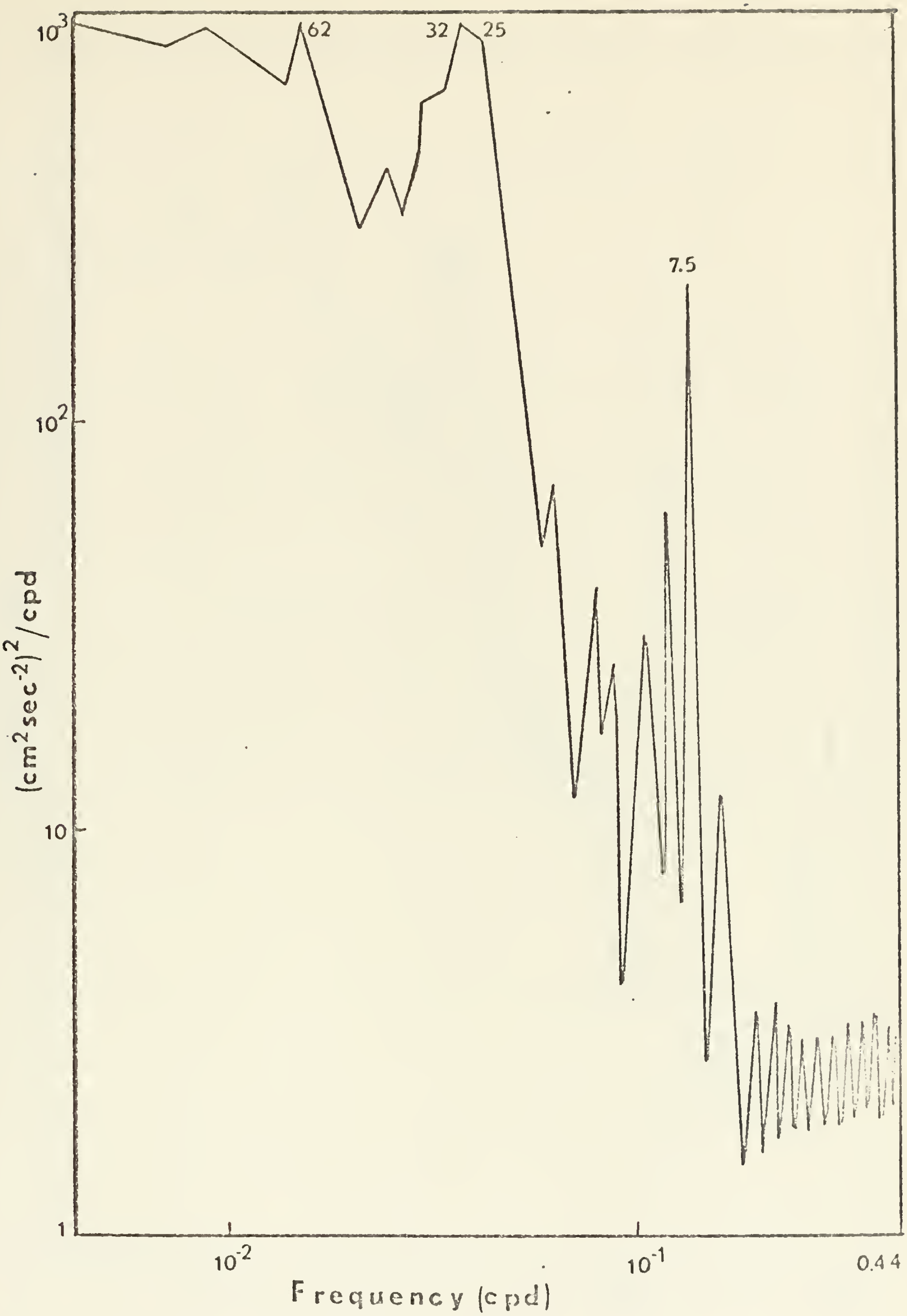

Figure 65. Power spectrum of ocean kinetic energy at 500 meters at point C in phase I. Periods of spectral peaks indicated in days.

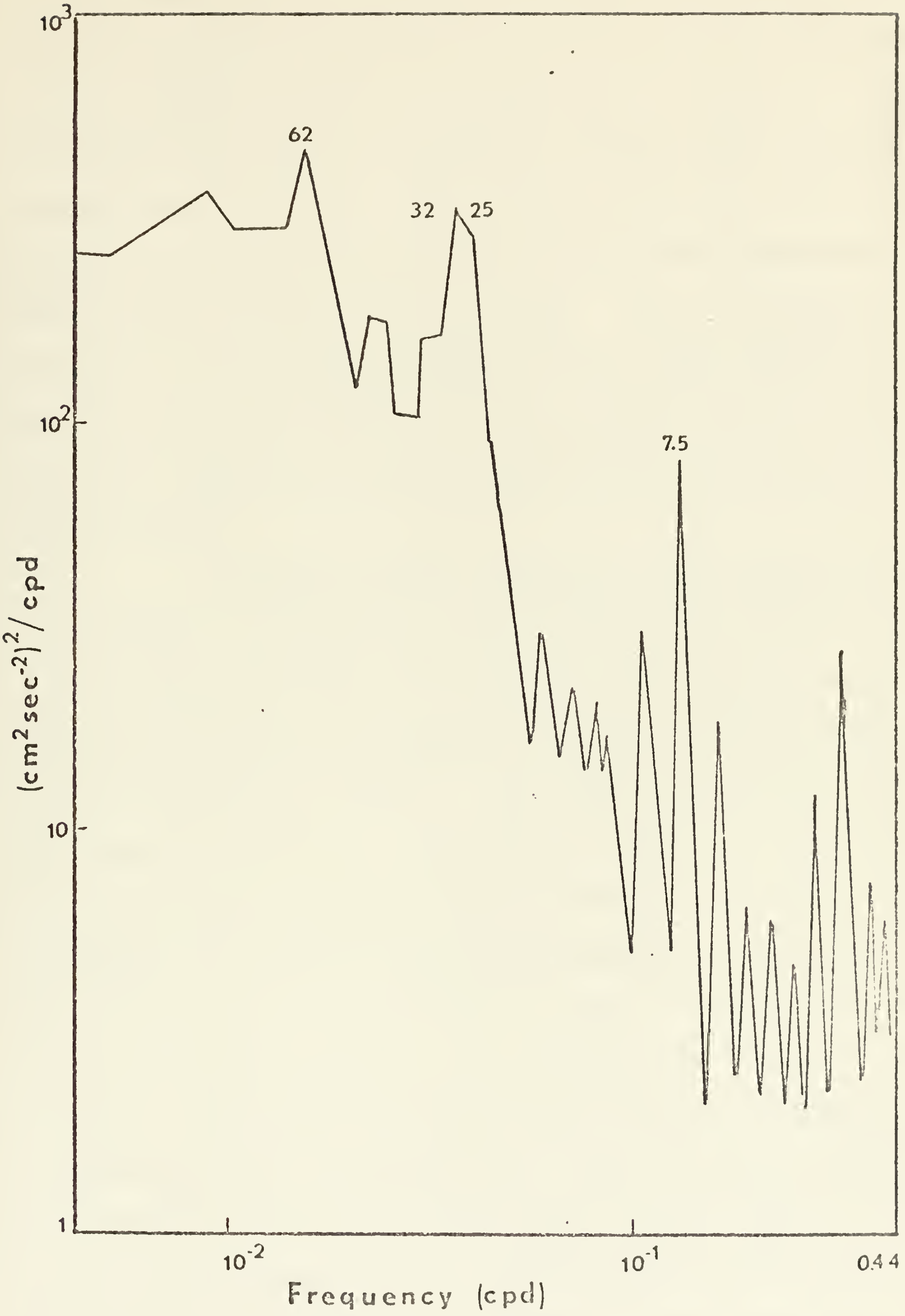

Figure 66. Power spectrum of ocean kinetic energy at 1300 meters at point C in phase I. Periods of spectral peaks indicated in days.

is the largest at the upper level while the amplitude of the 62 day period and 25-32 day period are about the same at the two lower levels. A comparison of Figures 65 and 66 shows that the spectra for the two lowest levels in the model nearly coincide. The maximum amplitude in the power spectra decreased by an order of magnitude between the 100 meter level and the 500 meter level. This lessening in the variance of the kinetic energy between these levels is not surprising since the lower levels are less active. The amplitude remained about the same between the 500 and 1300 meter levels.

Thompson (1971) analyzed a long series of data recorded by the Woods Hole Oceanographic Institution at a site located at 39 20N, 70W in the North Atlantic. In the model this would be analogous to a position approximately 200 km northeast of point C. The data were recorded at 900 second intervals. The folding frequency associated with this small recording interval allowed Thompson to investigate the shorter period oscillations. Some gaps in the data forced the estimation of some of the spectra in the low frequency region. He analyzed the northward and eastward components of velocity and through a summing and averaging process calculated the "kinetic energy density" at several depths in the ocean (not shown). None of these spectra showed any peaks at periods greater than one day, although osciallations with periods of about ten hours were observed. The spectra for the three lowest depths were

nearly coincident, and there was a large decrease in the amplitude of the spectra between 100 meters and 500 meters. In this feature the study of Thompson and the study conducted in this work were similar.

b. Study of data at point A.

At point A (northeast area) the power spectrum of the coefficients A,B,C and D were greatly reduced [a maximum value of 16 $(cm^2 sec^{-1})^2$ cycles per day for A and B as compared to 675.0 at point C], although the peak in the spectra was at the same period, 7.5 days. An examination of the coefficient, E, shows the spectral peak at 32 and 62 days and a large peak at 120 days. Looking back at Figure 53, a smaller peak in the region of the 120 day period can be seen also. The oceanic stream function at point A shows oscillations that have smaller amplitudes in the power spectrum than do those of the same quantity at point C. The biggest difference between the power spectra of variables at point A and those at point C occurred with T_{sea}. There are no peaks at the 32 or 62 day periods and all the power is in the lowest frequency, much the same as seen in Figure 58, the same quantity in the ocean-only case.

At point A in the ocean-only phase, the power spectra resembled those from the same phase at point C. The maximum of the power spectrum that existed in the lowest frequency was increased but will not be discussed further since it adds no new information. An increase in the

power in the lowest frequency merely indicates that the long term change was larger. In the atmosphere-only phase, the power spectra for the Fourier coefficients resemble those at point C, except that the maximum of the spectra at the 8.4 day period is reduced to approximately 10% of the value it had at point C. At point A, the meridional temperature gradient is rather weak and the amplitude of the baroclinic wave is much less than in the lower latitudes of point C.

c. Study of data at Point B, D and E

At point B (central area) the power spectra of the coefficients A, B, C, and D were slightly larger than those at point C. This location at 45N is in an area of large thermal wind, so the amplitude should be greater. Except for the increase in amplitudes the spectra are very similar to those of the variables at point C (Figures 52 through 56). The power spectrum of T_{sea}, though, is more like that at point A, with all the power at the lowest frequency. This indicates extremely long period fluctuations, probably too long for this data record to portray.

The ocean-only variables at point B resemble those at point A and will not be discussed. The Fourier coefficients, A through D, have a peak at the same 8.4 day period and the maximum in the power spectrum is increased. No new information was obtained from point B.

A separate discussion of the data at point D will not be made because of similarity of results to point B. Strange results were obtained when the data at point E

were spectrally analyzed. The Fourier coefficients, A through D, had multiple peaks in the spectra that were not representative. It was decided that this point was selected too close to the southern boundary and the artificiality of the wall caused unusual oscillations in the atmospheric data. The results from point E were discarded with no further comment.

The results of the spectral study were that the ocean circulation caused transients to appear in the atmosphereic circulation in the one and two month periods and possibly with a period of 120 days and that similar transients appeared in the ocean circulation due to the presence of the fluctuating atmosphere. A great deal of information has been wrested from the spectral statistics discussed here, but a great deal more could be obtained if time permitted.

VII. SUMMARY

A numerical model of a combined atmospheric-ocean system was developed for use in an investigation of the long-term, large-scale air-sea interactions and the effect of these interactions on transients that appear in the atmosphere and oceanic circulations. The problems associated with observational studies of the air-sea system were eliminated by using a numerical model that could produce a long-term simulation of an interacting system in a reasonable amount of computing time.

The atmospheric model used in this study was fashioned after the two level, quasi-geostrophic model developed by Phillips (1956). New dependent variables were introduced by the use of a one-dimensional (in x) Fourier series, in which a single mode was retained, to represent the original variable. This method of approach allowed the rapid integration of the atmospheric equations since the number of degrees of freedom were greatly reduced. Without this modification the combined model could not have been integrated for a sufficiently long time period to obtain meaningful results.

The ocean model utilized in this work was a modified version of Haney's (1971a) primitive equation model. The modifications included a reduction in the number of levels, a reduction in horizontal region size (and the number of grid points), a reduction in the depth of the basin and the

conversion to β-plane (cartesian) geometry. The primary reason for these modifications was to increase the ratio of simulation time to computing time and permit a long term simulation which was accomplished.

The coupling of the model was accomplished through the exchange of momentum through the wind stress and the exchange of heat through the turbulent exchange process which was proportional to the air-sea temperature difference. Assumptions were made to simplify both of these exchanges. The atmospheric model, however, had to be restricted to simplified formulations if it was to be integrated successfully for the necessary length of time. The absence of moisture in the atmospheric model required further simplification in the formulation of the latent heat flux. These simplifications were indeed necessary and an examination of the results showed that the model produced atmospheric and oceanic circulations that were adequate for this experiment in their portrayal of the real atmosphere-ocean system.

The experiment was conducted in three phases. Phase I was a long term integration of the combined model. The computing time was reduced by the use of a larger grid size for the first portion of this phase. The 400 km grid distance was that used to accelerate the integration of the combined model equations in the first part of Phase I was just adequate to resolve the western boundary current. The coefficient of lateral diffusion of heat had been reduced to prevent large horizontal transports of heat by

diffusion and keep the meridional temperature gradient at a realisticly high level. The lateral diffusion of momentum was reduced, but could not be made small enough so that a truly nonlinear solution could be obtained without having the width of the boundary current become smaller than the horizontal grid distance. The unrealistic spatial oscillations seen in the results obtained with the 400 km grid were a direct result of the large grid size.

The spatial oscillations observed in the 400 km grid model results quickly disappeared in the 200 km grid version of the combined model. A state of quasi-equilibrium was reached in the long term integrations of the combined model. The results shown throughout this thesis were considered to be satisfactory for the purpose of investigating the effect of the oceanic (atmospheric) circulation on the time-dependent behavior of the atmosphere (ocean). Some features in the results considered worthy of note are summarized below.

A western boundary current developed with very strong northward flow, analogous to the Gulf Stream, on the west side of the sub-tropical gyre and strong southward flow, analogous to the Labrador Current, on the west side of the sub-arctic gyre. The gyres themselves are positioned as found in nature and are a result of the surface wind stress developed in the atmospheric model. The conditions in the northeast corner of the domain are similar to those found in the northeast Pacific. The warmer water is due to the convergence of the vertical shear current into the

northeastern boundary resulting in downwelling in that region. The region of warm water and weak currents in the south central region of the domain is analogous to the water found in the Sargasso Sea area of the Atlantic.

The zonal winds in the atmosphere develop a horizontal and vertical structure similar to that found in the real atmosphere. A three cell meridional circulation was formed and slowly meandered several degrees of latitude north and south of its mean position.

The second phase of the experiment consisted of a six year integration of the ocean-only model and a state of equilibrium was quickly reached. The upper level of the ocean had reached a state of almost steady temperature but the lower level still showed a very slow increase in the temperature. This was a good example of the extremely long time necessary for the vertical diffusion mechanism to bring the deep water into thermal equilibrium.

Phase III of the experiment consisted of the integration of the atmosphere-only model equations. Energy balance studies of the atmosphere from this phase were made and compared with the same studies from phase I. The energy studies compared favorably with each other and with the existing knowledge of atmospheric energy exchanges.

Data produced by the combined model and recorded at selected points were spectrally analyzed yielding peaks in the spectra of both oceanic and atmospheric variables at periods on the order of one and two months. Cross-spectrum

analyses and time series analyses of several atmospheric and oceanic variables led to the following conclusion about the air-sea interactions. The longer period oscillations were present in the data and were attributed to air-sea interaction. An increase in the mean atmospheric flow preceded a rise in the barotropic flow in the ocean by about 3.5 days. This increased oceanic flow caused an increase in the advection of heat and oscillations in the sea surface temperature about 7.6 days later. This change in sea surface temperature led an increase in the vertical heat flux between atmosphere and ocean and an adjustment of zonal mean atmospheric surface temperature. It is interesting to note that even with the limited model developed here, there are longer period interactions between the atmosphere and ocean. If the model was modified so that more freedom were allowed, then interactions at different periods might occur. There are several ways in which this model might be changed for future studies. Some suggestions are listed below.

The incorporation of continental land masses and the corresponding allowances for a zonal standing eddy into the model is a necessity. This effect would modify the heating in the model in that a more realistic longitudinal pattern of vertical heat flux would emerge. The effect of this change on the frequency of response in the model would be interesting to observe. The incorporation of a second harmonic into the atmospheric Fourier formulation would simulate the continental effect. This would also cause a shift

in the position of the short period oscillation or add a new period of interaction. A study of an atmospheric model with a two-wave structure was carried out by Trumbower (1972), showing the feasibility of including a second wave in the atmospheric formulation. Incorporation of the second wave in the atmosphere would require an increase in computing time but compared to the total time required for the experiment, it would be negligible.

A change in the sensible heat term should be incorporated in the model. In the term $H_1(T_{sea} - T_4)$, the quantity H_1 was held constant. This quantity should be divided into two parts, one that is constant and one that is a function of the surface wind speed. This would cause a portion of the vertical heat flux to be dependent on the wind speed and allow more freedom in the model resulting in other forms of interaction.

An analysis of the energy budget of the ocean should be incorporated in any future calculations. The transformation of energy between the vertical shear kinetic energy and the vertical mean kinetic energy and the dissipation of energy is an area well worth studying.

The phase III experiment should be carried out again with a sea surface temperature with an x dependence included. A zonal variation in the heating would be present and the frequency at which the variables oscillated may be changed.

For atmospheric prediction for periods shorter than a few weeks, an interacting model may not be necessary. An atmosphere-only model with an accurately-observed air-sea temperature difference may be sufficient. However, longer range predictions on the monthly or seasonal time scale should include some kind of simultaneous ocean calculation.

The atmosphere-ocean model was synchronously integrated for a 79 year simulation of the circulations of the two media. The interaction observed at periods of one and two months provides evidence of the importance of the effect of the ocean circulation on the transient behavior of the atmospheric circulation, and vice versa. Other periods of interaction surely exist but the investigation of all of them is beyond the scope of this work. It is hoped that the results presented in this paper are sufficient to motivate further research in the important realm of large-scale air-sea interaction.

APPENDIX A

Derivations of Equations (2.22) to (2.27)

Equation (2.14) may be rewritten

$$\frac{\partial}{\partial t}(\nabla^2\psi_M) + \mathbf{k} \times \nabla\psi_M \cdot \nabla(\nabla^2\psi_M) + \mathbf{k} \times \nabla\psi_T \cdot \nabla(\nabla^2\psi_T) + \beta_o \frac{\partial\psi_M}{\partial x} = -\frac{g}{\Delta p}\left[\frac{\partial\tau_y}{\partial x} - \frac{\partial\tau_x}{\partial y}\right]_4 , \quad (A1)$$

where

$$\psi_M = E(y,t) + A(y,t)\cos kx + B(y,t)\sin kx, \quad (A2)$$

$$\psi_T = F(y,t) + C(y,t)\cos kx + D(y,t)\sin kx, \quad (A3)$$

$$(\tau_x)_4 = \rho C_D\ |\mathbf{V}_4|\ u_4 \quad (A4)$$

and

$$(\tau_y)_4 = \rho C_D\ |\mathbf{V}_4|\ v_4 . \quad (A5)$$

An examination of quantities in Equations (A4) and (A5) shows

$$u_4 = -\frac{\partial\psi_4}{\partial y} ,$$

$$v_4 = \frac{\partial\psi_4}{\partial x} ,$$

and

$$|V_4| = \left[\left(\frac{\partial\psi}{\partial x}\right)^2 + \left(\frac{\partial\psi}{\partial y}\right)^2\right]^{1/2} . \quad (A6)$$

Linear interpolation was used to obtain

$$\psi_4 = \frac{3}{2}\psi_3 - \frac{1}{2}\psi_1 , \quad (A7)$$

and the relationships

$$\psi_M = \frac{\psi_1 + \psi_3}{2} ,$$

$$\psi_T = \frac{\psi_1 - \psi_3}{2} ,$$

$$\psi_1 = \psi_M + \psi_T$$

and

$$\psi_3 = \psi_M - \psi_T \ . \qquad (A8)$$

Then

$$\psi_4 = \psi_M - 2\psi_T \ . \qquad (A9)$$

Apply Equations (A2), (A3) and (A9) to (A6) to obtain (when 2k and higher order terms are neglected)

$$\begin{aligned} u_4 = -\frac{\partial E}{\partial y} + 2\,\frac{\partial F}{\partial y} &- \left(\frac{\partial A}{\partial y} - 2\,\frac{\partial C}{\partial y}\right) \cos kx \\ &- \left(\frac{\partial B}{\partial y} - 2\,\frac{\partial D}{\partial y}\right) \sin kx, \end{aligned} \qquad (A10)$$

$$v_4 = k(B - 2D) \cos kx - k(A - 2C) \sin kx, \qquad (A11)$$

and

$$\begin{aligned} |V_4| = \Bigg\{ & \left(\frac{\partial E}{\partial y} - 2\frac{\partial F}{\partial y}\right)^2 + \frac{1}{2}[\frac{\partial A}{\partial y} - 2\frac{\partial C}{\partial y})^2 + \left(\frac{\partial B}{\partial y} - 2\frac{\partial D}{\partial y}\right)^2 \\ & + (Ak - 2Ck)^2 + (Bk - 2Dk)^2] \\ & + (2\frac{\partial E}{\partial y}\frac{\partial A}{\partial y} - 4\frac{\partial E}{\partial y}\frac{\partial C}{\partial y} - 4\frac{\partial A}{\partial y}\frac{\partial F}{\partial y} \\ & + 8\frac{\partial C}{\partial y}\frac{\partial F}{\partial y}) \cos kx + (2\frac{\partial E}{\partial y}\frac{\partial B}{\partial y} - 4\frac{\partial E}{\partial y}\frac{\partial D}{\partial y} \\ & - 4\frac{\partial F}{\partial y}\frac{\partial B}{\partial y} + 8\frac{\partial D}{\partial y}\frac{\partial F}{\partial y}) \sin kx \Bigg\}^{1/2} . \end{aligned} \qquad (A12)$$

Equation (A12) is simplified by making the assumption that contributions of the disturbances are much less than the contribution of the zonal wind to the magnitude of the surface wind. The cosine and sine terms in (A12) are therefore neglected and a new formulation for $|\overline{V}_4|$ is obtained.

$$|\mathbb{V}_4| = \left\{ (\frac{\partial E}{\partial y} - 2\frac{\partial F}{\partial y})^2 + \frac{1}{2}[(\frac{\partial A}{\partial y} - 2\frac{\partial C}{\partial y})^2 + (\frac{\partial B}{\partial y} - 2\frac{\partial D}{\partial y})^2 + k^2(A-2C)^2 + k^2(B-2D)^2] \right\}^{1/2} . \quad (A13)$$

Equation (A4) is now

$$\tau_x = \rho C_D |\overline{\mathbb{V}}_4| \left\{ [-\frac{\partial E}{\partial y} + 2\frac{\partial F}{\partial y}] - (\frac{\partial A}{\partial y} - 2\frac{\partial C}{\partial y}) \cos kx - (\frac{\partial B}{\partial y} - 2\frac{\partial D}{\partial y}) \sin kx \right\} , \quad (A14)$$

and Equation (A5) is

$$\tau_y = \rho C_D |\overline{\mathbb{V}}_4| \left\{ k(B-2D) \cos kx - k(A-2C) \sin kx \right\} . \quad (A15)$$

The term $[\frac{\partial \tau_y}{\partial x} - \frac{\partial \tau_x}{\partial y}]_4$ can be written

$$[\frac{\partial \tau_y}{\partial x} - \frac{\partial \tau_x}{\partial y}]_4 = \rho C_D \left\{ -\frac{\partial}{\partial y}[|\overline{\mathbb{V}}_4| (2\frac{\partial F}{\partial y} - \frac{\partial E}{\partial y})] + \left[|\overline{\mathbb{V}}_4| k^2(2C-A) - \frac{\partial}{\partial y}[|\overline{\mathbb{V}}_4|(2\frac{\partial C}{\partial y} - \frac{\partial A}{\partial y})] \right] \cos kx + \left[|\overline{\mathbb{V}}_4| k^2(2D-B) - \frac{\partial}{\partial y}[|\overline{\mathbb{V}}_4|(2\frac{\partial D}{\partial y} - \frac{\partial B}{\partial y})] \right] \sin kx \right\} . \quad (A16)$$

When Equations (A2), (A3) and (A16) are substituted in Equation (A1) and terms of wave number 2k and higher are neglected, an equation of the form

$$\frac{\partial}{\partial t}[G_1(y,t) + G_2(x,y,t) \cos kx + G_3(x,y,t) \sin kx] = F_1(y,t) + F_2(x,y,t) \cos kx + F_3(x,y,t) \sin kx \quad (A17)$$

is obtained. Coefficients of the terms independent of x, coefficients of the cosine terms, and coefficients of the sine terms are equated to yield the following three equations:

$$\begin{aligned}\frac{\partial}{\partial t}[\frac{\partial^2 A}{\partial y^2} - k^2 A] = {} & k[\frac{\partial E}{\partial y}\frac{\partial^2 B}{\partial y^2} + \frac{\partial F}{\partial y}\frac{\partial^2 D}{\partial y^2} - \frac{\partial^3 E}{\partial y^3} B \\ & - \frac{\partial^3 F}{\partial y^3} D - k^2(\frac{\partial E}{\partial y} B - \frac{\partial F}{\partial y} D)] - \beta_o Bk \\ & + \frac{g}{\Delta p}\rho C_D \left\{ |\bar{V}_4| \; k^2(A-2C) + \frac{\partial}{\partial y}[|\bar{V}_4|(2\frac{\partial C}{\partial y} - \frac{\partial A}{\partial y})] \right\},\end{aligned} \tag{A18}$$

$$\begin{aligned}\frac{\partial}{\partial t}[\frac{\partial^2 B}{\partial y^2} - k^2 B] = {} & k[-\frac{\partial E}{\partial y}\frac{\partial^2 A}{\partial y^2} - \frac{\partial F}{\partial y}\frac{\partial^2 C}{\partial y^2} + \frac{\partial^3 E}{\partial y^3} A \\ & + \frac{\partial^3 F}{\partial y^3} C + k^2(\frac{\partial E}{\partial y} A + \frac{\partial F}{\partial y} C)] + \beta_o Ak \\ & + \frac{g}{\Delta p}\rho C_D \left\{ |\bar{V}_4| \; k^2(B-2D) + \frac{\partial}{\partial y}[|\bar{V}_4|(2\frac{\partial D}{\partial y} - \frac{\partial B}{\partial y})] \right\},\end{aligned} \tag{A19}$$

and

$$\begin{aligned}\frac{\partial}{\partial t}[\frac{\partial^2 E}{\partial y^2}] = {} & \frac{k}{2}\frac{\partial}{\partial y}(A\frac{\partial^2 B}{\partial y^2} - B\frac{\partial^2 A}{\partial y^2} + C\frac{\partial^2 D}{\partial y^2} - D\frac{\partial^2 C}{\partial y^2}) \\ & + \frac{g}{\Delta p}\rho C_D \frac{\partial}{\partial y}[|\bar{V}_4|(2\frac{\partial E}{\partial y} - \frac{\partial F}{\partial y})].\end{aligned} \tag{A20}$$

Rewrite Equation (2.15) to obtain

$$\begin{aligned}\frac{\partial}{\partial t} & (\nabla^2 - \mu^2)\psi_T + \mathbf{k} \times \nabla\psi_M \cdot \nabla(\nabla^2 - \mu^2)\psi_T \\ & + \mathbf{k} \times \nabla\psi_T \cdot \nabla(\nabla^2\psi_M) + \beta_o \frac{\partial \psi_T}{\partial x} = -\frac{\mu^2 \kappa \dot{Q}}{2f_o} \\ & - \frac{g}{\Delta p}\left\{ 2[\frac{\partial \tau_y}{\partial x} - \frac{\partial \tau_x}{\partial y}]_2 - [\frac{\partial \tau_y}{\partial x} - \frac{\partial \tau_x}{\partial y}]_4 \right\},\end{aligned} \tag{A21}$$

and examine the term $\mu^2\kappa\dot{Q}/2f_o$. Substitute for $\dot{Q}$ to obtain

$$\frac{\mu^2\kappa\dot{Q}}{2f_o} = \frac{\mu^2\kappa g}{2f_o \Delta p} H_1[T_{sea} - (\frac{2f_o}{R}\psi_T + 250.3 - (\frac{\partial T}{\partial z})(\Delta z)]. \tag{A22}$$

Define a constant, C_1, such that

$$C_1 \equiv (250.3 - (\frac{\partial T}{\partial z}) \Delta z)\frac{R}{2f_o} \qquad (A23)$$

and the term is then

$$\frac{\mu^2 \kappa g}{2f_o \Delta p} \quad H_1[T_{sea} - \frac{2f_o}{R}(\psi_T + C_1)]. \qquad (A24)$$

Substitute Equation (A3) for ψ_T and

$$\frac{\mu^2 \kappa \dot{Q}}{2f_o} = \frac{\mu^2 \kappa g}{2f_o \Delta p} H_1 \left\{ T_{sea} - \frac{2f_o}{R}[(F+C_1)+C \cos kx + D \sin kx] \right\} \qquad (A25)$$

is obtained.

The term $-g/\Delta p \; 2[\frac{\partial \tau_y}{\partial x} - \frac{\partial \tau_x}{\partial y}]_2$ is then examined. Recall that

$$\boldsymbol{\tau}_2 = (\rho\kappa)_2 \, (\frac{\rho g}{p})_2 (\mathbf{V}_3 - \mathbf{V}_1) \qquad (A26)$$

that can be broken up into its vector components

$$\tau_{x_2} = (\rho\kappa)_2 \, (\frac{\rho g}{p})_2 \, (u_3 - u_1) \qquad (A27)$$

and

$$\tau_{y_2} = (\rho\kappa)_2 \, (\frac{\rho g}{p})_2 \, (v_3 - v_1). \qquad (A28)$$

The quantity τ_x may be written as

$$(\tau_x)_2 = (\rho\kappa)_2 \, (\frac{\rho g}{p})_2 \, (- \frac{\partial \psi_3}{\partial y} + \frac{\partial \psi_1}{\partial y}) \qquad (A29)$$

that leads to

$$\frac{\partial \tau_x}{\partial y} = 2(\rho\kappa)_2 \, (\frac{\rho g}{p})_2 \, \frac{\partial^2 \psi_T}{\partial y^2} \quad . \qquad (A30)$$

The quantity τ_y may be written

$$\tau_y = (\rho\kappa)_2 \, (\frac{\rho g}{p})_2 \, (\frac{\partial \psi_3}{\partial x} - \frac{\partial \psi_1}{\partial x}) \qquad (A31)$$

which leads to

$$\frac{\partial \tau_y}{\partial x} = -2(\rho\kappa)_2 \left(\frac{\rho g}{p}\right)_2 \frac{\partial^2 \psi_T}{\partial x^2} \tag{A32}$$

and

$$\left[\frac{\partial \tau_y}{\partial x} - \frac{\partial \tau_x}{\partial y}\right]_2 = -2(\rho\kappa)_2 \left(\frac{\rho g}{p}\right)_2 \nabla^2 \psi_T . \tag{A33}$$

Finally

$$-\frac{g}{\Delta p}\, 2\left[\frac{\partial \tau_y}{\partial x} - \frac{\partial \tau_x}{\partial y}\right]_2 = \frac{g}{\Delta p}\, 4(\rho\kappa)_2 \left(\frac{\rho g}{p}\right)_2 \nabla^2 \psi_T \tag{A34}$$

and can be written in its Fourier components as

$$\frac{g}{\Delta p}\, 4(\rho\kappa)_2 \left(\frac{\rho g}{p}\right)_2 \left[\frac{\partial^2 F}{\partial y^2} - \left(Ck^2 - \frac{\partial^2 C}{\partial y^2}\right)\cos kx - \left(Dk^2 - \frac{\partial^2 D}{\partial y^2}\right)\sin kx\right]. \tag{A35}$$

Repeat the procedure previously used on Equation (A1) on Equation (A21) to obtain three equations. These are

$$\begin{aligned}
\frac{\partial}{\partial t}\left[\frac{\partial^2 C}{\partial y^2} - k^2 C - \mu^2 C\right] = {} & k\left[\frac{\partial E}{\partial y}\frac{\partial^2 D}{\partial y^2} + \frac{\partial F}{\partial y}\frac{\partial^2 B}{\partial y^2} - \frac{\partial E}{\partial y} D(k^2 + \mu^2)\right. \\
& \left. - \frac{\partial F}{\partial y} B(k^2 - \mu^2) - \frac{\partial^3 E}{\partial y^3} D - \frac{\partial^3 F}{\partial y^3} B\right] - \beta_o Dk \\
& - \frac{\mu^2 \kappa g}{2 f_o \Delta p} H_1\left(-\frac{2 f_o}{R} C\right) + \frac{g}{\Delta p}\, 4(\rho\kappa)_2 \left(\frac{\rho g}{p}\right)_2 \left(\frac{\partial^2 C}{\partial y^2} - Ck^2\right) \\
& + \frac{g}{\Delta p}\, \rho C_D \left[|\overline{V}_4|\, k^2 (2C - A) - \frac{\partial}{\partial y}\left[|\overline{V}_4|\left(2\frac{\partial C}{\partial y} - \frac{\partial A}{\partial y}\right)\right]\right],
\end{aligned} \tag{A36}$$

$$\begin{aligned}
\frac{\partial}{\partial t}\left[\frac{\partial^2 D}{\partial y^2} - k^2 D - \mu^2 D\right] = {} & k\left[\frac{\partial E}{\partial y} C(k^2 + \mu^2) + \frac{\partial F}{\partial y} A(k^2 - \mu^2)\right. \\
& \left. - \frac{\partial E}{\partial y}\frac{\partial^2 C}{\partial y^2} - \frac{\partial F}{\partial y}\frac{\partial^2 A}{\partial y^2} + \frac{\partial^3 F}{\partial y^3} A + \frac{\partial^3 F}{\partial y^3} C\right] + \beta_o Ck \\
& - \frac{\mu^2 \kappa g}{2 f_o \Delta p} H_1\left(-\frac{2 f_o}{R} D\right) + \frac{g}{\Delta p}\, 4(\rho\kappa)_2 \left(\frac{\rho g}{p}\right)_2 \left(\frac{\partial^2 D}{\partial y^2} - k^2 D\right) \\
& + \frac{g}{\Delta p}\, \rho C_D \left[|\overline{V}_4|\, k^2 (2D - B) - \frac{\partial}{\partial y}\left[|\overline{V}_4|\left(2\frac{\partial D}{\partial y} - \frac{\partial E}{\partial y}\right)\right]\right]
\end{aligned} \tag{A37}$$

and

$$\frac{\partial}{\partial t}\left[\frac{\partial^2}{\partial y^2} - \mu^2\right]F = \frac{k}{2}\left\{\frac{\partial}{\partial y}\left[\frac{\partial^2 D}{\partial y^2}A - B\frac{\partial^2 C}{\partial y^2}\right.\right.$$

$$\left.\left. + C\frac{\partial^2 B}{\partial y^2} - D\frac{\partial^2 A}{\partial y^2}\right] + \mu^2 \frac{\partial}{\partial y}[BC - AD]\right\}$$

$$- \frac{\mu^2 \kappa g}{2f_o \Delta p} H_1\left[T_{sea} - \frac{2f_o}{R}(F + C_1)\right]$$

$$+ \frac{g}{\Delta p} 4(\rho\kappa)_2\left(\frac{\rho g}{p}\right)_2 \frac{\partial^2 F}{\partial y^2} + \frac{g}{\Delta p} \rho C_D \frac{\partial}{\partial y}\left[|\overline{V}_4|\left(\frac{\partial E}{\partial y} - 2\frac{\partial F}{\partial y}\right)\right]. \qquad \text{(A38)}$$

This completes the derivation of the equations for predicting new values of the Fourier coefficients.

APPENDIX B

Derivation of ω and v_1 Equations.

Applied at level two, Equation (2.12) is written as

$$\frac{\partial}{\partial t}\left(\frac{\psi_3 - \psi_1}{\Delta p}\right) + \mathbf{k} \times \nabla\psi_2 \cdot \nabla\left(\frac{\psi_3 - \psi_1}{\Delta p}\right) + \frac{\sigma}{f_o}\,\omega_2 = -\frac{\kappa}{f_o p}\,\dot{Q}_2 . \qquad \text{(B1)}$$

Substitute from Equation (2.13) which yields

$$\frac{\partial}{\partial t}\,\psi_T + \mathbf{k} \times \nabla\psi_M \cdot \nabla\psi_T - \frac{\sigma \Delta p}{2 f_o}\,\omega_2 = \frac{\kappa}{2 f_o}\,\dot{Q}_2 . \qquad \text{(B2)}$$

Solve for ω_2 which gives

$$\omega_2 = \frac{2 f_o}{\sigma \Delta p}\left\{ \frac{\partial\psi_T}{\partial t} - \frac{\partial\psi_M}{\partial y}\frac{\partial\psi_T}{\partial x} + \frac{\partial\psi_M}{\partial x}\frac{\partial\psi_T}{\partial y} - \frac{\kappa}{2 f_o}\,\dot{Q}_2 \right\} . \qquad \text{(B3)}$$

Substitute Equation (2.16) and (2.17) into (B3) and neglect terms of wave number 2k and higher which gives

$$\begin{aligned}\omega_2 = \frac{2 f_o}{\sigma \Delta p}\Bigg\{ & \frac{1}{2}\left[k\left(B\frac{\partial C}{\partial y} - D\frac{\partial A}{\partial y}\right) + k\left(C\frac{\partial B}{\partial y} - A\frac{\partial D}{\partial y}\right)\right] \\ & + \frac{\partial F}{\partial t} - \frac{\kappa\dot{Q}_2}{2 f_o} + \left[\frac{\partial C}{\partial t} - k\left(\frac{\partial E}{\partial y}D - \frac{\partial F}{\partial y}B\right)\right] \cos kx \\ & + \left[\frac{\partial D}{\partial t} + k\left(\frac{\partial E}{\partial y}C - \frac{\partial F}{\partial y}A\right)\right] \sin kx\end{aligned}$$

or

$$\omega_2 = \overline{\omega} + (\omega_C) \cos kx + (\omega_D) \sin kx. \qquad \text{(B4)}$$

The quantity ω_2 is composed of a mean component and a disturbance component. The mean component may be written

$$\begin{aligned}\overline{\omega} = \frac{f_o}{\sigma \Delta p}\Bigg[& k\left(B\frac{\partial C}{\partial y} - D\frac{\partial A}{\partial y}\right) + k\left(C\frac{\partial B}{\partial y} - A\frac{\partial D}{\partial y}\right) \\ & + \frac{\partial F}{\partial t} - \frac{\kappa\dot{Q}_2}{2 f_o}\Bigg] \end{aligned} \qquad \text{(B5)}$$

and the disturbance part written as two components

$$\omega_C = \frac{2f_o}{\sigma \Delta p} [\frac{\partial C}{\partial t} - k(\frac{\partial E}{\partial y}D - \frac{\partial F}{\partial y}B)] \tag{B6}$$

and

$$\omega_D = \frac{2f_o}{\sigma \Delta p} [\frac{\partial D}{\partial t} + k(\frac{\partial E}{\partial y}C - \frac{\partial F}{\partial y}A)]. \tag{B7}$$

The mean meridional motion component can be derived from the zonally averaged continuity equation. This is written

$$\overline{\nabla \cdot \mathbb{V}}^x + \frac{\partial \overline{\omega}^x}{\partial p} = 0. \tag{B8}$$

Applied at level one this yields

$$\frac{\partial \bar{v}_1}{\partial y} = - \frac{\bar{\omega}_2}{\Delta p} \tag{B9}$$

and this is solved numerically to obtain v_1 at any point in the model, after obtaining $\bar{\omega}_2$ from (B5).

APPENDIX C

Derivation of Energy and Energy Transformation Equations.

To derive the energy relationships, the A, B, C, D, E and F equations [(2.22) to (2.27)] were multiplied by A through F, respectively. After further mathematical manipulation, the energy equations were obtained.

Multiply the A equation by A to obtain

$$A\frac{\partial}{\partial t}\left[\frac{\partial^2 A}{\partial y^2} - Ak^2\right] = kA\left[\frac{\partial E}{\partial y}\frac{\partial^2 B}{\partial y^2} + \frac{\partial F}{\partial y}\frac{\partial^2 D}{\partial y^2} - \frac{\partial^3 E}{\partial y^3}B - \frac{\partial^3 F}{\partial y^3}D - k^2\left(\frac{\partial E}{\partial y}B - \frac{\partial F}{\partial y}D\right)\right] - \beta_o ABk$$

$$+ \frac{g}{\Delta p}\rho C_D\, A\left\{|\overline{V}_4|\, k^2(A-2C) + \frac{\partial}{\partial y}\left[|\overline{V}_4|\left(2\frac{\partial C}{\partial y} - \frac{\partial A}{\partial y}\right)\right]\right\} \qquad \text{(C1)}$$

and the B equation by B, and add to Equation (C1) to get

$$A\frac{\partial}{\partial t}\left[\frac{\partial^2 A}{\partial y^2} - Ak^2\right] + B\frac{\partial}{\partial t}\left[\frac{\partial^2 B}{\partial y^2} - Bk^2\right] = k\left[A\frac{\partial E}{\partial y}\frac{\partial^2 B}{\partial y^2} - B\frac{\partial E}{\partial y}\frac{\partial^2 A}{\partial y^2} + A\frac{\partial F}{\partial y}\frac{\partial^2 D}{\partial y^2} - B\frac{\partial F}{\partial y}\frac{\partial^2 C}{\partial y^2} - AD\frac{\partial^3 F}{\partial y^3} + BC\frac{\partial^3 F}{\partial y^3} - k^2\left(\frac{\partial F}{\partial y}DA - \frac{\partial F}{\partial y}CB\right)\right]$$

$$+ \frac{g}{\Delta p}\rho C_D\left\{|\overline{V}_4|\, k^2[(A^2-2AC) + (B^2-2BC)] + A\frac{\partial}{\partial y}\left[|\overline{V}_4|\left(2\frac{\partial C}{\partial y} - \frac{\partial A}{\partial y}\right)\right] + B\frac{\partial}{\partial y}\left[|\overline{V}_4|\left(2\frac{\partial D}{\partial y} - \frac{\partial B}{\partial y}\right)\right]\right\}. \qquad \text{(C2)}$$

Treat the C and D equations similarly and add to obtain

$$C\frac{\partial}{\partial t}[\frac{\partial^2 C}{\partial y^2} - Ck^2 - C\mu^2] + D\frac{\partial}{\partial t}[\frac{\partial^2 D}{\partial y^2} - Dk^2 - D\mu^2] =$$

$$k[\frac{\partial E}{\partial y}(C\frac{\partial^2 D}{\partial y^2} - D\frac{\partial^2 C}{\partial y^2}) + \frac{\partial F}{\partial y}(C\frac{\partial^2 B}{\partial y^2} - D\frac{\partial^2 A}{\partial y^2})$$

$$- \frac{\partial^3 F}{\partial y^3}(BC - AD) - (k^2 - \mu^2)\frac{\partial F}{\partial y}(BC - AD)$$

$$+ \frac{g}{\Delta p}\rho C_D \left\{ |\overline{V}_4|\ k^2[(2C^2-AC)+(2D^2-BD)] - C\frac{\partial}{\partial y}[|\overline{V}_4|(2\frac{\partial C}{\partial y} - \frac{\partial A}{\partial y})]\right.$$

$$\left. - D\frac{\partial}{\partial y}[|\overline{V}_4|(2\frac{\partial D}{\partial y} - \frac{\partial B}{\partial y})]\right\} + \frac{g}{\Delta p}4(\rho\kappa)_2(\frac{\rho g}{p})_2[C(\frac{\partial^2 C}{\partial y^2} - Ck^2)$$

$$+ D(\frac{\partial^2 D}{\partial y^2} - Dk^2)]. \qquad (C3)$$

Combine Equations (C2) and (C3) and integrate over the region to obtain

$$\int_o^y \left\{ A\frac{\partial}{\partial t}[\frac{\partial^2 A}{\partial y^2} - Ak^2] + B\frac{\partial}{\partial t}[\frac{\partial^2 B}{\partial y^2} - Bk^2] + C\frac{\partial}{\partial t}[\frac{\partial^2 C}{\partial y^2} - Ck^2 - C\mu^2] + \right.$$

$$\left. D\frac{\partial}{\partial t}[\frac{\partial^2 D}{\partial y^2} - Dk^2 - D\mu^2]\right\} dy = \int_o^y \left\{ k[\frac{\partial E}{\partial y}(A\frac{\partial^2 B}{\partial y^2} - B\frac{\partial^2 A}{\partial y^2} + C\frac{\partial^2 D}{\partial y^2} - \right.$$

$$D\frac{\partial^2 C}{\partial y^2})$$

$$+ \frac{\partial F}{\partial y}(A\frac{\partial^2 D}{\partial y^2} - D\frac{\partial^2 A}{\partial y^2} - B\frac{\partial^2 C}{\partial y^2} + C\frac{\partial^2 B}{\partial y^2}) + \mu^2\frac{\partial F}{\partial y}(BC - AD)]$$

$$+ \frac{g}{\Delta p}\rho C_D \Big[(A-C)\Big(|\overline{V}_4|k^2(A-2C) + \frac{\partial}{\partial y}[|\overline{V}_4|(2\frac{\partial C}{\partial y} - \frac{\partial A}{\partial y})]\Big)$$

$$+ (B-D)\Big(|\overline{V}_4|k^2(B-2D) + \frac{\partial}{\partial y}[|\overline{V}_4|(2\frac{\partial D}{\partial y} - \frac{\partial B}{\partial y})]\Big)\Big]$$

$$\left. + \frac{g}{\Delta p}4(\rho\kappa)_2(\frac{\rho g}{p})_2[C(\frac{\partial^2 C}{\partial y^2} - Ck^2) + D(\frac{\partial^2 D}{\partial y^2} - Dk^2)]\right\} dy. \qquad (C4)$$

Perform the multiplications and apply the boundary conditions to acquire

$$\frac{\partial}{\partial t} = \int_{o}^{y} (\frac{\partial A}{\partial y})^2+(\frac{\partial B}{\partial y})^2+(\frac{\partial C}{\partial y})^2+(\frac{\partial D}{\partial y})^2+ k^2(A^2+B^2+C^2+D^2)+\mu^2(C^2+D^2)\,dy$$

$$= \int_{o}^{y} \Bigg\{ \frac{k}{2}[- \frac{\partial E}{\partial y}(A\frac{\partial^2 B}{\partial y^2} - B\frac{\partial^2 A}{\partial y^2} + C\frac{\partial^2 D}{\partial y^2} - D\frac{\partial^2 C}{\partial y^2}) - \frac{\partial F}{\partial y}(A\frac{\partial^2 D}{\partial y^2} - D\frac{\partial^2 A}{\partial y^2}$$

$$- B\frac{\partial^2 C}{\partial y^2} + C\frac{\partial^2 B}{\partial y^2}) - \mu^2\frac{\partial F}{\partial y}(BC-AD)] - \frac{g}{\Delta p}\rho C_D \Big[(A-C)\Big(|\bar{V}_4|k^2(A-2C)$$

$$+ \frac{\partial}{\partial y}[|\bar{V}_4|(2\frac{\partial C}{\partial y} - \frac{\partial A}{\partial y})] + (B-D)(|\bar{V}_4|k^2(B-2D) + \frac{\partial}{\partial y}[|\bar{V}_4|(2\frac{\partial D}{\partial y}$$

$$- \frac{\partial B}{\partial y})]\Big)\Big] - \frac{g}{\Delta p}4(\rho\kappa)_2(\frac{\rho g}{p})_2[C(\frac{\partial^2 C}{\partial y^2} - Ck^2) + D(\frac{\partial^2 D}{\partial y^2} - Dk^2)]\Bigg\}\,dy. \tag{C5}$$

Apply similar techniques to the E and F equations to obtain

$$\frac{\partial}{\partial t}\int_{o}^{y}[(\frac{\partial E}{\partial y})^2+(\frac{\partial F}{\partial y})^2+\mu^2F^2]\,dy = \int_{o}^{y}\Bigg\{\frac{k}{2}[\frac{\partial E}{\partial y}(A\frac{\partial^2 B}{\partial y^2} - B\frac{\partial^2 A}{\partial y^2} + C\frac{\partial^2 D}{\partial y^2}$$

$$- D\frac{\partial^2 C}{\partial y^2}) + \frac{\partial F}{\partial y}(A\frac{\partial^2 D}{\partial y^2} - D\frac{\partial^2 A}{\partial y^2} - B\frac{\partial^2 C}{\partial y^2} + C\frac{\partial^2 B}{\partial y^2}) + \mu^2\frac{\partial F}{\partial y}(BC-AD)]$$

$$+ \frac{\mu^2\kappa g}{2\Delta p f_o}H_1[T_{sea} - \frac{2f_o}{R}(F+C_1)]F - \frac{g}{\Delta p}\rho C_D[(E-F)\frac{\partial}{\partial y}|\bar{V}_4|$$

$$(2\frac{\partial F}{\partial y} - \frac{\partial E}{\partial y})] - \frac{g}{\Delta p}4(\rho\kappa)_2(\frac{\rho g}{p})_2[F\frac{\partial^2 F}{\partial y^2}]\Bigg\}\,dy. \tag{C6}$$

Define

P_z = zonal potential energy,

P_e = eddy potential energy,

K_z = zonal kinetic energy,

K_e = eddy kinetic energy,

C_p = conversion of P_z to P_e,

C_e = conversion of P_e to K_e,

C_k = conversion of K_e to K_z,

C_z = conversion of K_z to P_z,

G_z = generation of P_z by diabatic processes,

D_{ei} = dissipation of K_e by internal friction,

D_{es} = dissipation of K_e by surface friction,

D_{zi} = dissipation of K_z by internal friction

and

D_{zs} = dissipation of K_z by surface friction.

From Phillips (1956) and the basic definitions for ψ_T and ψ_M used in this work (Equation 2.13) equations for the potential and kinetic energy components can be written as

$$\int P_z \, dy = \frac{\mu^2}{2}\int F^2 \, dy, \tag{C7}$$

$$\int P_e \, dy = \frac{\mu^2}{2}\int (C^2 + D^2) \, dy, \tag{C8}$$

$$\int K_z \, dy = \frac{1}{2}\int [(\frac{\partial E}{\partial y})^2 + (\frac{\partial F}{\partial y})^2] dy, \tag{C9}$$

and

$$\int K_e \, dy = \frac{1}{2}\int [(\frac{\partial A}{\partial y})^2 + (\frac{\partial B}{\partial y})^2 + (\frac{\partial C}{\partial y}) + (\frac{\partial D}{\partial y})^2 + k^2(A^2+B^2+C^2+D^2)] dy. \tag{C10}$$

The right hand sides of Equations (C5) and (C6) yield expressions for energy generation, conversion and dissipation as follows:

$$G_z = \int \left\{ \frac{\mu^2 \kappa g}{2 \Delta p f_o} H_1 [T_{sea} - \frac{2 f_o}{R} (F + C_1)] F \right\} dy, \qquad (C11)$$

$$C_p = -\int [\frac{k}{2} \mu^2 (BC - AD) \frac{\partial F}{\partial y}] \, dy, \qquad (C12)$$

$$C_k = -\int \Bigg\{ \frac{k}{2} [\frac{\partial E}{\partial y} (A \frac{\partial^2 B}{\partial y^2} - B \frac{\partial^2 A}{\partial y^2} + C \frac{\partial^2 D}{\partial y^2} - D \frac{\partial^2 C}{\partial y^2}) + \frac{\partial F}{\partial y} (A \frac{\partial^2 D}{\partial y^2} - D \frac{\partial^2 A}{\partial y^2} - B \frac{\partial^2 C}{\partial y^2} + C \frac{\partial^2 B}{\partial y^2})] \Bigg\} dy, \qquad (C13)$$

$$D_{ei} = -\int \left\{ \frac{g}{\Delta p} 4 (\rho \kappa)_2 (\frac{\rho g}{p})_2 [C(\frac{\partial^2 C}{\partial y^2} - Ck^2) + D(\frac{\partial^2 D}{\partial y^2} - Dk^2)] \right\} dy, \qquad (C14)$$

$$D_{es} = -\int \Bigg\{ \frac{g}{\Delta p} \rho C_D \Bigg[(A-C) \Bigg(|\overline{V}_4| k^2 (A - 2C) + \frac{\partial}{\partial y}] |\overline{V}_4| (2 \frac{\partial C}{\partial y} - \frac{\partial A}{\partial y})] \Bigg), + (B-C) \Bigg(|\overline{V}_4| k^2 (B - 2D) + \frac{\partial}{\partial y} [|\overline{V}_4| (2 \frac{\partial D}{\partial y} - \frac{\partial B}{\partial y})] \Bigg) \Bigg] dy, \qquad (C15)$$

$$D_{zi} = -\int \left\{ \frac{g}{\Delta p} 4 (\rho \kappa)_2 (\frac{\rho g}{p})_2 [F \frac{\partial^2 F}{\partial y^2}] \right\} dy, \qquad (C16)$$

and

$$D_{zs} = -\int \left\{ \frac{g}{\Delta p} \rho C_D \left[(E-F) \frac{\partial}{\partial y} [|\overline{V}_4| (2 \frac{\partial F}{\partial y} - \frac{\partial E}{\partial y})] \right] \right\} dy. \qquad (C17)$$

The quasi-geostrophic first law of thermodynamics, Equation (2.8), can be manipulated in a similar manner to derive expressions for C_e and C_z. These are

$$C_z = -\int \frac{2 f_o}{\Delta p} \overline{\omega} \, F \, dy, \qquad (C18)$$

and

$$C_e = -\int [\frac{f_o}{\Delta p} (\omega_C C + \omega_D D)] \, dy. \qquad (C19)$$

APPENDIX D

The difference form of the equation for the prediction of the vertical shear current, u', analogous to Equation (3.8) is

$$\frac{u'^{(\ell+1)}_{ijk} - u'^{(\ell-1)}_{ijk}}{2\Delta t} = G^{\ell}_{ijk} - \frac{1}{H}\sum_{\kappa=1}^{km} G^{\ell}_{ijk}(\Delta z)_k$$

$$+ \Delta V_k f_j \; (\alpha v'^{(\ell+1)}_{ijk} + (1-\alpha) v'^{(\ell-1)}_{ijk}) \qquad (D1)$$

where

$$G^{\ell}_{ijk} = \frac{1}{(\Delta z)_k}\Big\{ -(I_1)_{ijk} - \frac{\Delta A}{4}[w_{ij} + w_{i+1j} + w_{ij+1} + w_{i+1,j-1})_{k-\frac{1}{2}}$$

$$(u)_{k-\frac{1}{2}} - (w_{ij} + w_{i+1j} + w_{ij+1} + w_{i+1,j+1})_{k+\frac{1}{2}} \; (u)_{k+\frac{1}{2}}]_{ij}$$

$$- \frac{1}{\rho_o}\,\Delta y(\Delta z)_k\,\frac{1}{2}[(P_{i+1j} + P_{i+1,j+1}) - (P_{ij} + P_{ij+1})]_k \Big\}^{\ell}$$

$$+ \frac{1}{(\Delta z)_k}\Big\{ (\Delta z)_k \;\; A_M[(u_{i+1j} - u_{ij}) - (u_{ij} - u_{i-1j})$$

$$+ (u_{ij+1} - u_{ij}) - (u_{ij} - u_{ij-1})]_k$$

$$+ \Delta A \;\; [\frac{k(u_{k-1} - u_k)_{ij}}{(\Delta z)_{k-\frac{1}{2}}} - \frac{k(u_k - u_{k+1})_{ij}}{(\Delta z)_{k+\frac{1}{2}}}]\Big\}^{\ell-1} \qquad (D2)$$

and

$$\Delta V_k = \Delta x \;\Delta y(\Delta z)_k$$

and

$$\Delta A = \Delta x \; \Delta y$$

and

$$\begin{aligned}
(I_1)_{ijk} \equiv {} & [\tfrac{1}{2}(u_{ij}+u_{i+1j})_k \; \frac{\Delta y(\Delta z)_k}{8} \Big((u_{i+1j}+ u_{i+1j-1}) \\
& + (u_{ij} + u_{ij-1}) + (u_{i+1j+1} + u_{i+1j}) \\
& + (u_{ij+1} + u_{ij})\Big)_k] \\
& - [\tfrac{1}{2}(u_{i-1j} + u_{ij}) \; \frac{\Delta y(\Delta z)_k}{8} \Big((u_{ij} + u_{ij-1}) \\
& + (u_{i-1j}+ u_{i-1j-1})+(u_{ij+1} + u_{ij})+(u_{i-1j+1} \\
& + u_{i-1j})\Big)_k] \\
& + [\tfrac{1}{2}(u_{ij}+ u_{ij+1}) \; \frac{\Delta x(\Delta z)_k}{8} \Big((v_{ij+1} + v_{i-1j+1}) \\
& + (v_{ij}+ v_{i-1j})+(v_{i+1j}+ v_{ij})+(v_{i+1j-1}+ v_{ij-1})\Big)_k] \\
& + \tfrac{1}{2}(u_{ij-1}+ u_{ij}) \; \frac{\Delta x(\Delta z)_k}{8} \Big((v_{ij} + v_{i-1j}) \\
& +(v_{ij-1}+v_{i-1j-1})+(v_{i+1j}+v_{ij})+(v_{i+1j-1}+v_{ij-1})\Big)_k].
\end{aligned} \tag{D3}$$

The difference form of the equation of the meridional component of the vertical shear current, v', analogous to Equation (3.9) is

$$\frac{v'^{(\ell+1)}_{ijk} - v'^{(\ell-1)}_{ijk}}{2\Delta t} = R^{\ell}_{ijk} - \frac{1}{H} \sum_{k=1}^{km} R^{\ell}_{ijk} \; (\Delta z)_k$$

$$-\Delta V_k f_j [\alpha (u')^{(\ell+1)}_{ijk} + (1+\alpha)\, u'^{(\ell-1)}_{ijk}] \qquad (D4)$$

where

$$\begin{aligned}
R^{\ell}_{ijk} \equiv \frac{1}{(\Delta z)_k} \Bigg\{ &-(I_2)_{ijk} - \frac{\Delta A}{4}[(w_{ij}+w_{i+1j}+w_{ij+1}+w_{i+1j+1})_{k-\frac{1}{2}} \\
&\cdot (v)_{k-\frac{1}{2}} - (w_{ij}+w_{i+1j}+w_{ij+1}+w_{i+1j+1})_{k+\frac{1}{2}}\ (v)_{k+\frac{1}{2}}]_{ij} \\
&- \frac{1}{\rho_o}\ \Delta x (\Delta z)_k\ \frac{1}{2}[(P_{ij+1}+P_{i+1j+1}) - (P_{ij}+P_{i+1j})]_k \Bigg\}^{\ell} \\
&+ \frac{1}{(\Delta z)_k} \Bigg\{ (\Delta z)_k \quad A_M[(v_{i+1j}-v_{ij}) - (v_{ij} - v_{i-1j}) \\
&+ (v_{ij+1} - v_{ij}) - (v_{ij} - v_{ij-1})]_k \\
&+ \Delta A \left[\frac{k(v_{k-1} - v_k)_{ij}}{(\Delta z)_{k-\frac{1}{2}}} - \frac{k(v_k - v_{k+1})_{ij}}{(\Delta z)_{k+\frac{1}{2}}}\right] \Bigg\}^{\ell-1} \qquad (D5)
\end{aligned}$$

and

$$\begin{aligned}
(I_2)_{ijk} \equiv \Bigg\{ &[\tfrac{1}{2}(v_{ij}+v_{i+1j})_k \cdot \frac{\Delta y (\Delta z)_k}{8} \Big((u_{i+1j} + u_{i+1j-1}) \\
&+ (u_{ij} + u_{ij-1}) + (u_{i+1j+1}) + (u_{ij+1} + u_{ij})\Big)_k] \\
&- [\tfrac{1}{2}(v_{i-1j} + v_{ij}) \cdot \frac{\Delta y (\Delta z)_k}{8} \Big((u_{ij} + u_{ij-1}) + (u_{i-1j} + u_{i-1j-1}) \\
&+ (u_{ij+1} + u_{ij}) + (u_{i-1j+1} + u_{i-1j})\Big)_k] \\
&+ [\tfrac{1}{2}(v_{ij}+v_{ij+1})\ \frac{\Delta x (\Delta z)_k}{8} \Big((v_{ij+1} + v_{i-1j+1}) \\
&+ (v_{ij} + v_{i-1j}) + (v_{i+1j} + v_{ij}) + (v_{i+1j-1} + v_{ij-1})\Big)_k] \\
&+ [\tfrac{1}{2}(v_{ij-1} + v_{ij}) \cdot \frac{\Delta x (\Delta z)_k}{8} \Big((v_{ij} + v_{i-1j}) \\
&+ (v_{ij-1} + v_{i-1j-1}) + (v_{i+1j} + v_{ij}) + (v_{i+1j-1} + v_{ij-1})\Big)_k] \Bigg\} . \qquad (D6)
\end{aligned}$$

At each time level ℓ, Equations (D1) and (D4) are solved together for the unknown shear currents, $u'^{\,\ell+1}_{ijk}$ and $v'^{\,\ell+1}_{ijk}$.

The difference form of the vorticity equation analogous to Equation (3.12) is

$$L(\psi_{ij})^{\ell+1} - L(\psi_{ij})^{\ell-1} = [\tfrac{1}{2}\left((I_3)_{ij} + (I_3)_{ij-1}\right) - \tfrac{1}{2}\left((I_3)_{i-1j} + (I_3)_{i-1,j-1}\right) - \tfrac{1}{2}\left((I_4)_{ij} + (I_4)_{i-1j} + \tfrac{1}{2}\left((I_4)_{ij-1} + (I_4)_{i-1j-1}\right) - \beta_o\left(\frac{\psi_{i+1j} - \psi_{i-1j}}{2\Delta x}\right)]^{\ell} \qquad \text{(D7)}$$

where

$$(I_3)^{\ell}_{ij} = \frac{1}{H}\sum_{k=1}^{km}\frac{1}{\Delta y}\Big\{-(I_1)^{\ell}_{ijk} + (\Delta z)_k\, A_M[(u_{i+1j} - u_{ij}) - (u_{ij} - u_{i-1j}) + (u_{ij+1} - u_{ij}) - (u_{ij} - u_{ij-1})]_k^{(\ell-1)} + \Delta A\left[\frac{k(u_{k-1} - u_k)_{ij}}{(\Delta z)_{k-\frac{1}{2}}} - \frac{k(u_k - u_{k+1})_{ij}}{(\Delta z)_{k+\frac{1}{2}}}\right]^{(\ell+1)}\Big\}, \qquad \text{(D8)}$$

$$(I_4)^{\ell}_{ij} = \frac{1}{H}\sum_{k=1}^{km}\frac{1}{\Delta x}\Big\{(-I_2)^{\ell}_{ijk} + (\Delta z)_k\, A_M[(v_{i+1j} - v_{ij}) - (v_{ij} - v_{i-1j}) + (v_{ij+1} - v_{ij}) - (v_{ij} - v_{ij-1})]_k^{(\ell-1)} + \Delta A\left[\frac{k(v_{k-1} - v_k)_{ij}}{(\Delta z)_{k-\frac{1}{2}}} - \frac{k(v_k - v_{k+1})_{ij}}{(\Delta z)_{k+\frac{1}{2}}}\right]_k^{\ell-1}\Big\}, \qquad \text{(D9)}$$

and

$$L(\psi)_{ij} = \tfrac{1}{2}[\psi_{i+1j+1} + \psi_{i-1j+1} + \psi_{i+1j-1} + \psi_{i-1j-1} - 4\psi_{ij}]. \qquad \text{(D10)}$$

Equation (D7) is solved by relaxation techniques to obtain $\psi_{ij}^{\ell+1}$.

The difference form of the thermodynamic equation analogous to Equation (3.16) is

$$\begin{aligned}
\frac{(T_{ijk}^{(\ell+1)} - T_{ijk}^{(\ell-1)})}{2\Delta t}\,\Delta V_k = & -[(I_5)_{ijk} + (w_{ij} + w_{i+1j} \\
& + w_{ij+1} + w_{i+1j+1})_{k-\frac{1}{2}}\,(T)_{k-\frac{1}{2}} - (w_{ij} + w_{i+1j} + w_{ij+1} \\
& + w_{i+1j+1})_{k+\frac{1}{2}}\,(T)_{k+\frac{1}{2}}]^{\ell} + (\Delta z)_k\, A_H[(T_{i+1j} - T_{ij}) \\
& - (T_{ij} - T_{i-1j}) + (T_{ij+1} - T_{ij}) - (T_{ij} - T_{ij-1})]_k^{(\ell-1)} \\
& + \Delta A\left[\frac{k(T_{k-1} - T_k)}{(\Delta z)_{k-\frac{1}{2}}} - \frac{k(T_k - T_{k-1})}{(\Delta z)_{k+\frac{1}{2}}}\right]_{ij}^{(\ell-1)} \\
& + \frac{(\Delta z)_k}{\Delta t}\,(\delta T)_C \qquad \text{(D11)}
\end{aligned}$$

where

$$\begin{aligned}
(I_5)_{ijk} \equiv \Big\{ \frac{1}{4}[& (T_{ij} + T_{i+1j})_k \cdot (u_{ij} + u_{ij-1})_k \\
& - (T_{i-1j} + T_{ij})_k \cdot (u_{i-1j} + u_{i-1j-1})_k \\
& + (T_{ij} + T_{ij+1})_k \cdot (v_{ij} + v_{i-1j})_k \\
& - (T_{ij-1} + T_{ij})_k \cdot (v_{ij-1} + v_{i-1j-1})_k] \Big\},
\end{aligned}$$

and

$\frac{(\Delta z)_k}{\Delta t}(\delta T)_C$ is the convective adjustment discussed previously.

REFERENCES

1. Arakawa, A., 1966: "Computational design for long term numerical integration of the equations of fluid motion: two-dimensional incompressible flow, Part 1." J. Comp. Phys., 1. 119-143.

2. Bjerknes, J., 1962: "Synoptic study of the interaction of sea and atmosphere in the North Atlantic." Geofysiske Publikasjoner Geophysica Novegica, 14, 3, 115-145.

3. Bryan, K., 1959: "A numerical investigation of certain features of the general circulation." Tellus, 11, 2, 163-174.

4. Bryan, K., 1963: "A numerical investigation of a non-linear model of a wind-driven ocean." Journal of the Atmospheric Sciences, 20, 5, 594-606.

5. Bryan, K., 1969: "Climate and the ocean circulation: III. The ocean model." Monthly Weather Review, 97, 11, 806-827.

6. Bryan, K., and M. D. Cox, 1967: "A numerical investigation of the oceanic general circulation." Tellus, 19, 1, 54-80.

7. Budyko, M. I., 1956: Teplovi balans zemnoi poverkhrosti, (Heat balance of the earth's surface), Gidrometeoizdat, Leningrad, 1956, 255 pp.

8. Dixon, W. J., 1970: BMD, Biomedical computer programs, University of California Publication in Automatic Computation No. 2., University of California Press, 600 pp.

9. Fisher, G., 1965: "A survey of finite difference approximations to the primitive equations." Monthly Weather Review, 93, 1, 1-10.

10. Fofonoff, N. P., 1954; "Steady flow in a frictionless homogeneous ocean." Journal of Marine Research," 13, 3, 254-262.

11. Gates, W. L., 1968: "A numerical study of transient Rossby waves in a wind driven homogeneous ocean." Journal of the Atmospheric Sciences, 25, 1, 3-22.

12. Gates, W. L., E. S. Botten, A. B. Kahle and A. B. Nelson, 1971: *A documentation of the Mintz-Arakawa two-level atmospheric general circulation model*. RAND Document, 1971, the RAND Corporation, Santa Monica, California 90406.

13. Haney, R. L., 1971: "Surface thermal boundary conditions for oceanic circulation models." *Journal of Physical Oceanography*, *1*, 4, 241-248.

14. Haney, R. L., 1971a: *A numerical study of the large scale responses of an ocean circulation to surface heat and momentum flux*. Ph.D. Thesis, UCLA, 191 pp.

15. Hellerman, S., 1967: "An updated estimate of the wind stress on the world ocean." *Monthly Weather Review*, *95*, 9, 607-626; and "Correction Notices," *Monthly Weather Review*, *95*, 12, 966 and *96*, 1, 63-74.

16. Kasahara, A., and W. Washington, 1967: "NCAR global general circulation model of the atmosphere." *Monthly Weather Review*, *95*, 7, 389-402.

17. Kesel, P. G., and F. J. Winninghoff, 1972: "The Fleet Numerical Weather Central operational primitive equation model." *Monthly Weather Review*, *100*, 5, 360-373.

18. Leith, C. E., 1965: "Numerical simulation of the earth's atmosphere," *Methods in Computational Physics*, *4*, Academic Press, New York, 1965, 1-28.

19. London, J., 1957: *A study of the atmospheric heat balance*. Final Report, Contract No. AF19 (122)-165, Department of Meteorology and Oceanography, New York University, 99 pp.

20. Lorenz, E. N., 1960: "Maximum simplification of the dynamic equations." *Tellus*, *12*, 3, 243-254.

21. Manabe, S., 1969a: "Climate and ocean circulation: I. The atmospheric circulation and hydrology of the earth's surface." *Monthly Weather Review*, *97*, 11, 739-774.

22. Manabe, S., 1969b: "Climate and ocean circulation: II. The atmospheric circulation and the effect of heat transfer by ocean current." *Monthly Weather Review*, *97*, 11, 775-805.

23. Matsuno, T., 1966: "Numerical integrations of the primitive equations by a simulated backward difference method." *Journal of the Meteorological Society of Japan*. Ser 2, *44*, 76-84.

24. Mintz, Y., 1964: Very long term global integration of the primitive equations of atmospheric motion. WMO/iu66 Symposium on Research and Development Aspects of Long Range Forecasting. Boulder, Colorado, 1964. Technical Note No. 66, 141-167.

25. Munk, W. S., 1950: "On the wind-driven ocean circulation." Journal of Meteorology, 7, 2, 79-93.

26. Namias, J., 1969: "Seasonal interaction between the North Pacific Ocean and the atmosphere during the 1960's." Monthly Weather Review, 97, 3, 173-192.

27. Oort, A. H., 1964: "On the estimates of the atmospheric energy cycle." Monthly Weather Review, 92, 11, 483-493.

28. Palmén, E., 1955: "On the mean meridional circulation in low latitudes of the Northern Hemisphere in winter and the associated meridional and vertical heat flux of angular momentum." Societas Scientiarum Fennica, Commentations Physico - Mathematical, 17, 8, 1-33.

29. Phillips, N. A., 1956: "The general circulation of the atmosphere: A numerical experiment." Quarterly Journal of the Royal Meteorological Society, 82, 123-164.

30. Phillips, N. A., 1963: "Geostrophic Motion." Review of Geophysics, 1, 2, 123-176.

31. Riehl, H., et al., 1951: "The northeast trade of the Pacific Ocean." Quarterly Journal of the Royal Meteorological Society, 77, 334, 598-626.

32. Richtmyer, R. D., 1957: Difference methods for initial value problems. Interscience Publishers, Inc., New York.

33. Rossby, C. G., and R. B. Montgomery, 1935: The layer of frictional influence in wind and ocean currents." Papers in Physical Oceanography and Meteorology, 3, 3, 101p.

34. Smagorinsky, J., 1963: "On the numerical integration of the primitive equations of motion for baroclinic flow in a closed region." Monthly Weather Review, 86, 12, 457-466.

35. Smagorinsky, J., S. Manabe, and J. L. Holloway, Jr., 1965: "Numerical results from a nine-level general circulation model of the atmosphere." Monthly Weather Review, 93, 12, 727-768.

36. Sverdrup, H. U., M. W. Johnson and F. H. Fleming, 1942: *The Oceans, Their Physics, Chemistry and General Biology*, Prentice-Hall, Inc., New York, 1087 pp.

37. Taylor, F. H., 1970: *General circulation experiments with a two-level quasi-geostrophic model including the nonlinear interaction between a single wave in the zonal direction and the mean flow.* M.S. Thesis, Naval Postgraduate School, Monterey, California, 49 pp.

38. Thompson, R., 1971: "Topographic Rossby waves at a site north of the Gulf Stream." *Deep-Sea Research*, *18*, 1-19.

39. Trumbower, G., 1972: "*General circulation experiments with a two-level quasi-geostrophic model including nonlinear interaction between two waves and the mean flow.* M.S. Thesis, Naval Postgraduate School, Monterey, California, 71 pp.

40. Veronis, G., 1963a: "On inertially-controlled flow patterns in a β-plane ocean." *Tellus*, *15*, 1, 59-66.

41. Veronis, G., 1963b: "An analysis of wind driven ocean circulation with a limited number of Fourier components." *Journal of the Atmospheric Sciences*, *20*, 6, 577-593.

42. Veronis, G., 1965: "On parametric values and type of representation in wind driven ocean circulation studies." *Tellus*, *17*, 1, 77-84.

43. Veronis, G., 1966: "Generation of mean ocean circulation by fluctuating winds." *Tellus*, *18*, 1, 67-76.

44. Wallace, J. M., 1971: "Spectral studies of tropospheric wave disturbances in the tropical Western Pacific." *Review of Geophysics and Space Physics*, *9*, 3, 557-612.

45. Wetherald, R. T., and S. Manabe, 1972: "Response of the joint ocean-atmosphere model to the seasonal variation of the solar radiation." *Monthly Weather Review*, *100*, 1, 42-59.

46. Yanai, M., T. Maruyomo, T. Nitta and Y. Hayaski, 1968: "Power spectra of large-scale disturbances over the tropical Pacific." *Journal of the Meteorological Society of Japan*, *46*, 4, 308-323.

INITIAL DISTRIBUTION LIST

		No. Copies
1.	Defense Documentation Center Cameron Station Alexandria, Virginia 22314	2
2.	Library, Code 0212 Naval Postgraduate School Monterey, California 93940	2
3.	Associate Professor Roger T. Williams, Code 51 Department of Meteorology Naval Postgraduate School Monterey, California 93940	10
4.	Lieutenant Commander Wayne Roger Lambertson Fleet Numerical Weather Central Naval Postgraduate School Monterey, California 93940	5
5.	Naval Weather Service Command Washington Navy Yard Washington, D. C. 20390	1
6.	Officer in Charge Environmental Prediction Research Facility 404 Franklin Street Monterey, California 93940	1
7.	Commanding Officer U. S. Fleet Weather Central COMNAVMARIANAS, Box 12 FPO San Francisco, California 96630	1
8.	Commanding Officer Fleet Weather Central Box 31 FPO New York, New York 09540	1
9.	Commanding Officer Fleet Numerical Weather Central Naval Postgraduate School Monterey, California 93940	1

10. ARCRL - Research Library 1
L. G. Hanscom Field
Attn: Nancy Davis/Stop 29
Bedford, Massachusetts 01730

11. Director, Naval Research Laboratory 1
Attn: Tech. Services Info. Officer
Washington, D. C. 20390

12. American Meteorological Society 1
45 Beacon Street
Boston, Massachusetts 02128

13. Department of Meteorology, Code 51 3
Naval Postgraduate School
Monterey, California 93940

14. Department of Oceanography, Code 58 1
Naval Postgraduate School
Monterey, California 93940

15. Office of Naval Research 1
Department of the Navy
Washington, D. C. 20360

16. Commander, Air Weather Service 2
Military Airlift Command
U. S. Air Force
Scott Air Force Base, Illinois 62226

17. Atmospheric Sciences Library 1
National Oceanographic Atmospheric Administration
Silver Spring, Maryland 20910

18. Professor Victor Starr 1
Department of Meteorology
M. I. T.
Cambridge, Massachusetts 03139

19. Dr. J. Pedlosky 1
Department of Geophysical Sciences
University of Chicago
Chicago, Illinois 60637

20. Dr. Joanne Simpson 1
Experimental Meteorology Branch
National Oceanographic Atmospheric Administration
Coral Gables, Florida 33124

21.	Dr. George Platzman Department of Geophysical Sciences University of Chicago Chicago, Illinois 60637	1
22.	Dr. A. Huss Department of Meteorology Hebrew University Jerusalem, Israel	1
23.	National Center for Atmospheric Research Box 1470 Boulder, Colorado 80302	1
24.	Dr. T. N. Krishnamurti Department of Meteorology Florida State University Tallahassee, Florida 32306	1
25.	Dr. Fred Shuman Director National Meteorological Center Environmental Science Services Administration Suitland, Maryland 20390	1
26.	Dr. J. Smagorinsky Director Geophysical Fluid Dynamics Laboratory Princeton University Princeton, New Jersey 08540	1
27.	Professor N. A. Phillips 54-1422 M. I. T. Cambridge, Massachusetts 02139	1
28.	Dr. E. N. Lorenz Department of Meteorology M. I. T. Cambridge, Massachusetts 02139	1
29.	Professor J. G. Charney 54-1424 M. I. T. Cambridge, Massachusetts 02139	1
30.	Professor K. Ooyama Department of Meteorology New York University University Heights New York, New York 10453	1

31. Dr. M. G. Wurtele 1
Department of Meteorology
UCLA
Los Angeles, California 90024

32. Dr. A. Arakawa 1
Department of Meteorology
UCLA
Los Angeles, California 90024

33. Dr. David Houghton 1
Department of Meteorology
University of Wisconsin
Madison, Wisconsin 53706

34. Dr. S. K. Kao 1
Department of Meteorology
University of Utah
Salt Lake City, Utah 84112

35. Dr. J. Holton 1
Department of Atmospheric Sciences
University of Washington
Seattle, Washington 98105

36. Dr. Yale Mintz 1
Department of Meteorology
UCLA
Los Angeles, California 90024

37. Dr. P. Thompson 1
National Center for Atmospheric Research
Box 1470
Boulder, Colorado 80302

38. Dr. Peter Stone 1
Pierce Hall
Harvard University
Cambridge, Massachusetts 02138

39. Dr. John Young 1
Department of Meteorology
University of Wisconson
Madison, Wisconsin 53706

40. Dr. George J. Haltiner 1
Chairman, Department of Meteorology
Naval Postgraduate School
Monterey, California 93940

41. Dr. Jerry D. Mahlman 1
Geophysical Fluid Dynamics Laboratory
Princeton University
Princeton, New Jersey 08540

42. Dr. Russell Elsberry 1
Department of Meteorology
Naval Postgraduate School
Monterey, California 93940

43. Commanding Officer 1
Pacific Missile Range
Attn: Geophysics Division
Point Mugu, California 93041

44. Professor Jacob Bjerknes 1
Department of Meteorology
UCLA
Los Angeles, California 90024

45. Lieutenant Commander Frank H. Taylor 1
U. S. Fleet Weather Central
Box 113
FPO, San Francisco, California 96610

46. Dr. Victor Barcilon 1
Institute of Geophysics and Planetary Physics
UCLA
Los Angeles, California 90024

47. Lieutenant G. C. Trumbower 1
Fleet Numerical Weather Facility
Naval Postgraduate School
Monterey, California 93940

48. Lieutenant Commander P. Kesel 1
Fleet Numerical Weather Facility
Naval Postgraduate School
Monterey, California 93940

49. Dr. Andrew P. Ingersoll 1
Division of Geological and Planetary Sciences
California Institute of Technology
Pasadena, California 91109

50. Dr. Robert L. Haney 5
Department of Meteorology
Naval Postgraduate School
Monterey, California 93940

51. Dr. Ron L. Alberty 1
Department of Meteorology
Naval Postgraduate School
Monterey, California 93940

52. Dr. W. L. Gates 1
Rand Corporation
1700 Main Street
Santa Monica, California 90406

53. Dr. Richard Alexander 1
The Rand Corporation
1700 Main Street
Santa Monica, California 90406

54. Commanding Officer 1
Fleet Weather Central
Box 110
FPO San Francisco, California 96610

55. Dr. K. L. Davidson 1
Department of Meteorology
Naval Postgraduate School
Monterey, California 93940

56. Dr. M. S. Tracton 1
Department of Meteorology
Naval Postgraduate School
Monterey, California 93940

57. Dr. F. L. Martin 1
Department of Meteorology
Naval Postgraduate School
Monterey, California 93940

58. Dr. J. A. Galt 1
Department of Oceanography
Naval Postgraduate School
Monterey, California 93940

59. Dr. N. E. Boston 1
Department of Oceanography
Naval Postgraduate School
Monterey, California 93940

60. Dr. U. R. Kodres 1
Department of Mathematics
Naval Postgraduate School
Monterey, California 93940

61. Dr. J. V. Sanders 1
Department of Physics
Naval Postgraduate School
Monterey, California 93940

62. Dr. K. Bryan 1
Geophysical Fluid Dynamics Laboratory
Princeton University
Princeton, New Jersey 08540

63. Dr. S. Manabe 1
Geophysical Fluid Dynamics Laboratory
Princeton University
Princeton, New Jersey 08540

64. Dr. George Veronis 1
Department of Geology and Geophysics
Yale University
Box 2161, Yale Station
New Haven, Connecticut 06520

65. Dr. H. Stommel 1
Department of Meteorology
M. I. T.
Cambridge, Massachusetts 02139

66. Dr. P. Welander 1
Göteborgs Universitet
Gothenburg, Sweden

67. Dr. R. O. Reed 1
Department of Oceanography
Texas A & M University
College Station, Texas 77843

68. Dr. T. Ogura 1
Laboratory for Atmospheric Research
University of Illinois
Urbana, Illinois 61801

69. Dr. Y. Sasaki 1
Department of Meteorology
University of Oklahoma
Norman, Oklahoma 73069

70. Dr. Adrian E. Gill 1
Department of Applied Mathematics
and Theoretical Physics
University of Cambridge
Cambridge, England

71. Dr. J. Huang 1
Department of Oceanography
Scripps Institution of Oceanography
P. O. Box 109
La Jolla, California 92037

72. Professor Robert Arthur 1
Department of Oceanography
Scripps Institution of Oceanography
P. O. Box 109
La Jolla, California 92037

73. Dr. Tim Barnett 1
Department of Oceanography
Scripps Institution of Oceanography
P. O. Box 109
La Jolla, California 92037

74. Mr. Jerome Namias 1
Department of Oceanography
Scripps Institution of Oceanography
P. O. Box 109
La Jolla, California 92037

75. Department of Oceanography 1
Scripps Institution of Oceanography
P. O. Box 109
La Jolla, California 92037

76. Woods Hole Oceanographic Institution 1
Woods Hole,
Massachusetts 02543

77. Provost M. U. Clauser 1
Naval Postgraduate School
Monterey, California 93940

78. Mrs. O. Haney 1
Environmental Prediction Research Facility
404 Franklin Street
Monterey, California 93940

79. Mr. Tom Baxter 1
Environmental Prediction Research Facility
404 Franklin Street
Monterey, California 93940

80. Mr. M. Endoh 1
Ocean Research Inst.
1-15-1 Minamidai
Nakano-Ku
Tokyo, 164, Japan

81. Dr. Jan Paegle 1
Meteorology Department
University of Utah
Salt Lake City, Utah 84112

82. Department of Meteorology 1
University of Belgrade
Dobracina 16
Belgrade,
Yugoslavia

83. Dr. Kenzo Takano 1
Rikagaku Kenkyusho
Yamato Machi
Saitama Prefecture
Japan

84. Dr. Vladimir Kamenkovich 1
Institute of Oceanography
USSR Academy of Sciences
I Letnyaya, Moscow ZH-387
U.S.S.R.

85. Dr. Edward Thornton 1
Department of Oceanography
Naval Postgraduate School
Monterey, California 93940

DOCUMENT CONTROL DATA - R & D

(Security classification of title, body of abstract and indexing annotation must be entered when the overall report is classified)

1. ORIGINATING ACTIVITY *(Corporate author)*

Naval Postgraduate School
Monterey, California 93940

2a. REPORT SECURITY CLASSIFICATION

Unclassified

2b. GROUP

3. REPORT TITLE

A Numerical Investigation of the Long-Term Transient Behavior in a Coupled Atmosphere-Ocean Model

4. DESCRIPTIVE NOTES *(Type of report and, inclusive dates)*

Doctor's Thesis; September 1972

5. AUTHOR(S) *(First name, middle initial, last name)*

Wayne R. Lambertson

6. REPORT DATE September 1972	7a. TOTAL NO. OF PAGES 229	7b. NO. OF REFS 46

8a. CONTRACT OR GRANT NO.

b. PROJECT NO.

c.

d.

9a. ORIGINATOR'S REPORT NUMBER(S)

9b. OTHER REPORT NO(S) *(Any other numbers that may be assigned this report)*

10. DISTRIBUTION STATEMENT

Approved for public release, distribution unlimited.

11. SUPPLEMENTARY NOTES

12. SPONSORING MILITARY ACTIVITY

Naval Postgraduate School
Monterey, California 93940

13. ABSTRACT

A two-level, quasi-geostrophic atmospheric model on a mid-latitude β-plane with a single wave in the x-direction was coupled with a three level primitive equation ocean model through the exchange of sensible heat and momentum to investigate the effect of the ocean circulation on transients in the atmospheric circulation and vice versa. A long-term (79 years) simulation of the atmosphere-ocean system was carried out. The experiment was conducted in three phases that consisted of integrating the combined, the ocean-only and the atmosphere-only model equations.

The combined model produced realistic patterns of both atmospheric and oceanic circulations. Energy studies of the atmosphere were completed with the results comparing favorably with the existing knowledge of the energy balance in the real atmosphere.

Data were retained at selected points on a daily basis and spectrally analyzed for a simulated six year period. Transients with periods on the order of one and two months appeared in the spectra of both atmospheric and oceanic variables from the combined model. These transients were not observed in the ocean-only or atmosphere-only phases of the experiment, and are attributed to the interaction occurring in the combined model.

14 KEY WORDS	LINK A		LINK B		LINK C	
	ROLE	WT	ROLE	WT	ROLE	WT
Numerical Investigation						
Long-Term Integration						
Transient Behavior						
Coupled Atmosphere-Ocean Model						
Spectrum Analysis						
Two-level, quasi-geostrophic atmospheric model						
Three-level, primitive equation ocean model						
Long-period oscillations						

DD FORM 1 NOV 65 1473 (BACK)
S/N 0101-807-6821

22MAY75 22122

Thesis 138208
L2545 Lambertson
c.1 A numerical investigation of the long-term transient behavior in a coupled atmosphere-ocean model.
22MAY75 22122

Thesis 138208
L2545 Lambertson
c.1 A numerical investigation of the long-term transient behavior in a coupled atmosphere-ocean model.

thesL2545
A numerical investigation of the long-te
3 2768 002 11301 1
DUDLEY KNOX LIBRARY